Università degli Studi di Genova
Facoltà di Scienze M.F.N.

Istituto Italiano di Tecnologia
Nanoscopy & NIC@IIT

PhD Thesis

Development of polarization-resolved optical scanning microscopy imaging techniques to study biomolecular organizations

Candidate: Ali Mohebi

Tutor:
Prof. Alberto Diaspro

Supervisor:
Dr. Aymeric Le Gratiet

Table of Contents

List of Figures

List of Tables

List of abbreviations

Abbreviation	Definition
AC	Alternating current
AFM	Atomic Force Microscopy
BS	Beam Splitter
B-SHG	Backward Second Harmonic Generation
CARS	Coherent anti-Stokes Raman scattering
CCD	Charge-Coupled Device
CD	Circular Dichroism
CIDS	Circular Intensity Differential Scattering
CL	Cylindrical lens
CLSM	Confocal Laser Scanning Microscopy
CMOS	Complementary Metal Oxide Semiconductor
CRC	Colorectal cancer
CT	Computed Tomography
DC	Direct current
DIC	Differential Interference Contrast
DM	Dichroic Mirror
DNA	Deoxyribo Nucleic Acid
DoA / DoAM	Division of Amplitude
DoAP	Division of Aperture
DoF	Division of Focal plane
DoP	Degree of Polarization
DOT	Diffuse Optical Tomography
FLIM	Fluorescence lifetime imaging
FOV	Field of View
FPM	Fluorescence Polarization Microscopy
FR	Fresnel Rhomb
F-SHG	Forward Second Harmonic Generation
HCoEpiC	Human Colon Epithelial Cells
HEK	Human embryonic kidney cells
HT29	Human Epithelial Colon Adenocarcinoma Cells
HWP	Half Wave-Plate
LB	Linear Birefringence
LCP	Left circular polarization
LD	Linear Dichroism
LP	Linear Polarizer
MM	Mueller Matrix
MPM	Multiphoton Microscopy

Abbreviation	Definition
2D	Two-Dimensional
2PEF	Two-Photon Excitation Fluorescence
MPLSM	Multiphoton Laser Scanning Microscopy
MRI	Magnetic Resonance Imaging
MOMIX	Multimodal Optical Microscopy Image Correlation Sensing
NA	Numerical Aperture
ND	Neutral Density
NIR	Near InfraRed
OCT/M	Optical Coherence Tomography / Microscopy
PA	Photo-Acoustic
PBS	Polarizing Beam Splitter
PDA	Amplified Photodetector
PEM	Photo-elastic Modulator
PET	Positron Emission Tomography
PF	Polarizing Filter
PL	Powell lens
PLM	Polarized Light Microscopy
PLST	Polarized Light Sheet Tomography
PM	Polarization Modulation
PMT	Photo-Multiplier Tube
PSA	Polarization State Analyzer
PSF	Point Spread Function
PSG	Polarization State Generator
P-SHG	Polarization-resolved Second Harmonic Generation
P-THG	Polarization-resolved Third Harmonic Generation
QWP	Quarter Wave-Plate
RCP	Right circular polarization
ROI	Region of Interest
RP-CARS	Rotating-Polarization Coherent Anti-Stokes Raman Spectroscopy
SEM	Scanning Electron Microscopy
SHG	Second Harmonic Generation
SLM	Scanning Laser Microscopy
SNR	Signal-to-Noise Ratio
TE	Telescope
THG	Third Harmonic Generation
TL	Tube lens
US	Ultrasound
WP	Wollaston Prism

General introduction

Light is electromagnetic radiation, in which fluctuations of the electric and magnetic fields transport energy through space and time. Light microscopy imaging and spectroscopy are methods used to determine a material's properties through light-matter interactions. The main interactions are transmission, absorption, scattering, reflection, and non-linear processes that can be quantified by determining the main characteristics of light, such as intensity, direction, wavelength, phase, and polarization.

The principal feature for biological cell functioning, development, growth, and reproduction is a genetic material called chromatin, a complex of macromolecules composed of DNA shaped like a double helix coiling around histone proteins in a highly compact way inside cell nuclei. Since the nucleic acid is organized in a helical way, it presents a chiral formation as the most commonly seen structure.

Optical microscopy tools have been widely used for the visualization of cellular structures and genetic analysis in cells *in-vitro* and *in-vivo*. Understanding the functioning procedures in bio-organisms can be achieved through a combination of different contrast mechanisms detected by multimodal biomedical imaging approaches and efficient measurement techniques capable of achieving nanometer resolution. Among the contrast mechanisms, fluorescence techniques are the most common and quantitative method available for studying samples. These techniques have the capability of detecting and quantifying sub-microscopic amounts of macromolecules down to single molecules. In this way, the sample's molecules are marked by fluorophores to show the structures of interest, which yields a detailed, specific, and reliable image. Detection and mapping of these anisotropies have played an important role in biomedical imaging and are useful for establishing biomarkers for non-invasive cellular investigations due to the high sensitivity of light polarization to microstructural organizations. Accordingly, the use of light polarization can bring a complementary degree of freedom to the investigations. Polarization has been known since 1808, when the French physicist Étienne Louis Malus discovered the refraction and polarization of light, and William Nicol invented a prism for polarization in 1829, as an indispensable part of the polarizing microscope for over 100 years. Polarization adds another dimension to quantifying the specific orientation of molecular anisotropies and provides a means of revealing hidden information that is not provided by most conventional imaging techniques. This is due to the

particular sensitivity of polarization to the amplitude and phase of light, allowing for more precise and detailed analyses of biological structures at the microscopic level.

The description of light polarization typically involves the use of two formalisms: Jones and Stokes-Mueller. The Jones formalism is an older method that characterizes light in terms of its physical properties, such as the electric field. However, it is limited in its ability to describe depolarization and is thus unsuitable for many biophysical systems, which often exhibit strong depolarization properties. Conversely, the Stokes-Mueller formalism is a more practical approach that enables researchers to work with easily measurable quantities, such as light intensity, enabling them to determine polarization interactions. This has made polarization-resolved imaging techniques a popular choice for biomedical diagnostic applications that require a detailed analysis of polarimetric effects, as they can provide valuable information on parameters such as retardance, diattenuation, and depolarization.

Among polarimetric techniques, Circular Dichroism (CD) microscopy has been shown to be the method of choice for determining the high-order structure of large biopolymers and is sensitive to the concentration of chiral molecules such as chromatin by measuring the differential interaction of light polarized circularly left or right with the specimen. The main part of the signal in CD microscopy is due to absorption and a weak scattering component of light and chiral polymers. Outside the absorption band and off the incident light axis, the scattering component of circular dichroism is called Circular Intensity Differential Scattering (CIDS), which is sensitive to chiral structures and provides information about the chirality and/or the handedness of the molecules of interest.

To combine the benefits of both polarization and fluorescence microscopy, fluorescence polarization microscopy (FPM) emerges as a valuable technique. This method not only capitalizes on the advantages of polarization and fluorescence but also leverages the benefits of endogenous anisotropy contrast. By employing FPM, a wealth of information regarding cellular composition, structure, and their implications for biological functions can be obtained. Polarization-resolved fluorescence imaging microscopy techniques hold immense potential in detecting molecular binding affinity, assessing structural characteristics, and quantifying deviations in bio-macromolecular arrangements when compared to control samples. As the progression of diseases often induces changes in the polarimetric signature of the sample, the measurement of two states enables the acquisition of information on fluorescence anisotropy, thereby serving as a valuable tool for cancer diagnosis. Notably, when applied in two-photon imaging microscopy, the utilization of longer excitation wavelengths enhances the depth of penetration into scattering media. Moreover, it facilitates the quantitative assessment of molecular interactions and intracellular disorders.

The aim of this thesis is to implement polarization-resolved imaging optical scanning techniques for the study of biological organization. It is divided into three main parts. Firstly, upgrading an existing multimodal CIDS/fluorescence microscopy. Secondly, proposing a new method for discriminating different cell types through this technique by comparing classical CIDS with an innovative phasor representation. Thirdly, implementing a polarization analysis of the fluorescence emission for pathology investigation. The established framework is aimed at creating sensitive mechanisms and defining specifications to track microscopic objects.

This thesis is composed of three chapters as follows:

In Chapter 1, the theory of light propagation and polarization is explained, along with the two main formalisms for describing polarization: the Jones and Stokes-Mueller formalisms. The discussion also covers the physical concepts involved in the modification of the polarization of the incident light when it interacts with an optical element in transmission and/or reflection. The next part of the chapter discusses image contrast in polarizing microscopes. This is based on the ability of polarized light to interact with polarizable bonds of ordered molecules in a direction-sensitive manner. The remaining sections focus on linear and non-linear polarization-resolved microscopy techniques and their related examples. Among the label-free methods, Mueller matrix microscopy is discussed as a comprehensive polarimetric method that provides complete polarization information of a sample. This technique is capable of capturing the full polarization response of light interacting with the sample, making it a powerful tool for studying biological structures and materials. Additionally, the chapter includes a discussion on linear and non-linear fluorescence polarization microscopy.

In Chapter 2, the label-free light scattering method known as CIDS is shown, using a homemade single point angular spectroscopy mode and a scanning microscopy imaging one. In this chapter, the previous work from a former PhD student is resumed. One of the main goals of this thesis is to upgrade the existing setup to enhance its performance based on an open configuration, calibration procedure, automation of a lock-in amplifier detection and the development of analytical routines for statistics. As a result, image processing programs have been developed to provide automated measurements using polarization-resolved laser scanning microscopy imaging integrated with confocal fluorescence microscopy of cells and chromatin inside cell nuclei, including the use of new types of samples such as progeria cells. To facilitate data analysis, a new, intuitive graphical representation is proposed through a phasor approach that is sensitive to polarimetric signal changes. This representation allows for image segmentation, cell discrimination, and easy interpretation of the polarimetric contrast in the corresponding frequency domain, making it accessible to new users. In this chapter, the potential of polarization imaging as an independent technique is investigated, with a comparison made to fluorescence imaging as the standard reference. Our findings demonstrate that polarization imaging possesses the capacity to unveil concealed information that is not easily discernible through fluorescence imaging alone.

In Chapter 3, multicellular cancerous cells are studied using polarization-resolved two-photon excitation fluorescence (2PEF) imaging microscopy. The goal is to utilize the additional polarimetric contrast provided by the polarization add-ins by building and developing a homemade 2PEF microscope prototype with a fixed excitation wavelength for the structural discrimination of colon cancer cells in spheroids and tissues at the sub-cellular level, due to the fluorescence anisotropic effect. The setup comprises two possible configurations of polarization modules to determine the impact of linear and circular polarized light on the excitation, according to absorption and spatial homogeneity. An innovative approach of phasor map is proposed for analyzing the image dataset, which is adapted to colon cancer diagnosis by mapping the extracted anisotropies from the nonlinear 2PEF signal in the reciprocal domain pixel-by-pixel. Building upon this foundation, our research in this chapter is advanced through the integration of polarization with fluorescence. By combining these techniques, significant advantages are realized, allowing for the extraction of valuable insights into the orientation of specific molecules. Through the utilization of the complementary strengths inherent in both techniques, a more comprehensive understanding of the samples under investigation is achieved.

Chapter 1

Light polarization formalism and microscopy application

1.1 Introduction

Light is an electromagnetic radiation described by theoretical propagating wave principles. Electromagnetic radiation propagates in the form of two orthogonally vector waves: an electric wave and a magnetic wave. Augustin Jean Fresnel advanced a theory of light in which waves exhibit transverse vibrations [1]. The properties of a light wave include its intensity, frequency, phase, direction of propagation, and polarization. For monochromatic light, the change in orientation of $\vec{E}(r,t)$ varies sinusoidally with time, amplitude, and phase in a plane perpendicular to the propagation of the wave. If the sum of the randomly oriented waves results in a wave whose direction of polarization changes rapidly and randomly, then the wave is defined as unpolarized light. The general form of polarized light with arbitrary amplitudes is elliptical polarization. When dealing with the same amplitudes but differing in phase by 90° of the electric orthogonal components, then the light is said to be circularly polarized. Otherwise, it leads to elliptical or linear polarization states. Polarization plays an important role in light-matter interactions. For example, the amount of light scattered by an optically active material depends on the polarization of the incident light. Thus, by manipulating the amplitude and phase of the orthogonal components of the incident light, the optical fingerprint of the scattering medium reveals the polarization properties such as birefringence, dichroism, and scattering that provide the sample composition and its microstructural information. This is the principle of polarimetry technique, which measures and interprets the polarization of light to characterize an object.

This chapter covers the theory of optical principles and formalism involved in light propagation and polarization followed by Jones Stokes and Stokes-Mueller formalisms as robust techniques in biomedical studies. The discussion also covers the physical concepts involved in modifying the polarization of incident light when it interacts with an optical element. The following sections of the chapter explore a range of linear and nonlinear polarization-resolved microscopy techniques, and provide several examples of their applications in biomedical studies. The Mueller matrix (MM) microscopy, which is a comprehensive method to provide the full polarimetric response of a sample, is explained. However, since interpreting the full MM of complex random biological media at a microscopic scale could be a challenging task, incomplete MM is discussed to determine only a few MM elements such as circular dichroism and linear birefringence, which are more sensitive to configurations of the medium. The final section of the chapter discusses both linear and nonlinear fluorescence polarization microscopy techniques, which allow for imaging of biological structures using fluorescent molecules.

1.2 Theory of light polarization

In physics, the term "light" may refer more broadly to an electromagnetic wave that is composed by an oscillating electric field and magnetic field whose vectors are reciprocally perpendicular and perpendicular to the direction of propagation of the wave [2]. The properties of light are intensity, propagation direction, frequency or wavelength spectrum and polarization. James Clerk Maxwell described light as a propagating wave of electric and magnetic fields. More generally, he predicted the existence of electromagnetic radiation so that coupled electric and magnetic fields travel as waves at a speed equal to the known speed of light in a specific medium. In 1865, he published a paper entitled "A Dynamical Theory of the Electromagnetic Field" and derived electromagnetic wave equations in close agreement with experimental validation as Maxwell’s equations [3]. The electromagnetic wave equation that describes the propagation of electromagnetic waves through a medium or in a vacuum is derived using Maxwell’s equations.

$$\nabla^2\vec{E}(r,t) - \frac{1}{v^2}\frac{\partial^2\vec{E}(r,t)}{\partial t^2} = 0 \tag{1.1}$$

where v is the speed of light in a specific medium and ∇^2 is the Laplace operator. This is in correspondence with the perpendicular situation of electric and magnetic fields and then the direction of propagation. Moreover, the equation (1.1) shows the dependence of the wave equation only on electric field oscillations. The "polarization" of electromagnetic waves refers to the temporal and spatial evolution of the electric field in a plane perpendicular to the propagation axis. The following equations show the evolution of an electric field from a propagating wave along the z-axis in a vacuum

$$\vec{E} = \begin{bmatrix} E_x(z,t) \\ E_y(z,t) \\ E_z(z,t) \end{bmatrix} = \begin{bmatrix} E_{0x}\cos(\omega t - \vec{k}.z + \varphi_x) \\ E_{0y}\cos(\omega t - \vec{k}.z + \varphi_y) \\ 0 \end{bmatrix} \tag{1.2}$$

where E_{0x} and E_{0y} are the amplitudes of the electric field components, ω is the frequency, $\vec{k}$ is the wave vector and φ_x, φ_y are phases defined between 0 and 2π. The propagation of E_x and E_y give rise to a vector describing a locus of points in space that generates a curve whose form can be derived using the previous equations. Assuming $z = 0$, we start by dividing out by the amplitude and applying the double angle formula to the argument of the cosine function

$$\frac{E_x}{E_{0x}} = \cos(\omega t)\cos(\varphi_x) - \sin(\omega t)\sin(\varphi_x) \tag{1.3}$$

$$\frac{E_y}{E_{0y}} = \cos(\omega t)\cos(\varphi_y) - \sin(\omega t)\sin(\varphi_y) \tag{1.4}$$

Rearranging terms, subtracting, and using the double angle formula again, the following two expressions can be written.

$$\frac{E_x}{E_{0x}}\sin(\varphi_y) - \frac{E_y}{E_{0y}}\sin(\varphi_x) = \cos(\omega t)\sin(\varphi_x - \varphi_y) \tag{1.5}$$

$$\frac{E_x}{E_{0x}}\cos(\varphi_y) - \frac{E_y}{E_{0y}}\cos(\varphi_x) = \sin(\omega t)\sin(\varphi_x - \varphi_y) \tag{1.6}$$

Eliminating the time dependence, squaring the above two expressions, and adding them together, the following equation occurs

$$\frac{E_x^2}{E_{0x}^2} + \frac{E_y^2}{E_{0y}^2} - \frac{2E_xE_y}{E_{0x}E_{0y}}\cos\varphi = \sin^2\varphi \tag{1.7}$$

where $\varphi = \varphi_x - \varphi_y$; The equation (1.7) corresponds to an ellipse, and the projection of the electric field on the cross section in the x-y plane is shown in Fig. (1.1). Note that the quantities E_{0x}, E_{0y} and φ are independent of time, which corresponds to a totally polarized wave. Thus, in the most

general case, the state of polarization of a fully polarized light wave is elliptical. This state is completely characterized by the quantities E_{0x}, E_{0y} and φ. In Fig. (1.1), a polarization state can then be described in relation to the geometrical parameters of the ellipse and its "handedness", that is, whether the rotation around the ellipse is clockwise or counterclockwise. For any polarization form, the ellipse is characterized by

- Its azimuth α, ranging in value from $0 \leq \theta \leq \pi$;

- Ellipticity, $\tan|\varepsilon| = b/a$, where $-\pi/4 \leq \varepsilon \leq +\pi/4$;

- Diagonal angle β ranging $0 \leq \beta \leq \pi/2$;

- b and a, are the lengths of its semi-minor and semi-major axes, respectively and positive values of ε signify right-handedness.

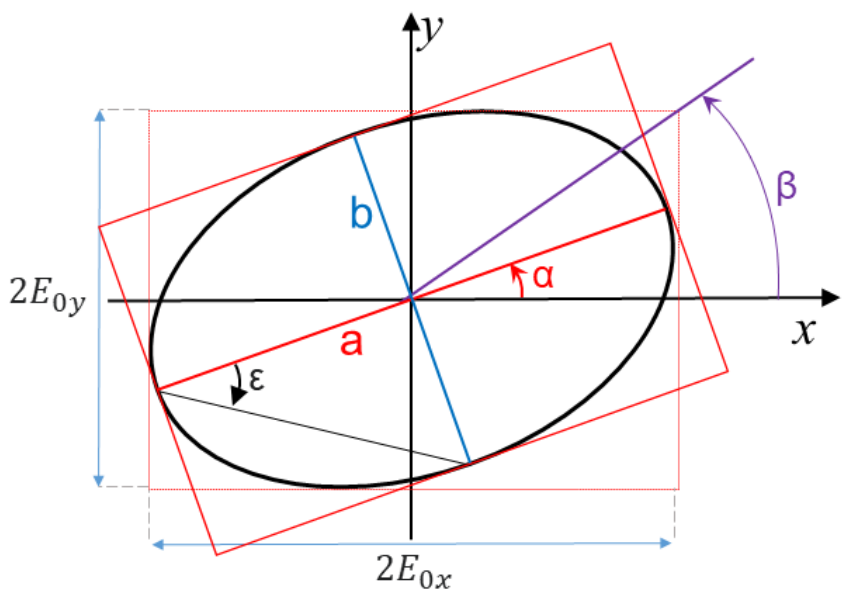

Figure 1.1. The polarization ellipse, with the orientation angle α, the ellipticity related to ε, the major a and minor b axis of ellipse and the E_{0x}, E_{0y} amplitudes of the electric field for light propagation in z-axis.

The relationships between these different quantities and the amplitudes E_{0x} and E_{0y} are given by

$$\tan\beta = \frac{E_{0y}}{E_{0x}} \tag{1.8}$$

$$\tan 2\alpha = \frac{2E_{0x}E_{0y}}{{E_{0x}}^2 - {E_{0y}}^2}\cos\varphi \tag{1.9}$$

$$\sin 2\varepsilon = \frac{2E_{0x}E_{0y}}{{E_{0x}}^2+{E_{0y}}^2}\sin\varphi \tag{1.10}$$

We can also establish the following relations

$$\cos 2\varepsilon \cos 2\alpha = \cos 2\,\beta \tag{1.11}$$

$$\cos 2\varepsilon \sin 2\alpha = \sin 2\beta \cos 2\,\varphi \tag{1.12}$$

$$\sin 2\varepsilon = \sin 2\beta \sin\varphi \tag{1.13}$$

For particular values of the amplitudes E_{0x}, E_{0y} and for the phase shift φ, the ellipse can be declined in particular forms, leading to specific polarization states. For instance, in the case where φ = 0, the two components of the electric field are in phase, and the light wave oscillates in a fixed direction as a linear polarization. In case φ ± π/2 and $E_{0x} = E_{0y}$, it is a right or left circular polarization depending on the sign of φ. Some particular polarization states are represented in Fig. (1.2). A wave is completely polarized if the quantities characterizing it, E_{0x}, E_{0y} and φ are independent of time. Conversely, if these quantities evolve randomly or in a completely non-deterministic way, like natural light, it corresponds to non-polarized light. A wave can be described as a linear combination of an unpolarized wave and a completely polarized wave, regardless of its polarization state, including partial polarization. In linear polarization, the electric or magnetic field oscillates in a single direction perpendicular to the direction of wave propagation. In contrast, in circular or elliptical polarization, the electric or magnetic field rotates at a constant rate in a plane perpendicular to the direction of wave travel. The rotation can have two possible directions; if the field rotates in a right-hand direction with respect to the direction of wave travel, it is called right circular polarization, while if the field rotates in a left-hand direction, it is called left circular polarization.

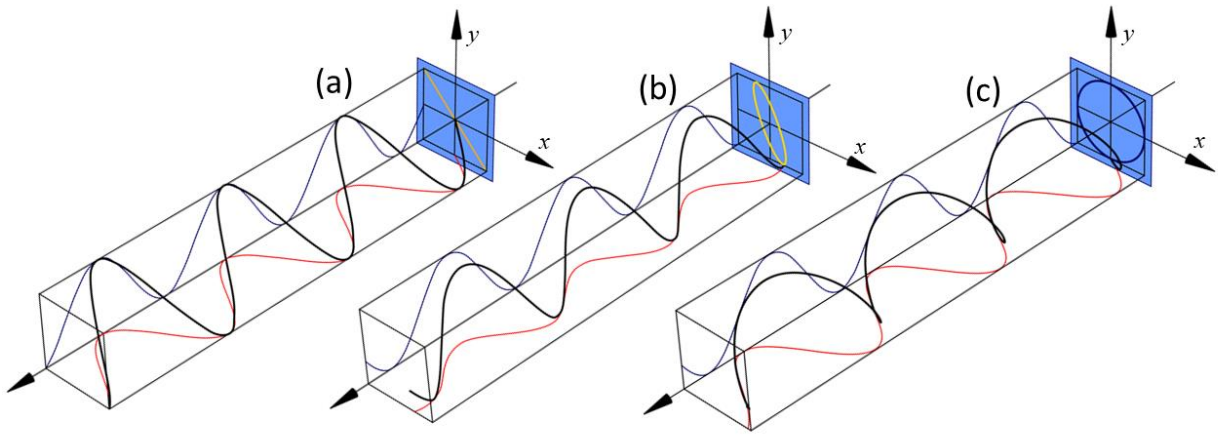

Figure 1.2. The representation of different particular polarization states; (a) linear polarization, (b) elliptical polarization, and (c) circular polarization.

The next step is to introduce a matrix formalism that allows for the description of polarization states for completely polarized waves, as well as their modification after crossing a medium.

1.2.1 Jones matrix formalism

In a series of articles published between 1941 and 1947, Robert Clark Jones introduced a new formalism to describe and calculate the behavior of polarized light and its interaction with a medium [4]. In particular, he introduced the Jones vector $\vec{J}$ of dimension 2×1 with complex coefficients entirely defined from the quantities E_{0x}, E_{0y} and φ in the following way

$$\vec{J} = \begin{bmatrix} E_x \\ E_y \end{bmatrix} = \begin{bmatrix} E_{0x}\, e^{i\phi_x} \\ E_{0y}\, e^{i\phi_y} \end{bmatrix} = \begin{bmatrix} E_{0x} \\ E_{0y}\, e^{i\phi} \end{bmatrix} \tag{1.14}$$

where i is the complex number such that $i^2 = -1$. Most often, this vector is represented in its normalized form.

$$\vec{J} = \frac{1}{\sqrt{{E_{0x}}^2 + {E_{0y}}^2}} \begin{bmatrix} E_{0x} \\ E_{0y}\, e^{i\phi} \end{bmatrix} \tag{1.15}$$

We can also write the vector as a function of the parameters α and ε of the polarization ellipse.

$$\vec{J} = \begin{bmatrix} \cos(\alpha)\cos(\varepsilon) - \mathrm{i}\sin(\alpha)\sin(\varepsilon) \\ \sin(\alpha)\cos(\varepsilon) + \mathrm{i}\cos(\alpha)\sin(\varepsilon) \end{bmatrix} \tag{1.16}$$

With this tool, we have the possibility to predict the state of polarization of the output wave, defined by the Jones vector $\vec{J}_{out}$ in a simple manner. Knowing the input Jones vector $\vec{J}_{in}$ and the Jones matrix of the optical element that is composed of one or more elements. The 2 × 2 matrix, denoted [T], is composed of four generally complex coefficients. The interaction is modeled simply as follows

$$\vec{J}_{in} = [T] \cdot \vec{J}_{out} \tag{1.17}$$

The major interest of this formalism is its ability to deal with the interaction of a totally polarized wave with an optical system composed of cascaded n-elements, as shown in Fig. (1.3).

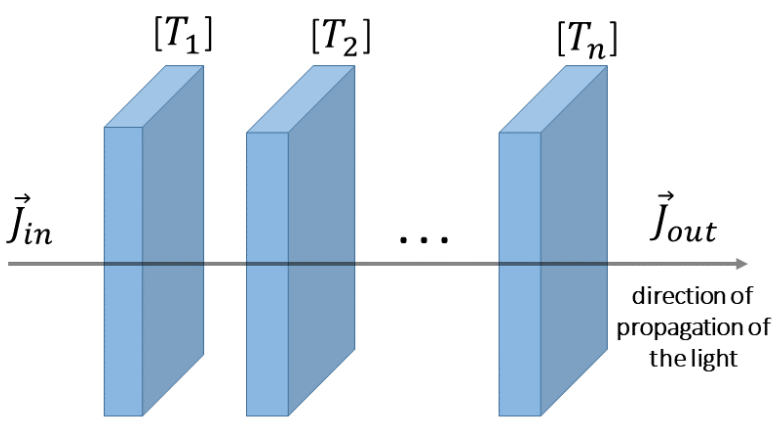

Figure 1.3. Schematics of the model of light interaction with N elements with their own Jones matrix, where the incident light Jones vector $\vec{J}_{in}$ is transformed in the vector $\vec{J}_{out}$; $[T_n]$ is jones matrix of the nth optical element.

Thus, it is enough simply to make the product of the n-matrices of Jones describing each optical elements such as

$$\vec{J}_{in} = [T_n] \dots [T_2][T_1] \ . \ \vec{J}_{out} \tag{1.18}$$

However, this formalism is limited to the description of completely polarized waves that is not suitable for processing uncoherent light like partially polarized or non-polarized electromagnetic waves.

1.2.2 Stokes-Mueller formalism

In 1852, Stokes introduced a mathematical formalism describing the polarization of an optical wave from the measurement of light intensities [5]. The polarization of light is entirely represented in the form of a single vector $\vec{S}$ of dimension 4 × 1 with real coefficients called the Stokes vector, such that

$$\vec{S} = \begin{bmatrix} S_0 \\ S_1 \\ S_2 \\ S_3 \end{bmatrix} = \begin{bmatrix} < {E_{0x}}^2 > + < {E_{0y}}^2 > \\ < {E_{0x}}^2 > - < {E_{0y}}^2 > \\ 2 < E_{0x}E_{0y} \cos \varphi > \\ 2 < E_{0x}E_{0y} \sin \varphi > \end{bmatrix} \tag{1.19}$$

The symbol "< >" corresponding to the expectation value operator, designates the spatial and temporal average on the detector. This way of noting the Stokes parameters has been deliberately omitted later to lighten the notation. The components of the Stokes vector for a fully polarized wave satisfy the relation

$$S_0^2 = S_1^2 + S_2^2 + S_3^2 \tag{1.20}$$

The four components of the Stokes vector are homogeneous at luminous intensities and can be written as follows for a completely polarized wave

$$\vec{S} = \begin{bmatrix} S_0 \\ S_1 \\ S_2 \\ S_3 \end{bmatrix} = \begin{bmatrix} I_0 \\ I_x - I_y \\ I_{+45^o} - I_{-45^o} \\ I_R - I_L \end{bmatrix} \tag{1.21}$$

where

- I_0 is the total intensity of the light beam;

- $I_x - I_y$ is the intensity difference for horizontal and vertical linear polarizations;

- $I_{+45^o} - I_{-45^o}$ is the intensity difference for linear polarizations at +45° and at −45°;

- $I_R - I_L$ is the intensity difference for right and left circular polarizations.

The Stokes parameters S_0, S_1, S_2 and S_3 have precise physical meanings. For a completely polarized wave, the Stokes vector normalized by S_0 can also be written in terms of the parameters of the polarization ellipse as follows

$$\vec{S} = S_0 \begin{bmatrix} 1 \\ S_1/S_0 \\ S_2/S_0 \\ S_3/S_0 \end{bmatrix} = \begin{bmatrix} 1 \\ \cos 2\varepsilon \cos 2\alpha \\ \cos 2\varepsilon \sin 2\alpha \\ \sin 2\varepsilon \end{bmatrix} = \begin{bmatrix} 1 \\ \cos 2\beta \\ \sin 2\beta \cos \varphi \\ \sin 2\beta \sin \varphi \end{bmatrix} \tag{1.22}$$

If the wave is completely unpolarized, the normalized Stokes vector with respect to S_0 becomes

$$\vec{S} = \begin{bmatrix} 1 \\ 0 \\ 0 \\ 0 \end{bmatrix} \tag{1.23}$$

If the wave is partially polarized, we can decompose its Stokes vector as the sum of a completely polarized wave and a completely unpolarized wave

$$\vec{S} = S_0 \begin{bmatrix} 1 \\ S_1 \\ S_2 \\ S_3 \end{bmatrix} = \begin{bmatrix} \sqrt{{S_1}^2 + {S_2}^2 + {S_3}^2} \\ S_1 \\ S_2 \\ S_3 \end{bmatrix} + \begin{bmatrix} S_0 - \sqrt{{S_1}^2 + {S_2}^2 + {S_3}^2} \\ 0 \\ 0 \\ 0 \end{bmatrix} \tag{1.24}$$

In this case, due to the partially polarized light, equation (1.20) becomes the inequality

$$S_0^2 \geq S_1^2 + S_2^2 + S_3^2 \tag{1.25}$$

Starting from the two extreme cases of polarization states that are fully polarized and non-polarized, the degree of polarization (DOP) of an optical wave is defined as

$$\mathrm{DOP} = \frac{\sqrt{S_1^2 + S_2^2 + S_3^2}}{S_0} \tag{1.26}$$

This quantity varies between 1 for a fully polarized wave and 0 for a non-polarized wave. Mueller introduced a linear relation between the Stokes vector at the input of an optical system $\vec{S}_{in}$ and at the output $\vec{S}_{out}$ given by [6]

$$\vec{S}_{out} = [M] \,.\, \vec{S}_{in} \tag{1.27}$$

where $[M]$ is the 4×4 MM. It is composed of 16 coefficients real components, denoted m_{ij} $(i, j = 0, 1, 2, 3)$, such that

$$[M] = \begin{bmatrix} m_{00} & m_{01} & m_{02} & m_{03} \\ m_{10} & m_{11} & m_{12} & m_{13} \\ m_{20} & m_{21} & m_{22} & m_{23} \\ m_{30} & m_{31} & m_{32} & m_{33} \end{bmatrix} \tag{1.28}$$

In the same way as the Jones formalism, one can describe the evolution of light polarization through an optical system that can be composed of elements placed in a cascade, as represented in Fig. (1.3). Mathematically, this simply translates to the product of the matrices associated with each element, arranged sequentially in the opposite direction of propagation of the light wave, such as

$$\vec{S}_{out} = [M_n] \ldots [M_2][M_1] \,.\, \vec{S}_{in} \tag{1.29}$$

This formalism completely describes the polarimetric properties of any optical system and determines the optical characterization of any environment. It is worth noting that other types of representations for polarization states and their modifications, such as the Poincaré sphere and the coherence matrix, are observed. [7, 8].

1.3 Polarization variations detection using Mueller matrix

The polarization of incident light waves can be altered through interaction with optical elements, which can cause three types of physical effects: linear and circular dichroism (amplitude effect), linear and circular birefringence (phase effect), and depolarization (spatial, temporal and/or spectral averaging effect). Diattenuators, retarders, and depolarizers are the three basic optical elements that represent these effects. This section will describe these elements and their associated Mueller matrices. It is assumed that the optical elements discussed are homogeneous and have orthogonal eigenstates of polarization [9].

1.3.1 Diattenuators

Dichroism is defined as a difference in transmission (or reflection) between two orthogonal polarization states. A diattenuator device is a dichroic element that has an absorption anisotropy, and the intensity of the emerging beam depends on the polarization state of the incident wave. Scalar attenuation can be defined as

$$D = \frac{T_{max} - T_{min}}{T_{max} + T_{min}} \tag{1.30}$$

The quantification of the diattenuator depends on D values. where $0 \leq D \leq 1$ and T_{max}, T_{min} are respectively the maximum and minimum energy transmittances. The energy transmittance for an unpolarized wave can be written as

$$T_0 = \frac{1}{2}\,(T_{max} - T_{min}) \tag{1.31}$$

In case D = 0, the transmittance or reflectance in intensity of this element does not depend on the state of polarization. When 0 < D < 1 the diattenuator is partial and D = 1 corresponds to a perfect polarizer. An attenuator element can polarize the incident wave linearly (Linear Dichroism), circularly (Circular Dichroism) or elliptically but the most general case is that of a partial elliptical

polarizer. Where the diattenuation of each component is dependent on the incident wave's polarization, we define the diattenuation vector $\vec{D}$ by

$$\vec{D} = \begin{bmatrix} D_H \\ D_{45^o} \\ D_C \end{bmatrix} \tag{1.32}$$

where

- D_H is the horizontal linear diattenuation and $-1 \leq D_H \leq 1$;

- D_{45^o} is the linear diattenuation at +45° with $-1 \leq D_{45^o} \leq 1$;

- D_C is the circular diattenuation, with $-1 \leq D_C \leq 1$. A diattenuator is linear if it does not present any circular diattenuation that means $D_C = 0$.

We can also write $\vec{D}$ with the components of azimuth α_D and ellipticity ε_D of the state corresponding to the maximum transmittance, as follows

$$\vec{D} = D \begin{bmatrix} \cos(2\varepsilon_D)\cos(2\alpha_D) \\ \cos(2\varepsilon_D)\sin(2\alpha_D) \\ \sin(2\varepsilon_D) \end{bmatrix} \tag{1.33}$$

Thus, a diattenuator is totally characterized by $\vec{D}$ and T_0. S. Y. Lu and R. A. Chipman have redefines the writing of such an element in matrix form [10], with

$$[M_D] = \begin{bmatrix} m_{D_{00}} & m_{D_{01}} & m_{D_{02}} & m_{D_{03}} \\ m_{D_{10}} & m_{D_{11}} & m_{D_{12}} & m_{D_{13}} \\ m_{D_{20}} & m_{D_{21}} & m_{D_{22}} & m_{D_{23}} \\ m_{D_{30}} & m_{D_{31}} & m_{D_{32}} & m_{D_{33}} \end{bmatrix} = \begin{bmatrix} 1 & \vec{D}^T \\ \vec{D} & [m_D] \end{bmatrix} \tag{1.34}$$

where $[m_D]$ is the reduced 3×3 diattenuation matrix written as

$$[M_D] = \sqrt{1 - D^2}[I_3] + (1 - \sqrt{1 - D^2})\hat{D}\hat{D}^T \tag{1.35}$$

$\widehat{D}$ is the unity vector representing the direction of the dichroic axis and $[I_3]$ is the 3×3 identity matrix. An ideal linear polarizer is a well-known diattenuator that transmits light uniformly vibrating in a single plane while fully absorbing the orthogonal plane.

1.3.2 Retarders

A retarding element is called birefringent or phase shifter that modifies the phase of the electrical field incident without altering its amplitude. It can be for example a uniaxial medium which has two different refractive indices of n_1 and $n_2 \neq n_1$. This leads to generate a phase delay between the two eigenstates associated with these two indices. We characterize a birefringent element of thickness l by its global delay or phase shift

$$R = |\phi_2 - \phi_1| = \frac{2\pi}{\lambda}.\Delta n.l \tag{1.36}$$

where $0° \leq R \leq 180°$, ϕ_2 and ϕ_1 are the phase shifts associated with the orthogonal eigenstates of the birefringent and $\Delta n = |n_2 - n_1|$ is the birefringence of the medium. This relation is valid for birefringent elements whose optical axis is perpendicular to the direction of wave propagation. Birefringent elements that can induce a delay by applying an electric field, such as liquid crystals, Pockels cells, or a mechanical constraint (e.g., photoelastic modulators), are essential in polarimetry to switch quickly between different states of polarization. Additionally, some biological samples, such as starch granules, exhibit linear birefringence, as demonstrated by the applications of polarization-resolved microscopy. The functioning of a linear birefringent waveplate is depicted in Fig. (1.4).

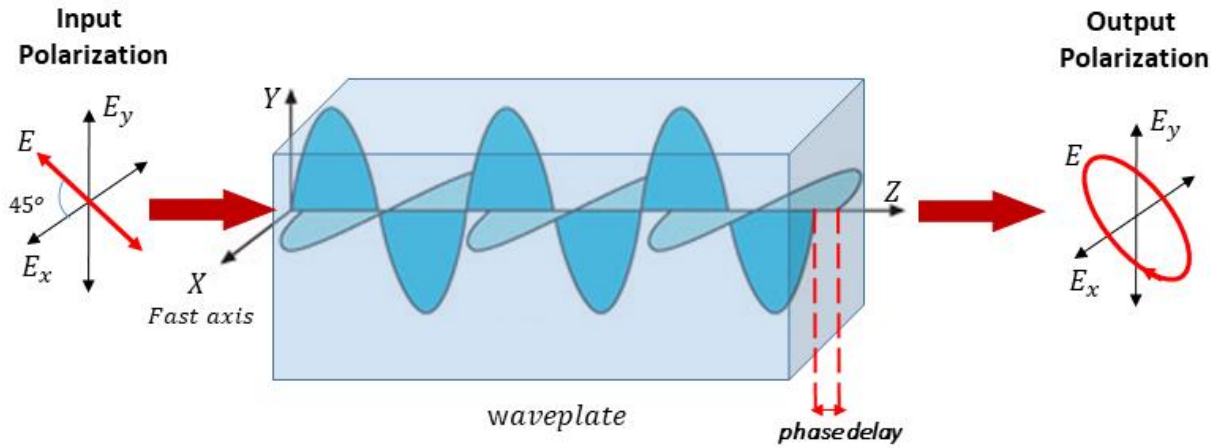

Figure 1.4. Action of a birefringent wave-plate, whose fast axis is oriented at 45°, on a light that is linearly polarized. The linearly polarized light enters the plate. The electric field can be resolved into two waves, parallel and perpendicular to the fast axis. In the plate, the perpendicular wave propagates slightly slower than the parallel one, resulting in an arbitrary phase shift between them to make elliptical polarization in general case at the output.

1.3.3 Depolarizers

Contrary to the previous optical elements, a depolarizer transforms a totally polarized light to a partially polarized state induced medium of the depolarization. This phenomenon appears as soon as a spatial, temporal or spectral averaging of the polarimetric properties takes place at the detection level. The depolarization engendered by a medium essentially comes from the phenomenon of light scattering and strongly depends on of the detection geometry used during the measurement. A depolarizing medium can be modeled, in the Stokes-Mueller formalism; by a depolarizer, in general form is the following

$$[\mathrm{M}_\Delta] = \begin{bmatrix} 1 & \vec{0}^{\mathrm{T}} \\ \vec{0} & [\mathrm{m}_\Delta] \end{bmatrix} \tag{1.37}$$

with $[\mathrm{m}_\Delta]$ is the 3×3 reduced matrix. The simplest case is that of a total depolarizer, where any Stokes vector is transformed into another Stokes vector describing a totally unpolarized light. The associated MM is then

$$[M_{\Delta total}] = \begin{bmatrix} 1 & 0 & 0 & 0 \\ 0 & 0 & 0 & 0 \\ 0 & 0 & 0 & 0 \\ 0 & 0 & 0 & 0 \end{bmatrix} \tag{1.38}$$

If the induced depolarization is partial and the medium depolarizes behave in the same way to all the incident polarization states (isotropic depolarization), the MM of the element is written as bellow

$$[M^{iso}{}_{\Delta partial}] = \begin{bmatrix} 1 & 0 & 0 & 0 \\ 0 & a & 0 & 0 \\ 0 & 0 & a & 0 \\ 0 & 0 & 0 & a \end{bmatrix} \tag{1.39}$$

where $0 \leq a \leq 1$. If the depolarization is different for each type of incident polarization state (depolarization anisotropic), the associated matrix becomes

$$[M^{aniso}{}_{\Delta partial}] = \begin{bmatrix} 1 & 0 & 0 & 0 \\ 0 & a & 0 & 0 \\ 0 & 0 & b & 0 \\ 0 & 0 & 0 & c \end{bmatrix} \tag{1.40}$$

where $0 \leq (|a|, |b|, |c|) \leq 1$. To quantify this phenomenon, we use the average depolarization factor which corresponds to the mean of the principal factors of $[m_\Delta]$

$$\Delta = 1 - \frac{|a|+|b|+|c|}{3} \tag{1.41}$$

There are three cases when $\Delta = 0$, the element is not depolarizing, $0 < \Delta < 1$, the element is a partial depolarizer, and $\Delta = 1$, the element is a total depolarizer. The phenomenon of depolarization can be generated after interaction of light with natural or manufactured elements such as milk, white paper, or metal [11]. More generally, any heterogeneous medium for the optical wave will generate depolarization [12]. Scattering is a process by which light is redirected in different directions by small particles or heterogeneous media, and it is an example of this phenomenon. When light undergoes scattering, it interacts with the particles, leading to a change in the polarization state of the light. As light scatters in different directions, its polarization state can change randomly, resulting in a loss of the original polarization information. Scattering can be influenced by several factors, including the size and shape of the scattering particles, the

wavelength of light, and the concentration of particles in the medium. As a result, microscopy can utilize scattering to gain useful insights into a sample. One such example is CIDS, the technique that enables the analysis of a sample's size, shape, and composition at the molecular and compaction level.

1.4 Polarization-resolved microscopy

In the field of optical microscopy research, various methods are available that offer essential information about the formation, function, and dynamics of molecular condensates. The choice of microscopy approach depends on the specific application. In particular, the development of molecular and inorganic fluorescent nanoprobes has revolutionized microscopy imaging for biology. These nanoprobes enable the chemical labeling of biomolecules, providing the ability to track their behavior through optical imaging. This approach provides high spatial resolution with sub-micron sizes, which is considered the gold standard for microscopy imaging. Fluorescent molecules provide both spatial and functional information through various contrast mechanisms such as specific absorption, emission, lifetime, anisotropy, photodecay, and diffusion. While one-photon fluorescence microscopy is a widely used tool for bio-imaging, nonlinear contrasts have emerged as interesting alternatives for various reasons. Nonlinear excitations involve near-infrared excitation wavelengths, which are less affected by scattering in tissues, allowing for deeper penetration in thick samples. However, the fundamental limitation of optical resolution imposed by the numerical aperture (NA) of the objective and the wavelength of light still follows the fundamental laws of diffraction defined by Ernst Abbe. To resolve objects below the classical diffraction limit of optical resolution, fluorescence imaging techniques are developed for super-resolution microscopy as a key method in modern biological and biomedical research to detect single molecules.

Despite the significant benefits provided by fluorescence techniques for observing the location and dynamics of biomolecules, they require the attachment of a probe to the biomolecule of interest, which may perturb its function. Fluorescent dyes used in fluorescence microscopy can be damaged or destroyed by prolonged exposure to light, causing loss of fluorescence signal over time, and high doses of excitation light can cause phototoxicity, leading to alterations in biological processes and potential cell death. In addition to auto-fluorescence, non-specific binding of fluorescent dyes to cellular structures can produce unwanted background fluorescence that interferes with accurate interpretation of results. Furthermore, this modality demands a prior knowledge of the sample to be labeled and requires costly and bulky instruments, including sources and special optical components.

On the other hand, label-free microscopy does not require the use of exogenous contrast agents that may alter the natural properties of the sample being imaged, making it a non-invasive imaging

technique that can provide information about the sample's natural properties without affecting its physiology or behavior. Another advantage of this technique is that it does not require wavelength specificity for implementation, which makes it suitable for integration with other modalities to provide complementary information about the sample being studied. Accordingly, label-free microscopy techniques can provide multiple types of information, such as structural and functional information, in a single imaging session, which is especially useful for studying complex biological processes and interactions. In table (1.1) some of the main advantages and disadvantages of the modalities are listed.

Modality	Advantages	Disadvantages
Label-free	(i) Non-invasive; (ii) No sample preparation; (iii) No high power laser source needed, more suitable for live-cell and tissue imaging; (iv) No specific wavelength is required: suitable for multimodal imaging;	(i) Contrast limitations arise from the inherent characteristics of the sample, which can restrict the available contrast; (ii) Reduced Sensitivity: when detecting low abundance of molecules or weak signals; (iii) Poor molecular specificity; (iv) Limited capabilities for the simultaneous detection of multiple targets;
Fluorescence	(i) Superior image resolution down to nm; (ii) Specificity: ability to specifically isolate and label molecules and structures of interest; (iii) Multiplexing: can be used to simultaneously image multiple fluorescent probes; (iv) Versatility: can be used in a variety of sample types;	(i) Exposure to fluorescent light can result in bleaching and loss of fluorescence intensity; (ii) Bulky setups with costly instruments; (iii) Photo-toxicity issues in high light doses for living cells; (iv) Auto-fluorescence;

Table 1.1. Some of the main advantages and disadvantages of label-free and fluorescence modalities. Each microscopy technique has strengths and weaknesses that are important to consider in microscopy approach.

While bio-imaging can provide information on complex biomolecular assemblies, the use of light polarization can bring a complementary degree of freedom to these investigations. In this section, the focus is on polarization-resolved optical scanning microscopy for imaging molecularly ordered objects. Although David Brewster is typically credited with inventing the polarizing microscope

around 1815, he acknowledged the priority of Henry Fox Talbot, who published his work in 1834 [13]. Polarization-based imaging techniques are powerful approaches that have the unique ability to produce specific contrasts for revealing hidden information that is not accessible with conventional imaging [14]. Its efficiency has been demonstrated in multiple areas, showcasing its particular sensitivity to the medium structure and orientation [15].

Polarized light microscopy (PLM) is a method that employs polarizing filters to obtain substantial optical property information about the observed material. This information can be combined with other microscopy techniques to confirm or elucidate the identity of an unknown material. Many biological samples, such as tissues and collagen matrices, show strong birefringence due to their asymmetrical material properties, which is not visible in conventional optical microscopy techniques. Image contrast in the polarizing microscope is based on the unique ability of polarized light to interact with the energetic bonds of ordered molecules in a direction-sensitive manner. Perturbations to waves of polarized light from aligned molecules in an object result in phase retardations between sampling beams, allowing interference-dependent changes in amplitude in the image plane. The degree of order encountered in objects ranging from near-perfect crystals to loosely ordered associations of asymmetric molecules or molecular assemblies. In bright-field illumination microscopy imaging, sample contrast comes from attenuation of the transmitted light in dense areas of the sample, showing dark regions of light absorbance. In a polarizing microscope, such structures may appear bright against a dark background. Fig. (1.5) shows the ability of a polarizing microscope to reveal the molecular arrangement in crystal starch grains within the potato cell cytoplasm, compared to an image obtained through scanning confocal light microscopy, which shows growth rings composed of alternate layers of amorphous and semi-crystalline regions.

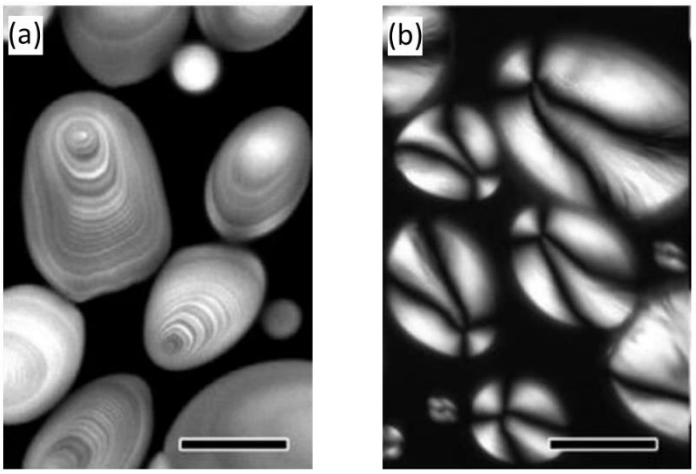

Figure 1.5. (a) Potato starch granules observed by scanning confocal light microscopy, (b) polarized light optical microscopy as viewed between crossed polarizers. Scale bars: 20 μm (figure reproduced from reference [16]).

At high powers, the material properties can change more rapidly, leading to a nonlinear response. This means that the material's response does not increase linearly with the intensity of the radiation. Nonlinear microscopy utilizes higher-order nonlinear effects to produce contrast, such as second-harmonic generation (SHG), third-harmonic generation (THG), and two-photon absorption, whereas conventional microscopy typically relies on linear effects such as absorption, scattering, and refraction. Considering both linear and nonlinear effects, the classification of polarization-resolved microscopy methods based on their historical order of development and technologies is stated as follows:

Polarizing Microscopy is the oldest form of polarization-resolved microscopy. It relies on the use of polarizers and analyzers to selectively transmit light of a particular polarization state, revealing birefringence and optical activity in materials such as crystals, fibers, and biological tissues. Differential interference contrast (DIC) microscopy is a type of polarized light microscopy that creates contrast based on the interference between two beams of polarized light. It is commonly used for imaging unstained biological specimens and for visualizing subcellular structures. Fluorescence polarization microscopy uses fluorescence to study the orientation and mobility of molecules in biological samples. It involves the use of polarizers and fluorescent probes that emit polarized light, which can be measured to determine the rotational diffusion of the probe molecules. MM microscopy is a polarization-resolved microscopy technique that uses a MM to describe the polarization properties of light after it interacts with a sample. SHG microscopy is a label-free technique that uses the nonlinear optical phenomenon of second harmonic generation to image the collagen fibers, muscle fibers, and other non-centrosymmetric structures in biological tissues. Coherent anti-Stokes Raman scattering (CARS) microscopy uses the nonlinear optical effect of Raman scattering to image the vibrational spectra of molecules in biological tissues. Polarization-resolved CARS microscopy can provide information about the orientation and anisotropy of molecular bonds. Polarization-Resolved THG microscopy is similar to SHG microscopy but uses the third harmonic of the excitation light to image non-centrosymmetric structures in biological tissues. Polarization-resolved THG microscopy can provide information about the orientation and anisotropy of lipid membranes and other biomolecules.

Polarization-resolved microscopy methods have been used to study the form and dynamics of many ordered cellular structures. Some studies have focused on mitotic spindle fibers in dividing cells [17], actin filament bundles in a variety of cell types [18], condensed chromatin in cell nuclei [19], helical strands of cellulose fibers in cells [20], virus crystals of organic compounds [21], and lipid bilayers of the cell plasma membrane [22]. In many cases, polarization microscopy is a robust technique available for studying the structure, formation, and dynamics of macromolecular assemblies or examining the effects of chemicals, drugs, or environmental conditions on cellular structures *in-vivo*. The interaction of polarized light with biological tissues, showing linear and circular birefringence, dichroism, and chirality, has made it possible to perform quantitative studies essential for biomedical diagnostics. The randomness of tissue structures results in fast depolarization of polarized light propagating in tissues. Therefore, for many optical imaging

methods, such as diffusion optical tomography, polarization effects are usually ignored. However, in certain tissues and cell structures, such as eye tissues, cellular monolayers, mucous membranes, and superficial skin layers, the degree of polarization of transmitted or reflected light remains measurable even when the tissue has considerable thickness [23].

1.4.1. Linear cross-polarization microscopy

Polarized-light microscopy is utilized in either transmitted or reflected light for the quantitative or qualitative characterization and identification of optically anisotropic materials. One of the simplest linear light polarization techniques is cross-polarization. A conventional light microscope can be converted into a polarizing microscope by placing two polarizing elements in the optical system. The schematic setup of cross-polarized light microscopy is shown in Fig. (1.6). The first polarizer is located between the light source and the object plane and converts non-polarized light into plane or linearly polarized light. The second polarizer (the analyzer), which is usually rotatable to detect different angular linear polarizations with respect to the optical axis of the first polarizer, is positioned between the objective and the eyepiece.

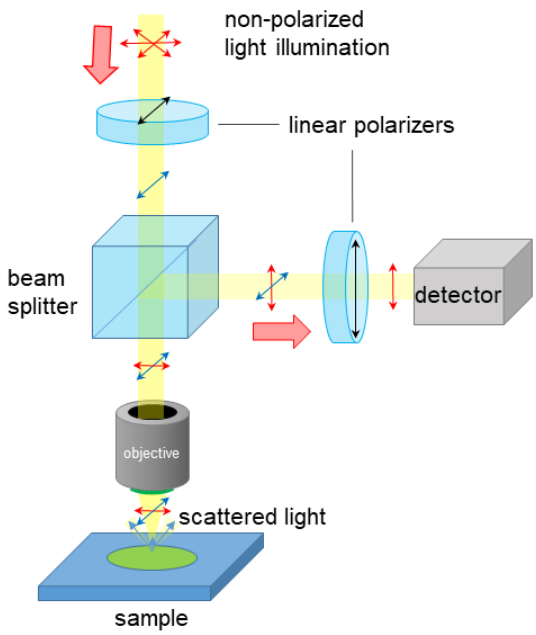

Figure 1.6. Schematic setup of a typical cross-polarization wide-field microscopy in reflective configuration.

For most applications, the two polarizing elements are "crossed," meaning the polarizing direction of the analyzer is perpendicular to the direction of the optical axis of the polarizer. In cross-polarized light illumination, polarimetric contrast is generated by the rotation of polarized light through the sample. This allows for the structural characterization of biological specimens containing birefringent materials without the need for staining or labeling. However, the intensity of light observed through a polarized light microscope when viewing a birefringent material depends on the angle of that material's optical axes relative to the transmission axis of the polarization filters. If the optical axis of the material is parallel to the transmission axis of the filter, the light passes through easily, resulting in a bright image. Conversely, if the optical axis is perpendicular to the transmission axis, the light is blocked, causing the image to appear dark. It should be noted that birefringent materials in a biological specimen, such as a histological section, may be oriented at different angles throughout the sample, and as a result, the observed light intensity varies depending on the orientation of the material's optical axis relative to the polarization filters.

Cross-polarization microscopy is a versatile technique that has found various applications in medical imaging. In dermatology, it has been utilized for non-invasive diagnosis of skin cancers by detecting changes in collagen structure and distribution, which can indicate cancerous growth. Similarly, in ophthalmology, it helps in imaging the retina and cornea and identifying changes in collagen fibers and other structures that indicate various eye diseases. This technique is also useful in histopathology for examining tissue samples and identifying structural changes that indicate diseases such as cancer and fibrosis. Furthermore, cross-polarization microscopy has been applied to imaging dental tissues, including enamel and dentin, and can detect changes in the structure and distribution of collagen fibers that indicate dental diseases such as caries and erosion. Lastly, it has been used in gastroenterology for imaging the gastrointestinal tract, specifically the esophagus, stomach, and colon, to identify changes in tissue structure that indicate various gastrointestinal diseases like inflammatory bowel disease and colon cancer [24].

As an example of the last application, a study in 2013 measured the THz reflectance of thick, fresh excisions of cancerous and normal colon tissue. The cross-polarized reflectance of normal colon was found to be lower than that of cancerous colon. This result was consistent for all sample sets, each consisting of one normal and one cancerous tissue measured in the study. Fig. (1.7) shows some of the images collected alongside digital photographs of the samples. The percent reflectivity difference between normal and cancerous colon tissue for both the cross-polarized and co-polarized data was also computed for each sample set while accounting for background [25].

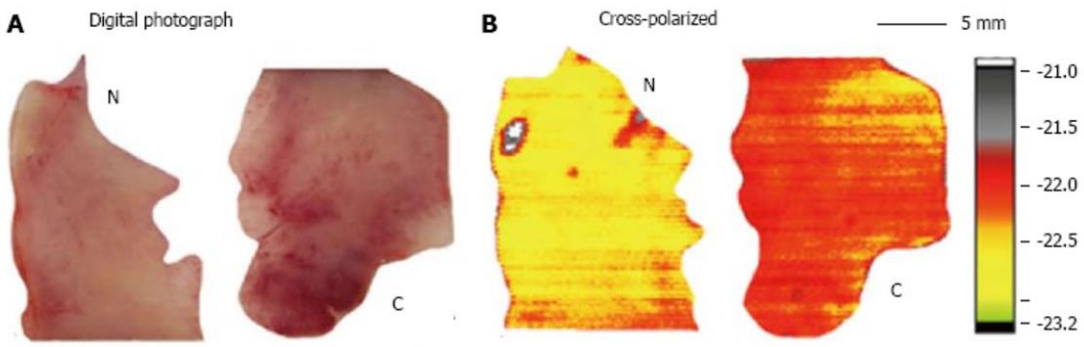

Figure 1.7. (A) Digital photograph and (B) corresponding terahertz reflectance images of normal (N) and cancerous (C) colon tissue (adapted from reference [25]).

Cross-polarization is routinely used for qualitative imaging but can sometimes provide ambiguous image contrasts in cases where several effects occur simultaneously. To obtain quantitative information and automate the measurement process, other schemes have been proposed involving compensators [26], rotating optical components or electro-optic modulators to give only a few examples [27, 28]. Compensators are optical elements that introduce a known amount of birefringence into the system, which can be used to calibrate the measurement and obtain quantitative information about the sample. Rotating optical components, such as a quarter-wave plate or a half-wave plate, can also be used to adjust the polarization state of the light before it interacts with the sample. This can help to reduce the ambiguity in the image contrast and improve the accuracy of the measurement. Electro-optic modulators, on the other hand, are devices that allow for the rapid modulation of the polarization state of the light. They can be used to rapidly switch the polarization of the light between two orthogonal states, allowing for the detection of birefringent materials with different orientations in the sample.

1.4.2 Polarized light sheet tomography

Light sheet microscopy (LSM) is typically considered a linear imaging technique as it relies on the linear scattering and absorption of light to generate contrast in the sample. Light sheet tomography measures the scattered photons orthogonally to the illuminating laser light sheet. This non-destructive, label-free technique uses a plane of light to optically section and view tissues and live biological samples in 3D with fast imaging times (ms) [29]. However, images of more turbid samples are largely degraded by multiple scattered photons, which are common to all light sheet techniques. It is important to take into account that photon polarization depends not only on the

number of scattering events but also on the nature of the scatterer encountered. Scattering occurs when photons interact with non-uniformities in the medium they are traveling through on a microscopic level. These non-uniformities result in deviations of the photon's travel direction from its initial path. In media with a low density of scatterers, detection of the scattered photons allows localization of the non-uniformity by simply back-projecting them along their direction of travel. In highly scattering media, a photon undergoes several of these scattering events before it can be detected, resulting in diffusion. The size of the object describes the scattering event as either Mie scattering, for the scattering of particles with a diameter comparable to or larger than the wavelength of the photon, or by the Rayleigh approximation, for particles and molecules smaller than the wavelength of the photon. In optical microscopy imaging techniques for highly scattering samples, the problem is addressed by utilizing the polarization aspect of light [30].

For example, in 2016, S. L. Reidt et al. presented polarized light sheet tomography (PLST) for imaging anisotropically scattering materials and its advantages in highly scattering turbid media [31]. The setup scheme is shown in Fig. (1.8). PLST is used for imaging biological samples and tissues with anisotropic scattering properties. It allows for imaging of samples with increased turbidity and is advantageous in highly scattering turbid media.

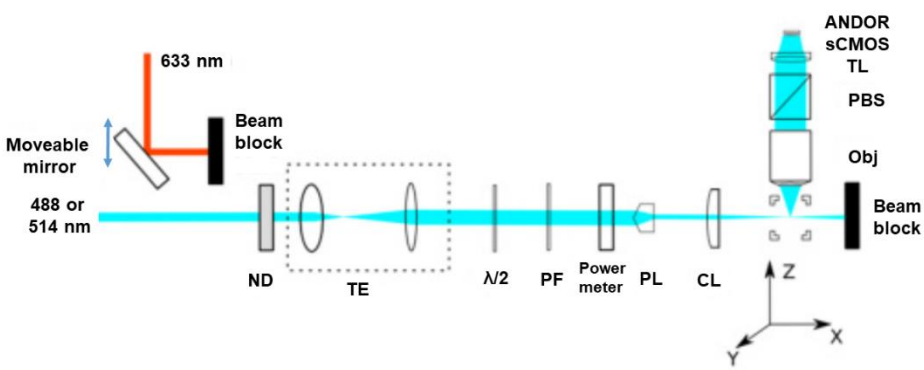

Figure 1.8. Schematic of PLST setup (top view). ND: Neutral density filter, TE: Telescope, PF: Polarizing filter, PL: Powell lens, CL: Cylindrical lens, Obj: Objective, PBS: Polarizing Beam Splitter, TL: Tube lens (adapted from reference [31]).

They showed side-scattered photons imaged by the PLST system. Fig. (1.9) shows a three-dimensional imaging technique to extract information from a turbid foam phantom using polarization effects of orthogonally scattered light.

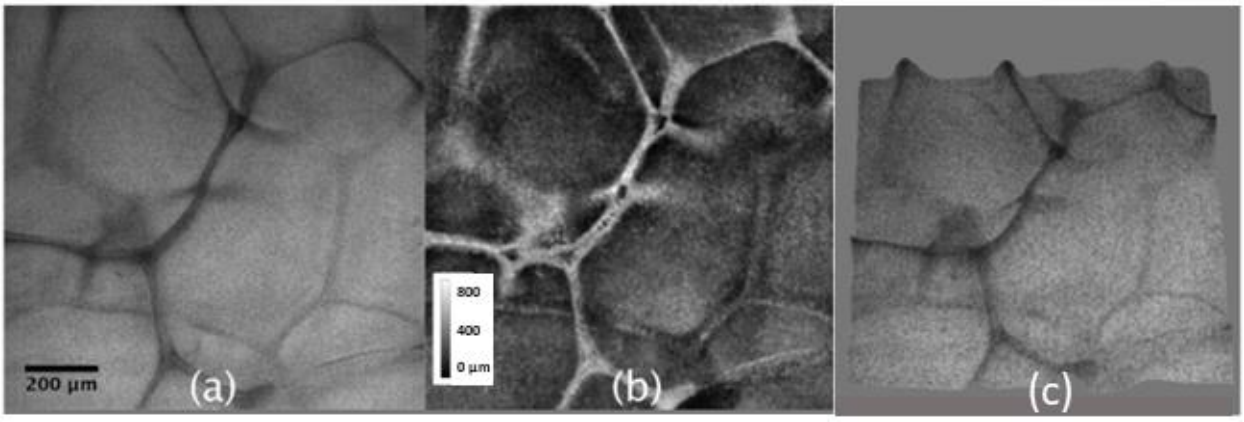

Figure 1.9. (a) Axial projection, (b) topology and (c) three-dimensional extended depth of field reconstruction of foam phantom using parallel co-polarized optics (adapted from reference [31]).

1.4.3 Mueller matrices microscopy

Optical microscopy techniques based on controlling the polarization of light have the potential to provide non-invasive label-free contrast, revealing hidden information about the structure and orientation of a medium. Specifically, MM polarimetry is the most comprehensive method, as it provides the full polarimetric response of a sample through its 4 × 4 MM. This polarization-resolved microscopy method consists of 16 independent elements that contain all the optical properties of a sample. The Stokes vector formalism has been widely applied to study the linear transmission of a sample to determine the MM. From this, parameters can be derived that offer insights into the physical processes engaged in the interaction between light and matter.

The first and most common approach for MM polarimetry incorporates the full-field imaging approach, which uses a CCD or CMOS camera, including full-field polarization coding and decoding stages. In this method, there is no need for specific light sources like coherent lasers. Furthermore, the conditioning of the detection system is influenced by both the system architecture and the desired information to be extracted from the sample. For example, a camera with full-field polarization coding and decoding stages can be used for imaging and spectroscopy approaches [32, 33]. However, this approach has limitations, including the loss of spatial resolution and the difficulty in implementing it with other imaging modalities due to the space required for the polarimetric optical features.

To preserve the axial optical resolution throughout the illumination volume, the second approach involves point-by-point scanning laser microscopy (SLM) of the sample. In SLM, the specimen is scanned by a diffraction-limited spot of laser light after reflection in galvanometric mirrors. The light is then transmitted or reflected by the in-focus illuminated volume element of the sample and focused onto a photodetector. Although the full-field technique is potentially faster than the scanning technique, the latter allows for the implementation of various imaging modalities on the same scanning microscope. In this section, the principle of MM polarimetry, as well as the different

means of generating and analyzing polarization states, are described. The general schematic of any Mueller polarimeter is shown in Fig. (1.10).

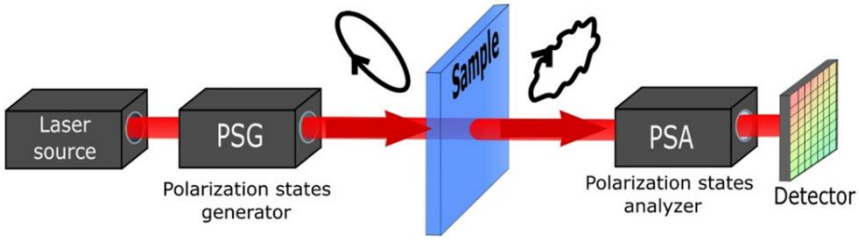

Figure 1.10. Basic principle of a Mueller polarimeter in transmission configuration. PSG: polarization state generator; PSA: polarization state analyzer.

The MM of an unknown specimen is determined by multiple polarization states that are generated to illuminate the sample, and its deformed response is then analyzed. The polarimeter is said to be "complete" if it measures all 16 coefficients of the MM and "incomplete" otherwise. If it is complete, the Polarization State Generator (PSG) shapes at least four different polarization states. After interaction with the sample, the modification of each of these states is analyzed through at least four different configurations of a Polarization State Analyzer (PSA). Hence, a system of at least 16 equations is obtained, enabling us to deduce the 16 coefficients of the matrix. The calibration steps usually consist of the measurement of the polarimetric contributions independently from the sample, the PSG and PSA blocks, and the optical microscope features fingerprints. The PSG and PSA can be calibrated separately according to their architectures using simple optical elements like rotated polarizers and waveplates for encoding the polarization states [34, 35].

The MM of the sample is extracted using matrices inversion based on the Mueller-Stokes formalism, as follows

$$\left[\mathrm{M}_{\mathrm{sample}}(\mathrm{x},\mathrm{y})\right] = \left[\mathrm{M}_{\mathrm{mes}}(\mathrm{x},\mathrm{y})\right] . \left[\mathrm{M}_{\mathrm{microscope}}(\mathrm{x},\mathrm{y})\right]^{-1} \qquad (1.42)$$

where $\left[\mathrm{M}_{\mathrm{sample}}(\mathrm{x},\mathrm{y})\right]$, $\left[\mathrm{M}_{\mathrm{microscope}}(\mathrm{x},\mathrm{y})\right]$, and $\left[\mathrm{M}_{\mathrm{mes}}(\mathrm{x},\mathrm{y})\right]$ represent the Mueller matrices of the sample, the microscope, and the total including the microscope and the sample, respectively.

1.4.3.1 Generation and analysis of polarization states

To shape the polarization of light, the PSG and PSA typically consist of linear polarizers and one or more phase shifters. These elements can have fixed orientations and/or phase shifts, or they can be controlled using mechanical or electrical means. In the following section, two domains for polarization modulation are explained: the time domain and the spectral domain [36]. These techniques involve point scanning approaches, where generated polarization-resolved images are acquired and then recombined in a post-data processing step to recover the full MM image.

1.4.3.1.1 Temporal domain

In the temporal domain (encoding), polarization states are sequentially generated and analyzed. This sequential method of generating and analyzing polarization states has been a major development for several years and is currently the most widespread method. The method involves acquiring at least 16 intensities sequentially, corresponding to 16 different combinations of polarization states during generation and analysis. Fig. (1.11) illustrates the principle of a typical setup in temporal Mueller polarimetry.

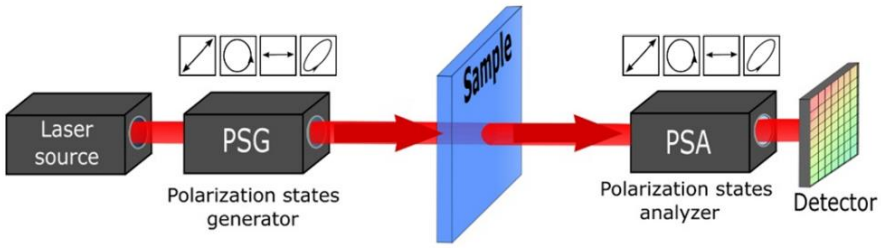

Figure 1.11. Principle of a sequential Mueller polarimeter. PSG: polarization state generator; PSA: polarization state analyzer.

To achieve sequential coding, rotating phase blades mounted on motors can be applied, either step-by-step or with continuous rotation [37-39]. The advantage of this approach is the use of homogeneous optical elements that are not very sensitive to the angle of incidence but remain relatively slow, so the modulation and analysis frequencies are in the order of a few Hz. Modulation frequencies can be reached in the tens of kHz range using Photoelastic Modulators (PEMs), which are discussed in detail in Chapter 2 [40-42]. Electro-optical modulators, such as Pockels cells, make it possible to control the phase shift electrically with modulation frequencies of several tens of MHz [43, 44]. However, they are highly sensitive to temperature and require high drive voltages up to several kV. The most widespread Mueller polarimeters mainly use modulators based on liquid crystals [45-47]. These devices have many advantages, such as their

low cost, high modulation frequencies of a few tens of Hz up to a few tens of kHz, and the fact that they require low control voltages of around a few volts. However, the fundamental limit of the temporal domain required to encode and decode all the polarization states essential to the determination of a MM is the temporal stability of the study medium during the measurement period.

1.4.3.1.2 Spectral domain

To dynamically characterize a sample, it is necessary for the MM polarimeter to acquire the full MM within the pixel dwell time, which is typically a few microseconds. This requires a very fast intensity modulation of the polarized light. In 1999, Kazuhiko Oka developed a Stokes polarimeter or channeled spectropolarimeter capable of measuring the four parameters of an incident light from a single spectrum I(λ) in the spectral domain. One advantage of this system is that it does not require any active elements, and the phase plates remain fixed during the measurement [48, 49]. Fig. (1.12) illustrates the principle of measuring a MM with this type of polarimeter.

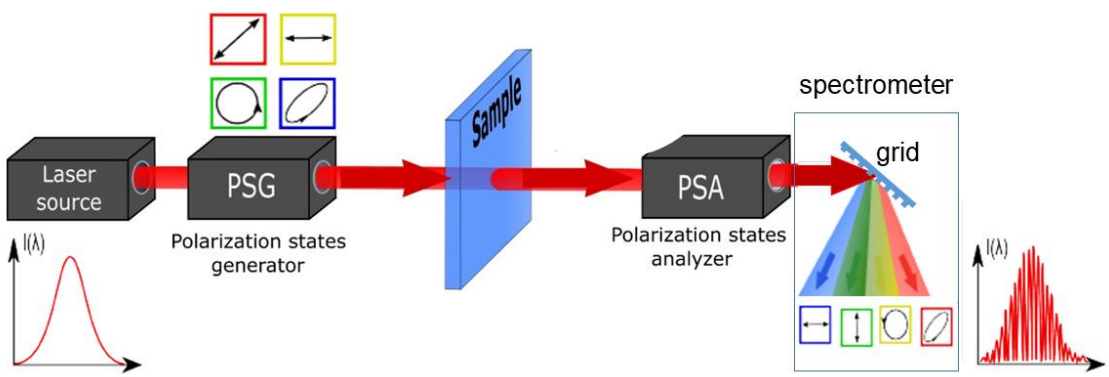

Figure 1.12. Scheme of a Mueller polarimeter by spectral coding. PSG: polarization state generator; PSA: polarization state analyzer.

Spectral encoding requires a light source with a broad enough bandwidth. Different polarization states are encoded at different wavelength intervals, and a spectrometer allows them to be analyzed separately, thereby enhancing the acquisition speed of the setup. Despite the extraordinary advantage offered by the speed of this technique, an important assumption is that the sample is achromatic within the excitation wavelength range. Additionally, the modeling of the instruments assumes that none of the linear retarders exhibit any diattenuation or depolarization.

1.4.3.1.3 Advantageous vs disadvantageous

In the field of complete MM with point scanning approaches, the typical performances reached by the imaging configurations are summarized in Table (1.2). The number of scans reported in the first column refers to the minimum number required to retrieve the 16 elements of the MM image. The first two approaches, single and multiple detection, use point scanning approaches and require scanning the sample multiple times to acquire the full MM image. Single detection is slower but simpler and cheaper, while multiple detection is faster but requires more precise alignment and calibration. Electro-optic modulators allow for real-time modulation of the polarization state and are compatible with point scanning approaches, but are expensive and have limited bandwidth. Spectral detection is a snapshot technique that captures the entire MM image in a single measurement, but requires precise alignment, heavy calibration, and complex modeling.

	Number of scans	Speed	Advantageous	Disadvantageous
Single detection	16	a few min	Simple calibration, cheap, compatible with electro-optic modulators	Precise alignment, Active elements, Successive scans, Post processing
Multiple detection	4 to 8	50 ms to 10 s	Snapshot detection, cheap, compatible with electro-optic modulators	Precise alignment Successive scans Heavy calibration Spacy
Electro-optics Modulators	1 or 2	µs to ms	Real-time, fast modulation, simple alignment, compatible with point scanning approaches	Expensive, limited bandwidth
Spectral detection	1	10 µs	Snapshot, compact, passive elements, compatible with electro-optic modulators	Precise alignment, heavy calibration, complex modeling, assumption of sample achromaticity within excitation wavelength range

Table 1.2. Main performances and capabilities of the single and multiple channel temporal MM acquisition (two first lines) comparing to the spectral detection for recovering the full MM image. The number of scan reported in the first column referred to the minimal number for retrieving the 16 elements of the MM image. The speed is a metric related to the full polarization modulation [36].

1.4.3.2 MM microscopy imaging applications

The polarization microscopy of scattered light from an object is fully described by the Stokes vectors of the incident and scattered light and a 4 × 4 MM that can be achieved using weak laser power down to a few milliwatts (mW). In recent years, Mueller polarimetry has been increasingly used for the analysis of biological tissues, with a view to proposing diagnostic medical tools [50, 51]. In scanning MM microscopy, the specimen is scanned by a diffraction-limited spot of laser light after reflection in galvanometric mirrors. Then, the light is transmitted or reflected by the in-focus illuminated volume element of the specimen and is focused onto a photodetector [36]. This section is dedicated to the description of examples of MM microscopy imaging in an optical scanning microscope, from the implementation of incomplete MM microscopy as the simplest case up to the retrieval of the full elements.

1.4.3.2.1 Incomplete MM microscopy

Interpreting the complete MM of complex random biological media at a microscopic scale can be an arduous task. The main challenge is extracting the localized polarimetric signature of a biological medium, which is difficult due to the extremely low signal-to-noise ratio (SNR) and the mix of numerous different structures confined in a small volume. Therefore, in a single-point measurement, the technique was based on differentially polarized linear or circular intensity collection, leading to the determination of only a few MM elements that are more sensitive to particular configurations of the medium [52, 53]. Thus, the method has been extended to an SLM configuration for imaging high-ordered macromolecules and biopolymers, such as chromatin [54, 55]. This is typically the case for CD, which is the m_{03} element of the MM defined using the intensities of the circular left and right polarization of the light scattered from chiral aggregates, arising from the media exhibiting an optical activity. It has been proven that the total CD signal comes mainly from absorption but also has a weak scattering component, which carries structural information at the single-molecule level. The scattering component of CD, named CIDS, is particularly important outside the absorption band of the sample. It originates from long-range chiral structures and is sensitive to the characteristics of chirality [56, 57]. It has been shown that the circular differential imaging method exhibits contrast from the difference in the optical activity from the surrounding molecules, which is directly linked to the sample fingerprint. The CIDS sign and magnitude of each chiral group are characteristic of structural properties that present changes as a function of time or the environment, such as the compaction level of the chromatin structure [54].

In the context of CIDS microscopy, depolarization effects can be considered negligible if the sample is well-controlled and the polarization state of the incident light is well-defined. This can be achieved using polarized light sources and carefully designed optical systems. Furthermore,

CIDS typically measures the difference in circular polarization between left and right circularly polarized light, which is relatively insensitive to depolarization effects [58]. It should be noted that the choice of input polarization can affect the contrast in microscopy images. Circularly polarized light, as homogeneous illumination, is less sensitive to scattering and depolarization compared to linear polarization [59]. The CIDS signal mainly arises from CD, and the scatterers' dispersive properties are not included in the CIDS signal, allowing the depolarization effect to be ignored. However, when using a high NA objective to perform CIDS on thick, random, and complex mediums, the depolarization effect becomes more significant. For bulk tissues, the dominant structural properties are usually highly depolarizing due to their complex microstructures. Additionally, most bulk tissues contain fibrous structures, such as collagen, elastic, and muscle fibers, which bring both anisotropic scattering and birefringence effects. Therefore, incomplete MM microscopes typically track only these two parameters.

MM microscopy finds its application in biomedical diagnosis, specifically in ophthalmology, where it offers a faster alternative for diagnosing pathologies than the eye motion. Moreover, when coupled with signal processing, it can also reduce exposure time to limit damage through the eye. However, the application of MM microscopy in ophthalmology is not without its challenges. The complicated polarization properties of ocular media and the retina, the fast motion and optical properties in the living eye, and the need to carefully choose wavelengths to limit radiation exposure and improve polarimetric SNR are some of the significant challenges [36].

In Fig. (1.13), an application proposed in 2002 shows the first row of the MM, including linear and circular dichroism for a retinal fundus region with blood vessels [60]. Linear dichroism which is shown by M_{02} is another crucial element of MM microscopy that is sensitive to linear anisotropies in proteins like actin filaments and microtubules.

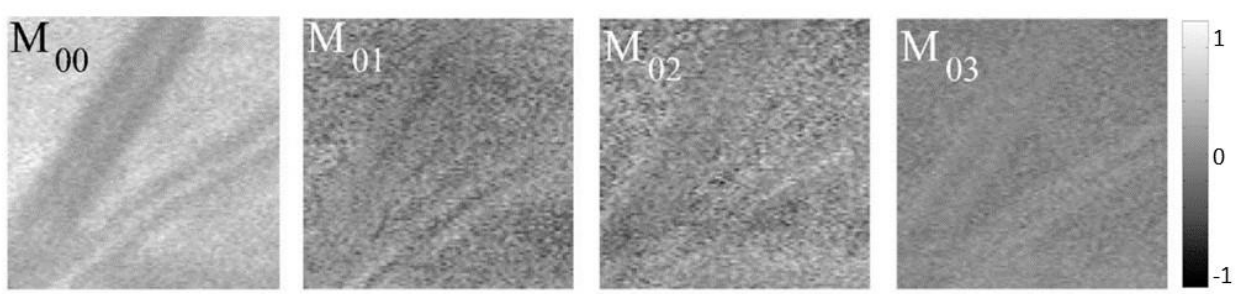

Figure 1.13. Elements of the first row of the spatially resolved Mueller matrix for retinal region with size of 4×4 mm^2. The gray-level code is shown at the right (reported from reference [60]).

Focusing on chirality imaging, in another study, bright-field CD (m_{03}) images of chloroplasts as both absorbing and scattering systems, were taken using a differential polarization microscope [61, 62]. Chloroplasts are photosynthetic organelles of highly organized molecular structure. The

efficiency of the photosynthetic conversion of light energy is largely determined by the organization of the photosynthetic pigment molecules embedded in the membranes contained in chloroplasts [63]. The images obtained using light inside the absorption band, by means of differential polarization microscopy, contain absorption ($\mathrm{CD}^{\mathrm{abs}}$) as well as scattering ($\mathrm{CD}^{\mathrm{sca}}$) contributions. CD images of chloroplasts obtained inside and outside the absorption band of the chromophores were shown to illustrate the sensitivity of the CD image to the wavelengths dependence of the scattering and absorption contributions. Images of chloroplasts were taken at 515 and 546 nm. 515 nm is the peak of absorption of chloroplasts in the green region of the visible spectrum, whereas 546 nm is outside the absorption band. All the chloroplasts examined were magnetically aligned to simplify the interpretation. The $\mathrm{CD}^{\mathrm{abs}}$ of an aligned chloroplast at 515 nm is shown in Fig. (1.14 a) and the $\mathrm{CD}^{\mathrm{sca}}$ at 546 nm in Fig. (1.14 b). Fig. (1.14 c) shows the difference between Figs. (1.14 a and b) pixel by pixel. All the differential images are shown in a gray scale where white and lighter grays encode positive values of the differential ratio, gray indicates a zero value, and darker grays and black encode negative values of the differential ratio. $\mathrm{CD}^{\mathrm{abs}}$ and $\mathrm{CD}^{\mathrm{sca}}$ are dominated by positive values (see figure caption), in agreement with the positive band and tail observed in the green region of the macroscopic spectrum of aligned chloroplast suspensions. The weakness of the signals in Fig. (1.14 c) indicates that in this case, the scattering at 546 nm cancels out most of the signals obtained at 515 nm, suggesting that scattering is a big part of $\mathrm{CD}^{\mathrm{abs}}$ at 515 nm.

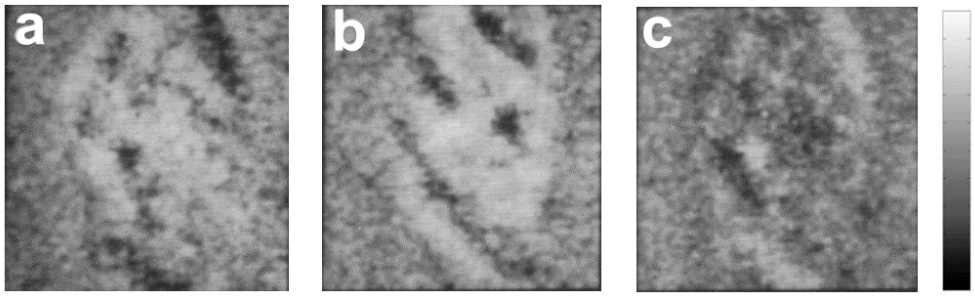

Figure 1.14. Differential polarization CD (m_{03}) images of an aligned chloroplast performed with a confocal scanning differential polarization microscope. The grey scale for the dichroic ratio is shown. (a) $\mathrm{CD}^{\mathrm{abs}}$ obtained by using light of wavelength = 515 nm. In this image, the integrated positive and negative values of the dichroic ratio were +5.8E-4 and -4.8E-4, respectively. The extremes of the grey scale correspond, in this image, to a dichroic ratio of +/-2.91E-3. (b) $\mathrm{CD}^{\mathrm{sca}}$ obtained by using light of wavelength = 546 nm. The integrated positive and negative values of the dichroic ratio were +6.7E-4 and -6.2E-4, respectively. The extremes of the grey scale correspond, in this image, to a dichroic ratio of +/- 1.4E-3. (c) Difference image between $\mathrm{CD}^{\mathrm{sca}}$ and $\mathrm{CD}^{\mathrm{abs}}$. $\mathrm{CD}^{\mathrm{sca}}$ was rescaled to 2.91E-3, before the subtraction was performed. The integrated positive and negative values of the dichroic ratio were +2.93E-4 and -2.96E-4, respectively. The extremes of the grey scale correspond, in this image, to a dichroic ratio of +/-2.91E-3. The size of the images is 6.4×6.4 μm^2 (reproduced from reference [61]).

The field of MM microscopy has seen a recent surge in research aimed at developing MM polarimeters to investigate how tissues are modified by pathology at the cellular and sub-cellular level [51, 64]. One of the main advantages of MM is its ability to track changes in a non-invasive and label-free manner, which allows researchers to investigate the early stages of pathologies. By coupling MM with SLM, it becomes possible to resolve the optical properties of sub-microscopic objects, providing a means to quantify pathologies in their early stages. MM microscopy is capable of imaging confined localized structures and bringing quantitative methods for staging the pathologies.

As an example, in a study, MM element images of chromatin were retrieved in an isolated HEK nucleus after extraction using a PEM configuration [65]. The images provided different contrast mechanisms from the raw data, demonstrating that the element images are sufficient to highlight differences in organization in the nucleus without the need for fluorescent labels. Five MM elements were extracted: $m_{00}, m_{02}, m_{03}, m_{22}$, and m_{23}, which were interpreted as total intensity, linear dichroism, circular dichroism, depolarization, and linear birefringence, respectively, as represented in Fig. (1.15). The m_{22} image is linked to the total transmitted light, which explains the strong contrast correlated to the total intensity m_{00} image.

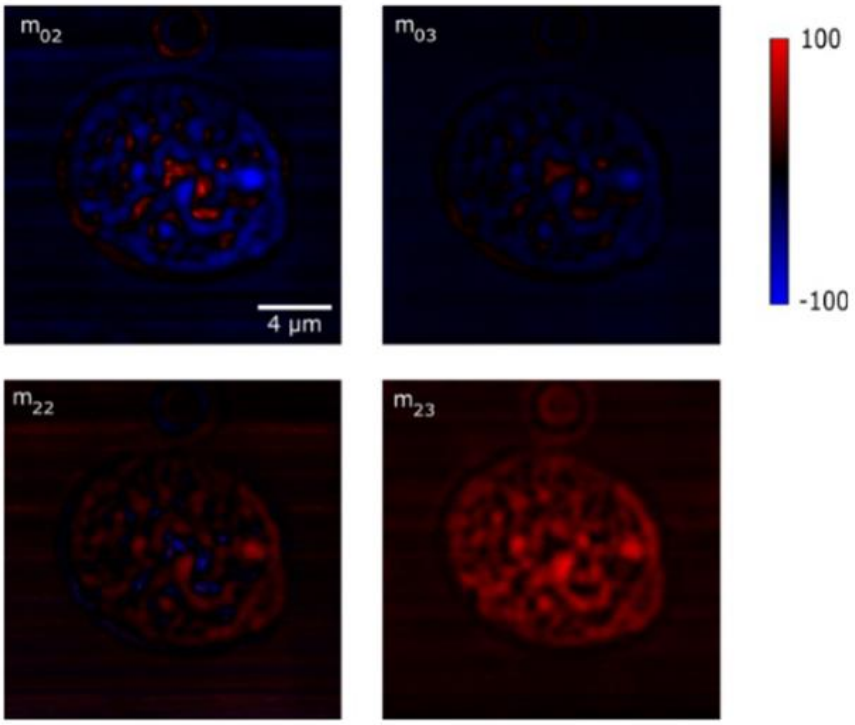

Figure 1.15. Mueller-matrix element images of an isolated HEK nucleus after extraction, available for the actual experimental configuration of the microscope. The color scale bar helps quantifying the polarimetric signal amplitude to distinguish the difference of compaction of the chromatin-DNA inside the nucleus (Figure reproduced from reference [65]).

1.4.3.2.2 Complete MM microscopy

Polarization-sensitive imaging is a powerful technique that enables the visualization of the polarization-dependent properties of living tissues and cells. Through the utilization of techniques capable of obtaining the complete MM elements, it becomes possible to unveil previously unidentified anatomical conditions that are sensitive to polarization. The MM contains information about how a sample alters polarized light, and obtaining the complete matrix elements enables us to fully characterize the sample's polarization properties. This information can be used to investigate pathological changes in tissues, such as those associated with cancer or other diseases, or to understand the underlying mechanisms of biological processes at the cellular level. Complete MM microscopy imaging has various applications in different fields, including biomedical imaging, material science, and remote sensing. In biomedical imaging, MM microscopy has been utilized in the detection of pathologies, including cancer, cardiovascular diseases, and dermatological diseases. For example, in dermatology, MM microscopy has been used to study the birefringence properties of collagen fibers in skin tissues to diagnose skin conditions. In ophthalmology, MM microscopy has been applied to study the polarization properties of the retina and diagnose ocular diseases such as cataracts and glaucoma. In material science, MM microscopy has been used to study the optical properties of anisotropic materials, including liquid crystals and biological tissues [36].

Recently, much research has been focused on developing MM polarimeters to investigate modifications of tissues induced by pathology at the cellular level. One area of interest is gynecology, which deals with the female reproductive system, including the uterine cervix, a part of the lower uterus. Polarization imaging is an effective means to measure optical anisotropy in birefringent materials, such as the cervix’s extracellular matrix [66]. The characterization of cervical collagen anisotropy and neural axons in the uterus is essential in identifying structural changes due to cervical cancer. Cervical Intraepithelial Neoplasia, also known as CIN, is staged as CIN1 or CIN2 when one third or two-thirds of the epithelium is involved, respectively, and CIN3 when the entire epithelium is affected. Fig. (1.16) shows the use of MM polarimetry to target the fibrous ultrastructure organization of the cervix in 2013 [67]. The depolarization and retardance parameters are used to differentiate between pre-cancerous lesions and healthy regions.

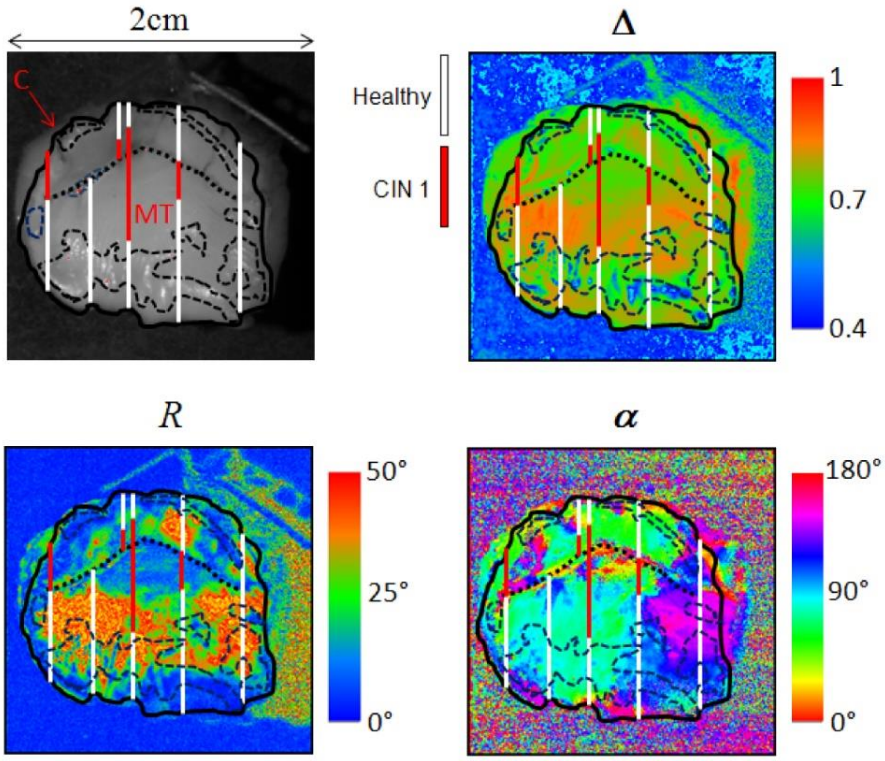

Figure 1.16. Images of intensity, depolarization (Δ), retardance (R) and orientation of the axis of birefringence (α) on a section of uterine cancer. The center of the image is marked by a dotted line that indicates the limit of the biopsy. The white hatched areas in the image correspond to healthy regions while the red areas indicate the pathological regions (reported from reference [67]).

Tissue monitoring with an endoscope is a valuable tool for detecting early signs of disease or tracking the progression of a condition based on optical intensity and wavelength metrics. However, integrating polarization contrast can reveal tissue scattering and absorption information from a different perspective and provide insight into directional tissue birefringence properties to monitor pathological changes in collagen and elastin microstructures and compositions. In 2016, a rigid Mueller polarimetric endoscope was developed, which incorporated PSG and PSA directly into the endoscopic head, allowing for several image contrast mechanisms, including linear depolarization, circular depolarization, cross-polarization, directional birefringence, and dichroism, in addition to traditional unpolarized radiation intensity [68]. Fig. (1.17) shows images of the parameters of diattenuation, retardance, and their orientations for evaluating a pig's bladder.

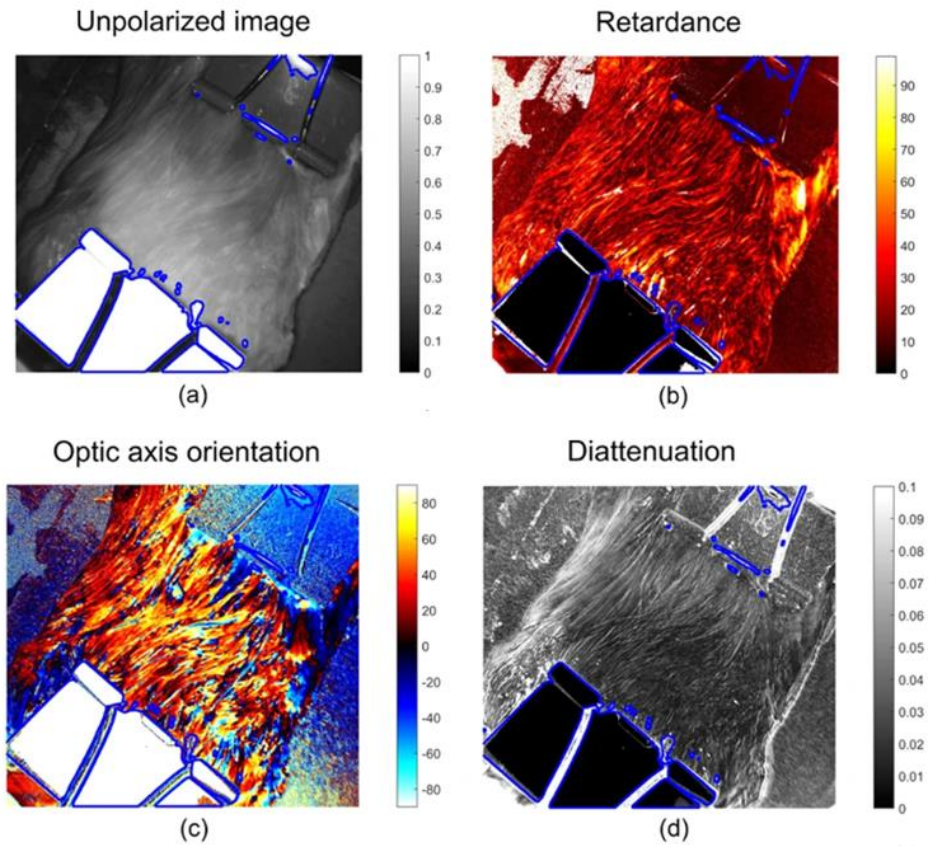

Figure 1.17. (a) An intensity image (non-polarized), (b) a retardance image, (c) an optic axis orientation map of the retardance, and (d) a diattenuation image of the bladder using the polarimetric endoscope. The presented images have a field of 7.8 × 7.8 cm^2 (adapted from reference [68]).

In 2008, a MM polarimeter was developed to extract complete MM elements, which was used to improve the detection of glaucoma. The study concluded that an increase in diattenuation on the retina may be associated with the development of this pathology, which is more important than the delay [69]. In 2010, a study demonstrated the use of a Mueller polarimeter in reflection to analyze the response of the human colon with tumor areas. Fig. (1.18) shows that the measured Mueller matrices are essentially diagonal, indicating the absence of diattenuation and delay. The colon tissues behave as partial depolarizers, which depolarize less in tumor areas than in healthy areas in the early stages of the disease [70]. Therefore, the MM microscopy technique can provide useful insights into the characterization of diseased tissues, which may have important implications in biomedical diagnosis and treatment.

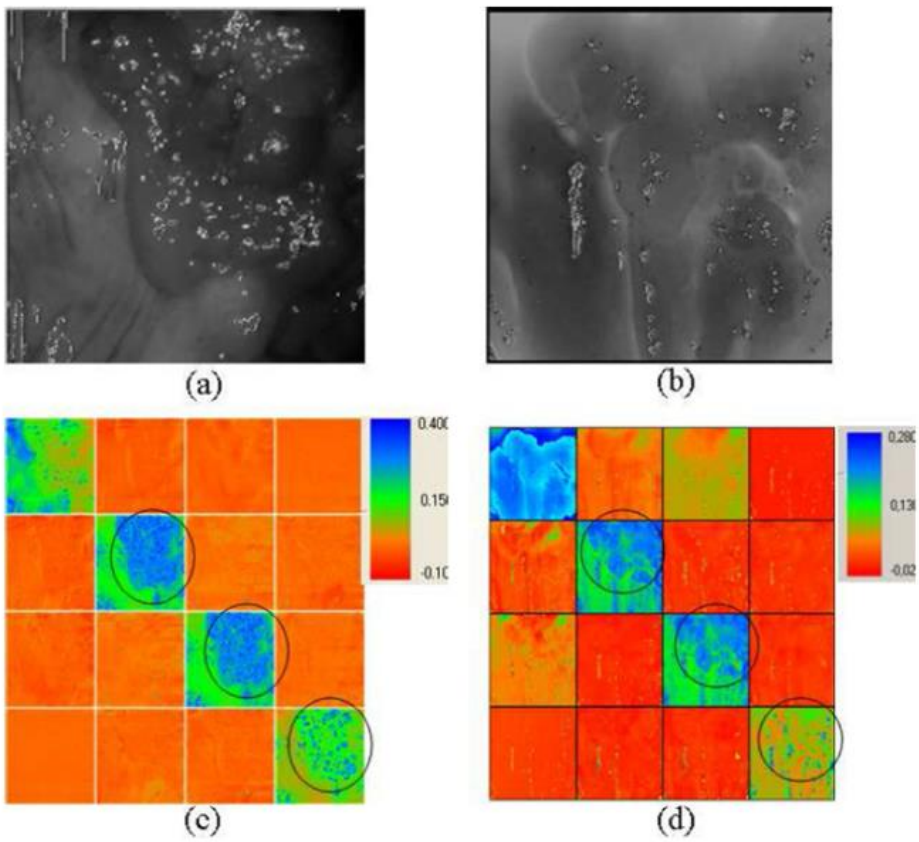

Figure 1.18. Intensity and Mueller images of a colon sample, a field of view of 5cm × 5cm. (a) Intensity image, taken at 600 nm. (b) Image of another sample, taken at 700 nm. (c) Normalized Mueller image of the sample in (a). (d) Normalized Mueller image of the sample in (b). The scales are indicated on the right of the Mueller pictures. Tumor areas are circled in black (adopted from the work of M.R. Antonelli [70]).

MM microscopy has numerous applications, including the ability to track specific polarimetric changes under certain conditions, as illustrated in Fig. (1.19). In this study, MM polarimeter was implemented in a commercial optical scanning microscope to characterize polarimetric transformations in zebrafish at various embryonic developmental stages [71].

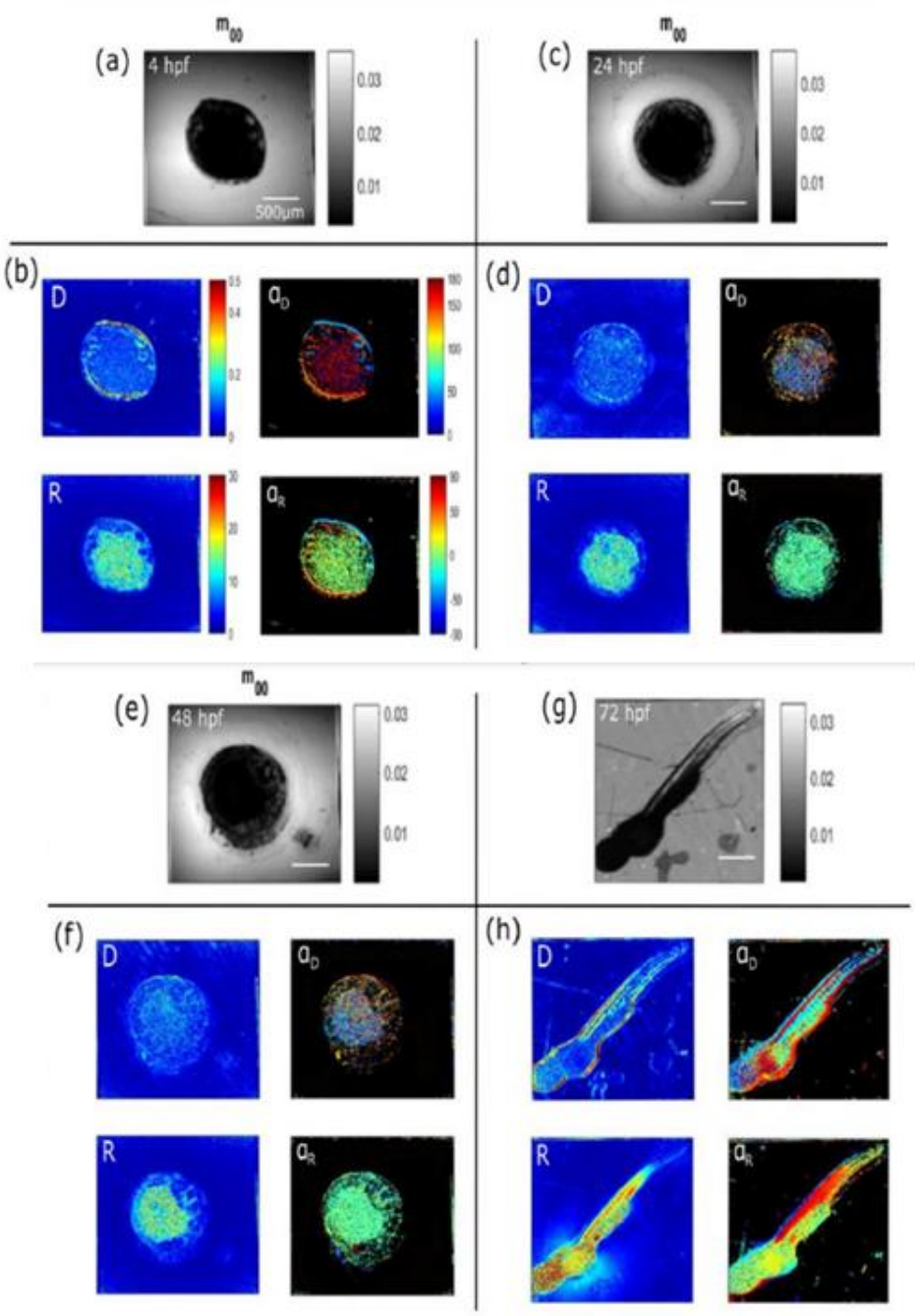

Figure 1.19. Polarimetric images of fixed zebrafish embryos and larvae at 4 hpf (hours post fertilization), 24 hpf, 48 hpf and 72 hpf. The images (a), (c), (e), (g) correspond to the total collected intensity from the MM, which is the m_{00} element. The images (b), (d), (f), (h) are images coded in Diattenuation (D), in retardance and its azimuthal orientations α_D and α_R, respectively. hpf: hours post fertilization (adapted from reference [71])

1.4.4 Polarization-resolved coherent nonlinear contrasts microscopy

Polarization-resolved coherent nonlinear contrasts microscopy are imaging techniques that combine the principles of nonlinear optics and polarization-resolved imaging. The polarization state of the incident light and the polarization of the nonlinear signal are measured to provide information about the sample's structural and optical properties. This is particularly useful for imaging biological samples, where the nonlinear signals arise from endogenous molecules. By exploiting the polarization dependence of these signals, polarization-resolved coherent nonlinear contrasts microscopy can provide additional information about the sample's structure and organization that may not be accessible with traditional linear imaging techniques.

In this section, examples of nonlinear coherent optical contrasts conducted in biological tissues, such as CARS, SHG, and THG, are described. Moreover, the features of these polarization modalities on tissues are explained.

1.4.4.1 Polarization CARS microscopy

CARS is a nonlinear process in which the energy difference of a pair of incoming photons matches the energy of the vibrational mode of a molecular bond of interest. This phonon population is coherently probed by a third photon and anti-Stokes radiation is emitted. CARS microscopy offers many advantages such as capability to monitoring dynamic process, temperature dependent and thus can be a thermometer, completely label free, chemically selective molecular imaging, ease of spectral separation from the single-photon fluorescence background, 3D sectioning capability with multicolor imaging to be applied *in-vitro*, *in-vivo* and in fixed samples. However, the presence of a spurious signal known as non-resonant background observed due to the interactions involving highly detuned electronic energy levels limiting the sensitivity of CARS is a major disadvantage.

In 2012, Giuseppe de Vito, et al., presented a novel approach known as rotating-polarization coherent anti-Stokes Raman spectroscopy (RP-CARS) yielding the intensity of the anti-Stokes emission, the directionality the molecular bonds of interest and their average orientation [72]. The scheme of the setup is shown in Fig. (1.20). They imaged myelinated axons in fixed mouse-brain slices have been imaged by RP-CARS. They detected the local average direction of the acylic chains of membrane phospholipids and their spatial anisotropy shown in Fig. (1.21).

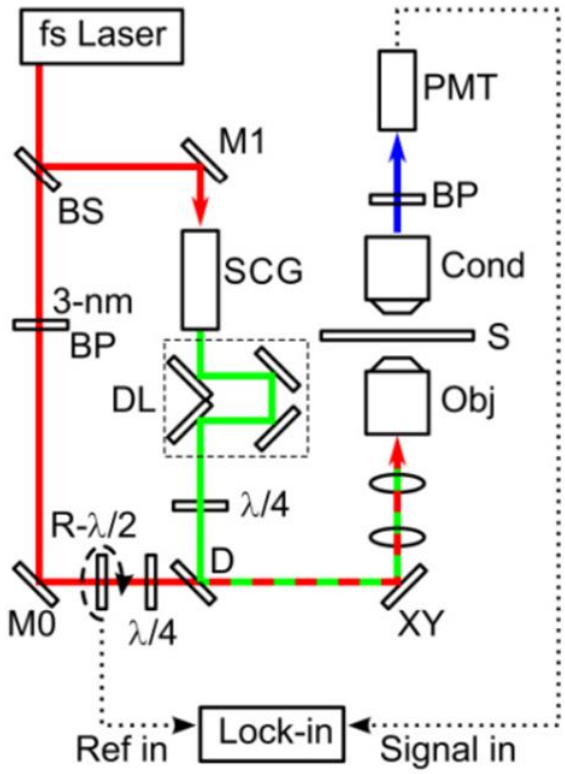

Figure 1.20. Schematic representation of the RP-CARS setup. The 800-nm pulses from the laser (fs Laser), shown as red lines, are split by a beam splitter (BS) and routed to the supercontinuum generator (SCG) and, through two 3-nm bandpass filters (3-nm BP) centered at 800 nm, to the rotating λ/2 retarder (R-λ/2). The linearly polarized broadband radiation (green lines) is delayed by a delay line (DL), transformed into circularly polarized light by a λ/4 retarder (λ/4), and recombined with the 800-nm radiation by means of a dichroic mirror (D). A second λ/4 retarder in the pump and probe path allows compensating for polarization distortions caused by D. The two are then routed to the high-numerical-aperture lens (Obj) through a pair of galvo-scanning mirrors, a scan lens and a tube lens. CARS signal is collected from the sample (S) by a condenser lens (Cond), band-pass filtered (BP), and routed to a photomultiplier tube (PMT). M0 to M2 are silver-coated mirrors. The output of the PMT is measured by phase-sensitive techniques by means of a lock-in amplifier. The reference phase and frequency for the lock-in amplifier is generated by a Hall sensor in close proximity to the rotor of the brushless motor that rotates R-λ/2 (reported from reference [72]).

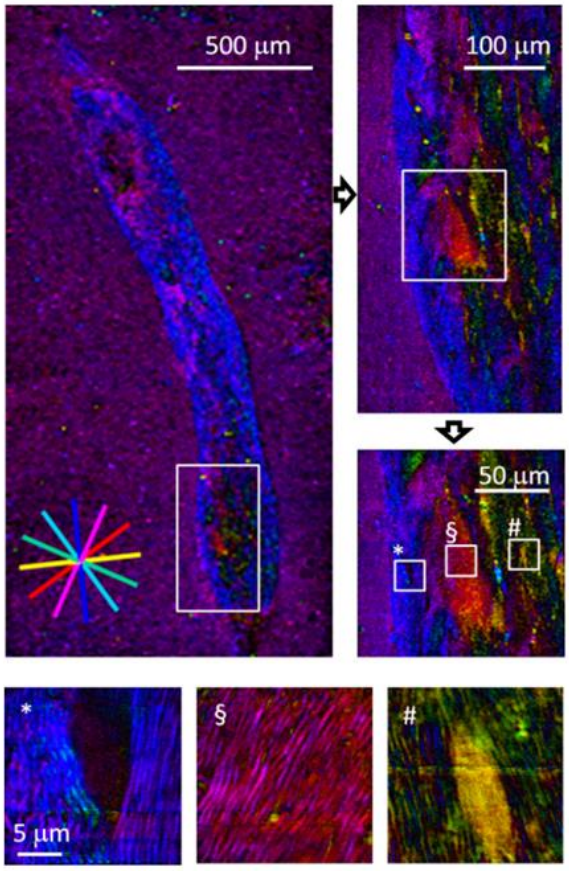

Figure 1.21. Coronal section of the mouse brain anterior commissure imaged at different magnifications. This multi-scale acquisition shows the degree of local asymmetry in the direction of the acrylic chains and their average spatial orientation. The white rectangles show the region magnified in the successive image of the series (indicated by an arrow). The colored lines in the top-left panel depict the color to orientation mapping. The last three images (*,§ and #) refer respectively to the three white rectangles in the preceding image. The pump and probe beam and the Stokes beam power was respectively 50 mW and 10 mW (reported from reference [72]).

1.4.4.2 Polarization SHG microscopy

Harmonic generation is a nonlinear optical process in which photons of intense incoming laser radiation interact with a nonlinear material and radiation with corresponding harmonics frequencies is generated. Label-free SHG process relies on a nonlinear optical interaction with hyperpolarizable non-centrosymetric and therefore occurs in specific structures and endogenous fibrillar proteins like collagen and myosin, causing scattered coherent radiation at twice the fundamental frequency. Thus, it has proved to be an extremely beneficial contrast mechanism for real-time and label-free imaging of these endogenous molecules *in-situ*, *in-vivo*, in physiological as well as in disease state. SHG signals arise from an induced polarization rather than from absorption, which leads to substantially reduced photobleaching and photo-toxicity relative to fluorescence methods [73]. However, SHG microscopy has limited applicability to a small number of non-centrosymmetric structures such as collagen fibrils, myosin filaments and microtubules. Other limitation of SHG microscopy are related to a backscattering signal that is less intense than forward one, a low intensity signal and the ability to penetrate and image highly scattering tissues not more than a few hundred micrometers of thickness depending on the scattering coefficient of the specific tissue.

Polarization dependent second harmonic generation (P-SHG) microscopy that enables quantification of organizational changes in fibrillar protein, is gaining increased popularity for investigating fibrillar collagen-rich tissues with the desire to extract as much structural information as possible. P-SHG imaging was introduced decades ago in ordered molecular samples [74]. Recent works have demonstrated that rich information is contained in polarization responses recorded from a tunable incident linear polarization in the sample plane. For instance, in 2012, G. Latour et al., proposed *in-vivo* structural imaging of the cornea by P-SHG that is highly sensitive to the sub-micrometer distribution of anisotropic structures. In this way, they retrieved the orientation of the collagenous fibrils at each depth of human corneas, even in backward SHG homogenous images [75]. The scheme of the setup is shown in Fig. (1.22). Their polarimetric method allows to map fibril orientation fields, independently of individual fibril contrast in the SHG image. Typical backward SHG (B-SHG) and forward SHG (F-SHG) images from *ex-vivo* human corneas are displayed in Fig. (1.23).

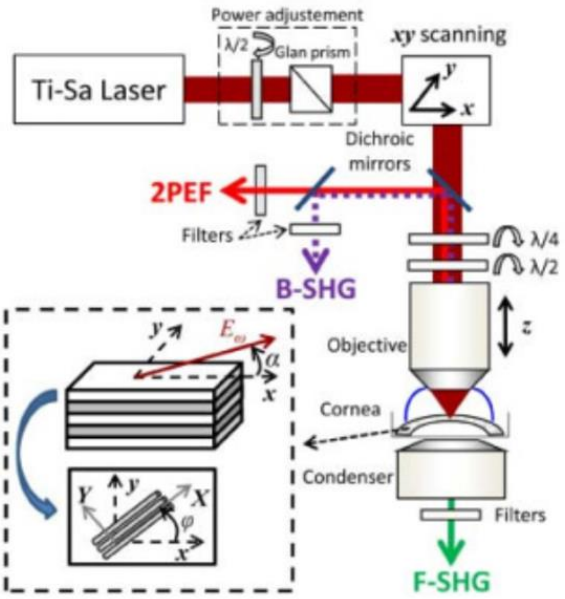

Figure 1.22. Experimental setup of laser scanning microscope with rotating wave-plates to control the polarization state of the excitation beam. Orientation of the linearly polarized excitation relative to the cornea morphology in the laboratory frame is indicated in the inset. 2PEF: Two-photon excitation fluorescence and B-SHG: Backward SHG are detected in the backward direction as required in *in-vivo* experiments. F-SHG: Forward SHG is also detected in *ex-vivo* experiments and correlated to polarimetric B-SHG data (reported from reference [75]).

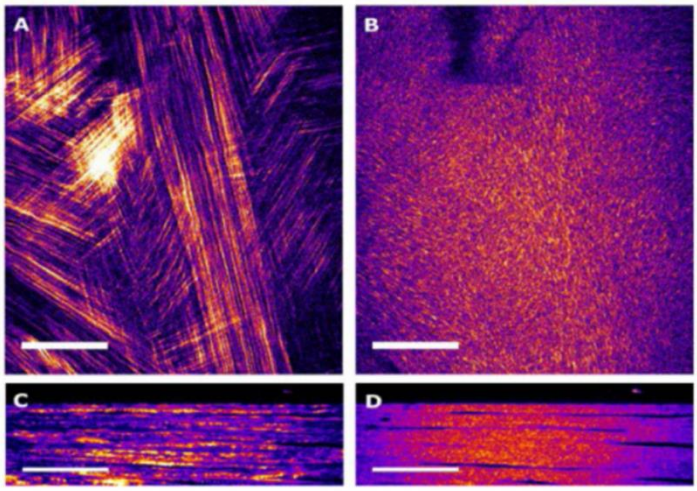

Figure 1.23. F-SHG and B-SHG images of posterior stroma from human corneas. (A) F-SHG and (B) B-SHG images obtained as the sum of all the raw images acquired with tunable linear incident polarization (60x 1.2 NA objective, scale bar: 30 µm, false colors); (C) F-SHG and (D) B-SHG x-z reconstruction from the previous data volume. Striated features (A) and stacked organization (C) are clearly visible in F-SHG images while B-SHG images (C) and (D) are spatially homogenous in (reported from reference [75]).

1.4.4.3 Polarization THG microscopy

Besides extensive work on SHG, some attempts have recently demonstrated the interest in other higher-order nonlinear coherent contrasts. THG is in particular interesting, since it is not non-centrosymmetric sensitive and can therefore give information about anisotropic, but centrosymmetric structures [76]. Due to its nonlinear nature, the third harmonic light is generated only in close proximity to the focal point. Since all materials have non-vanishing third order susceptibilities, THG microscopy can be utilized as a general-purpose microscopy technique. THG takes advantage of the discontinuity of third-order nonlinear susceptibility at material interfaces that is elicited by water-lipid and water-protein interfaces, including intra- and extracellular membranes, and extracellular matrix structures. This method delivers a versatile contrast modality, which allows completely label-free detection of cellular and molecular cell functions in three-dimensional tissue culture and small animals *in-vivo* and *in-vitro* with low risk of photo-damage [77]. However, since the microscope must operate in a transmission mode, good quality with high NA objective lenses should be used on both sides of the sample so that it requires thin samples and special mounting. In addition, dependence on the distribution of the signal and the need for high infrared wavelengths (>1200 nm) leads to scattering of the short-wavelength THG light that is deleterious to the image.

A recent study in cornea tissues made of stromal lamellae structures has shown that forward-radiated THG and SHG signals are generally anticorrelated, indicating that the THG signal originates from the lamellar interfaces whereas SHG originates from regions within the lamellae, principally from the collagen sub-structures [78]. The imaging method is shown in Fig. (1.24). Polarization-resolved THG (P-THG) imaging exhibits an isotropic component revealed upon linear excitation that is representative of cellular and anchoring structures, whereas its anisotropic component that is revealed upon circular excitation is representative of an alternate anisotropy direction between the lamellae, allowing the direct imaging of their stacking and heterogeneity with a micrometer-scale three-dimensional resolution shown in Fig. (1.25).

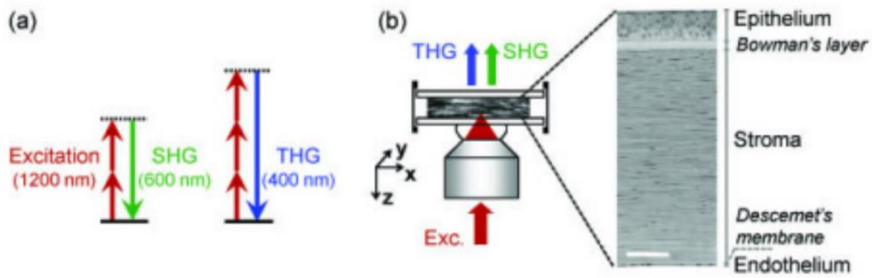

Figure 1.24. SHG vs THG imaging method. (a) Principles of multi-harmonic microscopy, and wavelengths involved. (b) Experimental geometry. In this study, intact excised corneas were mounted between glass coverslips, illuminated from the endothelial side and imaged in transmission. Right: histological image of a human cornea, shown for comparison with the THG-SHG images. Scale bar 100 µm (reported from reference [78]).

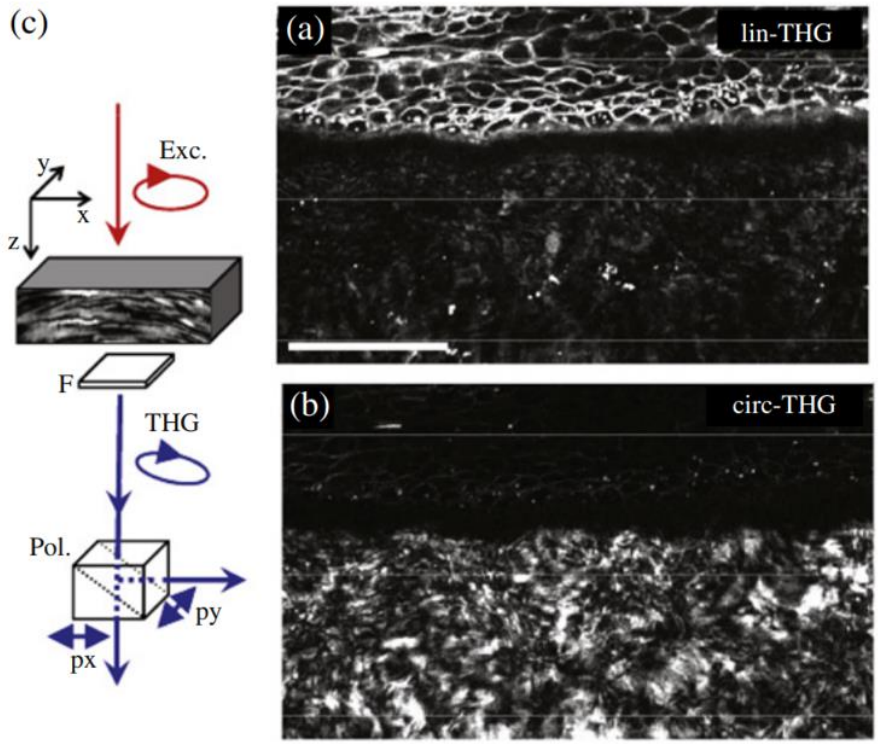

Figure 1.25. Polarization-sensitive THG imaging. THG imaging of a cornea with (a) linear and (b) circular incident polarization revealing anisotropic structures. Scale bar is 100 µm. (c) Principle of the experiment with polarization-resolved detection (reported from reference [78]).

1.4.5 Linear and nonlinear polarization-resolved fluorescence scanning microscopy imaging

Fluorescence results from two successive processes: the absorption of an incident photon and the emission of a fluorescence photon of lower frequency. These processes occur at different times, as the molecule relaxes from its high-energy excited state to its lowest one. The fluorescence emission of different molecules is incoherent, with no phase correlation between them. Fluorescence efficiency is proportional to the product of absorption between the ground and excited states and emission from the fluorescent state to the ground state [79].

FPM analyzes the polarization of light in a fluorescent microscope to determine the angular orientation and rotational mobility of fluorescent molecules. FPM detects the structural specificity of target molecules through fluorescence anisotropy, where the light emitted by a fluorophore has unequal intensities along different axes of polarization. FPM allows the detection of conformational changes of fluorescently labeled macromolecules in real-time and at the single-molecule level under physiological conditions. Early pioneers in the field include Aleksander Jablonski, Gregorio Weber, and Andreas Albrecht [80, 81]. In FPM, a polarized excitation filter is used to excite a fluorophore, and the polarized fluorescence is measured through an emission polarizer either parallel or perpendicular (or at any angle) to the exciting light's plane of polarization. The photo-selection process results in a nonrandom distribution of excited molecules' transition moments when randomly distributed labeled molecules are excited with linearly polarized light. When a linearly polarized light excites a single molecule, the highest probability of absorption occurs when its transition dipole moment is oriented parallel to the incident polarization.

Fluorescence polarization techniques have long been used to measure the orientational distributions and rotational diffusion of molecules in solution or suspension, offering the possibility of analogous studies on the surface or interior of small sub-volumes of cells and tissues. This technique has also been used to detect the binding of molecules to their partners in signaling cascades in response to certain cues. In 2017, C. Vinegoni et al., characterized the target engagement of fluorescently labeled drugs, using fluorophores with a fluorescence lifetime larger than the rotational correlation of the bound complex [82]. The ability to image and quantify drug-target engagement and drug distribution with subcellular resolution in live cells and whole organisms is a prerequisite to establishing accurate models of the kinetics and dynamics of drug action. Fig. (1.26) illustrates that if the excitation light is polarized along the z-axis as vertical polarization, molecules with transition moments oriented in the same direction will be preferentially excited, resulting in fluorescence intensity detected through a polarizer oriented along the horizontal x or y-axis. This is for molecules with parallel orientations of absorption and

emission transition moments and with absent molecular rotations or other depolarization processes. Accordingly, the fluorescence anisotropy for cylindrical symmetry is defined as:

$$r = \frac{I_{VV} - I_{VH}}{I_{VV} + 2I_{VH}} \tag{1.43}$$

where I is the intensity of the light, V is vertical and H is horizontal. The first symbol in the anisotropy equation refers to the polarization of the excitation light, and the second one is related to the orientation of the analyzer. The origin of anisotropy is the existence of transition moments for absorption and emission that lie along specific directions within the fluorophore structure. Moreover, a number of processes, such as rotational diffusion and energy transfer, can depolarize the fluorescence emission. All fluorophores have transition moments that occur along a specific direction in the molecular axis. Rotational diffusion changes the direction of the transition moments and is a common cause of depolarization. Radiationless energy transfer occurs only in concentrated solutions where the average distance between the fluorophore molecules is comparable to a characteristic distance, which is typically near 40 Å. Anisotropy measurements reveal the average angular orientation of the fluorophore relative to absorption and subsequent emission of a photon. In other words, when the absorption and emission dipoles are collinear, there are no processes that result in depolarization [83].

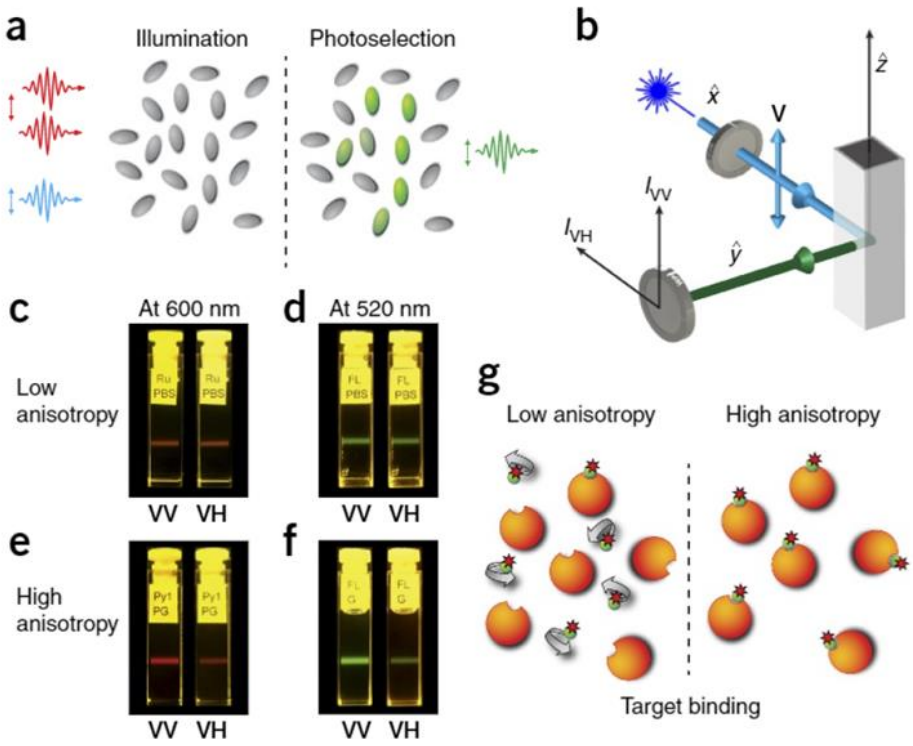

Figure 1.26. Fluorescence anisotropy principles and measurements. (a) Polarized light selectively excites fluorophores aligned along a preferential axis. If the rotation of the molecule occurs on a time scale that is shorter than its fluorescence lifetime, the fluorescence emission will present a certain degree of anisotropy. (b) Standard configuration for fluorescence anisotropy measurements. A sample is excited with vertically polarized light.The intensity of the emitted fluorescence is analyzed through a polarizer oriented parallel and perpendicular to the incident excitation vector field. $\hat{x}$, $\hat{y}$ and $\hat{z}$ indicate the unit vectors. (c-f) Images of fluorescence anisotropy for different dyes presenting low and high anisotropy. (g) Upon binding to their target, fluorescently labeled small-molecule drugs increase their fluorescence anisotropy value (reported from reference [82]).

Polarization-resolved fluorescence scanning microscopy is a type of FPM that utilizes both the excitation and emission light's polarization to provide additional information about the sample, such as molecular orientation and anisotropy, on a pixel-by-pixel basis. This is achieved by measuring the fluorescence emission intensity for different orientations of the polarization filter placed in front of the detector.

For instance, in a study in 2015, a fixed *E. coli* bacterium was fluorescently labeled with FM 1-43 membrane dye as molecular probes [84]. The FM dye aligns along lipids in the bacterial membrane, resulting in its dipole moment being orthogonal to the membrane when bound. A single cell was imaged using the fluorescence anisotropy image acquisition sequence, as shown in Fig. (1.27 a). The polarization information can be visualized using computed colors (Fig. 1.27 b), based on the reference color aster in Fig. (1.27 c). Alternatively, the data can be displayed as lines overlaid on the average image. A comparison of computed color vs. line display is shown in Fig.

(1.27 e), and Fig. (1.27 f) demonstrates that multi-focus polarization imaging of the *E. coli* bacterium consistently detects the expected orientation of the dye in the membrane throughout the depth of the sample. Fig. (1.27 g) depicts the frustule of the diatom *P. angulatum*, a type of phytoplankton, imaged in birefringence (transmission) mode. The shell's puncta have a pitch of 525 nm, and in birefringence data, color indicates the direction of the slow axis, which runs along the edges of this sample.

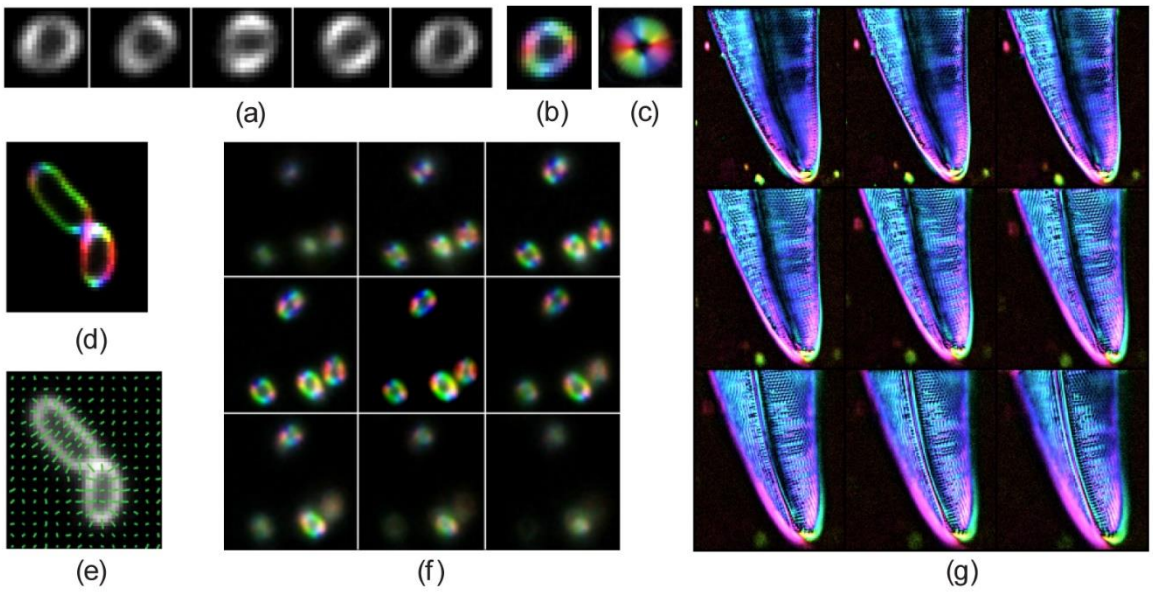

Figure 1.27. (a)-(f) Fluorescence polarization images of *E. coli* labeled with FM 1-43 membrane dye (Molecular Probes). (a) Raw data of the fluorescence polarization acquisition sequence: From left to right, the sample is illuminated by elliptically polarized light of directions 0, 45, 90, 135 degrees and the 0 degree orientation repeated at the end. (b) Color-processed data of **a**, showing dipole orientation encoded by color, according to the color reference aster in **c**. (c) The color orientation aster shows how the polarization anisotropy data is displayed. For example, horizontal dipole orientation in the image is displayed as red and vertical by turquoise. (d) Dye orientation in *E. coli* cell indicated by color, according to the orientation color reference aster in **c**. (e) Dye orientation of cell in **d** indicated by lines. Data has been smoothed and contrast adjusted. (f) Cropped out region of all nine planes of a multifocus image of bacteria shows that the orientation direction is correct and consistent in the entire multifocus image. Region of interest shown is $5.4 \times 6.3\ \mu m^2$ cropped out from an image of $33 \times 33\ \mu m^2$ total lateral field of view. (g) Birefringence multifocus image of the frustule of a diatom (reported from reference [84]).

Polarization-resolved fluorescence scanning microscopy can be conducted in both linear and nonlinear modes, which is particularly useful for studying the structure and properties of biomolecules as well as the function of macromolecules in complex systems. This approach has successfully probed the organization of cell membranes' lipids or actin filaments and can also be

extended to investigate the orientational modifications of membrane proteins. In solutions or intracellular environments, the excited molecules' rotational diffusion can scramble the emission dipoles' orientation, removing the preferential direction present in the fluorescence emission. The probability of linear fluorescence excitation is proportional to $\cos^2\theta$, where θ is the angle between the molecule's transition moment and the z-axis. During two-photon excitation, a nonlinear phenomenon occurs, where two low energy photons interact simultaneously with a molecule, exciting the fluorophore to its singlet state. The probability of the excitation is proportional to $\cos^4\theta$, resulting in a higher photoselection value that leads to a higher fluorescence anisotropy [82]. Two-photon excitation provides accurate optical sectioning imaging, allowing for precise probing of volumes on the order of/or below a femtoliter.

1.5 Conclusion

The chapter introduces the theoretical basis of light polarization, its methods, and applications. The interaction of a light wave with a medium can be described using linear mathematical tools like the Jones formalism. However, this description is limited to non-depolarizing media and cannot deal with depolarization phenomena. Therefore, the Stokes-Mueller formalism has been introduced to obtain the entire polarimetric signature of a medium in a single 4 × 4 MM composed of real coefficients. The elementary polarimetric effects corresponding to dichroism, birefringence, and depolarization are described. The concept of polarization-resolved microscopy is to study crystalline and fibrous structures through light-matter interactions. The chapter explains featured methods in linear optics in label-free polarization microscopy, working based on the polarization microscopy of scattered light from an object, such as cross-polarization, polarimetric light-sheet tomography, and MM microscopy techniques.

To experimentally determine the MM, the Mueller polarimeter encodes the light source in polarization and decodes its modifications after interaction with a medium. In the time domain, polarization is encoded and decoded sequentially, requiring active elements such as photo-elastic modulators for the measurement duration. The chapter also explains the spectral encodings domain that should be considered in Mueller imaging through real-time scanning. The MM setups are divided into two categories: complete Mueller, which retrieves the whole matrix, and incomplete Mueller, which is only capable of determining some of the elements. Moreover, the chapter notes that nonlinear optical contrasts applied to imaging benefit from significant progress made in polarization control, allowing distinguishing features that are not accessible through linear optics in polarization-resolved microscopy. Since these processes involve high-order interaction, tuning polarization states provides information on the structural behavior of molecular samples. Polarimetric CARS, SHG, and THG, along with their applications as non-linear label-free polarization-resolved microscopy methods, are discussed. In the final section, fluorescence anisotropy based on microscopy imaging of biological tissues and organelles is explained in terms of linear and non-linear fluorescence polarization microscopy, along with some applications provided. These approaches open new prospects towards read-out imaging of molecular order and symmetry properties, such as sub-cellular structural behavior related to specific biological functions.

In general, the chapter emphasizes how polarization-sensitive microscopy techniques can offer a powerful approach to studying cells and tissues by providing insights into their structural organization, polarization properties and diagnosis of pathological conditions by detecting abnormalities in tissue lesions, cell nuclei, and chromatin.

References

[1] B. A. Saleh, *Ray Optics*, in "*Fundamentals of Photonics*. ", p. 1-40, 1991.

[2] G. H. Smith, "*Camera Lenses: From Box Camera to Digital*. ", Society of Photo Optical, 2006.

[3] J. C. Maxwell, *A dynamical theory of the electromagnetic field.* Philosophical Transactions of the Royal Society of London, (155): p. 459–512, 1985.

[4] R. C. Jones, "*A New Calculus for the Treatment of Optical SystemsI. Description and Discussion of the Calculus.*" J. Opt. Soc. Am., vol. 31: p. 488-493, 1941.

[5] G. Stokes, "*On the composition and resolution of streams of polarized light from different sources.* Transactions of the Cambridge Philosophical Society", vol. 9: p. 339–416, 1852.

[6] H. Mueller, "*The foundation of optics.*" Journal of Optical Society of America, vol. 38 (661), 1948.

[7] E. H. Poincaré, "*Mathematical theory of light*." Gauthiers-Villars 2, Paris, 1892.

[8] E. Wolf and M. Born, "*Principles of Optics*", New-York: Pergamon Press., 1983.

[9] R.W. Wood, *Physical Optics. Macmillan.* 1911.

[10] S. Y. Lu and R. A. Chipman, "*Interpretation of Mueller matrices based on polar decomposition.*" J. Opt. Soc. Am. A., vol. 13: p. 1106-1113, 1996.

[11] F. Perrin, "*Polarization of light scattered by isotropic opalescent media.*" The Journal of Chemical Physics, vol. 10 (7): p. 415, 1942.

[12] V. V. Tuchin, "*Light scattering study of tissues. Physics.*" vol. 40(5): p. 495, 1997.

[13] W. H. Talbot, "*XLIV. Experiments on light". The London, Edinburgh, and Dublin Philosophical Magazine and Journal of Science.* vol. 5 (29): p. 321–334, 1834.

[14] W. H. Mcmaster, "*Polarization and the Stokes Parameters.*" Am. J. Phys. , vol. 22, p. 351–362, 1954.

[15] S. Huard, "*Polarization of Light. In Polarization of Light*." 1st ed. ed.: John Wiley & Sons Inc.: New York, NY, USA, 1997.

[16] D. Lourdin et al., "*Crystalline Structure in Starch,*" Springer, Tokyo, 2015.

[17] S. Inoué and R. Oldenbourg, "*Microtubule dynamics in mitotic spindle displayed by polarized light microscopy.*" Mol Biol Cell., vol. 9(7): p. 1603-7, 1998.

[18] A. Suzuki, et al., "*Formation of liquid crystalline phase of actin filament solutions and its dependence on filament length as studied by optical birefringence.*" Biophysical Journal, vol. 59(1): p. 25-30, 1991.

[19] M. L. Mello and B. C. Vidal., "*Polarization microscopy of extended chromatin fibers.*" Methods Mol Biol. , (1094): p. 71-8, 2014.

[20] H. S. Koppang, et al., "*Cellulose fibers from endodontic paper points as an etiological factor in postendodontic periapical granulomas and cysts.*" Journal of Endodontics, vol. 15(8): p. 369-372, 1989.

[21] M. Kornreich, et al.,"*Cross polarization compatible dialysis chip.*" Lab Chip, 2014. vol. 14: p. 3700-3704, 2014.

[22] A. Wenzel and M. Antonietti, "*Superstructures of lipid bilayers by complexation with helical biopolymers.*" Adv. Mat., vol. 9(6): p. 487-490, 1997.

[23] V. Tuchin, "*Polarized light interaction with tissues.* Journal of Biomedical Optics", vol. 21(7): p. 071114, 2016.

[24] J. C. Ramella-Roman, et al., "*A review of polarization-based imaging technologies for clinical and preclinical applications.*" J. Opt., vol. 22, 123001, 2020.

[25] P. Doradla, et al., "*Detection of colon cancer by continuous-wave terahertz polarization imaging technique.*" J Biomed Opt., vol. 18 (9): p. 090504–090504, 2013.

[26] A. M. Glazer, et al.,"*An automatic optical imaging system for birefringent media.* " Proc. R. Soc. Lond., (A 452): p. 2751–2765, 1996.

[27] N. J. Jan, et al., "*Polarization microscopy for characterizing fiber orientation of ocular tissues.*" Biomed. Opt. Express, (6): p. 4705–4718, 2015.

[28] S. B. Mehta,et al., " *Polarized light imaging of birefringence and diattenuation at high resolution and high sensitivity.*" J. Opt. , vol. 15: p. 094007, 2013.

[29] M. Weber, et al., "*Methods in Cell Biology: Chapter 11 - Light sheet microscopy*", Academic Press. Med. , vol. 123: p. 193-215, 2014.

[30] S. L. Jacques, et al., "*Imaging superficial tissues with polarized light*", Lasers Surg. Med. , vol. 26(2): p. 119–129, 2000.

[31] S. L. Reidt, et al., "*Polarised light sheet tomography.*" Opt. Express, (24): p. 11239-11249, 2016.

[32] O. Arteaga, et al., "*Mueller matrix microscope with a dual continuous rotating compensator setup and digital demodulation.* " Appl. Opt. , vol. 53: p. 2236–2244, 2014.

[33] A. Laskarakis, et al., "*Mueller matrix spectroscopic ellipsometry: formulation and application.* " Thin Solid Films, vol. 455–456: p. 43-49, 2004.

[34] S. Savenkov, et al., *Incomplete active polarimetry:* "*Measurement of the block-diagonal scattering matrix.* " J. Quant. Spectrosc. Radiat. Transf., vol. 112(11): p. 1796–1802, 2011.

[35] A. Le Gratiet, "*Développement d'un polarimètre de Mueller à codage spectral utilisant une Swept-source: application à la microscopie à balayage laser*. ", Université de Bretagne occidentale-Brest, 2016.

[36] A. Le Gratiet, et al., "*Review on Complete Mueller Matrix Optical Scanning Microscopy Imaging.*" Applied Sciences, vol. 11(4): p. 1632., 2021.

[37] M. H. Smith, "*Optimization of a dual-rotating-retarder mueller matrix polarimeter.* " Applied Optics, 2002. 41(13): p. 2488–2493, 2002.

[38] K. S. Ichimoto, et al., "*Photopolarimetric Measurement System of Mueller Matrix with Dual Rotating Waveplates*.", Publications of National Astronomical Observatory, 2006.

[39] D. H. Goldstein, "*Mueller matrix dual-rotating retarder polarimeter.* " Applied Optics, vol. 31(31): p. 6676–6683, 1992.

[40] R. A. M. Azzam, " *Photopolarimeter using two modulated optical rotators.* " Optics Letters, vol. 1(5): p. 181–183, 1977.

[41] J. L. Pezzaniti and R. A. Chipman, "*High-resolution mueller matrix imaging polarimetry for understanding high-resolution optoelectronic modulators*. " in *The International Society for Optical Engineering*. SPIE, 1995.

[42] J. W. Lewis, et al., "*Time-resolved circular dichroism spectroscopy: Experiment, theory, and applications to biological systems.* " J. Phys. Chem., 1992. vol. 96(13): p. 5243–5254, 1992.

[43] F. Delplancke, "*Automated high-speed mueller matrix scatterometer.* " Applied Optics, vol. 36: p. 5388–5395, 1997.

[44] T. Dartigalongue and F. Hache, "*Precise alignment of a longitudinal Pockels cell for time-resolved circular dichroism experiments.*", J. Opt. Soc. Am. B, vol. 20(8): p. 1780, 2003.

[45] A. De Martino, et al., "*Optimized mueller polarimeter with liquid crystals.*" Optics Letters, vol. 28(8): p. 616–618, 2003.

[46] A. Peinado, et al., "*Design and optimization of polarimeters based on liquid-crystal displays.* " SPIE Newsroom, 2013.

[47] E. Garcia-Caurel, et al., "*Spectroscopic Mueller polarimeter based on liquid crystal devices.*" Thin Solid Films, (455-456): p. 120–123, 2004.

[48] K. Oka, et al., "*Channeled spectropolarimeter using a wavelengthscanning laser and a channeled spectroscopic polarization state generator.*", SPIE, vol. 8160, p. 261-267, 2011.

[49] N. Hagen and E. L. Dereniak, "*Snapshot mueller matrix spectropolarimetry.* ", SPIE, vol. 6682, p. 668207–7, 2007.

[50] N. Ghosh and A. I. Vitkin, "*Tissue polarimetry : concepts, challenges, applications, and outlook.*" J. Bio. Opt., vol. 16(11): p. 110801–29, 2011.

[51] S. Alali and I. A. Vitkin., "*Polarized light imaging in biomedicine: emerging mueller matrix methodologies for bulk tissue assessment.*" J. Bio. Opt., vol. 20(6): p. 061104, 2015.

[52] I. Tinoco, et al., "*Use of circularly polarized light to study biological macromolecules.* " Pure Appl. Chem. , vol. 56: p. 1423–1428, 1984.

[53] A. Diaspro, et al., "*Polarized light scattering of nucleosomes and polynucleosomes-in situ and in vitro studies.*" IEEE Trans. Biomed. Eng., vol. 38: p. 670–678, 1991.

[54] A. Le Gratiet, et al., "*Circular Intensity Differential Scattering for Label-Free Chromatin Characterization: A Review for Optical Microscopy.* " Polymers (Basel), vol. 12(10), 2020.

[55] D. Keller, et al., "*Imaging of optically active biological structures by use of circularly polarized light.* " Proc. Natl. Acad. Sci. USA, vol. 82: p. 401–405, 1985.

[56] C. Bustamante, et al., "*Circular differential scattering can be an important part of the circular dichroism of macromolecules.*" Proc. Natl. Acad. Sci. USA, vol. 80: p. 3568–3572, 1983.

[57] C. Bustamante, et al., "*Expressions for the interpretation of circular intensity differential scattering of chiral aggregates.*" Biopolymers, vol. 24: p. 1595–1612, 1985.

[58] J. Qi, et al., "*Circular intensity differential scattering microscopy for label-free characterization of organized assemblies*." Nature Communications, vol. 10(1): p. 1–12, 2019. 2019.

[59] A. Van Eeckhout, et al. "*Depolarizing metrics for plant samples imaging*." PLOS ONE, vol. 14(3): e0213909, 2019.

[60] J. M. Bueno, et al., "*Confocal scanning laser ophthalmoscopy improvement by use of Mueller-matrix polarimetry*," Opt. Lett., vol. 27: p. 830-832, 2002.

[61] L. Finzi, et al., "*Differential polarization imaging. V. numerical aperture effects and the contribution of preferential scattering and absorption to the circular dichroism images*," Biophys. J., vol. 59, no. 6, p. 1183–1193, 1991.

[62] M. Kim and C. Bustamante, "*Differential polarization imaging. IV. Images in higher Born approximations*," Biophys. J., vol. 59, p. 1171–1182, 1987.

[63] J. Breton and A. Vermeglio, "*Photosynthesis*," Academic Press, New York, Govendjee, editor., vol. 1, p. 153-194, 1982.

[64] J. Qi and D. S. Elson, "*Mueller polarimetric imaging for surgical and diagnostic applications: a review.*" J. Biophotonics, vol. 10: p. 950–982, 2017.

[65] A. Le Gratiet, et al., "*Circular intensity differential scattering (CIDS) scanning microscopy to image chromatin-DNA nuclear organization*," OSA Continuum, vol. 1(3): p. 1068-1078, 2018.

[66] J. Chue-Sang, et al., "Use of Mueller matrix polarimetry and optical coherence tomography in the characterization of cervical collagen anisotropy.", J. of Biom. Opt., vol. 22(8): 086010, 2017.

[67] A. Pierangelo, et al., "*Polarimetric imaging of uterine cervix: a case study*," Opt. Express, vol. 21: p. 14120-14130, 2013.

[68] J. Qi and D. S. Elson, "*High definition Mueller polarimetric endoscope for tissue characterisation.*", Sci. Rep., vol. 6: 25953, 2016.

[69] K. M. Twietmeyer, et al., "*Mueller matrix retinal imager with optimized polarization conditions.* " Opt. Express, vol. 16(26): p. 21339–21354, 2008.

[70] M. R. Antonelli, et al., "*Mueller matrix imaging of human colon tissue for cancer diagnostics: how monte carlo modeling can help in the interpretation of experimental data.*", Optics Express, vol. 18(10): p. 10200–10208, 2010.

[71] A. Le Gratiet, et al., "*Zebrafish structural development in Mueller-matrix scanning microscopy.*" Sci. Rep., vol. 9: p. 1–10, 2019.

[72] G. De Vito, et al., "*Rotating-polarization CARS microscopy: combining chemical and molecular orientation sensitivity.* " Opt. Express, vol. 20: p. 29369-29377, 2012.

[73] W. R. Zipfel, et al., "*Nonlinear magic: multiphoton microscopy in the biosciences.*" Nature biotechnology, vol. 21: p. 1369–1377, 2003.

[74] M. Florsheimer, et al., " *Second-harmonic microscopy—a quantitative probe for molecular surface order.*", Adv. Mater., vol. 9(13): p. 1061–1065, 1997.

[75] G. Latour, et al. "*In vivo structural imaging of the cornea by polarization-resolved second harmonic microscopy*." Bio. Opt. exp. 3.1, p. 1-15, 2012.

[76] S. Brasselet, "*Polarization-resolved nonlinear microscopy: application to structural molecular and biological imaging.* " Adv. Opt. Photon., vol. 3(205), 2011.

[77] B. Weigelin, et al., "*Third harmonic generation microscopy of cells and tissue organization.*" Journal of Cell Science, vol. 129: p. 245-255, 2016.

[78] N. Olivier, et al., "*Harmonic microscopy of isotropic and anisotropic microstructure of the human cornea.* " Opt. Express, vol. 18, p. 5028–5040, 2010.

[79] J. R. Lakowicz, "*Principles of Fluorescence Spectroscopy*", Springer,1999.

[80] G. Weber, "*Rotational Brownian motion and polarization of the fluorescence of solutions.* " Adv. Protein Chem., vol. 8: p. 415-459, 1953.

[81] A. C. Albrecht, "*Polarizations and assignments of transitions: the method of photoselection.* " J. Mol. Spectrosc., vol.6: p. 84-108, 1961.

[82] C. Vinegoni, et al., "*Measurement of drug-target engagement in live cells by two-photon fluorescence anisotropy imaging.* " Nat Protoc, vol. 12: p. 1472–1497, 2017.

[83] J. R. Lakowicz, "*Principles of Fluorescence Spectroscopy*." Plenum Press, 1983.

[84] S. Abrahamsson, et al., "*MultiFocus Polarization Microscope (MF-PolScope) for 3D polarization imaging of up to 25 focal planes simultaneously,"* Opt. Express, vol. 23(6): p. 7734-7754, 2015.

Chapter 2

Circular Intensity Differential Scattering microscopy imaging and spectroscopy for chromatin characterization

2.1 Introduction

In the realm of biology, DNA plays a fundamental role as it contains the genetic information that determines an organism's characteristics. The chiral structure of DNA refers to its spiral shape, which is composed of two strands of nucleotides that coil around each other in a helical pattern. Chromatin is a complex, chiral macromolecule composed of the DNA double helix and proteins located in the nucleus of eukaryotic cells. Chromatin exists in two forms: euchromatin, which is less condensed and can be transcribed, and heterochromatin, which is highly condensed and is typically not transcribed [1]. Therefore, understanding its different compaction levels is essential for describing DNA function, as it plays a crucial role in cell differentiation by regulating gene expression during the cell cycle and controlling the specialization of cells [2].

There are various optical microscopy and spectroscopy methods available for detecting such organizations. Optical microscopy utilizes visible light to observe biological samples, whereas spectroscopy methods measure the interaction between light and matter to gather information about the sample's composition and structure. The detection of localized molecules of interest in chromatin-specific fluorescent probes using super-resolution optical microscopy methods is a widely used approach in the study of biological organizations [3]. Super-resolution fluorescence microscopy is a technique that detects single molecules of biological structures and processes, making it an essential tool for cell and tissue imaging. However, the need for expensive and bulky equipment makes it unaffordable for many laboratories. Furthermore, measuring the compaction level, medium structure, and orientation of molecular properties in chromatin requires a new

contrast dimension to obtain hidden information such as polarization-sensitive data. Polarization-based imaging techniques provide non-invasive label-free contrasts for revealing polarimetric hidden information, which has demonstrated significant potential in biology [4]. MM polarimetry is the most comprehensive method as it provides the full polarimetric response of a sample. The mathematical decomposition of this matrix leads to numerous polarimetric parameters, as the well-known properties such as the absorption, dichroism, birefringence and scattering, but the m_{ij} combinations could also provide the basic response that constitutes linear and circular dichroism (LD/CD), linear and circular birefringence (LB/CB) [5]. However, interpreting the full MM of complex, random biological media at a sub-microscopic scale can be an arduous task. The main reason for this difficulty is that extracting the localized polarimetric signature of a biological sample is challenging due to the extremely low SNR caused by weak absorption and strong scattering through complex structures. Additionally, the mix of numerous different structures is confined in a small volume. This is why polarimetric techniques are mostly dedicated to arranged and patterned inorganic material media. To overcome this limitation, early works have emphasized studying only a few elements of the MM that are more sensitive to particular configurations of the medium. This is typically the case for CD, which is defined using the intensities of the circular left and right polarization of the light scattered from the sample, arising from media exhibiting an optical activity that corresponds to the m_{03} element of the scattering MM. The main part of CD is due to the difference in absorbance exclusively in the forward direction, and a smaller component is due to differential scattering [6]. This signal is known as CIDS and occurs outside the absorption band and/or at a non-zero scattering angle. In general, CIDS can be an interesting non-invasive technique to study anisotropic specimens and the structure of biopolymers such as chromatin at the sub-microscopic level by revealing information about the chirality and/or handedness of the molecules of interest [7].

To perform typical CIDS measurements, circular right- and left-polarization states are generated by periodically stressing a birefringent crystal using electro-optical devices. The polarization of the incident light is modulated at a high-speed rate using a photoelastic modulator (PEM) to encode the circular polarization states in CIDS acquisition. The Stokes-Mueller formalism has shown that differential circular polarized light, coupled with a demodulation detection scheme using a lock-in amplifier (LA) at the reference frequency of the PEM, can analyze the differential intensity between the right and left circular polarization states in a few microseconds, allowing for the fast and robust extraction of the CIDS signal [8].

In this chapter, the general background is proposed based on the CIDS method to obtain information about the molecular structure of chromatin in the nucleus of a cell to gain insights into the higher-order structure and packing of the genome, which can provide important clues about gene expression and regulation. In particular, it covers the description of single point spectroscopic measurement as one of the most common applications of the CIDS, in which the scattering light from the whole illuminated sample volume is measured as a function of the scattering angle [9]. The interesting characteristic of the CIDS method is its versatility in being shifted from single

point spectroscopy to CIDS imaging acquisition through the microscopy approach without the requirement for numerous additional optical changes in the polarimetric pathway.

One of the main goals of this thesis was to upgrade the CIDS setup previously implemented by Riccardo Marongiu, a former PhD student under the supervision of Dr. Aymeric Le Gratiet [75]. The original setup was built into a bulky commercial Nikon scanning confocal fluorescence microscope, making modifications challenging. Additionally, the calibration procedure was not straightforward and required manual post-processing of raw data, leading to some results being irreproducible. To address the issues, several upgrades were implemented in the CIDS setup, with the aim of improving accuracy, efficiency, and reproducibility, as well as expanding its capabilities for studying chromatin molecular organization. The upgrades included:

- Building the setup in an open configuration, which made it adoptable with multiple modalities and allowed for easier modifications. This flexibility enabled the integration of various techniques and facilitated future adaptations to meet specific research needs.
- Ensuring that the results obtained using the upgraded setup maintained the same quality as those obtained previously. This involved meticulous testing and validation procedures to verify the consistency and reliability of the updated system.
- Developing a new calibration procedure that was both robust and easy to implement. The improved calibration process enhanced the accuracy and precision of measurements, ensuring more reliable and meaningful data.
- Creating Java macros and MATLAB routines specifically designed for systematic treatment of a high number of images. This automation significantly improved statistical analysis and data processing, enabling efficient handling of large datasets.
- Automating lock-in detection using data acquisition system. This automation streamlined the experimental process, and enhancing the overall efficiency of data acquisition.
- Proposing new types of samples, such as progeria cells, to expand the scope of the study. The inclusion of diverse samples enriched the research, allowing for a broader exploration of chromatin molecular organization and its implications.

These upgrades are aimed at improving the accuracy, efficiency, and reproducibility of the CIDS setup, and expanding its capabilities for studying chromatin molecular organization.

As an application, cellular identification between different cell types using CIDS imaging is demonstrated. The CIDS approach is validated with a classification calculating method to monitor chromatin and membrane morphology modifications of different intact cell types cultured on the same plate. After the CIDS imaging measurements, a numerical tool is presented that is able to recognize mouse cells from humans via a single image detection *in-situ*. The results are combined with fluorescence microscopy images as a benchmark for the label-free approach. The whole

image post-processing and representations outlined have been conducted and generated by the author as part of this thesis.

Despite the outstanding advantages of the CIDS technique, the localized contrasts related to the sample polarimetric properties in the illumination volume are averaged by this modality. Additionally, the detection sensitivity is affected by the confinement of the mixture of structures, making it an arduous task to discriminate the source of the signal. Thus, a new framework of analytical method, known as the phasor approach, is established as one of the aims of this thesis.

The single point spectroscopic configuration is specifically useful to study aggregated macromolecules in solutions, such as isolated human embryonic kidney (HEK) cell nuclei in acrylamide gel, to measure the signal coming from the chiral structures inside the chromatin. A phasor map combined with single point spectroscopic CIDS is shown to provide an intuitive view of the sample organization and recognize the presence of different molecular species in the illumination volume. The chapter covers the introduction of the phasor approach combined with CIDS, validation of the method by numerical simulations, and comparison of the results with that of experimental data of optical devices of reference.

To address the limitation of the CIDS imaging technique in detecting the signal from a confined blend of structures within the illumination volume, a new method has been developed. This method involves converting the pixel-by-pixel polarization modulation into an image phasor approach during the CIDS image acquisition. As a result, it becomes possible to obtain an insightful view of the cells. This approach allows us to distinguish anomalous subcellular organizations in diseased cells compared to healthy ones. To achieve the goal of identifying changes in chromatin compaction and distortion of nucleus morphology induced by the activation of the lamin-A gene from Hutchinson-Gilford progeria syndrome, a robust and innovative approach is proposed. Accordingly, the performance of the CIDS setup is developed by linking it to a lock-in amplifier for numerical measurement of polarimetric amplitude modulation and phase information through the acquisition channels without the need for Fourier transform and further analytical calculations. The phasor map is evaluated based on the amplitude modulation and phase data obtained directly from the CIDS imaging setup, and the polarimetric images are compared to the fluorescence modality of normal cells versus progeria. The method is validated by characterizing the polarization response of starch crystalline granules. Additionally, the conversion of polarization-resolved images into phasors is found to be useful for segmenting specific structures with varying optical properties under polarized light.

In this chapter, the focus is on polarization microscopy imaging, with fluorescence being employed as a benchmark technique. The findings presented herein demonstrate the ability of polarization imaging to uncover hidden information that extends beyond what can be revealed by fluorescence alone.

2.2 Chiral structures and CIDS

Chirality or handedness refers to the asymmetric structure of an object or molecule that cannot be superimposed on its mirror image by any translations or rotations. Chirality is an important concept for the spatial arrangement of atoms that form the structure of molecules and their manipulation. The properties of molecules are highly dependent on the chirality of their bonds. Most substances relevant to biology are chiral, such as starch, cellulose, and chromatin [10]. Chromatin is a particular case of chirality in helical structures, which are defined by handedness, pitch, and radius. The handedness of the helix determines the torsion direction to the left or right. The radius shows the distance between the central axis and the helix structure. Lastly, the pitch gives the distance needed for the helical structure to complete a whole revolution along the symmetry axis in a direction parallel to the axis itself. Chromatin is composed of short stretches of DNA as a double helix that wraps around a core of eight histone proteins at regular intervals along the entire length of the chromosome [11].

Considering the size of a typical human cell of about 10 µm, DNA must be tightly packaged to fit in the cell's nucleus and be readily accessible for gene expression. During some stages of the cell cycle, the long strands of DNA are condensed into compact chromosomes. Fig. (2.1) shows the number of ways that chromosomes are compacted to fit in the cell's nucleus and be accessible for gene expression. A DNA molecule in this form is about seven times shorter than the double helix without the histones. The histones are around 10 nm in diameter, in contrast to the 2 nm diameter of a DNA double helix. DNA wraps around histone proteins, forming nucleosomes, and the so-called "beads on a string" structure is known as euchromatin. The next level of compaction, known as heterochromatin, occurs as the nucleosomes and the linker DNA between them are coiled into a 30-nm chromatin fiber. This coiling further shortens the chromosome so that it is now about 50 times shorter than the extended form. In the third level of packing, a variety of fibrous proteins are used to pack the chromatin [12]. These fibrous proteins also ensure that each chromosome in a non-dividing cell occupies a particular area of the nucleus that does not overlap with that of any other chromosome.

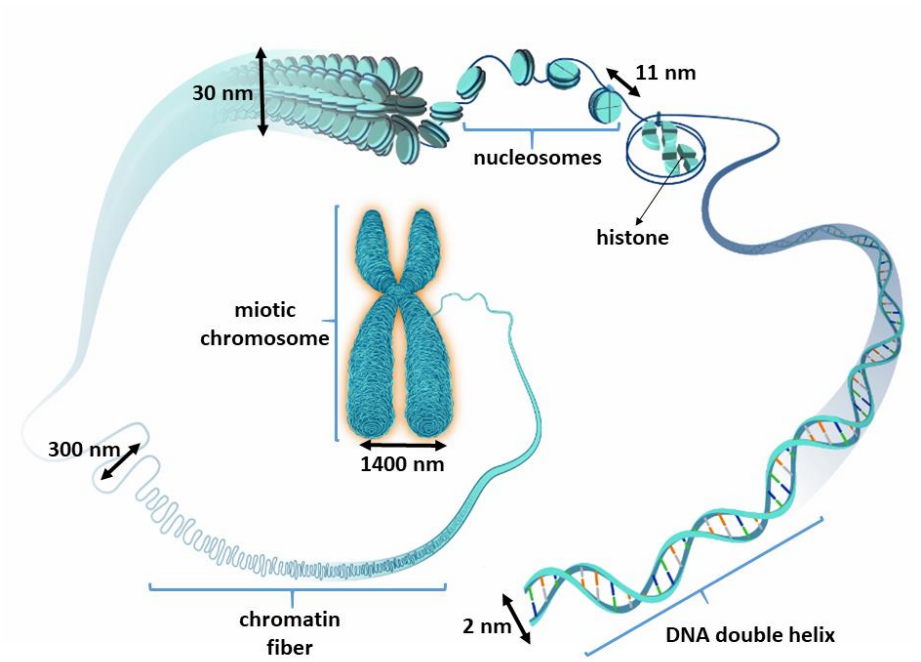

Figure 2.1. Scheme of the levels of compaction in chromatin across multiple scale sizes, ranging from the DNA double helix to an entire chromosome in human and animal cell nuclei (Figure reproduced from reference [13]).

Various optical spectroscopy and microscopy methods are available for detecting chromatin, including CD spectroscopy, which measures the differential absorption of left- and right-circularly polarized light by chiral molecules like DNA and proteins. CD spectroscopy is particularly useful for determining the secondary structure of chromatin, including its degree of helicity [14, 15]. Another technique that can be used to study the structure and chirality of chromatin is Raman spectroscopy. Raman spectra of chromatin typically exhibit vibrational modes associated with its various components, such as DNA, histones, and other proteins [16].

To quantify the polarimetric characterizations linked to the structure of molecular organizations, MM microscopy offers a comprehensive description of the sample's optical properties in a non-invasive and label-free manner. Chiral molecules can rotate the plane of polarization of plane-polarized light to the right or left as light passes through the sample, making CD one of the more sensitive MM elements for such configurations. Chiral molecules in CD may differentially absorb right and left circularly polarized light in the direct transmitted forward direction, causing a small portion of light to be differentially scattered in CIDS. The CIDS signal is angularly dependent and can be described by the following equation (2.1).

$$\mathrm{CIDS} = \frac{I_L - I_R}{I_L + I_R} \tag{2.1}$$

Here I_L and I_R represent the intensities detected for the left and right circular polarization states, respectively. Light scattering is the phenomenon of light being deflected in random directions by the atoms or molecules of the medium through which it passes. In biological samples, the wavelength of the light used in CIDS microscopes is typically on the order of a few hundred nanometers to a few micrometers, which is comparable in size to biological structures such as cells and nuclei. As a result, Mie scattering is the dominant regime for describing the light-matter interactions in these samples.

2.3 Photo-elastic modulator in CIDS setup

Experimental Mueller setups that use electro-optic modules are generally quite similar to one another. These setups typically rely on either a Pockels cell or a PEM to rapidly modulate the polarization states. PEM was first invented by J. Badoz in the 1960s and originally called a "birefringence modulator". This technology is composed of a passive crystal subjected to periodic mechanical stress, providing a time-varying birefringence due to the photo-elastic effect. The device can produce circular polarization states with alternating handedness at a rate ranging from tens of kHz to tens of MHz, depending on the device used [17]. PEM has a lot of advantages, such as a high optical quality based on high power handling capability, a large acceptance angle, large useful aperture, modulation purity and efficiency, and high retardation stability, making it an effective instrument in a wide variety of applications. The basic design of a PEM consists of a piezoelectric transducer and a half wave-plate. The principle of operation is based on the photo-elastic effect, in which a mechanically stressed sample exhibits birefringence proportional to the resulting strain. In other words, the photo-elastic effect is used to change the birefringence of the optical element. A PEM device is relatively insensitive to thermal deviation and due to its compact design is easy to handle. The schematic of PEM principle is shown in Fig. (2.2 a). A PEM consists of a piezoelectric transducer and a birefringent crystal, such as quartz. When an AC voltage is applied to the transducer, it vibrates at its resonant frequency, causing a periodic deformation of the crystal. The deformation changes the birefringence of the crystal periodically, and as a result, the polarization state of the incident light is modulated at the same frequency. The spectral response of a PEM is limited by the mechanical resonant frequency of the modulator. Typically, the resonant frequency of the PEM is in the range of a few hundred Hz to a few kHz. Additionally, the speed at which the PEM can modulate the polarization states is limited by its mechanical resonant frequency and the driving electronics. The modulation speed is typically in the range of a few kHz to a few tens of kHz, which may not be fast enough for certain applications that require high-speed polarization modulation [8].

In this part, the theoretical process of retrieving MM elements is explained. It is also noted that in practical experiments, one approach to determining MM elements is to extract the detected intensity signal at different harmonics using a LA that is capable of amplifying weak signals with respect to noise. To obtain the MM elements, a fast modulation of the polarization state of the incident light is essential. Thus, the setup architecture should allow for the measurement of the MM elements by modulating the polarization states of light with a PEM and detecting the resulting signal with a light detector. To ensure accurate and precise measurement of the MM elements, temporal coding and well-defined polarization states are utilized. The schematic of a single PEM in the Mueller setup is illustrated in Fig. (2.2 b).

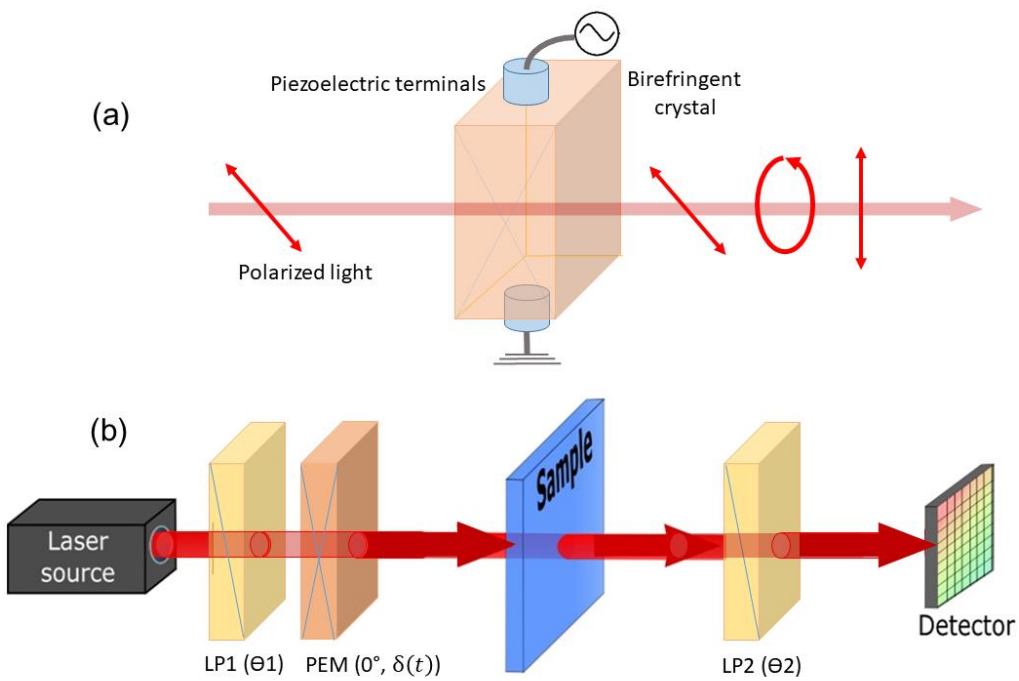

Figure 2.2. Shows the (a) working principle and core structure of a photoelastic modulator (PEM), and (b) a scheme of a PEM-based Mueller polarimeter utilizing temporal coding to obtain the Mueller matrix elements. The polarization state generator (PSG) consists of a linear polarizer and PEM, while the polarization state analyzer (PSA) block is composed of a linear polarizer (polarizing beam splitter) that decodes the signal for detection by a light detector. The angles between the optical axis of the birefringent elements are measured relative to the reference angle of the PEM, which is set at 0°.

In Fig. (2.2 b), a linear polarizer and PEM are making PSG to provide polarization states in sequence and the PSA is a polarizing beam splitter (e.g. Wollaston prism) separating the light in two orthogonal polarization states detected by two detectors (e.g. Photodiode). Considering the rotational angle of PEM at θ_{PEM} = 0° as reference angle, the angles for the first and second LP

should be θ_{LP1} = -45°, and θ_{LP2} = ±45°. The time dependent retardance of PEM is determined by the function $\delta(t)$ defined in Equation (2.2).

$$\delta(t) = A.\sin(\omega t + \Phi) + \delta_0 \tag{2.2}$$

Here, A represents the modulation amplitude or peak retardation of $\delta(t)$, ω is performance frequency of the PEM, Φ is the phase of the PEM assuming to be close to 0 and δ_0 represents the static retardation related to residual birefringence when the PEM is turned off [18]. Accordingly, the resulting detected light can be represented as a Stokes vector and calculated mathematically based on the Stokes-Mueller matrix formalism as follows:

$$\vec{S}_{out} = [M_{PSA}].[M_{Sample}].[M_{PSG}].\vec{S}_{in} = [M_{LP2}].[M_{Sample}].[M_{PEM}].[M_{LP1}].\vec{S}_{in} \tag{2.3}$$

where the related matrices of the optical element are described as following equations:

$$[M_{LP1}(-45°)] = \begin{bmatrix} 1 & 0 & -1 & 0 \\ 0 & 0 & 0 & 0 \\ -1 & 0 & 1 & 0 \\ 0 & 0 & 0 & 0 \end{bmatrix} \tag{2.4}$$

$$[M_{LP2}(\pm 45°)] = \begin{bmatrix} 1 & 0 & \pm 1 & 0 \\ 0 & 0 & 0 & 0 \\ \pm 1 & 0 & 1 & 0 \\ 0 & 0 & 0 & 0 \end{bmatrix} \tag{2.5}$$

$$[M_{PEM}(0°)] = \begin{bmatrix} 1 & 0 & 0 & 0 \\ 0 & 1 & 0 & 0 \\ 0 & 0 & \cos(\delta) & \sin(\delta) \\ 0 & 0 & -\sin(\delta) & \cos(\delta) \end{bmatrix} \tag{2.6}$$

Here, $[M_{LP1}(-45°)]$, $[M_{LP2}(\pm 45°)]$ and $[M_{PEM}(0°)]$ are the Mueller matrices of initial linear polarizer oriented at $-45°$, linear polarizers at $\pm 45°$ and PEM at 0° respectively; In this way, in case of $[M_{LP2}(+45°)]$, the detected intensity signal I(t) is determined by equation (2.7).

$$I(t)_{+45^\circ} = m_{00} - m_{20} - (m_{03} + m_{23})\sin(\delta) + (m_{02} + m_{22})\cos(\delta) \tag{2.7}$$

We note that the time dependent intensity is realized by multiplication of horizontal unpolarized Stokes vector. The detected signal has a form of a waveform represented in the Fourier domain by complex modulation amplitudes at frequencies corresponding to the PEM reference one and its harmonics. After simplifications, the output intensity $I(t)$ measured by the detector is the combination of DC and AC currents as equation (2.8).

$$I(t) = I_{DC} + I_c\big(\sin(\delta(t)\big) + I_s\big(\cos(\delta(t)\big) \tag{2.8}$$

where at $+45°$, $I_{DC} = (m_{00} - m_{20})$ is the DC intensity linearly polarized, $I_c = (-m_{03} - m_{23})$ is the first harmonics and $I_s = (m_{02} + m_{22})$ is the second harmonics of the time dependent intensity at the detection point. Here, static retardance and phase of the modulator is assumed to be close to 0. Since $\delta(t)$ is a sinusoidal function, to quantify the measurement of the $\cos(\delta(t))$ and $\sin(\delta(t))$ functions, we apply Bessel function identities:

$$\sin(\delta(t)) = 2\sum_{k=1}^{\infty} J_{2k-1}(A).\sin((2k-1)\omega t) \tag{2.9}$$

$$\cos(\delta(t)) = 2\,J_0(A) + 2\sum_{k=1}^{\infty} J_{2k}(A).\cos((2k)\omega t) \tag{2.10}$$

where A is the amplitude of the $\delta(t)$ function and J_k are the Bessel coefficients such that for A = 2.4 $J_0(A) = 0$ and $J_1(A) \approx 0.5$ according to the plot of Bessel function of first kind in Fig. (2.3)

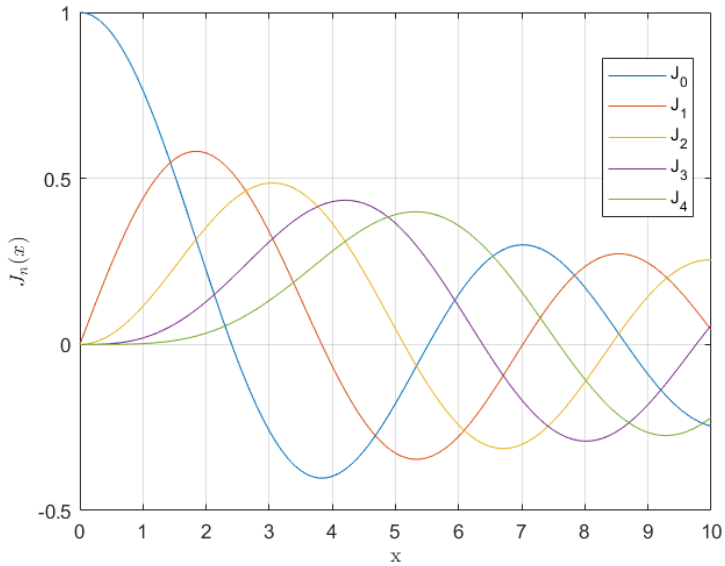

Figure 2.3. Plot of Bessel function of first kind J_n for integer orders $n = 0,1,..,4$.

The access to frequency is up to the second order since the amplitudes are too small at the upper orders to be measured. Thus the approximation is:

$$\sin(\delta(t)) \approx 2J_1(A).\sin(\omega t) \tag{2.11}$$

$$\cos(\delta(t)) \approx J_0(A) + 2J_2(A).\cos(2\omega t) \tag{2.12}$$

Having these results, we are able to explain the basic principle to extract m_{ij} using PEM technology by equation (2.13). The PEM device links between a reading of the modulation amplitudes at ω and 2ω frequencies and the m_{ij}. In this way, the modulations is extracted using a LA that is locked to the reference frequency of the PEM.

$$I(t) = m_{00} - m_{20} + J_0(m_{22} - m_{02}) + 2J_1(-m_{03} - m_{23})\sin(\omega t) + 2J_2(m_{02} + m_{22})\cos(2\omega t) \tag{2.13}$$

In this way, the relations are summarized in Tables (2.1) and (2.2).

Frequency	Amplitude (LP2) $\theta = -45°$	Amplitude (LP2) $\theta = +45°$
DC	$m_{00} + m_{20}$	$m_{00} - m_{20}$
AC (ω)	$2J_1(-m_{03} + m_{23})$	$2J_1(-m_{03} - m_{23})$
AC (2ω)	$2J_2(m_{02} - m_{22})$	$2J_2(m_{02} + m_{22})$

Table 2.1. The Mueller matrix elements with respect to the second LP positioned as PSA in two orthogonal angles of 45° and -45° linked to the PEM performance frequency at ω and 2ω.

Accordingly, each element is realized by sum and subtract of the two signals.

Frequency	$I_{-45°} - I_{+45°}$	$I_{-45°} + I_{+45°}$
DC	$2m_{20}$	$2m_{00}$
AC (ω)	$4J_1 m_{23}$	$4J_1 m_{03}$
AC (2ω)	$4J_2 m_{02}$	$4J_2 m_{22}$

Table 2.2. The Mueller matrix elements by adding up and subtracting the intensities coming from the same LP oriented at orthogonal angles of 45° and -45° linked to the PEM performance frequency at ω and 2ω.

Based on this configuration, it is possible to retrieve six elements of the MM. However, in order to obtain all 16 elements, at least 16 intensities are required, which can be achieved by utilizing higher orders of harmonics of the PEM frequencies. This is a practical challenge as the higher harmonics provide the same equations in an odd and even manner. Another method to obtain the full MM is to modify the setup by changing the orientation of the optical axis of additional components, such as a quarter wave plate (QWP) before the linear polarizer (LP). The other elements that can be retrieved by modifying the setup are summarized in Table (2.3).

$\theta\ LP_1$	$\theta\ PEM$	$\theta\ QWP$	$\theta\ LP_2$	MM elements
$-45°$	$0°$	-	$\pm 45°$	$m_{00}, m_{02}, m_{03}, m_{20}, m_{22}, m_{23}$
$-45°$	$0°$	-	$0°/90°$	$m_{00}, m_{02}, m_{03}, m_{10}, m_{12}, m_{13}$
$-45°$	$0°$	$0°/90°$	$45°$	$m_{00}, m_{02}, m_{03}, m_{30}, m_{32}, m_{33}$
$0°$	$45°$	-	$0°/90°$	$m_{00}, m_{01}, m_{03}, m_{10}, m_{11}, m_{13}$
$0°$	$45°$	-	$\pm 45°$	$m_{00}, m_{01}, m_{03}, m_{20}, m_{21}, m_{23}$
$0°$	$45°$	$0°/90°$	$45°$	$m_{00}, m_{01}, m_{03}, m_{30}, m_{31}, m_{33}$

Table 2.3. The Mueller matrix elements measured in the PEM setup by changing the angle of each optical element.

2.4 CIDS optical microscopy imaging

MM microscopy imaging has found wide application in the field of biomedical research due to its label-free and non-invasive approach, allowing for contrast without requiring contact or prior knowledge of the sample. Moreover, MM microscopy is an inexpensive and easily designed tool that can be used with white light sources or simple laser diodes, CCD cameras, and photodiodes. However, imaging microscopy is difficult due to the diffraction limit in the linear optics regime and the challenge of preserving polarization across all fields of view (FOVs) using microscope objectives [19, 20].

Circular differential imaging configuration was first discussed in detail by D. Keller, et al. as a method for mapping the optical activity of the sample in two dimensions [21]. The circular differential imaging method provides contrast from the difference in the optical activity of the surrounding molecules correlated to the sample's optical fingerprint. One of the main advantages of CIDS imaging is its ability to define the handedness and compaction level of chiral groups of molecular structures that may be too small to be resolved by conventional microscopy methods. Two configurations for CIDS imaging have been considered: (1) reflection or dark-field imaging, and (2) transmission or bright-field imaging. It has been demonstrated that the circular reflection differential imaging configuration is more sensitive to large chiral groups with dimensions similar to the wavelength of illumination, while the transmitted configuration is more sensitive to short-range molecular order.

In CIDS imaging microscopy, the main contribution of the signal is still CD in the forward direction, while scattering information at non-zero angles can be accessed proportional to the numerical aperture (NA) of the objective, which can provide additional insights into the sample under investigation [22]. The presence of scattering signal peaks at off-axis angles has been demonstrated through various methods. For example, a pinhole can be inserted in the plane of the aperture diaphragm to select a specific angle of light emission by an objective at different off-axis positions [23]. In this example, to obtain SHG angular intensity pattern of each scanned image, the aperture diaphragm was removed from the condenser and replaced by a movable dark screen with a pinhole, which is shown in Fig. (2.4). A motorized *xy* stage was used to move the pinhole over the entire field of the aperture diaphragm.

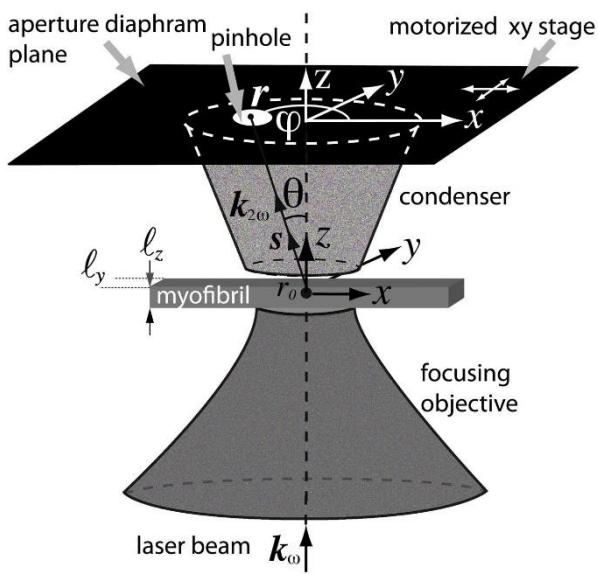

Figure 2.4. Schematic of the experiment. Excitation IR laser beam is propagating in the *z* direction and is focused at $x = y = z = 0$. A pinhole is inserted in the plane of the aperture diaphragm to select a particular angle of light emission. Forward second harmonic generation (SHG) angular intensity pattern is obtained after acquisition of an image for each position of the pinhole that is moved by a motorized stage over the entire field of the aperture diaphragm; $\theta \sim 42.6°$, NA = 0.9 (Figure reproduced from reference [23]).

At our working wavelength of 770 nm, which is significantly distant from the DNA absorption band at 200-300 nm, the signal is predominantly due to scattering [24]. Although there is a significant peak of scattering signal at zero angle, smaller off-axis peaks at non-zero angles can still be accessed. To improve the SNR of this weak signal, lock-in amplified detection is incorporated. Consequently, the higher NA allows for a broader range of angular scattering, resulting in a slight enhancement of the contrast.

Fig. (2.5) provides a schematic representation of the difference between CIDS and CD for a chiral conformation, based on the differential absorption and scattering.

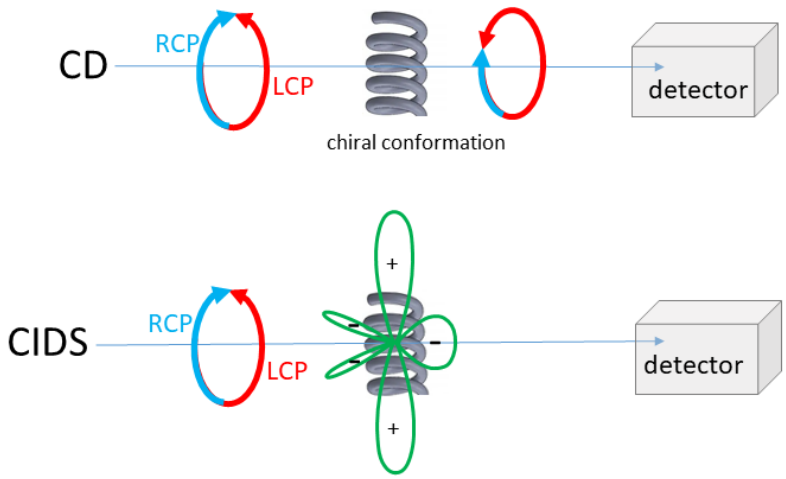

Figure 2.5. The two possible contributions of CD (Circular Dichroism) interaction with a helical sample; CD by differential absorption and CIDS (Circular Intensity Differential Scattering) by differential scattering where the preferential scattering is depicted by the characteristic lobes of alternating sign; RCP: Right Circularly Polarized light; RCP: right circularly polarized light; LCP: left circularly polarized light. In CD, RCP and LCP light are differentially absorbed in the forward direction to produce the CD signal. In CIDS, the chiral sample generates a scattering response that is characterized by the intense lobes with alternating signs, whose intensity and sign depend on the scattering angle.

In the 1980s, a series of articles were published that explained the theoretical background for the full MM imaging configuration [25]. It has been demonstrated that the interpretation of the differential CD images for chiral samples strongly depends on the sample's thickness and degree of anisotropy. Therefore, the study of only a few MM elements, such as those associated with CIDS (i.e., m_{03} or m_{23}) is motivated [26]. Optical scanning confocal microscopy can address the issue of cross-interaction between chiral groups that can affect optical sectioning pixel-by-pixel. However, it can also introduce artifacts in the point spread function (PSF) volume, leading to contamination of the CIDS signal [27].

2.4.1 CIDS Imaging to identify different cell types

Murine cells, being eukaryotic bio-organisms, have a fascinating array of subcellular structures that play crucial roles in energy balance, metabolism, and gene expression. The nucleus contains almost all of the chromatin, which is surrounded by a network of fibrous intermediate filaments [28, 29]. Mouse cells are considered a convenient model system for studying gene-targeting experiments in the case of pathologies due to their similarities in genetics and behavioral characteristics compared to humans, according to the Foundation for Biomedical Research [30, 31]. Since human and mouse cells differ based on chromatin distribution and membrane morphology, we chose to study these two "opposite" cases with similar geometry as a starting point to propose a new fast method for classifying healthy and diseased cells in tissues and solid tumors as a future implementation. This highlights the necessity of providing a complete functional model to identify the discrepancies and similar features when dealing with an ensemble of cells together. For this reason, fluorescence techniques using specified labeling probes are considered the gold standard and a quantitative means [32, 33]. Notably, there are highly compacted chromatin regions varying in the nuclei of mouse and human cells called nucleoli, which are transcriptionally active regions found within the cell nucleus responsible for producing and assembling the cell's ribosomes by a specific chromosome. The plural of nucleolus is termed nucleoli [34, 35]. Fluorescence-based techniques are limited due to the possibility of perturbations in cell organization and autofluorescence issues [36].

Optical microscopy techniques based on the control of the polarization of light have shown their proficiency in imaging samples and revealing disguised information in a non-invasive procedure. For instance, classification of morphologically similar algae and cyanobacteria using MM imaging and convolutional neural networks [37-42]. The significant advantage of CIDS is to determine the structure and compaction level of chiral molecular groups that are unresolvable by conventional microscopy imaging methods. CIDS imaging involves measuring the microscope's illumination volume pixel-by-pixel. In this study, CIDS imaging is validated as a method to monitor chromatin and membrane morphology modifications of both mouse and human intact cell types in the same plate. CIDS image acquisition is coupled with a two-photon excited fluorescence (2PEF) as a benchmark to indicate the presence of genetic material besides the label-free polarization approach. The technique allows classification by defining a threshold on the related modulus of CIDS normalized intensity to ignore the CIDS sign linked to handedness effect, which is then compared to that of 2PEF images pixel-by-pixel [43]. The 2PEF imaging modality also provides validation of the CIDS recognition to detect mouse cells based on the number of nucleoli. Our work proves the capability to effortlessly classify types of the entire bunch of mouse cells without the requirement of labeling or nuclei isolation procedure, as the CIDS modality brings chiral characterizations of the cell membrane morphology based on roughness and geometry. The image acquisition rate is estimated to be around tens of seconds. Thus, in case of a need for averaging an image, a minute is approximated.

2.4.1.1 CIDS imaging experimental setup

One of the primary objectives of this thesis was to rebuild and redesign the CIDS setup in an open configuration that could be easily adapted to multiple modalities and facilitate modifications [44]. The original CIDS setup was built on a commercial Nikon microscope body, which limited its versatility and hindered the integration of new technologies, such as MM microscopy and multiphoton imaging, into a multimodal optical microscopy image correlation sensing (MOMIX) environment that was envisioned. Therefore, the CIDS setup was reconstructed in an open configuration, without the microscope body, to provide the research group with the flexibility to add various modalities and leverage the latest advancements in the field. With the new open setup, the capability to combine spatial super-resolution microscopy and spectroscopic techniques using multiple laser sources controlled by a high-speed field programmable gate arrays (FPGA) card is provided. This upgrade allows for more accurate and precise measurements and offers the potential to adapt and upgrade the system in the future as new techniques emerge.

Fig. (2.6) shows the bimodal setup utilized in the experiments. The CIDS signal is measured from samples that reveal an optical polarimetric influence and are integrated with confocal fluorescence modality to collect the 2PEF emission pixel-by-pixel. The CIDS setup relies on illuminating a PEM with a linear polarization at a specific orientation of the optical axis to generate right and left circular polarization states at a working frequency of 50 kHz. A 20X/0.5 NA Nikon objective (DIC-M Plan Fluor, Nikon Instruments, Yokohama, JP) is utilized to focus the light on the sample, which is placed in the focal plane with a diffraction-limited lateral resolution of ≈ 0.8 µm. Another identical objective collects the light as a condenser. To analyze the transformed polarization states, two orthogonal polarized detections are employed, which enable CIDS measurement at the pixel-dwell time without any active optical components (such as a rotating component). The two channels are synchronously coupled to the demodulated signals at the first harmonic of the PEM using Lock-in Amplifier (HF2LI Zurich Instruments AG, SUI) to amplify the weak CIDS signal. Additionally, besides the acquisition of harmonics (AC) signals of CIDS, fundamental (DC) intensity signals are also acquired to provide conventional intensity microscopy and normalize the demodulated polarimetric images.

Furthermore, a channel connected to the conventional confocal fluorescence module collects the 2PEF emission as a descanned signal image. To automate the acquired image data set in post-processing imaging steps, a macro was developed in ImageJ to plug in all the raw images, along with initial calculations. A specialized homemade routine was also written in the Matlab program (Matlab, R2017a, Mathworks) for further processing.

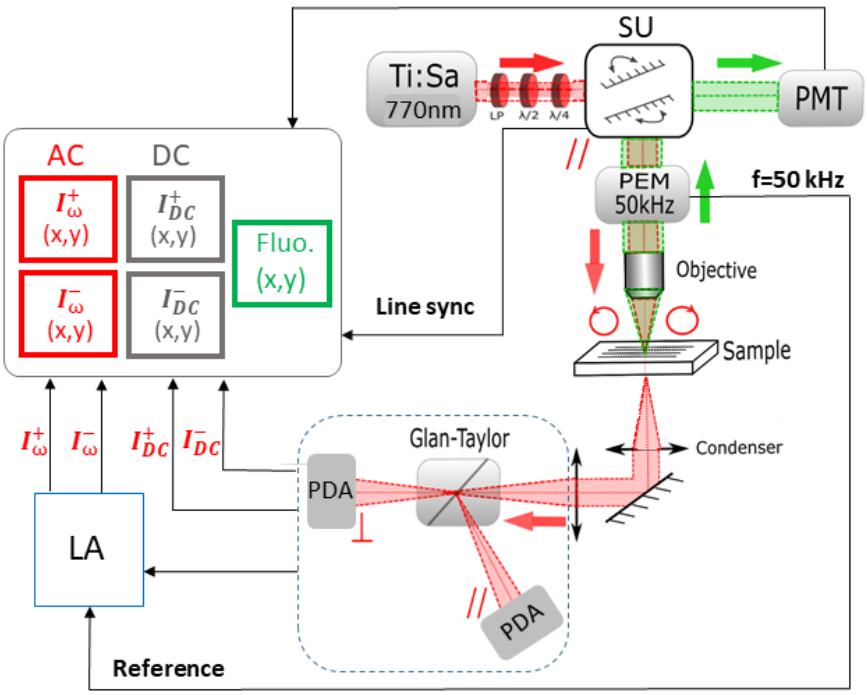

Figure 2.6. Block diagram of the bimodal scanning microscopy setup. Ti:Sa: Titanium-Sapphire coherent laser source tuned at 770 nm. SU: Scanning Unit. PEM: Photo-elastic Modulator at 50 kHz resonant frequency. Glan-Taylor prism to provide parallel and cross polarization. $PDA_{\perp}$, $PDA_{//}$: Photodiode-Array detectors for parallel and cross polarization detection after the prism. LA: Lock-in Amplifier, PMT: Photomultiplier Tube. Input channels of the LA, locked at 50 kHz from the reference signal of the PEM. The two PDAs both connected to each channel of the LA and directly to the control unit. The terms I^+ and I^- are the detected intensities for the mentioned polarization projections after the prism, respectively. The red and green colors indicate optical path correspond to the transmitted polarimetric and to the reflected fluorescence path, respectively.

2.4.1.2 Performances of the polarization reconstructions

Following the setup upgrades based on the open configuration, the calibration procedure was improved to facilitate the mounting and angular rotation of different optical elements such as LP and HWP. Neutral-density filters were used to uniformly reduce the light intensity without any dependence on wavelength or other parameters. Accordingly, the data post-processing procedure was updated to include the normalization of intensities, the phase wrapping effect due to lock-in amplifier filtering, and the imperfections of waveplates based on the residual birefringence and retardance accuracy obtained from the Thorlabs datasheet. This allowed the CIDS imaging calibration to account for any optical polarization influences and potential misalignment of the optical orientations of the microscope devices.

It is important to note that the scanning configuration may result in a loss of generated circular polarization within the FOV due to Fresnel's law and systematic errors caused by objective perturbations and reflections at the interface between the glass and the sample. To compensate for any illumination gradient across the FOV, a tenfold zoom was applied at the center. Total intensity light is measured by two photodiodes (PDA36A - Si Switchable Gain Detector, Thorlabs, Inc., USA) after light splits into two orthogonally polarized beams (concerning initial LP in PSG) by a Glan-Taylor (GT10 - Thorlabs, Inc., USA) prism. LP and HWP were rotated from 0º up to 180º with the steps of 10º and measured the two intensities provided by the GT prism as $I_{\perp}$ transmitted (DCT) along with $I_{||}$ reflected (DCR) and a combination of them (DCT + DCR) as total intensity signal at each azimuthal angle. Finally, the intensities are averaged over all the FOV, and the results are reported in Fig. (2.7). The pixel dwell time and the LA integration time, both of which are set at 20 µs, determine the quality of the image. To improve the SNR, four-frame averaging is performed. As a result, it takes around 20 seconds to acquire a single image.

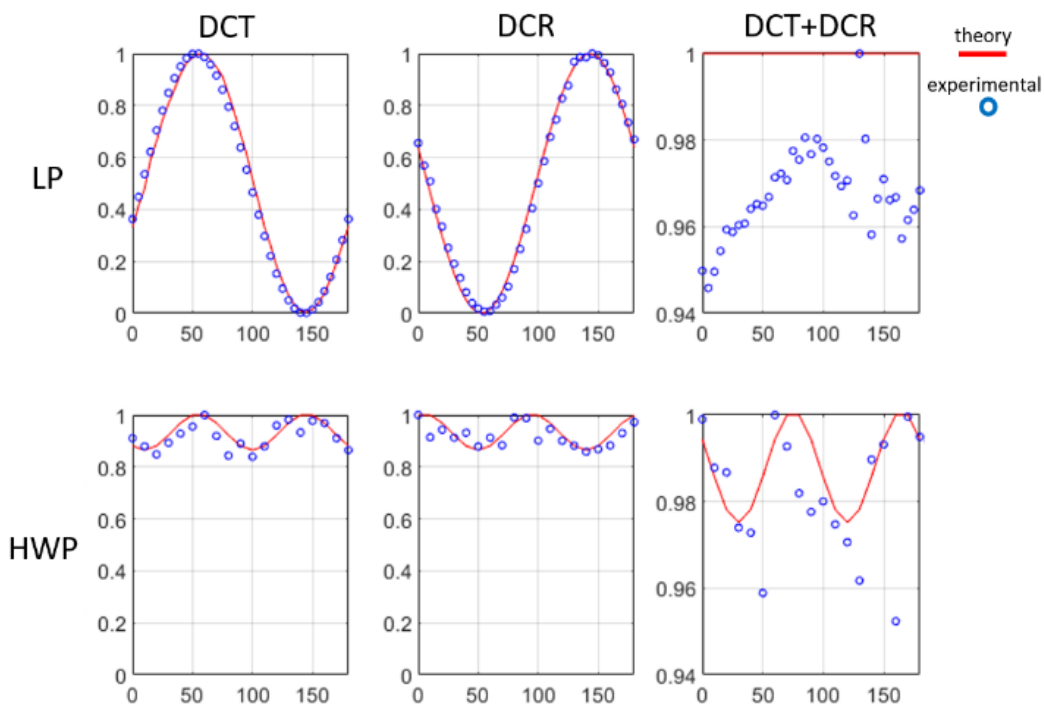

Figure 2.7. calibration steps using linear polarizer (LP) and half wave plate (HWP) are shown by plotting the detected normalized intensity signal versus azimuthal angle and comparing it to the corresponding theoretical expected curves. The red line represents the theoretical curve, while the experimental data is represented by the plotted points. DCT: transmitted light; DCR: reflected light.

	DCT Error (%)	DCR Error (%)	DCT+DCR Error (%)
LP	6.1	4.3	5.4
HWP	7.8	9.8	4.7

Table 2.4. Maximum polarimetric error percentage of the LP and HWP from the corresponding expected value.

In Fig. (2.7), it can be seen that in the case of LP, both channels exhibit a phase difference of 90° between crossed polarizations. This error is introduced by the optical elements' fingerprint and slight misalignment of the polarization optics. The corresponding error percentages for each channel, as shown in Table (2.4), are below 10%, and the sum of both channels is compared to the expected values. This automated and reproducible process is used to align the setup before conducting experiments.

2.4.1.3 Sample preparation

MCF7 human breast cancer cells were grown in Dulbecco's Modified Eagle Medium (DMEM), 2mM Glutamine, 1% Non-Essential Amino Acids (NEAA) and 10% Fetal Bovine Serum (FBS). Moreover, NMuMG CRL-1636 mouse mammary gland cells from NAMRU, were grown in DMEM, 2 mM Glutamine, 10 μg/ml Insulin and 10% FBS, all from Merck, Darmstadt, Germany. Both cell lines were seeded on the very same coverglass at the concentration of 10^5 cell/cm^2 and grown for 48h in DMEM, 2mM Glutamine, 10 μg/ml Insulin and 10% FBS. Cells were fixed in 4% paraformaldehyde (PFA) (wt/vol) at room temperature for 10 min; after fixation the samples were stained with Hoechst 34580 at 1 μg/ml and mounted with ProLong™ Diamond Antifade Mountant which all were from Invitrogen.

2.4.1.4 Data analysis and image processing

The previous manual procedure for loading the dataset was enhanced by automating it through the use of macros in ImageJ. Additionally, MATLAB routines were employed to systematically process a large number of images, leading to improved statistical analysis. Our setup configuration is modeled through the Stokes-Mueller formalism, and it has been shown that the reference frequency (50 kHz) and its harmonics (100 kHz, 150 kHz, etc.) are linear combinations of only six MM elements, despite a total of 16 possible elements. The equations are as follows:

$$I(t) = I_{DC} + I_{\omega} \cos(\omega t) \tag{2.14}$$

where $I_{DC} = m_{00} \pm m_{02}$, $I_{\omega} = m_{03} \pm m_{23}$ and the $\pm$ signs depend on the analyzing detection polarization orientation.
In this section, attention is directed towards a single element, specifically m_{03}, which is associated with CIDS and can be extracted through odd frequency utilizing 50 kHz (ω). This allows to obtain CIDS signals at higher frequencies, potentially speeding up acquisition, but at the cost of drastically reducing the SNR due to lower amplitudes at high frequencies. The measured CIDS signal is the result of the interaction between circularly polarized light and the sample. The acquired total intensity and CIDS can be described by equation (2.1), where the intensities of right and left circular polarization are related to detected parallel and perpendicular polarization states, respectively, with respect to the initial linearly polarized light at the illumination part. The retrieved CIDS and fluorescent images are normalized directly for each pixel by dividing them by the maximum value of the image pixels, as follows:

$$CIDS_N(x, y) = \frac{CIDS\ (x,y)}{CIDS_{max}(x,y)} \tag{2.15}$$

$$2PEF_N(x, y) = \frac{2PEF\ (x,y)}{2PEF_{max}(x,y)} \tag{2.16}$$

The background was manually ascertained by selecting an arbitrary polygonal region of interest (ROI) over the image. The average intensity measured in the background ROI was then subtracted from the intensities of each pixel in the image. To distinguish mouse cells, a threshold was assigned using a global image thresholding routine, which classified the data into different colors.

2.4.1.5 Multimodal CIDS-fluorescence imaging microscopy for cell types identification

Human and mouse as mammals, exhibit biological similarities and share genetic functions, leading to the inheritance of traits in a similar manner. Mouse cells, which have a higher metabolism rate, are commonly used as a model in biomedical research to gain insights into the progression of chronic diseases and cancerous regulations in human cells [45, 46]. Identifying both genetic structural differences and geometric similarities between mouse and human cells can pave the way for future studies focusing on the identification of pathological cells within tissues. Previous

studies have demonstrated the capability of the CIDS modality to image the chromatin of isolated nuclei *in-situ* by treating them with a chemical solution that digests non-nucleus components. These isolated nuclei were suspended in a water solution through centrifugation [42, 44]. Additionally, CIDS has been coupled with expansion microscopy in another study to enable sensitivity to the chiral organization of biopolymers. It was found that by increasing the distance between chiral groups, this new imaging contrast provides better resolution of the chromatin-DNA organization *in-situ* [47].

It should be noted that biological tissues and cell structures typically exhibit strong depolarization due to scattering in thick and/or random environments. Since CIDS focuses on a single element (m_{03}) rather than the complete MM, direct access to the depolarization corresponding to the diagonal terms of the matrix (m_{11}, m_{22}, m_{33}) is not available. In our specific case, this information is not necessary for highlighting the CIDS imaging contrasts. However, depolarization likely transforms the circularly polarized light into incoherent light when scattering is significant. As a result, this scattering phenomenon contributes to reducing the amplitude of the CIDS signal.

In this section, bimodal scanning microscopy is utilized to capture CIDS and 2PEF images of mouse and human cell microscopy. The CIDS method is validated to observe chromatin modifications and evaluate any potential influence of cell membrane morphology on the CIDS signal in intact cells. The findings are presented in Fig. (2.8). The cell nuclei are labeled with Hoechst, which operates within the spectral window of 510 nm to 540 nm. The 2PEF microscopy images serve as a benchmark and provide evidence of accurate recognition of genetic material and its distinct spatial organization within the nuclei. A comparison is made between individual human and mouse cells, as well as a cluster of both cell types. The transmitted intensity images qualitatively depict the roughness of the cell membrane morphology. A notable distinction in the 2PEF images between mouse and human cell nuclei is observed based on the number of nucleoli, which results in dark round spots in human cells and bright dots in mouse cells. The CIDS images, represented by blue and red colors, reveal the degree and direction of the circular scattering effect in addition to the relative fluorescent contrast images.

It is observed that CIDS microscopy images exhibit higher contrast when imaging intact mouse cells, primarily due to the contribution of membrane curvature that dominates and scatters light before the light-matter interaction with chromatin. The corresponding line intensity profiles along the orange arrow in Fig. (2.8 j) and Fig. (2.8 k) are depicted in Fig. (2.8 m) and Fig. (2.8 n), respectively. The CIDS intensity profiles and images reveal greater variation limits in the signal for mouse cells compared to humans. Furthermore, a notable difference is observed between the two modalities in terms of intensity profile fluctuations. The CIDS signal exhibits a smoother profile, mainly influenced by the membrane's smoother morphology curvature, as opposed to the chromatin details within the nuclei in the 2PEF images. This disparity in contrast dynamics between the two modalities is evident.

It is important to note that the nuclei are nearly round-shaped, and therefore, theoretically, the plot profile should remain unchanged regardless of the line direction. This highlights the higher contrast dynamics and spatial frequency of 2PEF compared to CIDS.

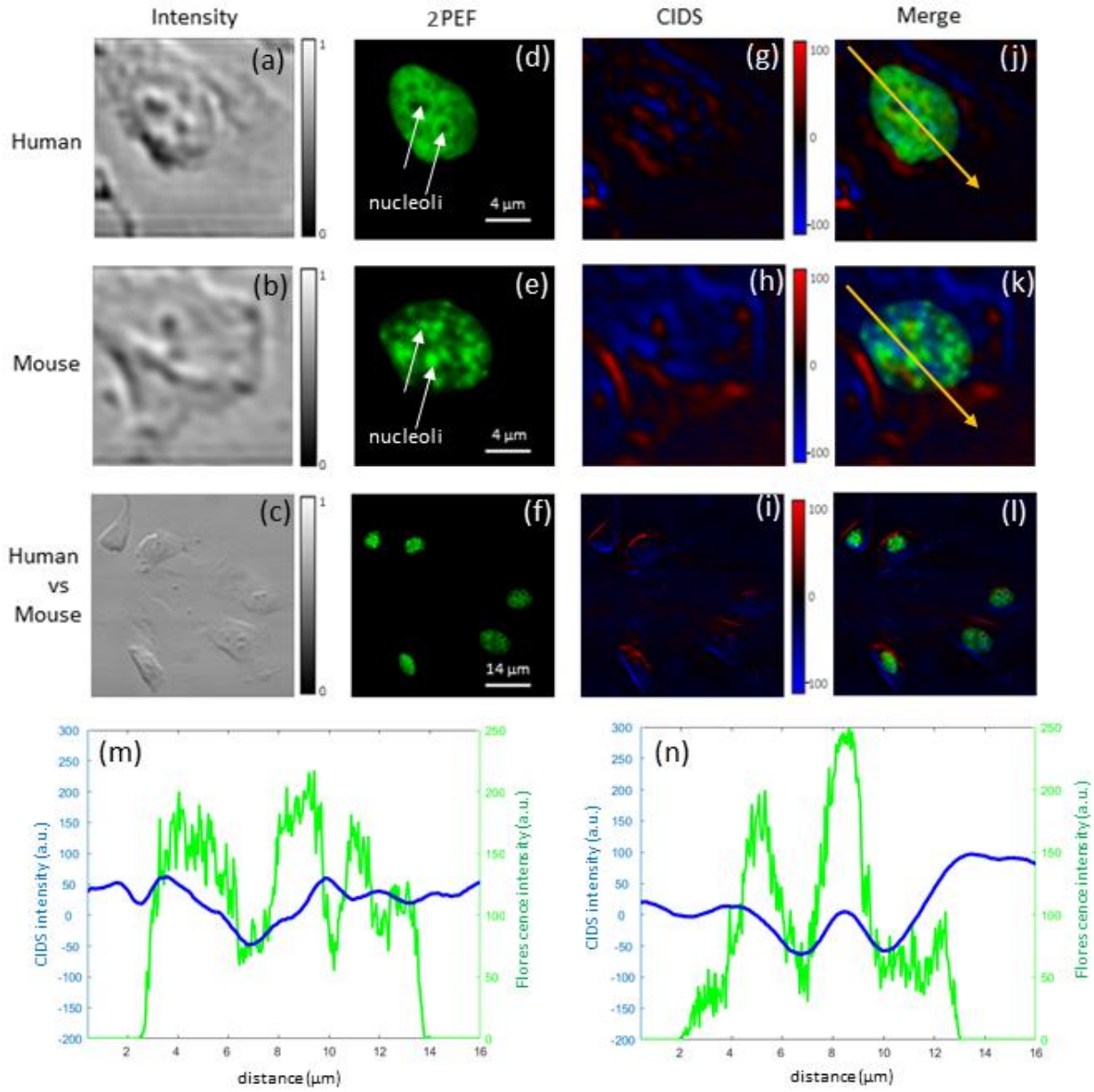

Figure 2.8. Multimodal scanning microscopy 512×512 images of human and mouse cells. (a-c) Total intensity, (d-f) Two-photon excitation fluorescence (2PEF) along with nucleoli indicated by white arrows and (g-i) circular intensity differential scattering (CIDS) microscopy images are compared respectively. The 2PEF results labeled with Hoechst show the genetic material differences between human and mouse based on nucleoli. (m) and (n) are the intensity profile plots of human and mouse cells respectively from the orange arrows in (j) and (k) merge images. The blue curves are the intensity profiles of the CIDS images, and the green ones are the relative Hoechst profiles.

The primary sources of CIDS contrast from the membrane are phospholipid bilayers, actin, and myosin filaments, which act as optically active elements influencing circularly polarized light. It is worth noting that the higher spatial resolution of fluorescent microscopy imaging serves as the second reason for the pronounced fluctuations observed in the fluorescent profiles [44]. The results demonstrate that the greater range of signal variations in the CIDS signal is associated with mouse cells, indicating the capability of this method to distinguish between cell types based on the signal range. To ensure consistency, the absolute value of the CIDS signal is taken to disregard the CIDS sign, and both modality images of human and mouse cells are normalized and presented in a 3D view in Fig. (2.9). The images reveal that higher intensities are predominantly observed in the mouse cell category for both modalities. In CIDS images, the contribution of membrane morphology is particularly pronounced along the membrane boundaries, with a more significant effect observed in mouse cells. The higher intensity in 2PEF images for mouse cells can be attributed to the greater number of nucleoli present in their nuclei, resulting in brighter points of illumination. In contrast, the background in 2PEF images is relatively flat as the signal source is primarily the chromatin. Conversely, in CIDS images, a notable background is observed due to residual materials that perturb the signal, leading to weaker contrast and an added noise component.

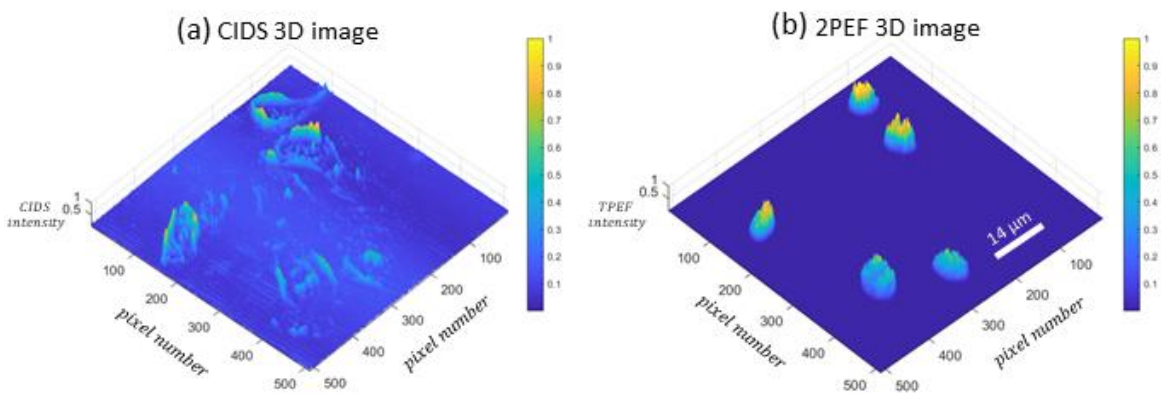

Figure 2.9. Shows the normalized CIDS and 2PEF intensities versus pixels for the human and mouse cells in a 3D view, represented by (a) and (b) respectively.

Accordingly, a classifying algorithm was developed to detect mouse cells in a sectioning manner. Global image thresholding using Otsu's method was applied to each pixel value after normalizing the CIDS image signals by the maximum intensity pixel. The proposed threshold value of 0.4, which was determined by minimizing the intra-class variance of the thresholded pixels in the normalized images, was utilized to facilitate cell identification. This approach allows specific regions of the mouse cell membrane to be highlighted in red, representing the highest CIDS signal,

while regions below the threshold are displayed in green. Fig. (2.10) shows the results of the sectioning process, with Fig. (2.10 a) showing the fluorescent signal intensity sectioning and Fig. (2.10 b) displaying the CIDS signal intensity sectioning. The histogram of the CIDS intensity plot in Fig. (2.10 c) provides further insight into the distribution of pixels occupying intensities above and below the determined threshold.

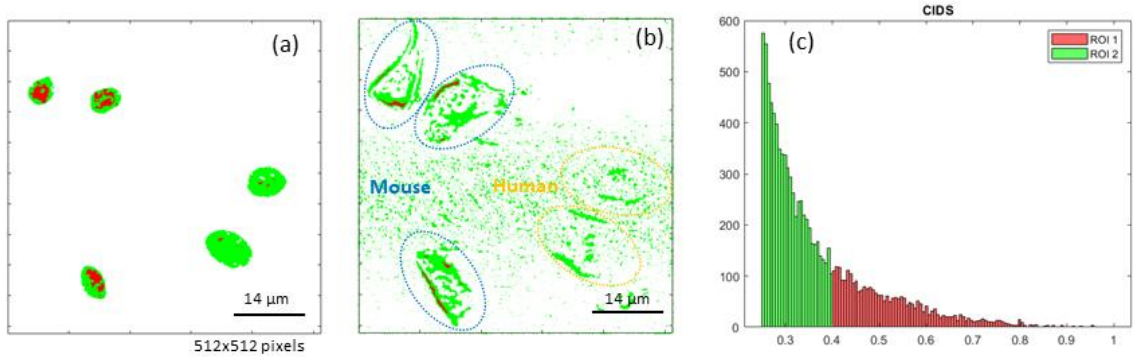

Figure 2.10. (a) 512×512 2PEF image of human and mouse cells. (b) Corresponding CIDS signal intensity sectioning image. (c) Histogram of different regions above and below the threshold marked by red and green colors respectively.

The procedure was repeated using multiple similar human and mouse cell images to ensure repeatability. The results obtained from analyzing 12 different samples further confirmed the potential of the CIDS method in quickly identifying mouse cells, as indicated by the statistical analysis presented in Fig. (2.11). The analysis revealed that the membrane sizes of mouse cells exhibited a wider range compared to those of human cells. This trend was also observed in the mean CIDS data, where mouse cells displayed a higher intensity signal due to their greater contribution from membrane morphology. Conversely, in the case of mean 2PEF data, which focuses solely on the nuclei and their genetic material, human cell nuclei exhibited a wider range of fluorescent intensities. Notably, the CIDS mean data for mouse cells demonstrated a significantly higher standard deviation (STD), contrasting with the 2PEF mean data.

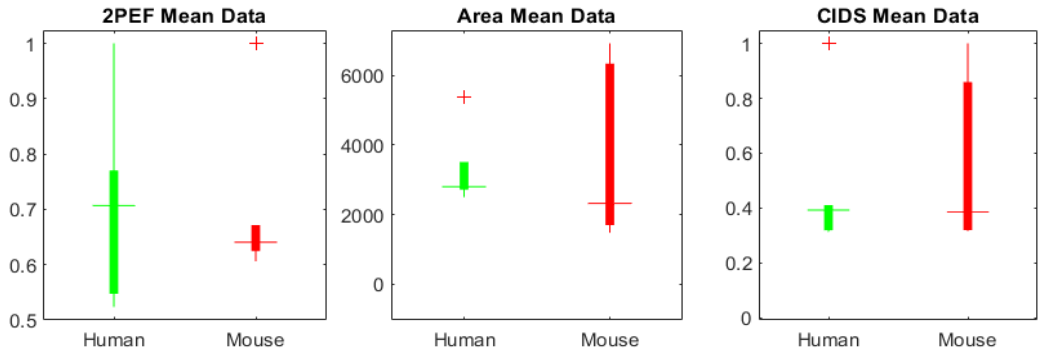

Figure 2.11. The statistical analysis of 12 samples per type ($p<0.012$) to identify human and mouse cells indicated by green and red respectively.

The statistical results highlight the significant influence of cell membrane morphology, specifically lipid bilayers composed predominantly of phospholipids and proteins, on the interaction of circularly polarized light compared to the role of chromatin within nuclei. To further validate this conclusion, a t-test evaluation was conducted, yielding a statistically significant result ($p<0.012$). These findings underscore the role of the CIDS signal in identifying mouse cells without the need for labeling or isolating nuclei, offering an alternative approach to fluorescence or other labeling techniques. Rather than replacing existing methods, this polarization-based modality provides a complementary tool for studying chiral structures, catering to the specific information requirements and conditions of complex biological materials.

2.5 Phasor map approach

In real experimental data, there are challenges related to the low sensitivity in detecting orientation parameters of polarimetric properties, as well as the presence of numerous different structures confined within a small volume. These factors make it difficult to determine the unique fingerprint of the sample [45]. Additionally, the encoding and decoding steps required in the process can lead to a significant post-processing burden when dealing with large image datasets, making analysis and interpretation of the contrast source challenging.

To address these issues, the phasor plot technique has been employed to provide a graphical analysis of spectra obtained from various microscopy techniques. Initially introduced in fluorescence lifetime imaging (FLIM) analysis as an alternative to multi-exponential decay fitting [48, 49], the phasor plot approach has been extended to the analysis of other microscopy data types, including spectral images [50], image correlation spectroscopy data [51], and super-resolution

images [52, 53]. The application of the phasor approach into the CIDS method is introduced for the first time as one of the goals of this thesis. The upcoming sections focus on the application of the phasor approach in CIDS, encompassing both single-point spectroscopy and scanning microscopy imaging modes. The phasor approach offers a valuable tool for extracting meaningful information from complex datasets and facilitates an efficient analysis and interpretation of the acquired output.

2.5.1 Phasor map data analysis of spectroscopic CIDS

Turbidity in liquids arises when small suspended particles exhibit a different refractive index compared to the surrounding medium. This phenomenon leads to the reflection, absorption, and scattering of incident light. The CIDS technique has emerged as a widely used label-free method for investigating the molecular conformation of complex biopolymers, such as chromatin [54]. In the context of CIDS, one configuration of particular interest is the single-point spectroscopic measurement of solutions [55]. Angular measurements provide a viable approach for implementing spectroscopic CIDS. By measuring the CIDS signal at various angles, complete angular information about the signal's evolution with respect to the rotational angle is obtained. Therefore, equation (2.17) elucidates the underlying principle of CIDS, relating to its angular dependence.

$$\mathrm{CIDS} = \frac{\mathrm{I_L}(\theta) - \mathrm{I_R}(\theta)}{\mathrm{I_L}(\theta) + \mathrm{I_R}(\theta)} \tag{2.17}$$

where the right and left intensities of the CIDS signal depend on the scattering angle θ. To encode these polarization states during CIDS acquisition, a polarization encoding modulator is employed to modulate the incident light's polarization at a high-speed rate [16]. By utilizing LA detection, the weak scattering signal can be extracted through demodulation of the reference frequency generated by the PEM.

The experimental setup, which is presented in Fig. (2.12) uses a single wavelength at 560 nm, with a beam size of 1 mm, considering far from the absorption band for measuring the CIDS signal from samples exhibiting an optical activity [56]. The PSG is composed of a zero-degree oriented linear polarizer (ColorPol® VIS 600 BC5 CW01, contrast >100000:1, Codixx AG, BRD) and a PEM at 0º (PEM-100, Hinds Instruments Inc, Hillsbro, OR, USA), resulting a time-varying intensity signal [57]. After, interaction with the sample composed of suspended particles inside the aqueous solution, the scattered light collected at each angle (with steps of 10º) through a collecting lens. The motorized detection arm is using a simple rotation stage linear polarized, rotating at +45º and -45º, allowing the decoding of the transformed light intensities collected by a

photomultiplier tube (PMT, R5108, Hamamatsu, JA). The system is fully automatized through a LabView® routine (National Instrument, ATX, USA) allowing the storage of the modulated signal via a Data board Acquisition (DAQ, National Instrument, ATX, USA). The demodulated frequencies at ω and 2ω are extracted angle-by-angle from a fast Fourier transform (FFT) of the signal using Matlab program (Matlab, v.R2017a, Mathworks) in order to determine properties such as CIDS of the sample. Due to the mechanical moving arm, the full angular polarimetric signals are acquired in around 10 min. Thus, the post-processing data consists in simply performing a Fourier transform of the modulated signal, which takes less than a few seconds to extract the full angular CIDS fingerprint.

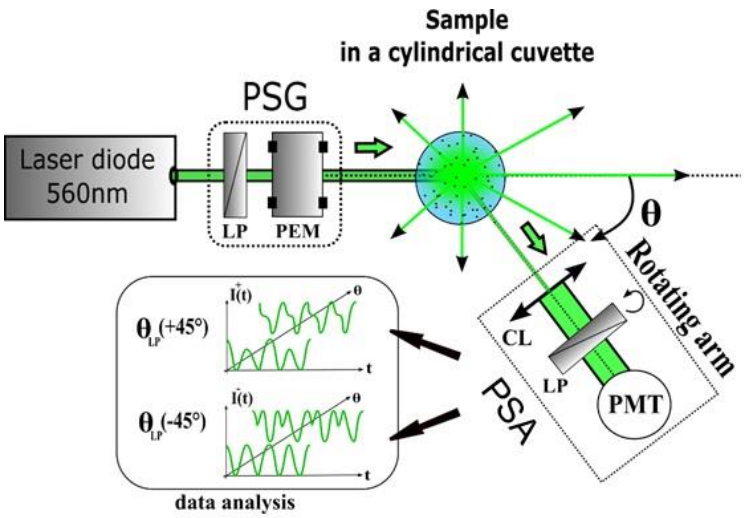

Figure 2.12. Scheme of the spectroscopic CIDS setup with a rotational arm to measure two orthogonally polarized signals by LP at different scattering angle θ. Modulated signal is then transformed to acquire CIDS data versus θ; PSG: Polarization States Generator. PSA: Polarization State Analyzer. CL: Collecting Lens. LP: Linear Polarizer. PMT: Photomultiplier Tube (adapted from reference [56]).

This setup can be employed to investigate the conformation of chromatin commonly conducted in its liquid-crystalline state. By altering its compaction and structure in an aqueous solution, the conformation of DNA can be studied [58]. The phasor map method coupled with the spectroscopic CIDS is introduced to simplify the polarimetric representation in an intuitive approach [56]. The validation of this approach involved examining the signal obtained from reference optical devices, such as LP and different retardation wave-plates, as a function of the azimuthal fast axis. Furthermore, this method is applied to a single-point spectroscopic experimental CIDS data set, specifically targeting chiral biomaterials and complex biopolymers, including chromatin in isolated nuclei *in-situ*.

2.5.1.1 Polarimetric data analysis

The detected signal has a form of a waveform represented in the Fourier domain by complex modulation amplitudes at frequencies corresponding to the PEM reference one and its harmonics. After simplifications, the output intensity $I(t)$ measured by the PMT detector is the combination of DC and AC currents as follows

$$I(t) = I_{DC} + I_{\omega}.\sin(\omega t) + I_{2\omega}.\cos(2\omega t) \tag{2.18}$$

where I_{DC} is the DC intensity of the modulated signal and I_{ω} is the modulation intensity at ω = 50 kHz and 2ω = 100 kHz. Each frequency modulation amplitude is a combination of MM elements m_{ij}, as demonstrated in their previous work. With the specific optical orientations of 45º, 0º, and ±45º, they are able to extract the CIDS signal, which corresponds to the m_{03} element. The transformation of polarized light is recorded permitting the detection of CIDS that is the m_{03} of MM (Equations 2.19, 2.20). Accordingly, the MM is the signature of the sample obtained by Mueller formalism [43, 59]. Thus, the modulated intensity $I(t)$ detected at +45º (I^{+}) and -45º (I^{-}), determines the total intensity (m_{00}) and CIDS elements as follows:

$$I_{DC} = I_{DC}^{+} + I_{DC}^{-} = \frac{(m_{00} + m_{02}) + (m_{00} - m_{02})}{2} \tag{2.19}$$

$$I_{\omega} = I_{\omega}^{+} + I_{\omega}^{-} = \frac{(m_{03} + m_{23}) + (m_{03} - m_{23})}{2} \tag{2.20}$$

$$I_{2\omega} = I_{2\omega}^{+} + I_{2\omega}^{-} = \frac{(m_{02} + m_{22}) + (m_{02} - m_{22})}{2} \tag{2.21}$$

where I_{ω}^{+}, I_{ω}^{-}, $I_{2\omega}^{+}$ and $I_{2\omega}^{-}$ are amplitudes of the intensities of the first and second harmonics for the cross (+) and parallel (-) polarization states (with respect to initial polarization state) provided by PSA unit. m_{02}, m_{03}, m_{23}, and m_{22} can be obtained through elementary algebraic operations, as demonstrated in our previous paper [44]. Information from the optical fingerprint of the sample is obtained by scanning it across a 180° angle. However, as indicated by equation (2.20), the modulated signal at frequency ω (I_{ω}), is a combination of m_{03} and m_{23}. This mixing makes it challenging to distinguish between linear birefringence and circular dichroism, posing a potential issue. To address this problem, an analytical framework of the phasor approach established in our simulation, along with experimental data, is utilized. This framework enables the diagnosis of both linear birefringence and circular dichroism and is further explained in the phasor map analysis section.

2.5.1.2 Phasor analysis and formalism

Analyzing the polarization-resolved modulated signal $I(t)$ gives rise to understanding the optical properties of the scattering sample under illumination, such as the molecular chirality (in terms of magnitude and sign ±) and orientation. Any data, which has a modulated intensity sequence, can be analyzed in the frequency domain using a Fourier transform, and converted into a phasor analysis providing a number of intrinsic advantages like the possibility to fast data analysis and unmixing different species in the ROI based on spectrum response [48]. This makes phasor analysis a general approach, which can be applied to any intensity-varying data acquired by any system, such as fluorescence [52]. The phasor coordinates, g and s, are the normalized intensity with the cosine and sine terms of the first and second harmonic of the Fourier transform of the data, related to the modulation and phase values, m and φ, by the trigonometric relations (see Fig. 2.13).

$$g = m.\cos(\varphi) \tag{2.22}$$

$$s = m.\sin(\varphi) \tag{2.23}$$

where m and φ called modulation and phase are given by m $=\sqrt{s^2 + g^2}$ and φ = arctan (s/g). In our case, the extension of phasor analysis to a time sequence analysis begins with the definition of phasor coordinates. The modulated signal is based on a temporal histogram that captures the arrival times of photons, which is then subjected to analysis using the phasor approach. In our setup, the width of the histogram bins is determined by the period of the modulated signal divided by the number of samples per period, ensuring compliance with the Nyquist sampling criterion. Specifically, the sampling rate matches the number of histogram bins. Following this definition, $I(t)$ represents the total number of collected photons reaching the detector within specific time bins (time intervals). Consequently, the phasor associated with the modulated signal is characterized by coordinates $g(\omega)$, $s(\omega)$, as given by:

$$g(\omega) = \frac{\sum I(t)\cos(2\pi f.t)}{\sum I(t)} \tag{2.24}$$

$$s(\omega) = \frac{\sum I(t)\sin(2\pi f.t)}{\sum I(t)} \tag{2.25}$$

where $\omega = 50\text{kHz}$ is the modulation angular frequency of the reciprocal time-dependent signal used for the Fourier transform and each frequency-dependent component g and s normalized by total photon counts $\sum I(t)$. The vertical axis shows imaginary and the horizontal one indicates real parts of the first and second harmonics. Every periodic signal has a vector in the phasor space with the two phasor coordinates (g, s). The phasor approach defines m between 0 and 1, and φ between

0 and 2π [60]. The g-axis, which is associated with linear birefringence, and the s-axis, which represents the circular dichroism of the sample, are defined in this configuration. It is important to note that in the CIDS extraction, the multiple harmonics, including both odd and even frequencies, can be expressed as a linear combination of the m_{ij} parameters. Higher harmonics with frequencies exceeding 50 kHz and 100 kHz can be obtained more rapidly, although their intensity decreases. For instance, CIDS can be acquired at 600 kHz, but the SNR at this frequency is below the detection capability of our photodiode. The calculations for it are presented at the beginning of this chapter in section (2.3). It should be emphasized that with a single PEM and two channels, only two harmonics can be obtained. Adding another PEM (following a similar frequency approach as proposed by O. Arteaga [61], would yield more m_{ij} parameters and additional harmonics, but it would slow down the process and may not be suitable for a scanning laser architecture. Therefore, only the modulation amplitude and corresponding phase of the first harmonic have been considered.

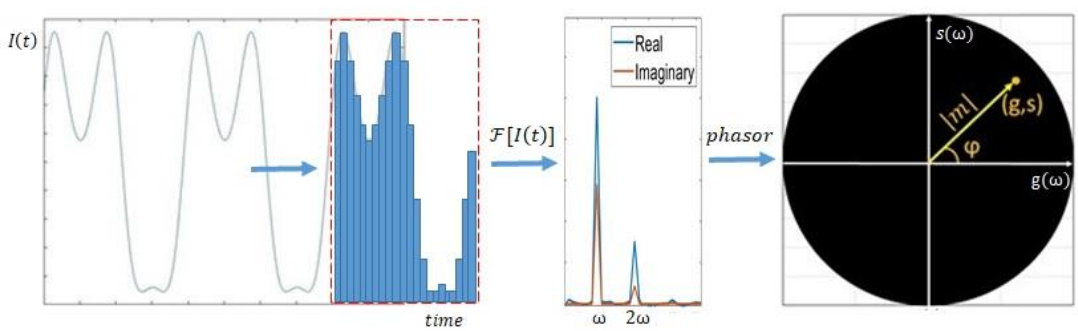

Figure 2.13. Schematic conversion of the signal I(t) collected experimentally into a phasor space at the coordinates (g, s). As signal after at least one period recorded, the single photon counts in terms of time bins assigned into histogram. Then the histogram is Fourier transformed to harmonics and the first harmonics represented here as a phasor position (based on the Equations 2.24 and 2.25). Each height of histogram bar shows the total number of arrived photons in corresponding time bin. The modulation and phase are obtained by $m = \sqrt{s^2 + g^2}$ and $\varphi = \arctan(s/g)$ equations respectively. The point with distance of |m| from the center of the black circle is linked to circular dichroism and birefringence of samples that is known as phasor map. From the phasor map of pure deterministic optical elements, we infer that the g axis deals with linear birefringence of the material and the s one is bound to circular dichroism so that one would recognize the contribution of these two polarimetric effects in a glance. The importance of this conclusion becomes more remarkable when the sample is suspended in acquis buffer as the refractive index role becomes crucial to perturb the decoded result.

2.5.1.3 Sample preparation

Microspheres with sizes of 15 μm in polystyrene (SIGMA Chem. Corp., St. Louis, MO) are used to calibrate the instrument and control the optical alignment of the components. The microspheres were suspended in dilute solution of deionized water (concentration 1:1000). Arabinose (SIGMA Aldrich, Chem. Corp., St. Louis, MO) and Isolated HEK 293 nuclei are placed in a matrix polyacrylamide gel to avoid aggregations. HEK 293 cells are grown in DMEM medium supplemented with 10% FBS, 1% penicillin – streptomycin, 1% glutamine. We obtain the isolation of nuclei by using a hypotonic buffer (10 mM Hepes pH 7.5, MgCl2 2 mM, KCl 25 mM, 1 mM PMSF, 1 mM DTT and Halt protease inhibitor cocktail from Thermo Fisher Scientific, Waltham, Massachusetts, USA) for 30 min in ice, which swells the cells. Then, the cells can be easily lysed with a glass Dounce pestle with a clearance range of 0.025-0.076 mm Technovetro s.r.l. Monza, Italy). While monitoring the cell lysis through a bright field microscope, sucrose at final concentration of 250 mM is added to the nuclei solution and the samples are centrifuged at 1200g for 10 min. The isolated nuclei are collected on pellet and are resuspended in nuclear buffer (10 mM Hepes pH 7.5, MgCl2 2 mM, KCl 25 mM, 250 mM sucrose and Halt protease inhibitor cocktail). Finally, the extracted nucle are resuspended in a fixation solution consisting in 3.2% Paraformaldehyde (PFA) and 0.1% Glutaraldehyde (GA) in polyacrylamide gel.

2.5.1.4 Numerical simulations and experiments on reference samples

As part of the objectives of the thesis, the validation of the phasor map approach is conducted through numerical simulations and a comparison with experimental data from reference optical devices. This allows for the simulation of the behavior of well-known reference samples, enabling an understanding of the conversion process from polarimetric properties to phasor space representation.

The first step involves applying the method to air, without a sample in the illumination volume, to investigate different SNRs and their influence on the position of the phasor plot. This analysis provides an approximation of acceptable noise levels for experimental modulated signals with varying degrees of depolarization. Next, the behavior of LP and wave-plates with respect to the azimuthal fast axis is studied through simulation. This helps to explore the impact on the resulting phasor plot positions. In addition, a modulated signal by a CP is simulated as a reference for a chiral material, with different scattered phasors generated based on varying SNRs. These simulations further contribute to the validation of the phasor map approach and its applicability to different scenarios. In parallel, experimental data is presented to validate the optical features discussed in the simulations. To obtain the m_{ij} phasor, five elements out of the sixteen in the MM

are considered. These elements are associated with the total intensity (m_{00}), linear dichroism (m_{02}), circular dichroism (m_{03}), linear birefringence (m_{23}), and linear depolarization (m_{22}).

2.5.1.4.1 Air sample

The phasor signature in the absence of a sample in the illumination volume (i.e., air sample) is simulated. The corresponding air signal, which is independent of sampler rotation, is converted into frequency space by applying equations (2.24) and (2.25) show zero values at the coordinates (g, s). All the contributions of real and imaginary parts of frequency space are depicted as the phasor plot. MM elements provided by Fourier Transform of the signal from air based on adding up and subtracting the first harmonics (m_{03}, m_{23} respectively) and the second harmonics demodulated amplitude (m_{02}, m_{22} respectively) to exhibit birefringence and dichroism of air that is zero for all. Fig. (2.14) shows the associated phasor plot provided from the analysis of the signal and we use only the DC and AC first harmonics to recover the normalized CIDS signal. The phasors of theoretical and experimental data do not match totally because of the existence of noise in the experimental signal. We address this issue by taking an uncertainty at the position of the phasor of experimental data into account specified for the noise and the experimental error is measured below 10% based on reference samples demonstrated in our work.

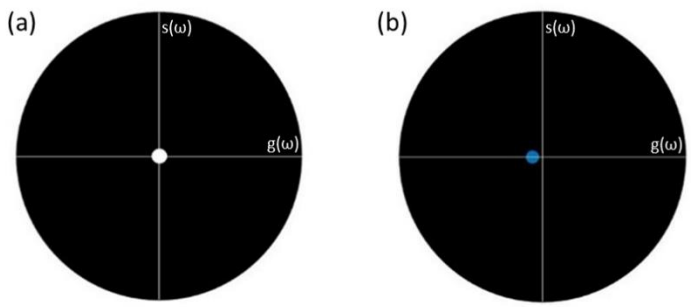

Figure 2.14. (a) Phasor plot for the simulation of the modulated signal of air resulting from the integration of all contributions from the real and imaginary amplitudes of the corresponding reciprocal space in which located at the center of the phasor. (b) Phasor plot for the experimental modulated signal of air (along with around 10% of noise) located slightly different from the center.

2.5.1.4.2 Limit of sensitivity evaluation

The signal of air is studied with different artificially added noises to observe the relevant phasor map, aiming to estimate the minimum required SNR for the conversion of signal data into the phasor map. This analysis is particularly important as this approach will be combined with measurements that are highly affected by the scattering effect in a low signal regime. Indeed, this analysis is of interest considering this approach will be combined with measurements highly affected by the scattering effect in a low signal regime. Fig. (2.15) shows the phasor map resulting from added Gaussian noise (ΔI = 0% up to 100%) to the simulated signal and the variation of $|m|$ corresponding to the distance of the noisy phasor spot according to the theoretical one in terms of SNR (dB) = $10\log(1 + \Delta I)$ is shown. Accordingly, from 0% up to 30% of noise, the fitted curve increases based on cumulative distribution, and the error bar is relatively small, which shows the phasor is located to the adjacent of expected one. However, a significant increase is observed from 30% to 40%, accompanied by larger variations indicated by the corresponding error bars, which further escalate up to 100%. Consequently, an evaluation is conducted to determine the acceptable level of noise, which is limited to 30% and represented by a white circle. This restriction aims to confine the placement of noisy yellow phasors around the central point. It is important to note that this limitation introduces some degree of uncertainty regarding the positioning of the phasor map when dealing with experimental data.

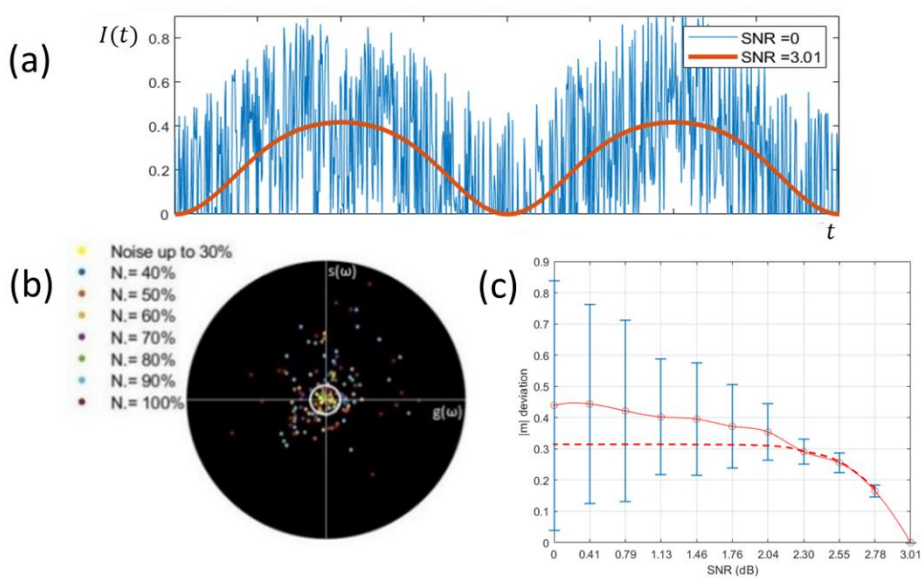

Figure 2.15. (a) Theoretical modulated signal of air when signal to noise ratio (SNR) = 0, 3.01, where y axis = 0 to 1 and x axis = 0 to 20 µs. (b) Phasor map of 20 simulated noisy signals each from 0% up to 100% shown by color labeled dots. The dots inside the white circle correspond to less than 30% of noise. (c) Corresponding |m| variation versus SNR curve; the maximum value of SNR corresponds to 0% of noise. Each error bar is provided from 20 simulated signal trials with each SNR. The dashed red line corresponds to the mentioned cumulative distribution.

2.5.1.4.3 Pure deterministic optical elements

In the following stage, the phasor map of a LP is investigated as an illustrative example of a dichroic material. Furthermore, the examination is extended to various wave plates with different retardation values and fast axis orientations. By utilizing the MM approach, the phasor plot of the LP is simulated based on the signals obtained at the specified angular rotations of the LP. The simulation is conducted as follows:

$$M_{LP} = \begin{bmatrix} 1 & \cos(2\theta) & \sin(2\theta) & 0 \\ \cos(2\theta) & \cos^2(2\theta) & \cos(2\theta)\sin(2\theta) & 0 \\ \sin(2\theta) & \cos(2\theta)\sin(2\theta) & \sin^2(2\theta) & 0 \\ 0 & 0 & 0 & 0 \end{bmatrix} \tag{2.26}$$

where θ is the fast axis azimuthal angle of the LP. Fig. (2.16 a) presents the phasor plot of simulated LP data at different angles.

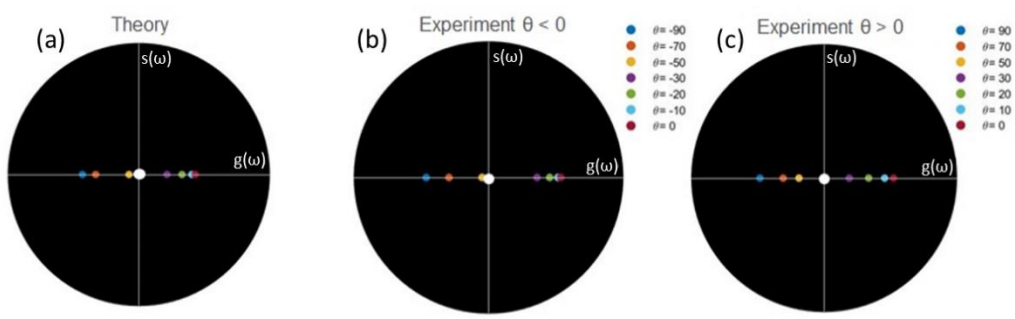

Figure 2.16. (a) Phasor map of simulated linear polarizer (LP) at 0º, ±10º, ±20º, ±30º, ±50º, ±70º and ±90º corresponding with colored points. The white point at the center of the phasor is corresponding to the LP at ±45º that is identical to air. (b), (c) Phasor maps of experimental LP data at 0º, ±10º, ±20º, ±30º, ±50º, ±70º and ±90º. The experimental results show a close accordance to the theoretical simulations.

The signal of the LP exhibits symmetry at positive and negative rotational angles, indicating an even function. Therefore, the phasors at positive angles are expected to be similar to those at negative angles. In the case of the LP, symmetric orientations around zero result in similar signals with minor variations attributed to noise. Time-varying signals with orientations spanning from -π to π of the LP are obtained using the experimental setup. This facilitated the application of MM elements and the phasor map approach for analysis (see Figs. 2.16 b and 2.16 c). The results confirm the phasor map from simulated data despite small errors (<%10), the order of angles is the same and show the phasor of LP lays on g-axis at any orientation angle.

Next to study is the experimental phasor map of a zero-order half wave plate (HWP, Thorlabs, WPH05M-561, NJ, USA) as birefringent samples. Birefringence, as the predominant polarimetric parameter, exhibits significant imaging contrast in biological samples. This contrast arises from variations in the sample's refractive index, which can be represented as a complex number with both real and imaginary components. To analyze the phasor map of birefringent materials with varying retardance or fast axis phase shifts, the following MM is employed in our simulations:

$$MM_{wp}=\begin{bmatrix} 1 & 0 & 0 & 0 \\ 0 & \cos^2(2\theta)+\sin^2(2\theta).\cos(R) & \cos(2\theta).\sin(2\theta).(1-\cos(R)) & \sin(2\theta).\sin(R) \\ 0 & \cos(2\theta).\sin(2\theta).(1-\cos(R)) & \sin^2(2\theta)+\cos^2(2\theta).\cos(R) & -\cos(2\theta).\sin(R) \\ 0 & -\sin(2\theta).\sin(R) & \cos(2\theta).\sin(R) & \cos(R) \end{bmatrix} \quad (2.27)$$

$$R=\frac{2\pi.\Delta n.d}{\lambda} \quad (2.28)$$

where θ is azimuthal fast axis of the wave plate, R stands for the retardance, $\Delta n = (n_e - n_o)$ is the birefringence (n_e and n_o are extraordinary and ordinary refractive indexes of the material), d is the thickness of the sample and λ is the excitation wavelength. The domain of the orientation angle remains the same as in the previous case, ranging from -π to π. In Fig. (2.17 a), the phasor map of the simulated HWP is presented, while in Fig. (2.17 b), the phasor map of the experimental HWP is shown.

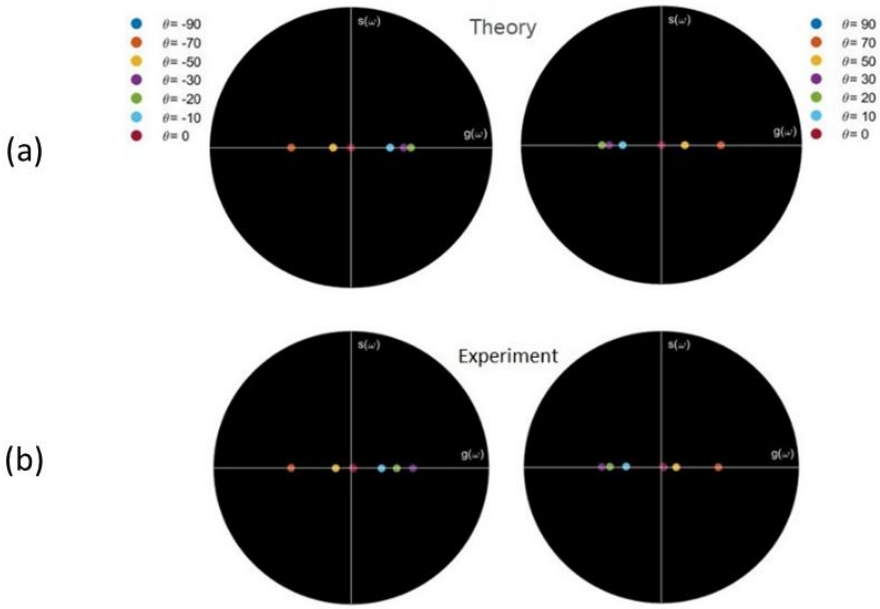

Figure 2.17. (a) Phasor map of simulated half wave plate (HWP) at 0º, ±20º, ±50º, ±70º and ±90º corresponding with colored points. The points are representing only the first harmonics for the sake of simplicity. The overlapped points at the center of the phasor is corresponding to the wave-plate at ±45º, ±90º and 0º that is identical to air at which all the MM elements are zero. (b) Phasor map of experimental HWP data at 0º, ±10º, ±20º, ±30º, ±50º, ±70º and ±90º. The overlapped points at the center of the phasor is corresponding to the wave-plate at ±45º, ±90º and 0º that is identical to air.

Results indicate that for the HWP, the only non-zero MM element is linear dichroism (m_{02}). The phasor of LP at ±45º and HWP at θ = 0º, ±45º, and ±90º coincide with that of air, as there is no polarization change when the input polarized light aligns with the fast axis of the birefringent sample, consistent with the polarization formalism. However, specific angles such as θ = 0º allow discrimination between LP and HWP on the phasor map, as the phasor map for HWP aligns along the g-axis, similar to LP. Further simulations of other birefringent wave plates are conducted to capture the general behavior on the phasor map (Figs. 2.18 a and 2.18 b). For example, in the case of the QWP, all four quadrants of the phasor map are covered from θ = -π to π. Notably, discrimination between HWP and QWP is possible when the phasor is non-zero, such as at θ = ±45º, where they behave similarly to air. This discrimination holds true for other retardant wave plates with different phase shifts, as the trajectory of the corresponding phasor map for different fast axis orientations θ is unique and depends on the retardance value. Consequently, the values of R and θ can be determined from the phasor map plots. When 0 < R < π, the trajectory exhibits an S shape with varying curvatures based on R. In the case of HWP (R = π), the phasor map displays a line of points aligned along the g(ω) axis, resembling that of LP (Fig. 2.16). Additionally, it should be noted that s(ω) is associated with the chirality of the sample.

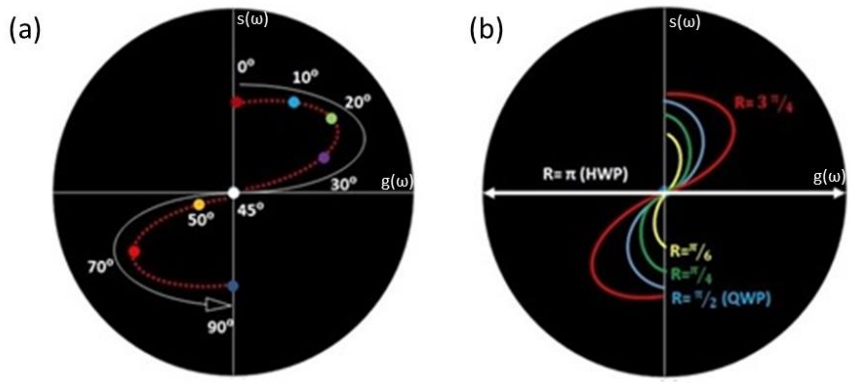

Figure 2.18. (a) Phasor map of simulated 3π/4 retardant plate data at 0º, 10º, 20º, 30º, 45º, 50º, 70º and 90º. The phasor of negative angles is the reverse image of the shown trajectory with respect to vertical axis $s(\omega)$. The points are representing only the first harmonics for the sake of simplicity. (b) Scheme of the phasor map pattern for different retardant wave plates R = π/6, π/4, π/2, π and 3π/4 as a function of angular rotation from θ = 0º to π and for θ = 0º to –π the shape has the reverse symmetricity with respect to vertical s(ω) axis. The phasor is zero at θ = ±45º for all of the wave plates.

From the phasor map, it is observed that as the values of R decrease, it becomes increasingly challenging to differentiate between angular rotations of the birefringent object due to the close proximity of the curvature ends to the center. In other words, lower R values result in weaker signal modulations, making it nearly impossible to distinguish each angular position of the sample. Additionally, when θ = ±45º, it is not possible to differentiate between different wave plates in this representation, as the corresponding phasors are equivalent to those of air, yielding no contrast difference in microscopy at this specific orientation. However, this limitation does not pose an issue when dealing with pure chiral and scattering samples, such as chromatin, as they do not exhibit birefringence and dichroism. Therefore, taking all these parameters into consideration, it is feasible to reconstruct and interpret an image of a bio-sample based on the birefringence and dichroism effects using the phasor map approach.

The next investigation focuses on a circular polarizer (CP), which serves as an example of a reference chiral material in our CIDS approach [62]. It is assumed that the sample in this study can be modeled as a simple chiral material, with any measured birefringence considered as systematic errors that are accounted for during the calibration step. The signal of the CP is examined to observe the corresponding phasor map, and the simulation of the CP signal is performed using the following MM:

$$M_{CP} = \begin{bmatrix} 1 & 0 & 0 & \pm m_{03} \\ 0 & 0 & 0 & 0 \\ 0 & 0 & 0 & 0 \\ \pm 1 & 0 & 0 & 1 \end{bmatrix} \tag{2.29}$$

where m_{03} is the circular chiral element (related to CD) which is considered to be from -1 up to 1 with 0.5 steps. An experimental phasor map of a homogenous right-handed circular polarizer (CP1R532 - Right-Handed Circular Polarizer, Thorlabs, CP1R532, USA) is studied to be compared to the simulations.

Figs. (2.19 a) and (2.19 b) show the simulated signal $I(t)$ with 10% noise in histogram shape realized from a circular polarizer and corresponding phasor map respectively. Fig. (2.19 c) shows the associated phasor plot of simulated CPs and obviously, all the chiral CPs are located on the s-axis. When the chirality is equal to zero (represented by the yellow point), a similar situation arises as in the case of air, with a trivial difference.

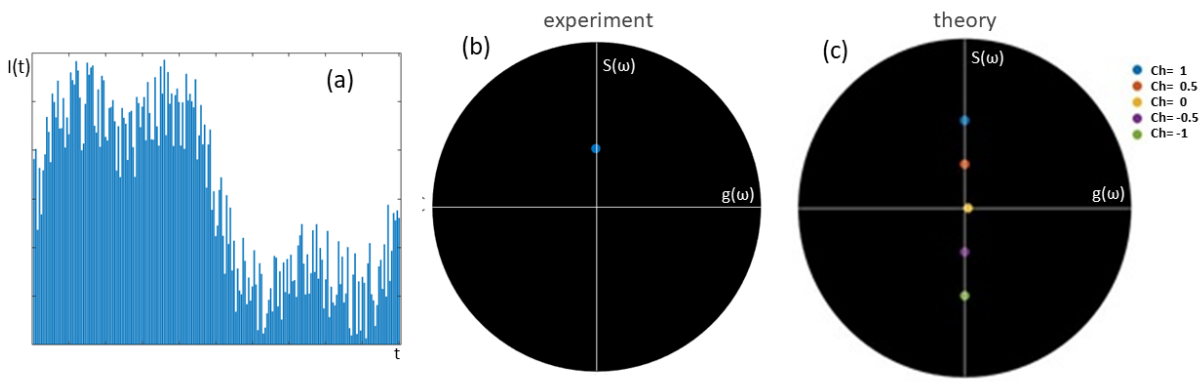

Figure 2.19. (a) Histogram of signal $I(t)$ collected by simulation from the circular polarizer (CP) with added noise; (b) Associated phasor map at the coordinates (g, s); (c) Phasor map of simulated CP data for m_{03} = -1, -0.5, 0, 0.5 and 1 corresponding with colored points. CP has pure circular dichroism effect as the phasor map is on the $s(\omega)$ axis based on the amount of chirality. The points are representing only the first harmonics for the sake of simplicity.

2.5.1.5 Phasor analysis on biological samples

2.5.1.5.1 Single point CIDS spectroscopy of arabinose

Arabinose, a monosaccharide with five carbon atoms and an aldehyde functional group, is chosen as the organic sample for study [63]. Due to its pure chiral nature and absence of complex structural features, arabinose serves as an ideal example for our phasor map approach to highlight the polarimetric contrast. The amorphous crystal shape and arbitrary position of the sample in an aqueous buffer lead to disordered chirality at various scattering angles ranging from $-\pi$ to π, as observed in the phasor map results (Fig. 2.20). Interestingly, there exists a symmetry of birefringence between positive and negative angles, similar to the findings obtained for HWP phasor results.

To further investigate the influence of arabinose concentration on the phasor map, experimental signals are examined for different molar concentrations (2M, 1M, and 0.25M). The results indicate that at 2M concentration, the phasors can be discriminated at different angles. While arabinose is known to possess chirality, its solvated state diminishes the contribution of chirality, resulting in negligible variations in the $s(\omega)$ values compared to the dominant $g(\omega)$ values. This suggests that the birefringent effect remains largely unaffected by solvation, while dichroism plays a relatively minor role. Comparing Fig. (2.20 b) and Fig. (2.20 c), it is evident that there is minimal sensitivity observed at around 1M concentration of arabinose.

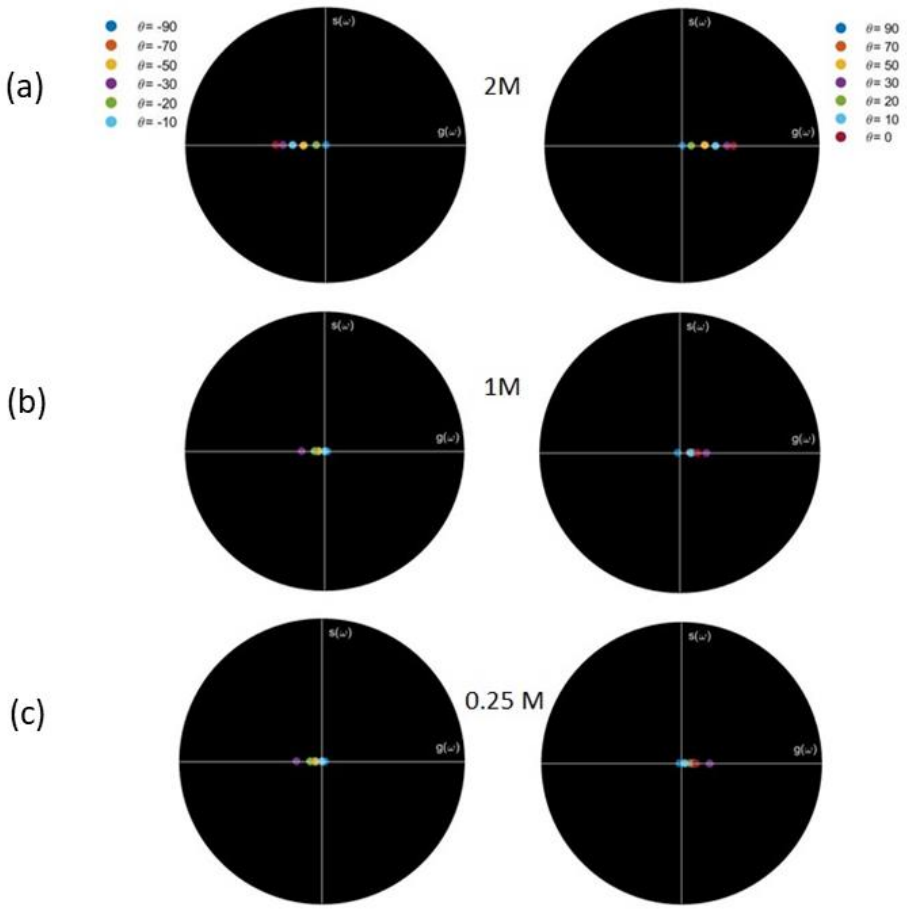

Figure 2.20. (a) Phasor map of experimental 2M arabinose data at 0º, ±10º, ±20º, ±30º, ±50º, ±70º and ±90º. The results at ±90º is identical to air and highest amount of birefringence is at 0º considering cross and parallel polarization state before detection. (b), (c) Corresponding phasor map of arabinose with concentrations of 1M and 0.25M respectively at the same angular rotation degrees. For these densities the phasor at angles between 0º to ±90º are not easily distinguishable.

2.5.1.5.2 Single point CIDS spectroscopy of isolated cell nuclei

The final goal of the spectroscopic CIDS study is to investigate and gain insights into the organization of chromatin at various levels of compaction. Chromatin is a complex structure composed of DNA strands and proteins, primarily found in the nuclei of eukaryotic cells [64]. Its main function is to compact and condense long DNA molecules into denser structures. Therefore, it is expected that chromatin would exhibit strong chirality, providing a contrast in the CIDS and other MM signal contributions, particularly when the refractive index of chromatin mismatches with the surrounding solution, which is often the case. By detecting the chirality of chromatin in different regions within the cell nuclei, it becomes possible to differentiate between active (heterochromatin) and non-active (euchromatin) regions in terms of gene expression [65]. This information helps in understanding the differences in compaction levels within the nucleus. Through the application of the CIDS method, it is also possible to observe the spatial conformation of chromatin and its role in cellular functioning during different phases [19, 66].

In this section, isolated HEK cell 293 nuclei is studied within an acrylamide gel buffer using a phasor approach. The results are compared to those obtained from polystyrene microspheres, both before and after the addition of the nuclei sample (Fig. 2.21). Based on the results, it is observed that the behavior of acrylamide is consistent with expectations, exhibiting similarity to air. Acrylamide does not introduce any perturbation to the signal of HEK cell nuclei and microspheres, and it does not exhibit any chirality effect on the signal. This is attributed to the transparency of acrylamide and its close refractive index matching with chromatin. Consequently, acrylamide can be added to the buffer containing cell nuclei in an acrylamide gel without significant impact on the signal.

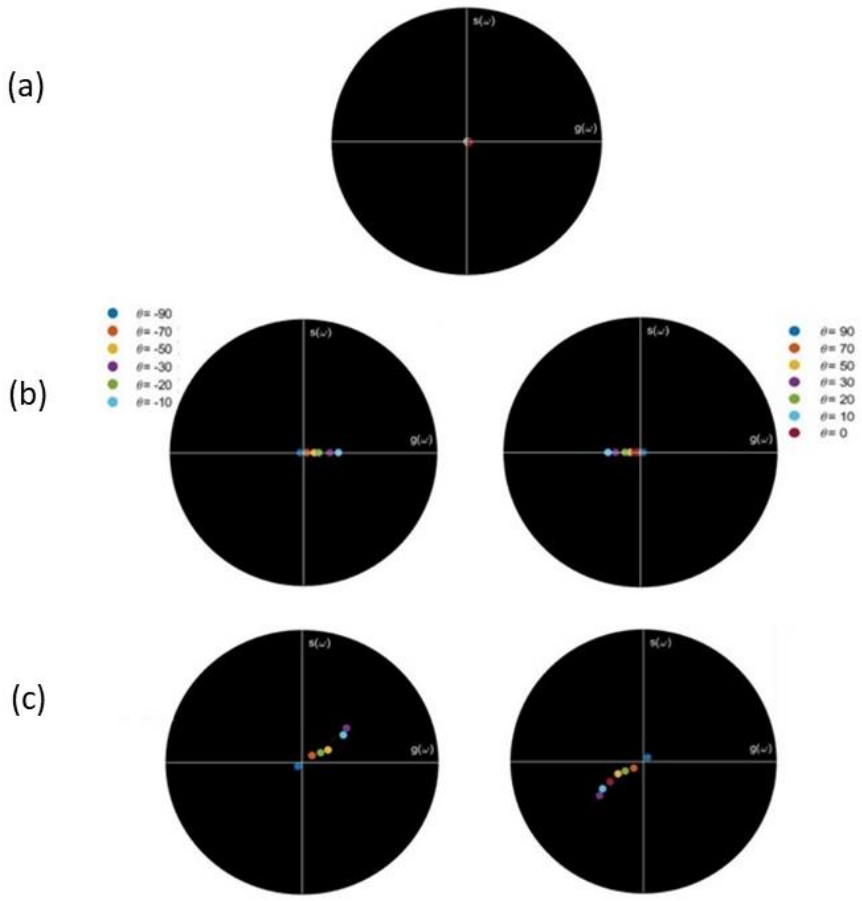

Figure 2.21. (a) Phasor map of acrylamide gel (acquired with around 10% of noise) at all the angles we show the behavior is close to air. (b) Phasor map of experimental polystyrene microspheres data at 0º, ±10º, ±20º, ±30º, ±50º, ±70º and ±90º. It represents that there is no chirality effect. (c) Phasor map of HEK cell nuclei data at 0º, ±10º, ±20º, ±30º, ±50º, ±70º and ±90º. The highest chirality and birefringence occur at ±30º and corresponding lowest one is at ±90º.

2.5.2 Phasor map data analysis of CIDS imaging

Despite the advantages mentioned for CIDS scanning microscopy imaging, the CIDS imaging technique suffers from spatial averaging of information, which makes it insensitive to different mixtures of structures within the confined illumination volume defined by the PSF. Therefore, it becomes challenging to specifically track the polarimetric signature of organelles at the subcellular level, especially in label-free imaging of cells. This limitation hampers the identification of different cell types and the detection of cell structures such as chromatin in the nuclear membrane. To address this issue, the utilization of Fourier transform analysis of modulated signal sequences in the frequency domain is proposed, enabling mapping into a single point on a phasor plot. The concept of phasor mapping was initially introduced for super-resolution microscopy, specifically for fluorescence lifetime imaging (FLIM) signal analysis, and has subsequently been extended to spectral imaging [22, 48, 51]. However, the use of phasor plots in label-free microscopy techniques, such as SHG microscopy, has been reported in only a few studies [67].

In the previous sections, a study was presented, demonstrating the remarkable capability of phasor data analysis for recognizing different structures that exhibit strong birefringent and dichroic responses in turbid media. Additionally, the application of this approach in measuring the polarimetric fingerprint of isolated cell nuclei was demonstrated using a single-point spectroscopic architecture, with acquisition of angular scattering modulated signals through a rotational detection arm [56]. In this section, the proposal is made to adapt the approach to an imaging architecture, showcasing its ability to provide a robust and distinctive analytical method for capturing polarimetric variations of different types of particles within the PSF volume.

Here, the image acquisition is coupled with a 2PEF modality, which serves as a benchmark technique for detecting the presence of genetic material throughout the PSF volume. It is important to note that the data represented in the phasor analysis solely arises from the interaction between polarized light and chiral structures. In our study, the fluorescence images are presented as a benchmark for lamin-A and chromatin organization and are compared with polarization-resolved images. To validate the analytical approach, starch granules are primarily imaged as deterministic optically active complex bio-particles, ideal for highlighting the sensitivity of the approach and enabling segmentation of different microscopic molecular regions as a phasor guideline map. Furthermore, the application of the image phasor approach to polarimetric images for tracking different stages of Hutchinson-Gilford progeria syndrome is demonstrated. The polarization response changes induced by the deformation of the nucleus in the presence of the pathology were intuitively and directly observed compared to normal cells. The advantage of the image phasor map over the previously reported single-point approach lies in its ability to handle multiple points indicating the finest contrast mapped from polarimetric microscopy images at the sub-microscopic level. In the last section, the robust polarization response of the syndrome is illustrated compared to normal cells through confocal fluorescence images, alongside microspheres serving as a

reference, providing relevant statistics and interpretations. Overall, in the following sections, a sensitive graphical analytical method for polarimetric images are proposed, enabling the discrimination of different developmental stages in cells.

2.5.2.1 Phasor map analysis of CIDS imaging to investigate Hutchinson-Gilford progeria

The perception of chromatin compartments as chiral-group structures composed of DNA double helix and proteins inside eukaryotic nuclei is crucial to identify enriched expressed gene regions based on different compaction levels of chromatin [68, 69]. Deformation into chromatin compaction would affect artificial gene expression as it is in the case of progeria for instance. Progeria is derived from the Greek words pro (προ) and geras (γέρας), meaning premature aging which is a specific type of progeroid syndrome called Hutchinson-Gilford syndrome, a genetic disease that causes children to age rapidly within the first two years of life [70]. This happens by a mutation in the lamin-A (LMNA) gene that is responsible to make a defective protein that holds the nucleus of the cell together and causes the nuclei to be unstable which leads to multiple morphological anomalies of cell nuclei and disturbances in heterochromatin organization, mitosis, DNA replication and repair, and gene transcription. As there is no known cure, people with progeria due to complications of severe atherosclerosis, either cardiac disease or stroke, typically live to an age of mid-teens to early twenties [61-73]. It has been an interesting bio sample for image microscopy as a suitable study case to show how deformation in the cell structures is induced by a bad transcription of the genes. In fact, the most common and quantitative method available for studying this pathology is fluorescence and super-resolution techniques. To investigate for instance chromatin at the nanoscale and single molecule localization [74]. However, fluorescence-based techniques are limited due to the possibility of perturbation of the organization of biomaterial, the potential of photo-bleaching in high illuminating doses of light, operator dependency, and the requirement of expansion instruments [36]. A way to overcome such issues has been demonstrated by polarization-based microscopy techniques commonly used to enhance contrasts discerning polarimetric characteristics of anisotropic structures and chiral organization of macromolecules [75]. The technique is based on employing Mueller-Stokes polarimetry formalism that confers a complete description of the optical properties of the sample [5, 38, 76]. The polarimetry method is linked to dichroism and birefringence of the specimen [77, 78]. One of the technologies to acquire the pixel dwell time rate in a few microseconds could be provided by the use of photo-elastic modulators [19]. Chromatin imaging is of great interest to us as it comprises an aggregation of proteins and chiral molecules that strongly interact with circularly polarized light. Understanding the characteristics of this molecule is crucial as it encodes all genetic information and plays a significant role in defining the properties of an organism. Consequently, the chromatin compaction level is fascinating to investigate through polarization

that is sensitive to the molecular organization, and cellular/nuclear shape and very interesting if we want to diagnose genetic pathology such as progeria syndrome as a progressive genetic disorder [79].

2.5.2.2 Sample preparation

Microspheres of 15 μm in polystyrene (SIGMA Chem. Corp., St. Louis, MO) are used to calibrate the instrument polarimetric properties. The refractive index of the spheres at the excitation wavelength (770 nm) is 1.58. The microspheres were suspended in dilute solution of deionized water (concentration 1:10000). The starch granules (SIGMA Chem. Corp., St. Louis, MO) are used as reference chiral sample. The starch granules were suspended in dilute solution of deionized water (concentration 1:1000) solution at room temperature (20°C). Then, a drop of a dilute starch-water suspension was placed on a microscope slice and fixed by a coverslip.

Human embryonic kidney 293 cells (HEK 293) were used to obtain progeria cellular phenotype. The control cell line was wild type HEK 293. Cells were grown in complete medium Dulbecco's Modified Eagles Medium (DMEM High-Glucose, Gibco) + 1% L-Glutamine, supplemented with 10% fetal bovin serum (Sigma-Aldrich), 1% non essential aminoacids and 1% pen/strep, with 5% CO_2, 90% relative humidity at 37 °C. To obtain the progeria cellular phenotype HEK 293 cells were stably transfected with the plasmid simultaneously encoding for the mutant protein Δ50 lamin-A and enhanced green fluorescent protein (eGFP) (Addgene plasmid #17653). Wild type HEK293 and progeria cells were plated at 50% confluency on 18 mm coverglass, previously threated with a solution of poly-L-Lysine (0.01%, Sigma-Aldrich) for 10 minutes to promote adhesion, and grown overnight. After fixation with 4% PFA for 10 minutes at room temperature cells were rinsed twice for 5 minutes with fresh PBS. Then, cells were stained with a solution 4 μM of Hoechst 33342 (10 mg/mL, ThermoFisher) for 20 minutes and rinsed twice with PBS. Next, wild type lamin A in HEK293 cells was stained using conventional immunostaining protocol. After fixation, cells were incubated in Blocking Buffer (3% Bovine Serum Albumin, 0,2% Triton 100X in PBS) for 1 hour at RT. The incubation with primary antibody (anti-lamin A antibody, ab26300 from AbCam, dilution 1:1000, in 3% BSA in PBS) was performed overnight at 4°C. After three washes in PBS, the sample was incubated with secondary antibody (AlexaFluor 488, dilution 1:200, in 3% BSA in PBS) for 1 hour at RT. Next, cells were washed three times with PBS. Samples were mounted on glass slides using 10 μl of Prolong Antifade mounting medium and then were ready to image.

2.5.2.3 Data analysis and statistics

In this section, the polarization-resolved microscopy technique is categorized as temporal domain encoding polarization states and decodes the transformed ones by using the Stokes-Mueller formalism to extract the polarization fingerprint of the specimen [5]. The outcome signal is the result of the interaction between the circularly polarized light and the sample thus, the resulting intensity can be described by equation (2.14)

The signal is then demodulated directly through lock-in detection, and the outputs of the mixers pass through configurable low-pass filters, resulting in two output components: the real part (I_ω^{Re}) and the imaginary part (I_ω^{Im}), also known as the in-phase and quadrature components, respectively. By utilizing a lock-in amplifier connected to the Nikon C2+ controller, the modulation (R) and phase ($\theta^{\pm}$) images are simultaneously obtained in three channels, following equations (2.30-2.33).

$$I_\omega \equiv R = \sqrt{g^2 + s^2} \tag{2.30}$$

$$\theta \equiv \pm \arctan\left(\frac{s}{g}\right) \tag{2.31}$$

$$g = R.\cos(\theta) \tag{2.32}$$

$$s = R.\sin(\theta) \tag{2.33}$$

The images are then processed pixel-by-pixel using NIS Elements software. The demodulated signal is represented using the (g, s) phasor representation, where I_ω corresponds to the modulation R obtained from g and s. The phase θ is obtained by transforming the Cartesian coordinates into polar coordinates, as described by Equation (2.31), allowing for a phase angle output range that covers all angles from -π to π. This representation accounts for the circular polarization response of the matter, excluding the contribution of parallel polarized light at the output, which differs from CIDS [44]. It is worth noting that the temporal input signal is split separately and multiplied with a reference signal from a PEM modulated at a frequency of f = 50 kHz, along with a 90° phase-shifted copy of it. Due to the limitation of NIS Elements software, the phase is shifted to the second channel to obtain the absolute data, which can be further processed by subtracting the first channel from the second one. The results of polarization-resolved microscopy are interpreted using the MM formalism, where the polarization characteristics of the sample are analyzed in terms of its linear birefringence and circular dichroism signatures corresponding to the detected signal [44, 47]. The interpretation of the results is validated by statistical analysis of samples, including normalization of the intensity values and calculation of the mean and STD for all pixels within a ROI in both R and θ images.

2.5.2.4 Image processing

The retrieved modulation R simply normalized, $R_N(x, y)$ for each pixel by the maximum value and positive/negative phase ($\theta^{\pm}$) then normalized θ_N by the STD multiplied with the maximum of θ as follows:

$$R_N(x, y) = \frac{R\,(x,y)}{R_{max}(x,y)} \tag{2.34}$$

$$\theta_N = \frac{\theta}{std * max(\theta)} \tag{2.35}$$

A MATLAB routine is used to manually determine the background by drawing an arbitrary polygon over the image. The intensities of all pixels in the image are then subtracted from the average intensity of the pixels corresponding to the background. This process helps remove the gradient caused by the inhomogeneous intensity FOV for both the normalized phase and modulation. The resulting phase and modulation data are presented as 2D images and subjected to phasor analysis. Additionally, thresholds for modulation and phase are determined to enable data segmentation, with different colors representing different segments within the ROI.

2.5.2.5 Image phasor analysis

The phasor of polarized modulated signal $I(t)$ pixel-by-pixel provides a 2D graphical view of the demodulated signal at reference frequency in terms of amplitude and phase distributions. The phasor coordinates (g, s) related to the product of the intensity of the demodulated first harmonics via Fourier transform of the signal by sine and cosine terms for each pixel, as the modulation (R) and phase (θ) values, by the trigonometric relations (Equations 2.36 and 2.37).

In our case, the modulation and phase for each pixel are supplied via Lock-in Amplifier (LA) by the convolution of sine and cosine terms as remarked in the previous section. Sampling then settled corresponding to the pixel-dwell time (20μs) of the signal detector pixel-by-pixel. According to the definition, the phasor associated with the modulated signal has coordinates $g(\omega)$, $s(\omega)$ similar to equations (2.24) and (2.25), are given by

$$g(\omega) = \frac{I(t)\cos(\omega.t)}{max[I(t)]} \tag{2.36}$$

$$s(\omega) = \frac{I(t)\sin(\omega.t)}{max[I(t)]} \tag{2.37}$$

where $\omega = 50$ kHz is the modulation angular frequency of the reciprocal time dependent signal used for the Fourier Transform and each frequency dependent component X and Y normalized by maximum $I(t)$ value. The vertical axis $s(\omega)$ shows imaginary and the horizontal one $g(\omega)$ indicates real parts of the first harmonics. The phasor approach defined R between 0 and 1, and φ between 0 and 2π.

2.5.2.6 Polarized-resolved phasor analysis of starch granule

A specimen that exhibits a dependence of refractive index on the polarization propagation direction of light is referred to as birefringent. This property results in a distinctive intensity variation when the light passes through a polarizer. The combination of an image phasor approach with MM has already demonstrated its potential in studying biological birefringent materials like collagen and myosin fibers. This approach provides a direct interpretation and polarization fingerprint of retardance images, revealing structural information about the sample without the need for modeling. Previous studies have shown the effectiveness of this method in samples with low dichroic and depolarizing (scattering) components [80].

In this section, dichroism and birefringence in starch granules are investigated using an incomplete MM microscopy approach combined with the image phasor map. The aim of the assessment is to determine the polarimetric contrast to evaluate the sensitivity of the imaging technique. Starch granules are composed of living particles that possess unique structures known as amylopectin, which contribute to their distinctive optical activity characterized by anisotropy, polarization, and depolarization effects. Advanced microscopy techniques, including scanning electron microscopy (SEM), SHG microscopy, and atomic force microscopy (AFM), have been employed to study the molecular structure of starch granules [81, 82, 83]. It has been demonstrated that the positive birefringence exhibited by starch granules, along with their radial alignment of crystallinity, allows for direct inference of their molecular symmetry through polarization analysis.

The optical structure of starch granules, with its diverse optically active regions, presents intriguing properties suitable for our phasor approach. This enables the capture of imaging polarimetric contrast across the entire FOV and facilitates 2D imaging segmentation to indicate phase and modulation characteristics. The sensitivity and recognition of molecular formations in different microscopic regions are evaluated by examining our microscopy method and analysis approach using well-known starch granules. The results, as depicted in Fig. (2.22), shows a pixel-by-pixel assessment of various microscopic regions.

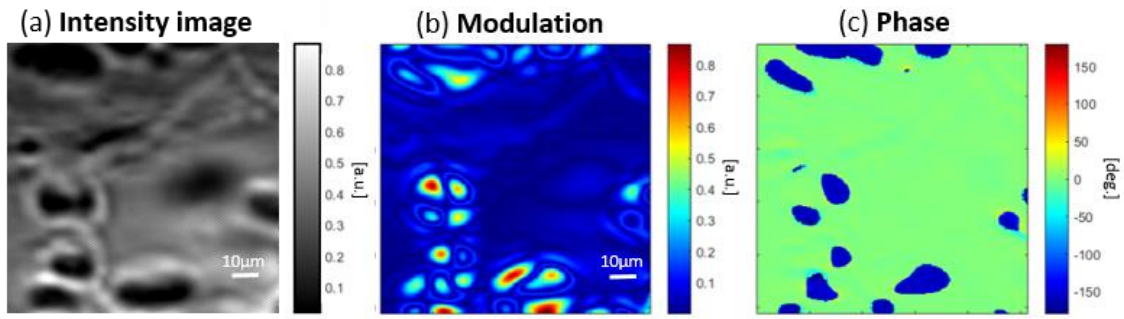

Figure 2.22. (a) The total intensity (absorption) image of starch granules is compared to (b) the corresponding module polarization-resolved image. (c) The 2D phase microscopy images of starch granules are displayed, with the color scale indicating the values of the parameters.

The intensity microscopy image represents the total intensity or absorption of the starch granules. On the other hand, the corresponding polarization-resolved modulation and phase images of the starch granules provide additional information about the polarization characteristics of the granules.

In Figs. (2.23 a), (2.23 b), and (2.23 c, d), the phasor approach is employed as a tool for tracking a specific region of the sample through the segmentation of the phasor plot. It should be noted that the variations in shape and size of the starch are associated with different degradation conditions of the sample caused by external factors such as temperature fluctuations. The phasor analysis resulted in a cluster of points, with each point corresponding to a pixel in the polarization-resolved image and represented by its normalized modulation amplitude and phase. Based on the image phasor map, elongated modulations are observed at 0º and around 210º, intersected by a cluster of points with a circular shape at a certain threshold radius of less than 0.2.

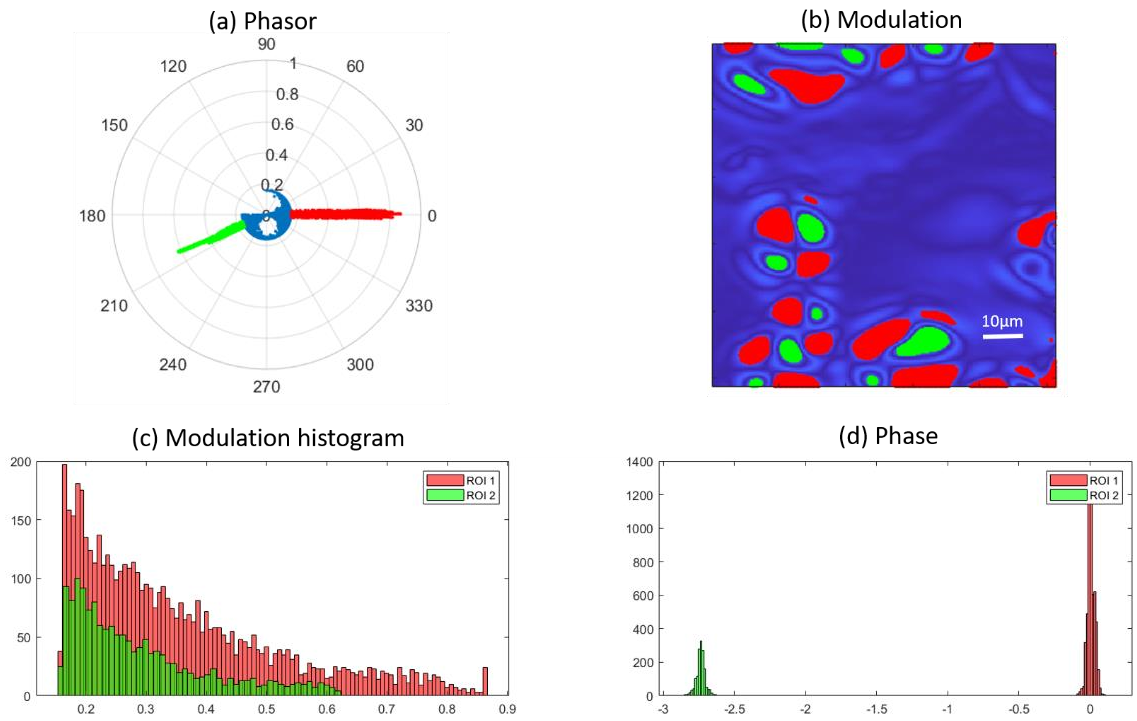

Figure 2.23. (a) Segmentation of different regions in phasor map graph and (b) Corresponding 2D modulation image. (c, d) Histogram of different regions of interest marked by green and red colors for modulation and phase effects.

The quadrature birefringent regions in starch are correlated with the red and green parts, while the blue part represents the background. It is evident that the modulation effect is minimal within the radius of the blue circle-like phasor, and maximum within the crystalline granule structures. The abundance histogram of the image is also calculated in terms of modulation and phase, revealing the dominant role of modulation at 0º compared to the modulation at around 210º. In previous literatures, there has been a lack of clear determination regarding the chirality of starch crystals. However, in this study, a preference for left circular polarization emission is observed. The observed optical responses are derived from the organization of the double helical amylopectin chains within the crystalline layers of starch granules. The variations in modulation R and phase are dependent on the birefringence and crystal orientation of the starch granules, which exhibit characteristics of uniaxial materials. Due to the limitations in the number of channels for data acquisition directly by the lock-in amplifier in their developed polarization-resolved imaging setup, one of the two intensities split by the Wollaston prism is selectively detected, instead of capturing the differential signal from both intensities. Additionally, due to the differences in the helicity of the amylopectin chains, they appear to exhibit the preferential emission of left circularly polarized light.

2.5.2.7 Polarized-resolved phasor analysis of progeria vs normal cell nuclei

It was reported that the polarization-resolved light is sensitive to a long-range organization of chiral structures like chromatin [22]. Therefore, in order to investigate chromatin compaction as highly chiral material inside a normal isolated HEK 293 cell nuclei, the circular polarization resolved microscopy method has been integrated with a homemade confocal fluorescent microscope similar to the one reported in our previous works [44, 47]. A new paradigm is presented here, utilizing image phasor map analysis as a robust and effortless tool for distinguishing between progeria and normal HEK cell nuclei. This distinction is based on differences in chromatin compaction, spatial organization of chromatin within the nuclei, and deformation of the lipid double membrane that surrounds the nuclear genetic material. The changes in birefringence and dichroism can be easily discerned through a simple graphical representation, where each pixel of the image is mapped into the reciprocal frequency space.

The ultimate goal is to directly observe the differentiation of normal cells from progeria images, pixel-by-pixel, using the image phasor map approach. The samples, labeled with Hoechst, indicate the presence of DNA-based molecules exclusively within the nuclear membrane. Fig. (2.24) displays the 2PEF and polarization-resolved microscopy images of microspheres, serving as references for HEK cell nuclei and progeria, respectively. The fluorescence images are employed to identify the ROI and present the results of modulation and phase microscopy. Additionally, results are provided for fluorescent 15 μm beads, serving as a baseline reference for polarization measurements and the corresponding modulation and phase images.

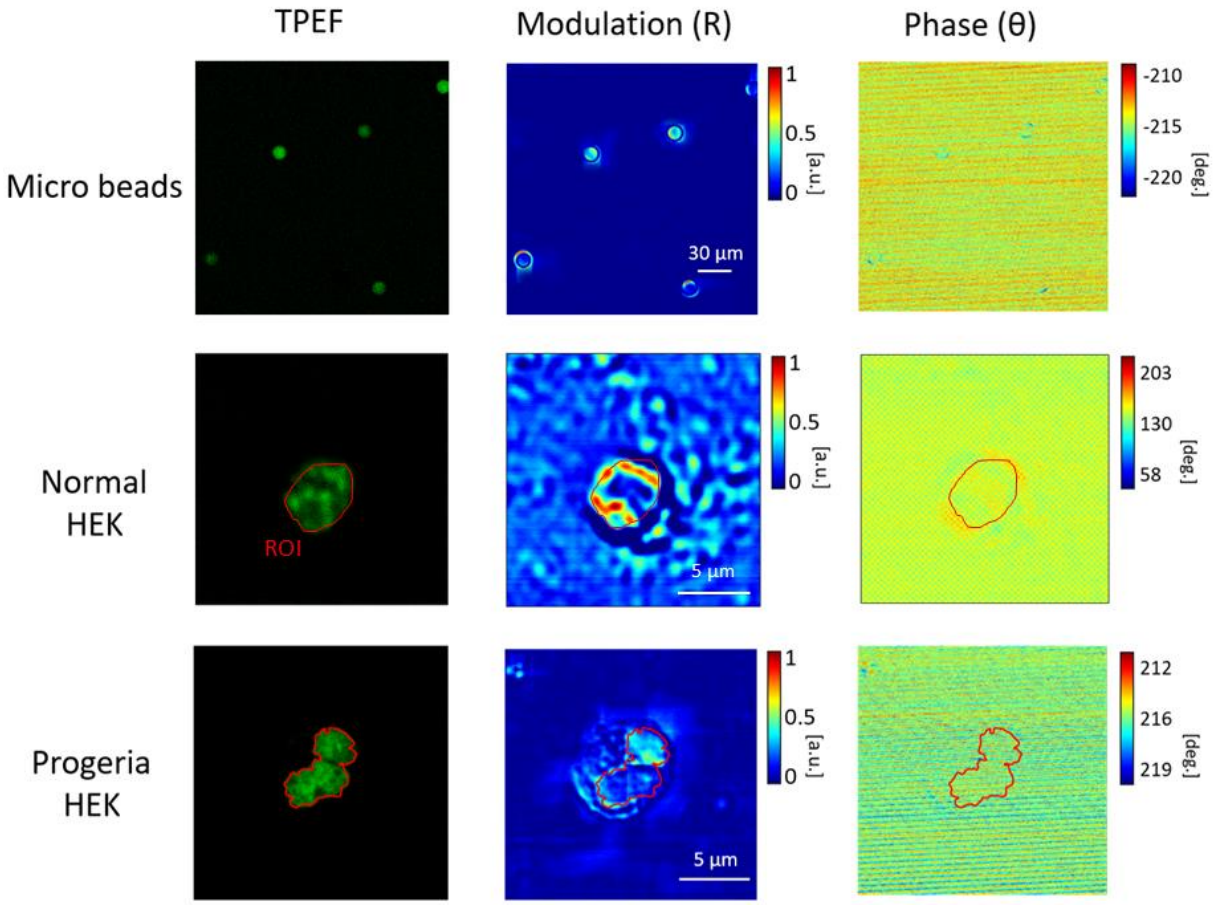

Figure 2.24. Fluorescence images of microbeads as reference, the isolated normal HEK nucleus and progeria HEK syndrome compared to corresponding polarimetric modulation and phase images.

Consequently, it is demonstrated that the modulation in progeria HEK cells is weaker compared to normal cells. The situation worsens when analyzing phase images, as the phase image of progeria almost disappears due to minor optical phase changes within the nuclei. This critical factor enables the discrimination of normal HEK cells from progeria on the phasor map representation. The contrast in terms of modulation and phase images is significantly reduced, owing to the less compacted chromatin within the deformed shape of the nuclear membrane, resulting in stronger scattered light emitted by the distorted cell structure. The background is subtracted from the polarimetric images in order to eliminate artifacts and background effects. Thus, the process is focused only on the modulation and phase of ROI associated with the nuclei of normal and progeria cells. Subsequently, the values of each pixel in the modulation and phase images are normalized based on the image phasor map, as depicted point-by-point in Fig. (2.25).

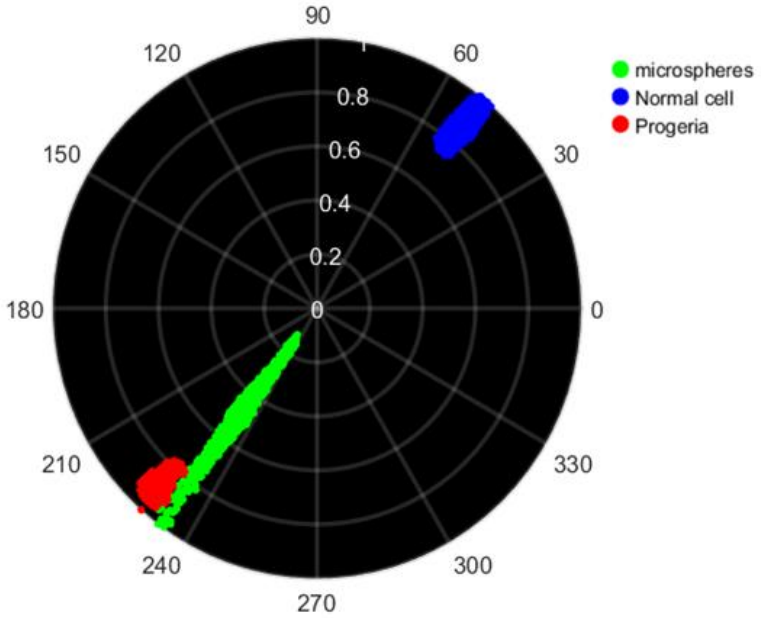

Figure 2.25. Image phasor map of microspheres as reference, control normal HEK cell data compared to progeria HEK cell syndrome discriminated by green, blue and red respectively.

The differences between progeria and normal cells, in terms of chromatin condensation and nuclear membrane morphology deformation, can be discerned using the image phasor map. These differences are evident in the phase and modulation changes, which are normalized based on the maximum values. The modulation R of the reference microspheres shows elongation from nearly 0.2, representing the threshold of the background region, up to 1. The phase θ is non-zero, as illuminating edge effects dominate the modulation and phase variations in perfect isotropic spherical particles. It should be emphasized that the phasor analysis relies solely on the polarimetric signal, and variations resulting from different fluorescent types have negligible impact on the image phasor. The statistical analysis aimed to assess the sensitivity of the phasor approach for discrimination is shown in Fig. (2.26).

The amplitude modulation and phase is measured directly by lock-in amplifier. This is achieved using a dual-phase demodulation process. The input signal is split and separately multiplied with the reference signal and a 90 degrees phase-shifted copy of it. The outputs results in s and g, termed the in-phase and quadrature component. The amplitude and the phase are easily derived from s and g by a transformation from Cartesian coordinates into polar coordinates. In terms of amplitude modulations, it is observed from Fig. (2.25) that the normal HEK exhibits higher modulation compared to progeria, despite the minimal phase differences between them. This highlights the significance of amplitude modulation, similar to the use of phasors in FLIM or super-resolution imaging, where phase modifications are trivial and amplitude modulation plays a crucial role. Moreover, the standard deviations are different for both types of cells just by considering their shape. Normal HEK cells are uniformly round, while progeria cells exhibit more diverse shapes.

Therefore, discrimination between the two cases can be achieved without relying only on significant phase differences. Consequently, even in the presence of pi-dephasing artifacts, the modulation effect remains reliable for discrimination.

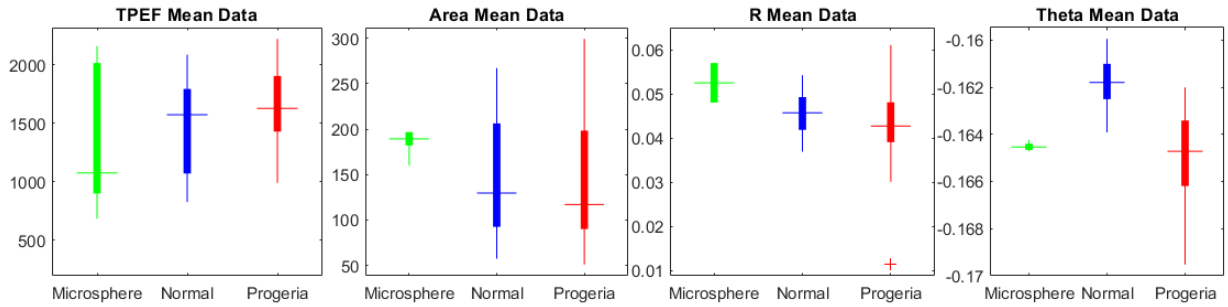

Figure 2.26. The statistical analysis to assess the sensitivity of the phasor approach for discrimination. The size of the nucleus, 2PEF intensities, mean values of modulation and phase, as well as their corresponding skewness and kurtosis, are considered. The results indicated a higher sensitivity for phase compared to modulation, as the phase is directly linked to retardance.

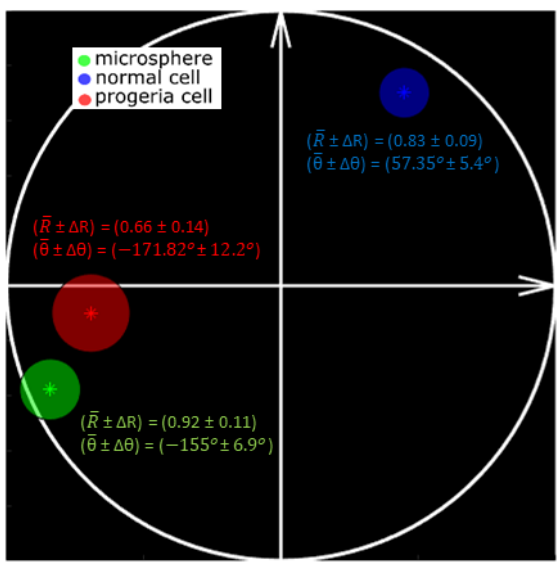

Figure 2.27. Image phasor map analysis on the statistical information out of microspheres as reference, normal HEK cell and progeria HEK syndrome determined by green, blue and red circles. The center of each represents mean value and the radius shows the STD.

The size distribution is observed to be more dispersed in progeria cells compared to normal cells, indicating a greater diversity in the shapes of progeria nuclei. In the case of 2PEF, the distribution exhibits more differences between normal and progeria nuclei, as the asymmetric 3D shape of progeria results in a loss of fluorescence signal. This poses a greater challenge in obtaining consistent fluorescence throughout the entire cell, compared to normal cells.

The results suggest that the random 3D distribution in progeria nuclei reduces the quality of circular polarization in the illumination PSF. Therefore, it is recommended to focus on the mean value, as it offers better discrimination between normal and progeria cells. The phasor plot in Fig. (2.27) presents the averaged analysis of 30 isolated progeria images and an equal number of normal cell nuclei. By applying the image phasor approach to normalized modulation R and phase, the graph clearly separates the phasor of normal cells from progeria cells based on mean values. The radius of the colored phasors represents the STD for each group.Thus, the image phasor analysis allows for the distinct separation of normal cell and progeria nuclei. The dispersion is significantly higher in progeria cells compared to control normal samples and the microsphere reference.

To conclude the discussion, while the need for non-parametric clustering approaches is acknowledged to enhance the value of this work, in this preliminary work, the results were constrained by the project's specified time frame. The limited duration allowed for setup upgrades, experimental implementation, simulations, and analytical calculations. Therefore, this work serves as a foundation for future implementations of non-parametric clustering approaches and classification methodologies. These future endeavors aim to generate comprehensive comparative results and explore real-time modality scanning.

2.6 Conclusion

In this chapter, the discussion commenced with an exploration of chromatin, a complex structure comprising the DNA double helix and proteins localized within cell nuclei. The two forms of chromatin, euchromatin and heterochromatin, exhibit distinct characteristics. Euchromatin is characterized by reduced condensation and a higher transcriptional potential, whereas heterochromatin is highly compacted and displays limited transcriptional activity. The encoding of genetic instructions governing essential cellular processes, such as development, functioning, growth, and reproduction, relies on the fundamental role fulfilled by chromatin. Understanding chromatin compartments as chiral-group structures is of utmost importance, as it enables the identification of gene expression-enriched regions influenced by varying degrees of chromatin compaction. This comprehensive understanding significantly impacts gene regulation and the precise control of cell specialization throughout the intricate process of cell differentiation.

A range of optical microscopy and spectroscopy techniques can be employed to detect these organizations. Optical microscopy employs visible light to observe biological samples, while spectroscopy methods analyze the interaction between light and matter to gather insights regarding the composition and structure of the sample. Among them, super-resolution fluorescence microscopy is a powerful method used to detect individual molecules in biological structures and processes, making it invaluable for cell and tissue imaging. However, the high cost and bulky nature of the required equipment limit its accessibility to many laboratories. Additionally, accurately measuring the compaction level, medium structure, and molecular orientation within chromatin necessitates a new contrast dimension to uncover hidden information, such as polarization-sensitive data. Polarization-based imaging techniques offer non-invasive label-free contrasts that can reveal polarimetric hidden information, showing great promise in biological applications.

The use of MM polarimetry allows for a comprehensive understanding of a sample's polarimetric response. However, the interpretation of the full MM becomes challenging when dealing with complex biological media at a sub-microscopic scale due to a low SNR caused by weak absorption and strong scattering. Additionally, the presence of diverse structures within a confined volume adds further complexity to the analysis. To overcome these challenges, researchers have focused on investigating specific elements of the MM that exhibit greater sensitivity to the unique configurations of the medium. CD, which measures the difference in absorbance and scattering between left and right circularly polarized light, is a widely studied element. The specific signal, known as CIDS, is typically observed outside the absorption band and/or at non-zero scattering angles.

Polarized light scanning microscopy techniques, such as CIDS, are non-invasive modalities that enhance contrast and facilitate the investigation of anisotropic specimens and chiral organizations. The use of CIDS imaging to monitor modifications in chromatin and membrane morphology are

discussed and validated. It is demonstrated that the CIDS microscopy imaging modality, which is based on the polarization effect, provides a simple and non-invasive label-free technique for identifying cell types that exhibit different circular dichroism influence, such as murine cells. The method is combined into a confocal fluorescence optical microscope, and data are analyzed using statistical methods to validate the conclusion. The bimodal imaging method is employed on human and mouse cells, and the cells are analyzed by segmenting optically active regions based on the threshold of the normalized intensity signal images. The identified mouse cells are verified by comparing the fluorescent images with the corresponding CIDS images in a sectioning manner. The CIDS images predominantly provide information about the cell membrane morphology of intact cells. The combination of both modalities yields complementary information at the cellular level. It is indicated that rodent cells can be easily distinguished by their membrane morphology without the necessity of labeling or post-cellular treatments. This approach provides complementary information at the cellular level and paves the way for a non-invasive classification method with direct identification of healthy and diseased cells in tissues and solid tumors in a clinical environment.

The spectroscopic one-point measurement configuration to study biological macromolecule aggregates is illustrated as the first and most common application of CIDS. In this configuration, a certain portion of the sample is illuminated, and data is collected at different light scattering angles using a detector mounted on a rotating mechanical arm. The application of this modality in studying chromatin conformation in an aqueous buffer is discussed. However, it was found that such arrangements are insensitive to the confined blend of structures within the illumination volume. To address this issue, the phasor approach, an analytical method, is introduced. This approach provides a simple and intuitive graphical representation for interpreting the polarimetric properties of a sample in microscopy modalities. The combination of CIDS and some other elements of MM with the phasor approach is represented to interpret the results in terms of the two significant characterizations of samples: birefringence and dichroism. This interpretation does not require any pre-knowledge of formalism or special post-processing skills. The modulated signal from reference optically active materials is simulated, and the data are analyzed graphically using the phasor map approach. A comparison is made with experimental data for the first time. It is demonstrated that the phasor map allows us to understand the contribution of different MM elements at a single point on samples and visualize the overall phasor map as a result of those elements. The application of the phasor approach to bio-samples, such as isolated nuclei, shows sensitivity in discriminating between linear birefringence, circular dichroism, and facilitated fast interpretation of the analysis. The least reliable SNR of a modulated signal is also estimated and graphically represented on the phasor map.

The application of the phasor approach is extended from CIDS single-point spectroscopy to implement polarization-resolved microscopy imaging, enabling the visualization of polarimetric contrasts in localized regions for a better understanding of isolated cell nuclei. The combination of the image phasor with the complete MM has already been demonstrated for studying biological birefringent materials. In this work, the focus is on studying incomplete MM microscopy

specifically for dichroism using the image phasor map. Hutchinson-Gilford progeria syndrome is investigated through polarization-resolved microscopy imaging using the phasor map data analysis, which is of great interest in the field of biomedical diagnosis. The polarimetric imaging method is integrated into a confocal fluorescent optical microscope, and data are analyzed using statistical methods for multiple trials. The results are graphically represented by the image phasor map based on birefringence and dichroism effects. The application of the introduced phasor approach to chiral biosamples allows for the discrimination between normal HEK cells and progeria syndrome based on chromatin compaction and nuclei morphology deformations using multimodal optical scanning microscopy. The phasor approach is proposed as a possible and complementary representation tool that is sensitive to the polarization effect and can be applied in conjunction with other analytical techniques. The phasor map approach holds potential for future applications in *in-situ* and remote diagnosis of pathologies and diseases, which could aid in histopathological evaluation.

Based on this preliminary work, a detailed interpretation of the phasor approach is not pursued, and the manuscript does not currently include a classification methodology for clustering the phasor map. A clustering approach would provide a means to group and classify data points within the phasor map based on their similarities or patterns. This would enhance the analysis and interpretation of the polarimetric data obtained through the phasor approach and would enable us to gain a deeper understanding of the underlying characteristics and relationships present in the phasor map. In this way, a systematic framework will be provided for organizing and interpreting the polarimetric data, potentially revealing new insights and correlations between different polarization effects and sample properties. Therefore, it is believed that further studies should be conducted to explore and integrate a clustering approach as an outlook of this work.

References

[1] R. Kornberg and Y. Lorch, "*Twenty-five years of the nucleosome, fundamental particle of the eukaryote chromosome*," Cell, vol. 98, p. 285–294, 1999.

[2] H. Phan, et al., "*ChromEMT: Visualizing 3d chromatin structure and compaction in interphase and mitotic cells*," Science, vol. 357, p. 285–294, 2017.

[3] L. Schermelleh, et al., "*Super-resolution microscopy demystified*," Nature Cell Biology, vol. 21, p. 72–84, 2019.

[4] S. Huard, Polarization of Light, New York, NY, USA: 1st ed.; John Wiley & Sons Inc., 1997.

[5] H. Mueller, "*The foundations of optics*," J. Opt. Soc. Am., vol. 38, p. 661–662, 1948.

[6] B. Ranjbar and P. Gill, "*Circular Dichroism Techniques*," Biomolecular and Nanostructural Analyses- A Review, p. 101–120, 2009.

[7] A. Diaspro and C. A. Nicolini, "*Circular intensity differential scattering and chromatin-DNA structure*," Cell Biophysics, vol. 10, p. 45–60, 1987.

[8] E. Huber, et al., "*Polarization modulation ellipsometry: A compact and easy handling instrument*," Rev. Sci. Instruments, vol. 56, p. 2222–2227, 1985.

[9] M. Maestre, et al., "*Circular dichroism studies on single Chinese hamster cells*," Biochemistry, vol. 24, p. 5152–5157, 1985.

[10] W. Xiao, et al., "*Microscopic origin of chiral shape induction in achiral crystals*," Nature Chemistry, vol. 8, no. 4, p. 326–330, 2016.

[11] J. Hansen, "*Human mitotic chromosome structure: what happened to the 30-nm fibre?*" The EMBO Journal. , vol. 31, no. 7, p. 1621–1623, 2012.

[12] K. Maeshima, et al., "*Dynamic chromatin organization without the 30-nm fiber*," Current opinion in cell biology, vol. 58, p. 95–104, 2019.

[13] C. Seiwert, "*Human Biology: An Exploration of Structure and Function*," Pearson Education Inc, 2019.

[14] G. M. Donald, et al., "*Circular dichroism spectroscopy of DNA*," Methods in enzymology, vol. 211: p. 389-406, 1992.

[15] A. Sharma, et al., "Circular Intensity Differential Scattering Reveals the Internal Structure of Polymer Fibrils," The J. of Phys. Chem. Lett., vol. 10(24): p. 7547-7553, 2019.

[16] B. Schrader, ed. "*Infrared and Raman spectroscopy: methods and applications*," John Wiley & Sons, 2008.

[17] J. C. Kemp, "*Piezo-optical birefringence modulators: New use for a long-know effect*," J. Opt. Soc. Am., vol. 59, p. 950–954, 1969.

[18] S. N. Jasperson and S. E. Schnatterly, "*An improved method for high reflectivity ellipsometry based on a new polarization modulation technique*," Review of Scientific Instruments, vol. 40, p. 761–767, 1969.

[19] A. Le Gratiet, et al., "*Circular Intensity Differential Scattering for Label-Free Chromatin Characterization, A Review for Optical Microscopy*," Polymers, vol. 12, p. 24-28, 2020.

[20] R. Oldenbourg and P. Török, "*Point-spread functions of a polarizing microscope equipped with high -numerical-aperture lenses*," Appl. Opt. , vol. 39, p. 6325–6331, 2019.

[21] D. Keller, et al., "*Imaging of optically active biological structures by use of circularly polarized light*," Proc. Natl. Acad. Sci., vol. 82, p. 401–405, 1985.

[22] L. Finzi, et al., "*Differential polarization imaging. V. numerical aperture effects and the contribution of preferential scattering and absorption to the circular dichroism images*," Biophys. J., vol. 59, no. 6, p. 1183–1193, 1991.

[23] D. Rouède, et al., "*Theoretical and Experimental SHG Angular Intensity Patterns from Healthy and Proteolysed Muscles*," Biophysical Journal, vol. 104 (9), p. 1959-1968, 2013.

[24] A. Rodger, "*Encyclopedia of Biophysics*," In: Roberts, G.C.K. (eds), Springer, Berlin, Heidelberg. p. 2714–2718, 2013.

[25] M. Kim, et al., "*Differential Polarization Imaging I: Theory and Applications*," Polariz. Spectrosc. Ordered Syst., vol. 242, p. 313–356, 1987.

[26] M. Kim and C. Bustamante, "*Differential polarization imaging. IV. Images in higher Born approximations*," Biophys. J., vol. 59, p. 1171–1182, 1987.

[27] C. J. R. Sheppard and D. Shotton, Confocal Laser Scanning Microscopy. In Confocal Laser Scanning Microscopy, 1st ed., New York, NY, USA: Garland Science, 1997.

[28] E. A. Martin, Macmillan Dictionary of Life Sciences (2nd ed.), London: Macmillan Press., 1983.

[29] H. Collins, Collins Dictionary of Human Biology. Glasgow: Youngson RM, 2006.

[30] A. Rangarajan and R. A. Weinberg, "*Comparative biology of mouse versus human cells: modelling human cancer in mice*," Nat Rev Cancer, vol. 3, p. 952–959, 2003.

[31] R. Holliday, "*Neoplastic transformation: the contrasting stability of human and mouse cells*," Cancer Surv., vol. 28, p. 103–115, 1996.

[32] S Rana, et al., "*Array-Based Sensing of Metastatic Cells and Tissues Using Nanoparticle–Fluorescent Protein Conjugates*," ACS Nano , vol. 6, no. 9, p. 8233-8240, 2012.

[33] A. Strebel, et al., "*Green fluorescent protein as a novel tool to measure apoptosis and necrosis*," Cytometry Part A, vol. 43, no. 2, pp. 126-133, 2001.

[34] S. Standring, "*Basic structure and function of cells*," in Gray's Anatomy (Forty Second edition), Elsevier Limited, 2018.

[35] F. M. Boisvert, et al., "*The multifunctional nucleolus*," Nat Rev Mol Cell Biol, vol. 8, no. 7, p. 574-85, 2007.

[36] A. Cornea and P. M. Conn, Fluorescence Microscopy: Super-Resolution and other Novel Techniques, Academic Press, 2014.

[37] K. M. Twietmeyer, "*Mueller matrix retinal imager with optimized polarization conditions*," Opt. Express, vol. 26 , no. 16, p. 21339–21354, 2008.

[38] A. Le Gratiet, et al., "*Review on Complete Mueller Matrix Optical Scanning Microscopy Imaging*," Appl. Sci., vol. 11, no. 1632, 2021.

[39] N. Mazumder, et al., "*Mueller matrix signature in advanced fluorescence microscopy imaging*," J. Opt. , vol. 19, no. 2, p. 025301, 2017.

[40] A. Fernández-Pérez, et al., "*Polarimetric Detection of Chemotherapy-Induced Cancer Cell Death*," Appl. Sci., vol. 9, p. 2886, 2019.

[41] X. Li, et al., "*Classification of morphologically similar algae and cyanobacteria using Mueller matrix imaging and convolutional neural networks*," Appl. Opt., vol. 56, p. 6520-6530, 2017.

[42] C. T. Gregg, et al., "*Rapid Microbial Identification by Circular Intensity Differential Scattering*," in Rapid Methods and Automation in Microbiology and Immunology, Berlin Heidelberg, Springer-Verlag, 1985.

[43] A. Le Gratiet, et al., "*Scanning Mueller polarimetric microscopy*," Opt. Lett., vol. 41, no. 18, p. 4336–4339, 2016.

[44] A. Le Gratiet, et al., "*Circular intensity differential scattering (CIDS) scanning microscopy to image chromatin-DNA nuclear organization*," OSA Contin., vol. 1, no. 3, p. 1068–1078, 2018.

[45] W. Schormann, et al., "*Tracking of human cells in mice*," Histochem cell biol., vol. 193, no. 2, p. 329-338, 2008.

[46] A. T. Norton and O. Zehner, "*Which Half is Mommy? Tetragametic Chimerism and Trans-Subjectivity*," WSQ, vol. 36, no. 3, p. 106-125, 2008.

[47] R. Marongiu, et al., "*ExCIDS: a combined approach coupling Expansion Microscopy (ExM) and Circular Intensity Differential Scattering (CIDS) for chromatin-DNA imaging*," OSA Continuum, vol. 3, no. 7, p. 1770-1780, 2020.

[48] M. A. Digman, et al., "*The phasor approach to fluorescence life time imaging analysis*," Biophys. J., vol. 94, p. L14–L16, 2007.

[49] F. Fereidouni, et al., "*Spectral phasor analysis allows rapid and reliable unmixing of fluorescence microscopy spectral images*," Opt. Express, vol. 20, p. 12729–12741,, 2012.

[50] L. Scipioni, et al., "*Phasor Analysis of Local ICS Detects Heterogenity in Size and Number of Intracellular Vesicles*," Biophys. J., vol. 111, p. 619–629, 2016.

[51] L. Scipioni, et al. "*Local raster image correlation spectroscopy generates high-resolution intra celular diffusion maps*," Commun. Biol., vol. 1, p. 1-10, 2018.

[52] L. Lanzanò, et al., "*Encoding and decoding spatio-temporal information for super-resolution microscopy*," Nat. Commun. , vol. 6, p. 1-9, 2015.

[53] M. J. Sarmento, et al., "*Exploiting the tunability of stimulated emission depletion microscopy for super-resolution imaging of nuclear structure*," Nat. Commu., Vols. 1-11, 2018.

[54] C. Bustamante, et al., "*Circular differential scattering can be an important part of the circular dichroism of macromolecules*," PANS, vol. 80, no. 12, p. 3568-3572, 1983.

[55] M. Maestre, et al., "*Circular Dichroism Studies on Single Chinese Hamster Cell*," Biochemistry, vol. 24, no. 19, p. 5152–5157, 1985.

[56] A. Mohebi, A. Le Gratiet, et al., "*Combined approach using circular intensity differential scattering microscopy under phasor map data analysis*," Appl. Opt. 60, vol. 60, p. 1558-1565, 2021.

[57] S. Y. Lu and R. A. Chipman, "*Interpretation of Mueller matrices based on polar decomposition*," J. Opt. Soc. Am. , no. A13, p. 1106–1113, 1996.

[58] A. L. F. Livolant, "*Condensed phases of DNA: Structures and phase transitions*," Prog. Polym. Sci., vol. 21, no. 6, p. 1115–1164, 1996.

[59] C. J. Bustamante, "*Circular Intensity Differential Scattering of chiral molecules*," Ph.D Thesis, California Univ., Berkeley, 1980.

[60] Q. S. Hanley and A. H. A. Clayton, "*AB-plot assisted determination of fluorophore mixtures in a fluorescence lifetime microscope using spectra or quenchers*," J. Microsc., vol. 218, p. 62-67, 2005.

[61] O. Arteaga, et al., "*Circular dichroism with multiple photoelastic modulators*." Chim. Oggi vol. 30, p.6-9, 2012.

[62] K. J. Gåsvik, "*Optical Metrology (3rd ed.),*" John Wiley and Sons, p. 219–221, 2003.

[63] C. Weast, "*CRC Handbook of Chemistry and Physics (62nd ed.),*" FL: CRC Press, p. C-110, 1981.

[64] T. Mondal, et al., "*Characterization of the RNA content of chromatin*," Genome Res., vol. 20, no. 7, p. 899–907, 2010.

[65] D. Zink, et al., "*Nuclear structure in cancer cells*," Nat. Rev. Cancer, vol. 4, no. 9, p. 677–687, 2004.

[66] H. D. Ou, et al., "*ChromEMT: Visualizing 3D chromatin structure and compaction in interphase and mitotic cells,*" Science, vol. 357, p. 285–294, 2017.

[67] F. Radaelli, et al., "*μMAPPS: a novel phasor approach to second harmonic analysis for in vitro-in vivo investigation of collagen microstructure*," Sci. rep., vol. 7, no. 17468, 2017.

[68] N. Gilbert, et al., "*Chromatin architecture of the human genome: gene-rich domains are enriched in open chromatin fibers*," Cell, no. 118, p. 555–566, 2004.

[69] K. L. Huisinga and B. Brower-Toland, S. C. R. Elgin, "*The contradictory definitions of heterochromatin: transcription and silencing*," Chromosoma, no. 115, p. 110–122, 2006.

[70] V. S. Miller, Neurocutaneous Disorders, Cambridge University Press, 2004.

[71] V. V. Ashapkin, et al. "*Are There Common Mechanisms Between the Hutchinson–Gilford Progeria Syndrome and Natural Aging?"* Front. Genet, vol. 10: 455, 2019.

[72] K. Hsiao, "*Advances in Clinical Chemistry*," Academic Press, vol. 33, p. 10, 1998.

[73] M. Eriksson, et al., "*Recurrent de novo point mutations in lamin A cause Hutchinson–Gilford progeria syndrome*," Nature, vol. 423, p. 293–298, 2003.

[74] C. Flores, "*DNA and chromatin imaging with super-resolution fluorescence microscopy based on single-molecule localization*," Biopolymers, vol. 5, no. 95, p. 290-7, 2011.

[75] S. Ippolito, "*Polarized high-resolution imaging*," Nature Photonics, vol. 2, p. 273–274, 2008.

[76] O. Arteaga and A. Canillas, "*Measurement of the optical activity of anisotropic samples by transmission Mueller matrix ellipsometry*," Polariz. Meas. Anal. Remote Sens., vol. XI, no. B, p. 9099, 2014.

[77] A. Le Gratiet, et al., "*Zebrafish structural development in Mueller-matrix scanning microscopy*," Sci. Rep., vol. 9, p. 1–10, 2019.

[78] E. Huber, et al., "*Polarization modulation ellipsometry: A compact and easy handling instrument*," Rev. Sci. Instruments, vol. 56, p. 2222–2227, 1985.

[79] A. Mohebi, et al., "*Phasor map analysis to investigate Hutchinson–Gilford progeria cell under polarization-resolved optical scanning microscopy*," Sci. Rep., vol. 12, no. 1679, 2022.

[80] A. Le Gratiet, et al., "*Phasor approach of Mueller matrix optical scanning microscopy for biological tissue imaging*," Biophysical Journal, vol. 120, issue 15, p. 3112-3125, 2021.

[81] J. L. Jane, et al., "*Anthology of Starch Granule Morphology by Scanning Electron Microscopy*," Wiley, vol. 46, no. 4, p. 121-129, 1994.

[82] Z. Y. Zhuoa, et al., "*Second harmonic generation imaging – A new method for unraveling molecular information of starch*," Journal of Structural Biology, vol. 171, no. 1, p. 88-94, 2010.

[83] M. J. Ridout, et al., "*Using AFM to image the internal structure of starch granules*," Carbohydrate Polymers, vol. 50, no. 2, p. 123-132, 2002.

Chapter 3

Polarization-resolved two-photon excitation laser scanning microscopy of colon cancer cells

3.1 Introduction

Early cancer diagnosis has become a vital component of disease prevention in modern healthcare. Detecting cancer at an early stage not only improves patient health and treatment prognosis but also reduces the financial impact on healthcare systems [1]. The early stages of cancer are typically identified through small changes in cellular morphology and metabolism, using current non-invasive screening techniques.

To develop diagnostic tools, it is necessary to define measurable parameters as biomarkers for specific diseases. Cancer screening modalities make use of various biomarkers. Diffuse optical tomography relies on biomarkers such as hemoglobin concentration, oxygen saturation, blood flow, and tissue scattering properties. Photoacoustic imaging utilizes biomarkers like hemoglobin concentration, oxygen saturation, melanin, and specific contrast agents. Multiphoton microscopy employs biomarkers such as sub-cellular morphology and fluorescence signals from targeted probes. Radiologic modalities utilize biomarkers like tumor size, shape, density, and metabolism. Optical spectroscopy focuses on biomarkers such as tissue optical properties, metabolic changes, and molecular signatures [2]. These biomarkers play a crucial role in detecting and characterizing cancer during screening.

Among the technologies, biophotonic imaging methods have demonstrated significant potential for non-invasive, real-time tissue classification [3, 4, 5]. While one-photon fluorescence (1PEF) microscopy has become the gold standard tool, nonlinear excitations, especially with near-infrared

excitation wavelengths, offer advantages in terms of reduced scattering in tissues, enabling deeper imaging in thick samples. Additionally, these nonlinear excitation techniques provide intrinsic spatial resolution while minimizing out-of-plane photobleaching and phototoxic effects. Specifically, multiphoton microscopy (MPM) and multiphoton laser scanning microscopy (MPLSM) have emerged as dynamic and fruitful fields that offer multiple contrast mechanisms, including 2PEF [6, 7, 8]. Fluorescence microscopy has the ability to investigate intricate cellular processes in isolated cells and tissues, offering a high potential for imaging dynamic phenomena at a nanoscale spatial resolution.

Knowledge of molecular orientational information is essential to understanding the interactions that drive the structure and morphology of biomolecular assemblies, from membrane proteins aggregates to biopolymers and in biological functions. Measuring such anisotropy properties in a sample requires retrieving information that is polarization sensitive. In both one- and two-photon excitation scenarios, when a single molecule is excited by linearly polarized light, the highest probability of absorption occurs when its transition dipole moment aligns parallel to the incident polarization [9]. This property, known as angular photo-selection, is at the origin of the polarization dependence of the fluorescence process. Polarized light microscopy (PLM) incorporates the interaction of light with different elements, including spatial fluctuations in scattering media, which cause a loss of intensity coherency. Moreover, the presence of dipolar layered structures induces a phase effect that modifies polarization properties. Consequently, PLM allows for the assessment of parameters such as depolarization, retardance, and optical rotation, which provide insights into molecular structure. These parameters can be employed to differentiate between pathological cells and healthy cells by quantitatively comparing them using suitable tools [10]. The complementary use of light polarization in fluorescence imaging, introduced decades ago to measure molecular orientational behaviors is an evolving field, mostly because of its apparent complexity in terms of technical implementation, like directions of excitation polarization that impose a geometry that does not give access to all possible orientations in an ordered sample. Whereas analyzing the fluorescence light polarization along a given direction is very sensitive to depolarization mechanisms such as energy transfer or scattering of the emitted light in turbid media [11, 12]. Polarized microscopy schemes were initially proposed based on the use of two states of polarization, either on the excitation, detection paths or on both excitation and detection paths to extract fluorescence anisotropy [13, 14, 15]. Accordingly, by the analysis and interpretation of the fluorescence light polarization along given directions, the consequent optical effects of molecular structure in cells can be quantified as a biomarker to determine cancer grades caused by molecular disorders [16, 17].

In this chapter, the research is enhanced by the integration of polarization and fluorescence. This integration offers significant advantages, enabling valuable insights into the orientation of specific molecules. By combining the strengths of both techniques, a more comprehensive understanding of the studied samples could be achieved. To ensure the robustness of tissue models for diagnostic purposes, it is necessary to evaluate them under various controlled environmental influences.

Additionally, it is of interest to compare the diagnostic performance of novel devices to established technologies. In this work, tissue models are created by adapting cancerous cells into spheroids. Multicellular spheroids of the cancerous colon (HT29) are examined as a representative cancerous cell line, while human colon epithelial cells (HCoEpiC) isolated from early passage human colonic tissue are presented as a normal cell line. The evaluation is performed using a 2PEF imaging microscope based on a polarization mechanism. As part of the objectives of this thesis, a custom-made 2PEF scanning microscope with a fixed excitation wavelength in the near-infrared (NIR) has been fully built, and characterized. The microscope is equipped with a fluorescence spectrometer, white light microscopy, and polarization add-ins, which allow for the incorporation of additional polarimetric contrast to enhance structural discrimination. To analyze irregular structures, a stack of 2PEF polarimetric images captured at different angles, either in the excitation or detection modules, is evaluated.

For the data analysis, as the ultimate goal of this thesis, an image phasor approach is introduced with a distinct post-treatment protocol compared to the one introduced in Chapter 2. In this manner, a stack of images of the angular polarimetric fluorescence signal is constructed pixel-by-pixel, which can be plotted in the phasor space to differentiate cancer cells based on the anisotropy effect by directly examining the phasor map. The underlying concept of this work is to combine a polarimetric technique with the data analysis tool to generate polarization-based contrast from nonlinear phenomena. This approach aims to enrich the information available about the sample under investigation and facilitate the visualization of optical effects for easier representation in clinical diagnosis.

3.2 Staging and screening of colorectal cancer

Biomarkers make cancer detectable and provide measurable parameters for clinical diagnosis [18]. These biomarkers aim to reveal the characteristics that differentiate diseased tissue and cells from normal ones. Although the findings regarding these characteristics are often specific to particular diseases, methods for discriminating anomalies from control cells can potentially be applied to various types of cancer.

Although cancers vary greatly, changes in metabolic pathways and morphology could be common aspects, often due to poor differentiation [19]. These changes can be observed in various cancers, including breast cancer, lung cancer, colorectal cancer, prostate cancer, pancreatic cancer, leukemia, skin cancer, ovarian cancer, lymphoma, and more. The specific metabolic alterations and morphological characteristics differ across cancer types but contribute to the aggressive nature and altered cellular behavior seen in these diseases. For example, in colorectal cancer (CRC), there are metabolic alterations involving increased glucose consumption and changes in lipid metabolism that support the growth and survival of cancer cells. Morphologically, poorly differentiated colorectal cancer cells exhibit increased nuclear size, disruption in sub-cellular architecture, and a high mitotic rate. According to the presented studies, CRC remains the second-leading cause of cancer-related deaths [20, 21]. The colon has the typical histological structure as the digestive tube consisting of the mucosa, submucosa, muscularis and serosa shown in Fig. (3.1).

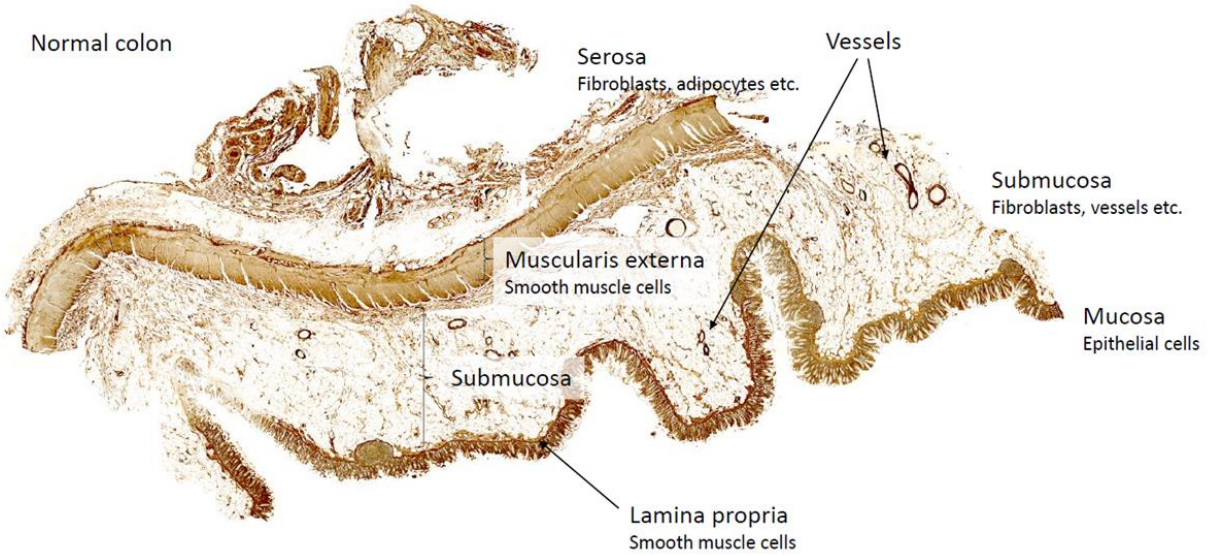

Figure 3.1. A cross-section of colon tissue biopsy provides a visual representation of the histological layers, including the mucosa, submucosa, muscularis, and serosa (Image credit: B. S. Nielsen, Bioneer A/S, Denmark).

Each layer of the colon possesses distinct anatomical structures and neuronal tissue contents, thereby serving different biomechanical roles in colon physiology and pathophysiology [22]. The innermost layer is the mucosa, comprising the epithelium, lamina propria, and muscularis mucosae. Sensory nerve endings extend to the lamina propria between the crypts, surveying the contents of the mucosa [23]. Surrounding the mucosa is the submucosa, a layer of fibrous connective tissue containing major branches of blood and lymph vessels. The muscularis propria consists of two layers of smooth muscle: an inner circular muscle layer and an outer longitudinal muscle layer. Finally, the outermost layer of the intestinal wall is the serosa, composed of a continuous sheet of squamous epithelial cells called the mesothelium [24]. Colon cancers progress within the mucosa layer, transitioning from local adenomas in the intestinal epithelium to invasive carcinomas. The mucosa is lined by a simple columnar epithelium (lamina epithelialis) characterized by long microvilli [25]. The distinguishing feature of the mucosa layer is the presence of colonic crypts. The invaginations punctuate the epithelial inner surface of the colon, resembling microscopic thick-walled test tubes with a central hole running the length of the tube.

Despite advancements in clinical practices, minimal prognostic factors are available to personalize treatment. Improved diagnostic technologies would greatly benefit CRC since its high recurrence rate leads to increased treatment costs, while early treatment significantly improves the survival rate [26]. One advantageous aspect of potential screening methods is the ability to identify diagnostic locations, as 96% of CRC develops from adenomatous polyps [27]. Colorectal adenocarcinoma, a form of neoplasia originating in colon glands from epithelial cells, is the most common type of CRC and also occurs frequently in other glandular tissues such as the prostate, breast, esophagus, stomach, lung, and pancreas [21]. In the colon, the progression from normal epithelium to carcinoma follows a sequence shown in Fig. (3.2).

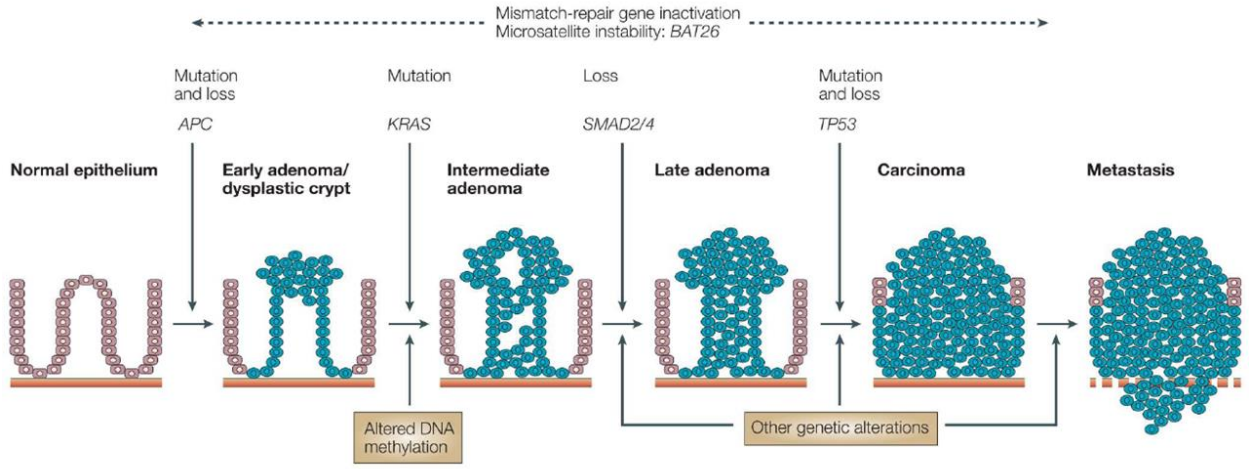

Figure 3.2. The colorectal adenoma–carcinoma sequence. Progression from normal epithelium through adenoma to colorectal carcinoma is characterized by accumulated abnormalities of particular genes. Mutations in mismatch-repair genes cause microsatellite instability and the successive mutation of target cancer genes, which can occur at any point in the adenoma–carcinoma sequence (adopted from reference [28]).

Along the lines of the adenoma-carcinoma sequence, several observations can be derived at different stages through colonoscopy, potentially providing diagnostic information. Colonoscopy is the preferred procedure for diagnosing and removing colorectal polyps. In the early stages, a few cells may exhibit dysplastic behavior, characterized by changes in phenotype and a failure to differentiate into specialized glandular or epithelial cells. Consequently, these cells display morphological differences compared to their normal counterparts, including irregular shapes, sizes, an increased nuclear-cytoplasmic ratio, and asymmetric cell division [26, 29]. As dysplasia progresses to neoplasia, tissue growth becomes excessive, potentially enlarging existing polyps and reducing tissue differentiation. The increased cellular metabolism in a growing number of cells results in localized oxygen deficiencies [30]. Hypoxia intensifies as dysplasia advances, leading to necrosis and elevated levels of cell-free DNA in the blood and feces [31]. In later stages, the lesion invades surrounding tissue layers, referred to as a tumor, while blood vessels proliferate to compensate for oxygen deficiencies [32]. This newly formed vascular network typically exhibits distinct morphological features compared to the surrounding vasculature. The low vascular density and uneven distribution of blood vessels contribute to an inefficient oxygen supply. Symptoms usually arise at this stage, shortly before or during metastasis, as the disease spreads to different sites in the body.

Cancer screening is an approach to cancer prevention that targets the population at large, considering both the benefits and drawbacks, and involving thorough review of strategies [33].

Early disease diagnosis through cancer screening is one of several proactive measures in cancer prevention. Typically, one or more imaging modalities are utilized based on a balance between imaging resolution and penetration depth, either in response to positive screening results, symptoms, or risk factors [28]. These imaging modalities include diffuse optical tomography (DOT) [34], photoacoustic (PA) [35], multiphoton microscopy (MPM) [36], radiologic modalities, such as X-ray imaging, computed tomography (CT), magnetic resonance imaging (MRI), ultrasound, and positron emission tomography (PET), employ different forms of radiation to visualize the body's internal structures in detail [37], and optical spectroscopy (OS) [38]. Achieving a compromise between penetration depth and image resolution requires a trade-off between FOV and imaging speed, with individual considerations for each modality while maintaining a fixed sampling rate at a desired SNR. Table (3.1) presents various imaging modalities along with their approximate limitations in spatial resolution, imaging depth and time acquisition. The time acquisitions provided are approximate ranges and can vary depending on various factors, including the specific equipment, imaging protocol, and clinical context.

	DOT	PA	MPM	radiologic modalities	OS
Optical resolution	10 mm	10 μm	0.5 μm : 1 μm	10 mm	0.5 μm : 10 μm
Penetration depth	< 10 cm	1 mm : 1 cm	< 1 mm	10 cm	< 0.5 mm
Time acquisition	several minutes to hours	milliseconds to several minutes	fractions of a second to several minutes	fractions of a second to several minutes	seconds to several minutes

Table 3.1. Imaging modalities with related spatial resolution and imaging depth. Typically, a tradeoff between these two parameters has to be accepted. The time acquisition for radiologic modalities can vary depending on the specific technique, equipment, and imaging parameters used. DOT: diffuse optical tomography, PA: photoacoustic, MPM: multiphoton microscopy, OS: optical spectroscopy.

3.3 Polarization-resolved two-photon excitation fluorescence microscopy

In just over two and a half decades since the initial demonstration of a multiphoton microscope, MPM has emerged as a dynamic and highly productive field. MPM has proven invaluable for noninvasive imaging of deep tissues, including biological tissues, which are known for their scattering properties. It provides valuable insights into the structure, function, and dynamics of biological specimens [39, 40].

Due to the advantage of endogenous contrast mechanisms and the comparability of morphological information to conventional pathological examinations on stained biopsy slides, MPLSM is a promising method in tissue diagnosis [36]. In MPLSM, NIR excitation is scanned similar to confocal laser scanning microscopy (CSLM). However, the high spatially and temporally confined excitation in MPLSM allows for effective nonlinear processes, enabling imaging at a resolution comparable to CSLM while reducing photo-bleaching and greatly increasing penetration depth for subcellular imaging [41]. The most commonly applied contrast mechanisms in MPLSM are based on 2PEF and SHG, which rely on nonlinear processes combining the energy of multiple photons. This is achieved using high NA excitation optics and ultra-short laser pulses in the femtosecond regime at infrared wavelengths. These features offer deep tissue penetration (>500 μm) by reducing light scattering and absorption, inherent to infrared excitation wavelengths used in investigations.

In fluorescence microscopy, a fluorescent molecule is composed of atoms whose spatial arrangement interacts with light and determines a defined transition dipole moment. In the schematic representation shown in Fig. (3.3), vertically polarized light passes through a sample containing fluorophores, which are fluorescent molecules. Fluorescent molecules possess associated transition dipoles. Molecules with transition moments parallel to the incoming polarized light are excited to a higher state. The probability of molecule excitation is related to the angle θ, which is already discussed in Chapter 1 (section 1.4.5). Here, θ represents the angle between the electric field vector of the incident light and the transition dipole moment of the fluorophore. When the excited molecule returns to the ground state, it emits fluorescence [42]. Consequently, the population of excited state molecules can exhibit a well-defined set of alignments.

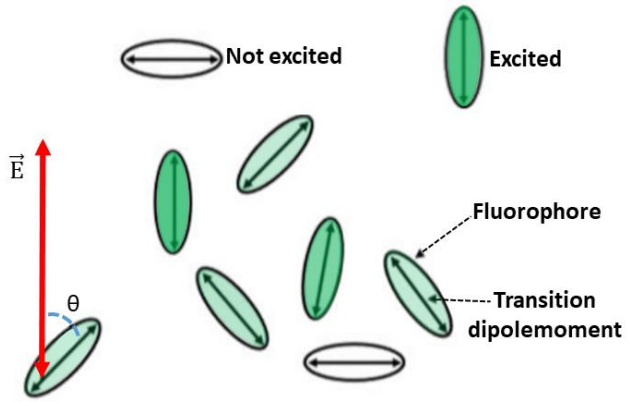

Figure 3.3. Schematic representation of photo-selection and fluorescence anisotropy. The excitation polarization of vertically oriented light is illustrated by the double-headed red arrow; θ shows the angle between the electric field vector of the incident light and the transition dipole moment of the fluorophore (figure adapted from reference [42]).

The specific transition dipole moment plays a crucial role in the interaction with target proteins and serves as a significant indicator of potential sub-cellular organization [43]. While 2PEF microscopy allows for the characterization of fluorescence intensity, morphology, and sub-cellular structures, an important piece of information that is often missing is the orientation of genetic material, proteins, and lipids within molecular structures. This limitation arises from the isotropic nature of the averaged fluorescence signal detected. However, fluorescence anisotropy or fluorescence polarization offers a solution by capturing the unequal intensities of light emitted by a fluorophore along different polarization axes. By measuring the modulation of signal upon the rotation of linear excitation polarization, molecular orientation becomes accessible. Polarization demodulation enables the distinction of structures or molecules based on the orientation of fluorescent dipoles. Furthermore, FPM allows for the measurement of the molecular orientation of targeted proteins or structures, particularly those connected rigidly with fluorescent dipoles. This technique has been instrumental in quantifying the degree of anisotropy and orientation of fluorescent labels, enabling the analysis of drug-target entanglement, protein-ligand conjugations, and identification of anomalies in cells [44, 45].

Several clinical applications highlight the significance of fluorescence polarization, such as the use of methylene blue as a quantitative marker for breast cancer at the cellular level [46], the quantification of collagen networks in mammary tumors [47] and the assessment of changes in human epithelial cancers at the cellular level [48]. By leveraging fluorescence polarization, valuable insights can be gained into the orientation and organization of molecular structures, thus advancing our understanding of cellular processes and enabling early diagnosis in various clinical settings.

Although 1PEF microscopy has been widely adopted as the gold standard technique, nonlinear excitations, particularly using NIR excitation wavelengths, present several advantages that can

enhance imaging capabilities. One key advantage is the ability to minimize out-of-plane photobleaching, which refers to the undesired photobleaching of fluorophores in regions above and below the focal plane. This is particularly beneficial when imaging thick samples or three-dimensional structures, as it helps preserve the fluorescence signal within the focal plane and reduces the loss of important information due to photobleaching. In addition to minimizing out-of-plane photobleaching, nonlinear excitations with NIR wavelengths also offer the advantage of reducing phototoxic effects. Phototoxicity refers to the potential damage caused to biological samples by the absorption of high-energy photons during the imaging process. By using NIR excitation, which has lower energy compared to shorter wavelengths, the risk of phototoxicity is significantly reduced. This allows for longer imaging sessions and increased viability of living specimens, enabling us to study dynamic processes and observe biological samples over extended periods without compromising their integrity.

Even though in 2PEF, the nonlinear nature of the excitation reduces the angular photo-selection and thus ameliorates the angular sensitivity of polarized measurements, it offers inherent advantages compared to 1PEF, including reduced scattering, enhanced optical penetration, and improved spatial resolution. Notably, polarization-resolved 2PEF overcomes the limitations of fluorescence anisotropy imaging by providing valuable information about molecular order without the need for any assumptions regarding the average orientation of the molecules. This breakthrough technique allows for a deeper understanding of molecular organization and provides a powerful tool for studying complex biological systems [49].

3.3.1 Experimental setup

One of the objectives of this thesis involved the construction of a homemade 2PEF imaging setup, which is developed by incorporating a polarization technique to analyze the anisotropic emission of fluorescence in response to various polarization states configurations. A typical polarization-resolved fluorescence microscope includes a light source for excitation, polarization components to control the polarization state of the light, a sample stage for specimen positioning, an objective lens to collect emitted fluorescence light, a detector to measure the intensity and polarization of the fluorescence signal, and data acquisition and analysis tools. These components work together to enable the analysis of polarization properties in fluorescence imaging, offering insights into the structure and function of biological samples. The entire process is carried out as part of the research, emphasizing to take the advantage of both fluorescence and polarization modules within the experimental setup.

The polarization state of the excitation light plays a crucial role in the processes of 2PEF absorption and emission utilized in microscopy [50]. During the 2PEF absorption process, the sum of angular momenta of the absorbed photons must be zero, as most fluorophores undergo electronic state transitions with no net angular momentum change [9]. Thus, linearly polarized light exhibits higher

two-photon absorption compared to circularly polarized light since it satisfies this condition more favorably. However, circularly polarized light ensures more uniform excitation of fluorophores across the spatial domain, while linearly polarized light's excitation probability strongly relies on the relative orientation between fluorophores and beam polarization, leading to photo-selection effects on the dyes. Therefore, a polarization-resolved fluorescence imaging approach is proposed, which involves two configurations of polarization adjustments at the excitation and detection stages. In Fig. (3.4 a), a schematic of the 2PEF microscopy setup is shown, utilizing a LP, half wave plate (HWP), and quarter wave plate (QWP) to achieve right circularly polarized input light, enabling non-preferential illumination of the sample. The assumption of a single molecular transition dipole is broken down by circular polarization, as additional angular momentum components that are not considered are introduced [51]. In addition, a module has been designed and installed, which incorporates a rotating LP positioned before the detector. This setup enables the decoding of the anisotropic nonlinear signal angle-by-angle with 10-degree steps, serving as the fluorescence anisotropy analyzer in the backward direction.

The other possible configuration for the fluorescence polarimetry is depicted in Fig. (3.4 b). In this approach, a rotating LP is employed to excite the sample with linear polarized light, and the fluorescence signal is detected after a second LP at a fixed angle. Both configurations are applied to compare the associated polarization–resolved image dataset and to validate the interpretations of the dataset analysis.

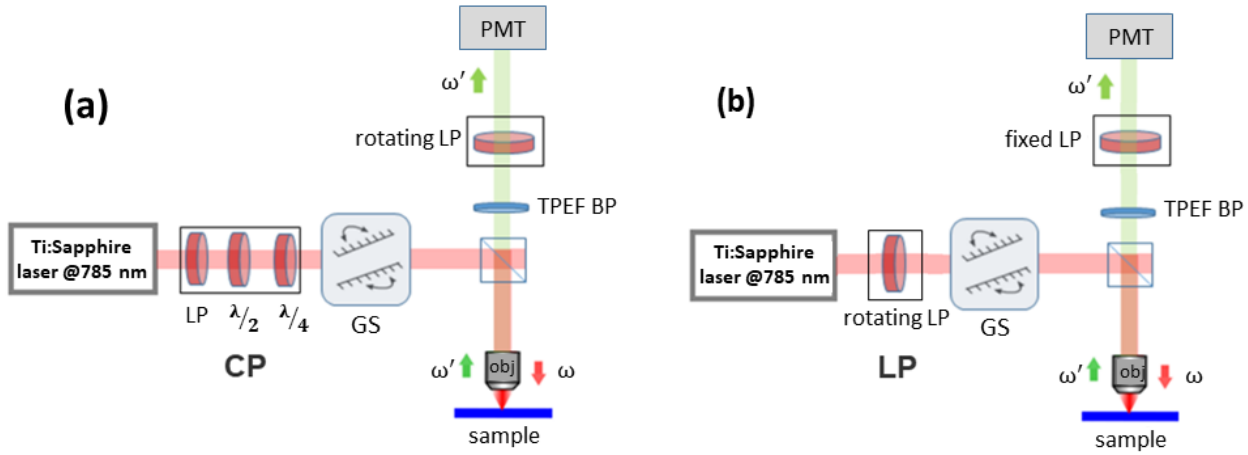

Figure 3.4. Polarization-resolved 2PEF microscope based on circular and linear polarization of light during excitation. (a) Circular polarized light is used for excitation, and the resulting fluorescence signal is analyzed using a LP that rotates at different angles. (b) Rotating linear polarized light is employed for excitation at various angles, and the fluorescence signal is then analyzed using a fixed linear polarized light. GS: Galvo-Scanning mirrors, TPEF BP: Band Pass filter of 2PEF, PMT: photomultiplier tube, λ/2: half wave plate, λ/4: quarter wave plate, CP: circular polarizer, LP: linear polarizer.

The system is fully assembled and built, based on an existing design with further development [18]. The experimental image of the 2PEF polarimetric setup with CP configuration is presented in Fig. (3.5). A femtosecond laser (Femtosource Compact Pro, Femtolasers GmbH, Austria) with a center frequency at 785 nm, a pulse length of 120 fs and a 74 MHz repetition rate is used for illumination. After passing a dispersion pre-compensation unit (Mosaic Pro V, Femtolasers GmbH, Austria), the beam passes through a power tuning unit including Half Wave-Plate (Achromatic HWP @690-1200 nm), Polarizing beam splitter (Mounted in 30 mm Cage System) and a beam block (IR Pulsed and CW) mounted. Next the beam is sent through a spatial filter (KT130, Thorlabs, USA), with a 15.3 mm focusing lens (C260TMD-B), a 10 µm pinhole, and a 19 mm collimation lens (AC127-019-B-ML), thus enlarging the beam which is then redirected to a variable neutral density (ND) filter (Thorlabs - NDC-50S-3M Mounted Step Variable ND Filter, Ø2.5", OD: 0.04-3.0) for the optimization of saturation. Light is then redirected through a LP (LPVIS050 - Ø12.5 mm Unmounted Linear Polarizer, 550 - 1500 nm), half wave plate (HWP-AHWP05M-980 - Ø1/2" Mounted Achromatic Half-Wave Plate, Ø1" Mount, 690 - 1200 nm) to compensate any polarimetric effect of the optical components in the setup, and quarter wave plate (QWP- AQWP05M-980 - Ø1/2" Mounted Achromatic Quarter-Wave Plate, Ø1" Mount, 690 - 1200 nm) generate right circular polarized input light for the excitation. It is assumed that the right circular polarization (RCP) is preserved from the optics to the sample through the Galvo-Scanning mirrors.

The laser beam is reflected onto the sample by Galvo-scanning mirrors (GVS012, Thorlabs, USA) with the assistance of relay lenses (AL2550H-B, AC254-150-B) to enlarge the beam and fill the back aperture of the objective. The beam passes through a long-pass filter (736/LP, Semrock, USA), is then reflected by a dichroic mirror (HC720SP, AHF, Germany), and focused by a 20X/1 water immersion objective (XLUMPLFLN 20XW, Olympus). The sample is securely positioned on a motorized scanning stage attached to Olympus IX71 inverted microscope body. The emitted fluorescence is collected through the same objective, filtered by the dichroic mirror and a short-pass filter (Thorlabs - FES0700 Ø1" Shortpass Filter, with a cut-off wavelength of 700 nm), and directed into a rotating Linear Polarizer (LPVIS050 - Ø12.5 mm Unmounted Linear Polarizer, 550 - 1500 nm). Subsequently, the light is focused by a 10X/0.3 objective (Olympus) into a fiber with a 600 µm core. The signals can be detected by a PMT (H7422, Hamamatsu, Japan) for imaging or by a spectrometer (QE Pro, OceanOptics, USA) for spectroscopy, allowing for characterization of the fluorescence's spectral range. The entire setup is controlled by a custom LabVIEW program. During imaging, an average power of 8 mW is used on the samples, with a pixel dwell time of 0.5 ms for 512 × 512 pixels images. Additionally, the setup is equipped for white light illumination microscopy using a Fiber-Lite DC-950H illuminator and a CCD camera (Thorlabs - DCC1545M - USB 2.0 CMOS Camera, 1280 x 1024) to facilitate locating the focal plane for fluorescence scan imaging.

The microscope is operated and controlled by a computer, with the devices connected using a custom LabView® routine through a National Instruments DAQ Module 16 AI, 24 DIO, 2 AO, USB-6353. The data analysis and post-processing imaging steps are performed using a specialized homemade routine in the Matlab program (Matlab, v.R2019b, Mathworks).

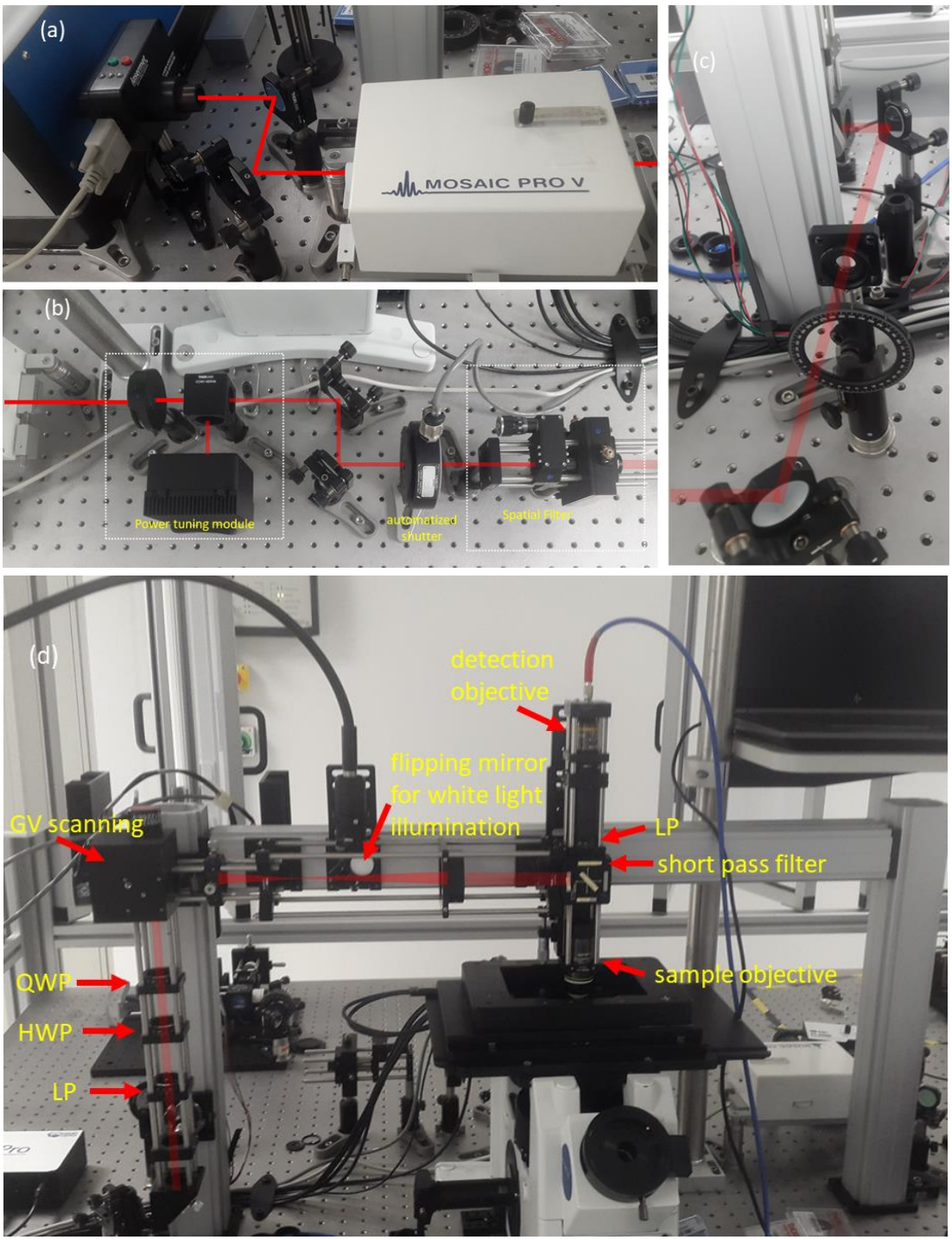

Figure 3.5. Picture of the custom polarization-resolved 2PEF microscope for CP configuration. (a) The beam passes through a magnetic shutter and enters the pre-compensation unit. (b) Power manipulation unit, automatized shutter and spatial filter to obtain fundamental mode. (c) The beam passes through variable ND filter. (d) CP is introduced before reaching the galvo scanning mirrors and relay lenses, which then illuminate the Olympus 20X/1 water immersion objective. The 2PEF signal passes through a short-pass filter, a rotating LP, and is focused by the detection objective into the fiber connected to the PMT. ND: neutral-density, GV: Galvo scanning mirrors, QWP: quarter wave plate, HWP: half wave plate, LP: linear polarizer, CP: circular polarization, PMT: photomultiplier tube.

3.3.2 Cancer model

Although biomarkers are best verified *in-vivo*, findings on a complex biological tissue may result from disease-related or environmental influences [52]. Thus, for robust diagnostic purposes, they need to be evaluated over a range of known environmental influences in a controlled manner. In this work, spheroids are adapted as tissue models, which aim to mimic the spatial configuration and signaling pathways of pathologic cells found *in-vivo* environment. In contrast to a 2D environment, where cells are in contact with the substrate, cell-to-cell contact is ensured in a spheroidal tissue model. Intrinsically, proliferating cells form the periphery of a spheroid, whereas in the core cells are dormant or undergo apoptosis and necrosis [53]. The structure of the spheroid is illustrated in Fig. (3.6), with a peripheral layer of proliferating cells surrounding a layer of non-proliferating (quiescent) cells, while necrotic cells accumulate in the core of the structure [54].

The cancerous 2D tumor spheroid human colorectal adenocarcinoma cell line (HT29) with epithelial morphology resembling colonic primary tumors and normal Human Colonic Epithelial Cells (HCoEpiC-N489) obtained from Bioneer A/S, Denmark, are included in the study. HT29, derived from a colorectal adenocarcinoma patient, is commonly utilized in cancer and toxicology research. The tissue biopsy samples were stained with various fluorescent dyes, including DAPI (blue), Aqua/DCC (blue), FITC (green), Rhodamine (bright red), Cyanine-3 (red), and Cyanine-7, covering a spectral wavelength range from 457 nm to 779 nm. Throughout the imaging process, a portion of the excitation energy is absorbed by the tissue and converted into heat.

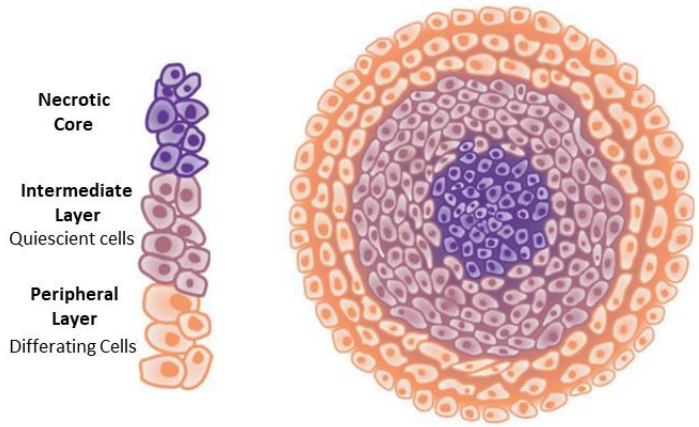

Figure 3.6. Schematic representation of the colon spheroid highlighting the spatial arrangement of different cell populations. Proliferating cells are depicted in orange and form the outermost layer, while quiescent cells are represented in violet and reside in the middle layer. Necrotic cells, shown in purple, are located at the core of the spheroid. The cellular density gradually decreases from the outer layer towards the core (Figure reported from reference [54]).

3.3.3 Calibration and characterization

A standard positive resolution test-target (Thorlabs R1DS1P) is used to measure the effective pixel size, FOV and true magnification. See Fig. (3.7) for the example image of the resolution target captured with the 20x objective and detected by the PMT. CW laser mode is used to avoid damaging the test sample. After scanning the target at different sizes for the FOV, the measured distances from the target elements in pixels, object side resolution, line width, and effective pixel size were determined to be 203.2 line pairs per millimeter (lp/mm), 2.46 μm and 228 nm respectively.

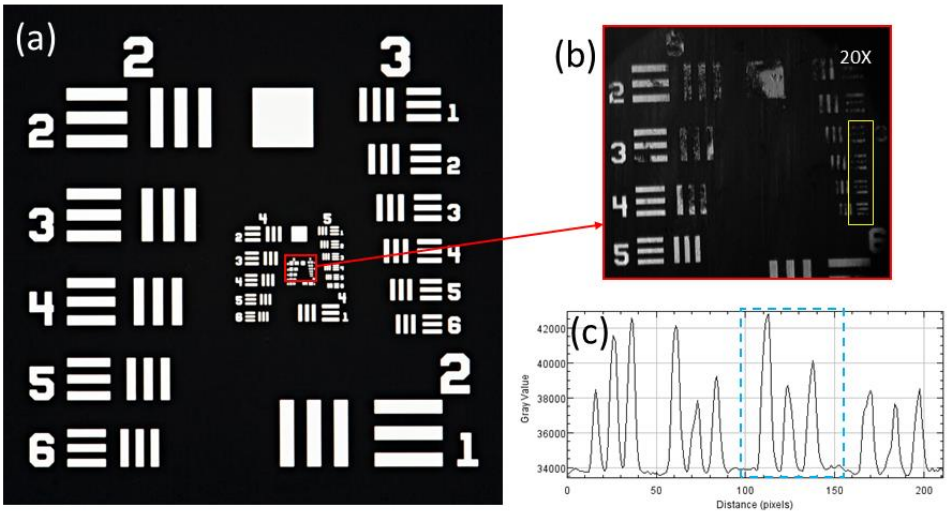

Figure 3.7. The characterization of microscopy using the United States Air Force (USAF) resolution test-target. (a) Shows the original photograph. (b) Displays the microscopy image captured using the 20X objective. (c) The intensity profile is presented, focusing on four line groups: [3,7], [4,7], [5,7], and [6,7]. Notably, the dashed box corresponds to group [5,7], which consists of lines with a width of 2.46 μm.

An image measured by an optical microscope is convoluted image of PSF and specimen. The microscope's PSF is usually measured by imaging a small fluorescent microsphere. Sub-resolution beads, also known also as fluorescent nanospheres, are suitable for PSF measurements due to their small size and precise localization properties. These beads have a diameter much smaller than the resolution limit of the microscope, typically on the order of tens to hundreds of nanometers. When the beads are imaged under a microscope, they appear as diffraction-limited spots in the image. The intensity distribution of the spot represents the PSF of the imaging system. By analyzing the shape and characteristics of these spots, the PSF can be accurately measured. Thus, to measure the PSF size, a sample containing sub-resolution fluorescent green ring stain polystyrene beads of 380

nm is tested, as shown in Fig. (3.8). x-y and z-series images of fluorescence beads in different positions are captured using the mode-locked laser. This approach allowed for the characterization of the PSF of the 2PEF microscope, revealing lateral and axial spatial dimensions of approximately 0.9 μm and 3.5 μm, respectively.

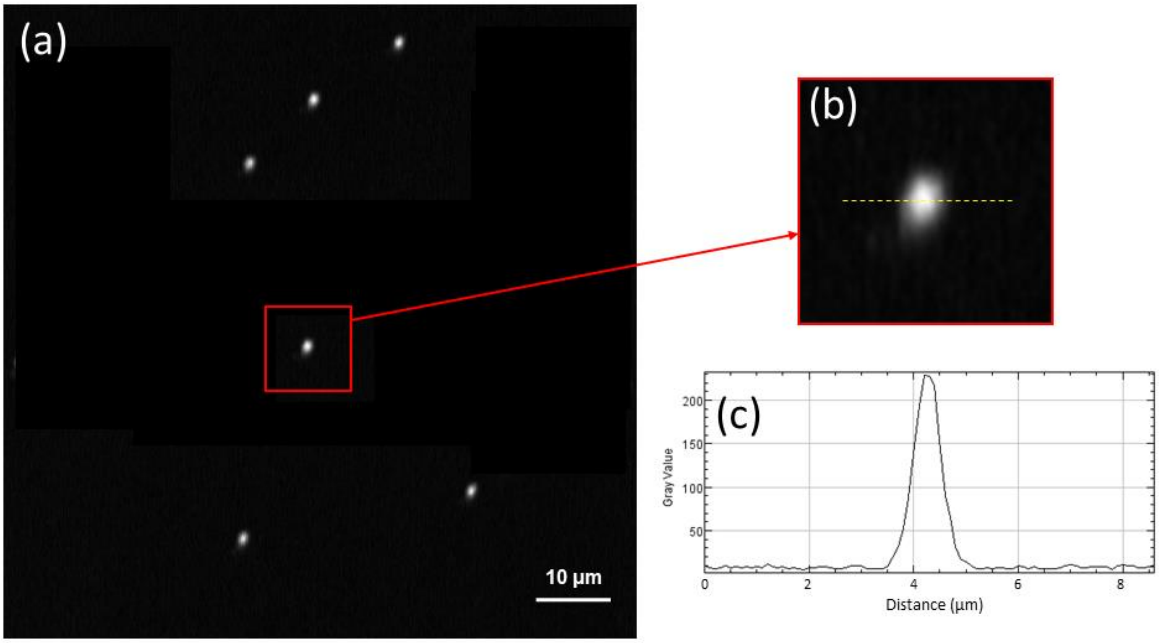

Figure 3.8. Shows the experimental measurement of the Point Spread Function (PSF) using microspheres. (a) shows a 512 × 512 image of a 380 nm microsphere, (b) displays a 3x zoomed-in microscopy image captured, and (c) represents the cross-section profile of the measured PSF along the dashed line in (b).

3.3.3.1 Imaging parameters and photobleaching

Generally, 2PEF has demonstrated limited photo-damage due to the confinement of excitation within the focal plane. Safe excitation powers of approximately 20 $\mathrm{mW}/\mu\mathrm{m}^2$ along with a pixel dwell time of 1 μs, have been established in relation to the input power [55, 56]. To prevent photobleaching during PMT imaging in this study, specific imaging parameters outlined in Table (3.2) are employed by following a stepwise approach. Initially, the excitation power was increased at a lower resolution until bleaching or signal saturation occurred. Subsequently, the excitation power was reduced by 30-50% and the resolution was enhanced on a shifted FOV, observing for any signs of photobleaching. Finally, at a further shifted FOV and a slightly reduced resolution, the pixel dwell time was increased until bleaching was observed. In the case of MPM, the shortest achievable pixel dwell time without image distortion was set at 10 kHz [18].

Detector	FOV (μm)	Definition (pixel per line)	Speed/Integration time	Excitation power at detector plane
PMT	64 × 64	128, 256, 512	0.1 ms	≤5 mW
Spectrometer	64 × 64	64	8-20 ms	12 mW

Table 3.2: The imaging acquisition parameters used throughout this study on the polarization-resolved 2PEF microscope.

3.3.3.2 Fluorescent microsphere imaging

To assess instrument misalignment or aberrations of the 2PEF microscope and investigate the detection of fluorescence spectrum in microscopy imaging, a test is conducted using 6.0 μm fluorescent microspheres labeled with NovaFluor Blue 555, which emits at a peak wavelength of 555 nm. The microspheres were obtained from ThermoFisher Scientific and are illustrated in Fig. (3.9). In order to examine the optical characteristics of the imaging system and evaluate the transmission optical window, a visible optical band-pass filter kit was employed. This allowed for the analysis of the fluorescent spectrum centered around 550 nm, which was found to align well with the transmission optical window of the system. By utilizing different band-pass filters during microscopy imaging of the fluorescent microspheres, it becomes possible to evaluate the performance of the microscope detector, optimize signal detection, enhance image quality, and gain insights into the specific fluorescence properties of the sample. This approach enables a comprehensive exploration of the microscope's capabilities and aids in obtaining accurate and informative results in fluorescence microscopy experiments.

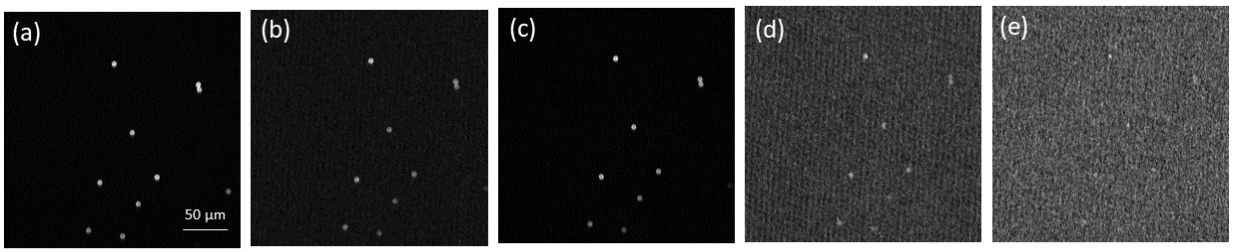

Figure 3.9. Microspheres image using (a) short-pass filter cut off at 700 nm; (b) Visible optical filter transmission at 600 nm with 40 nm BandWidth (BW); (c) Visible optical filter transmission at 550 nm with 40 nm BW; (d) Visible optical filter transmission at 500 nm with 40 nm BW; (e) Visible optical filter transmission at 460 nm with 40 nm BW. The fluorescence signal weakens down to bachground noise level from below 510 nm and above 620 nm.

From the microsphere images obtained, it is observed that there is no astigmatism present, as depicted in Fig. (3.10). Astigmatism refers to a distortion in the shape of an image, where the focal points in different planes do not coincide, resulting in blurred or elongated features. In this case, the absence of astigmatism indicates that the microscope optics and imaging system are properly aligned and optimized. However, an interesting observation is made regarding the intensity distribution of the fluorescence emitted by the microspheres. Due to the geometric and light-scattering properties of the microspheres, a phenomenon known as the edge effect becomes prominent. The edge effect refers to the phenomenon where the fluorescent intensity is higher at the edges of an object compared to its center. The edges of the microspheres, having a greater surface area compared to the center, are more exposed to the excitation light and exhibit stronger fluorescence emission. This observation is important to consider when analyzing and interpreting microscopy images of fluorescent microspheres. It highlights the need to account for the edge effect and consider the intensity variations across the microspheres' structure.

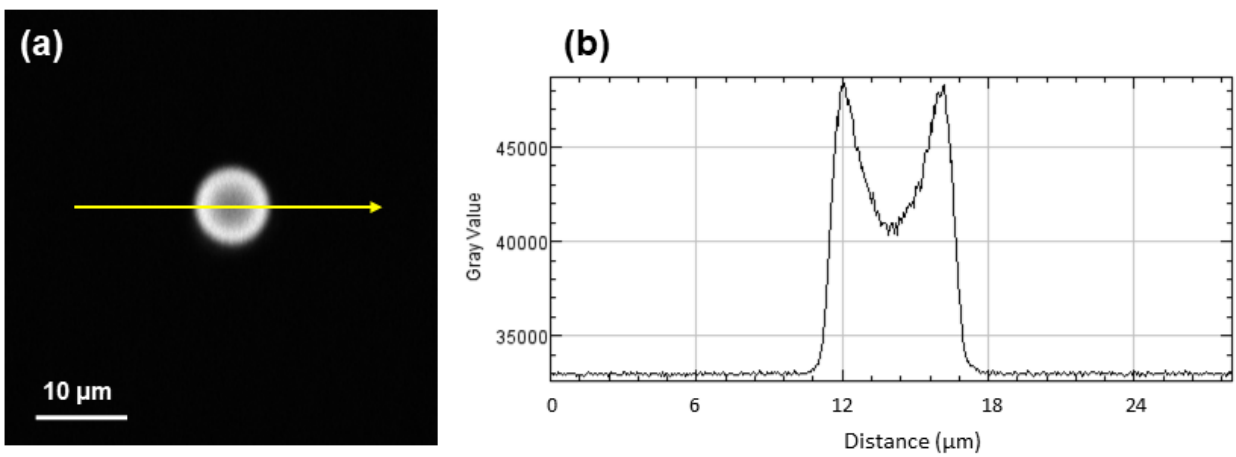

Figure 3.10. (a) 2PEF microscopy 512 × 512 image of 6 µm microsphere; (b) Corresponding line intensity profile along the yellow arrow in figure (b); Gray value represents the intensity in arbitrary units.

To verify the correct alignment of CP at the sample plane, a LP is employed at the *home* position of the galvo-scanning mirrors. This LP is positioned in the sample plane, serving as the CP analyzer, allowing the laser beam to pass through it perpendicularly. The excitation power of the laser light reaching the sample plane can vary depending on the angle of linear excitation due to the presence of the dichroic mirror. Any fluctuations in laser power caused by the optics in the microscope's optical path can introduce additional errors in the results. To compensate for the change in optical power at the sample plane, an adjustment of the optical power for each corresponding angle of linear excitation is performed. This calibration is employed during the excitation polarization measurements to ensure accurate and reliable results.

The laser power after the LP positioned in the sample plane is measured to account for any variations in CP with respect to the rotation angles of the LP. In theory, when considering circularly polarized light, the detected power through the LP at different rotational angles is expected to be uniform. However, due to potential errors introduced by polarization modifications in the optical system leading to the sample, a slight deviation from perfect CP towards elliptical polarization may occur. The corresponding results of the power measurements are depicted in Fig. (3.11 a). The red sinusoidal curve represents the theoretical variation. Fig. (3.11 b) illustrates the same power measurement data normalized in a polar plot with an elliptical shape. Ellipticity serves as a measure of the extent to which an ellipsoidal shape deviates from a perfect circle. It quantifies the elongation or flattening along the major and minor axes of the shape. The ellipticity, based on the definition in Chapter 1 (section 1.2), is calculated as the ratio of the minor to major elliptical axis, which is determined to be 0.92. In a perfect circle, this ratio is equal to 1.

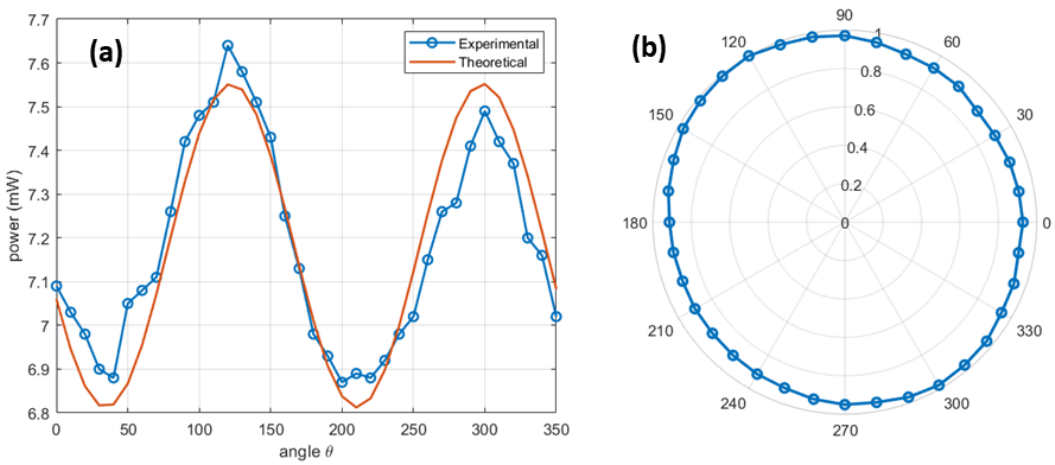

Figure 3.11. Intensities from the polarization analyzer are recorded as a function of the rotation angle. (a) The calibration process for the circular polarizer error is illustrated using a rotating test linear polarizer positioned in the sample plane. The experimental data is plotted along with the corresponding theoretical sinusoidal curve. (b) Shows the same data measurements of the detected power, normalized and represented on a polar plot.

The fluorescent microspheres are expected to exhibit isotropic fluorescence characteristics due to their spherical geometry. Therefore, the polarization-resolved 2PEF images of the 6 µm microspheres undergo calibration to investigate any potential variations arising from non-ideal or non-uniform circular polarization during the excitation stage. To evaluate fluorescence signal degradation, the images are repeatedly scanned while rotating the LP in the detection side, covering angles from 0 to 180 degrees in 20-degree increments, as shown in Fig. (3.12). This calibration process enables the calculation of the mean signal intensity for each image acquired at different LP angles. The results indicates that the mean intensity decreases from the initial image scan at 0° to the sixth scan at 100° of LP angular rotation. Subsequently, the mean intensity remains constant for the subsequent scanned images at higher angles. This information helps to evaluate and

understand the impact of LP rotation on the fluorescence signal and assess the performance of the polarization-resolved 2PEF imaging system.

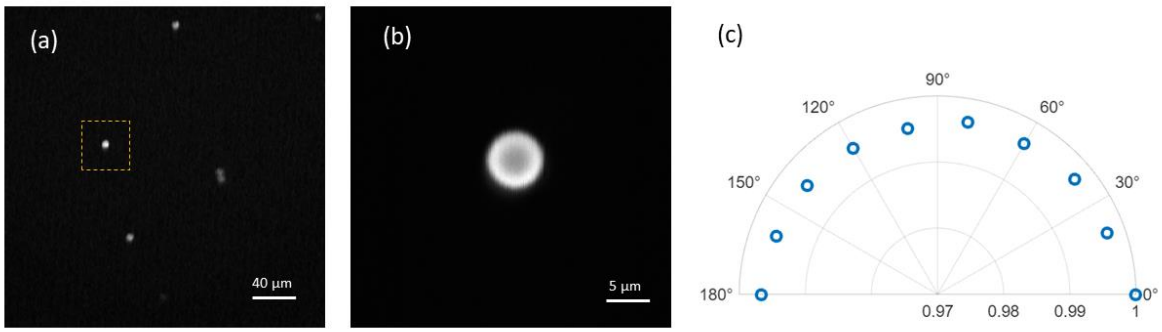

Figure 3.12. (a) Polarizetion-resolved 2PEF 512 × 512 image of microspheres. (b) 8x zoom in image of a certain microsphere. No variations in fluorophore orientation at different angles is observed. (c) Half-polar plot of the mean fluorescence intensity at different rotational angles of the LP located before the photomultiplier tube (PMT). The mean intensity exhibits a decrease from the first image scan at 0° to the sixth scan at 100° of linear polarizer angular rotation.

3.3.3.3 Fluorescence anisotropy characterization

To investigate the fluorescence anisotropy based on the photo-selection effect, the HCoEpiC sample is excited using a fixed LP, and the fluorescence intensity of the 37-stack images is measured at different angular rotations ranging from 0 to 360 degrees with 10-degree increments of the second LP on the detection side of the polarimetric 2PEF microscope. The obtained results are compared to the dark images (background) shown in Fig. (3.13). Subsequently, the mean signal intensity is calculated for each image in the stack, considering all the pixels angle-by-angle. Additionally, the STD of the total pixels within each image was computed using equation (3.1).

$$\mathrm{STD} = \sqrt{\frac{\sum_{i=1}^{n}(x_i-\bar{x})^2}{n-1}} \tag{3.1}$$

where n is the total number of the pixels, x_i is each of the pixel values and $\bar{x}$ is the mean of x_i. The STD evolution is in accordance with the variation of the mean intensity. By observing the correlation between the STD and mean intensity, it provides insights into the overall stability and consistency of the fluorescence measurements. A consistent trend between these two parameters suggests that any changes in the mean intensity can be attributed to genuine variations in fluorescence anisotropy rather than random noise or artifacts in the imaging process. According to the results, the mean and STD of the fluorescence signal exhibit changes depending on the angle θ, while the values of the background image remain constant. The fluorescence intensity variations

demonstrate an intensity modulation corresponding to the orientation of the analyzer, as illustrated in Fig. (3.13).

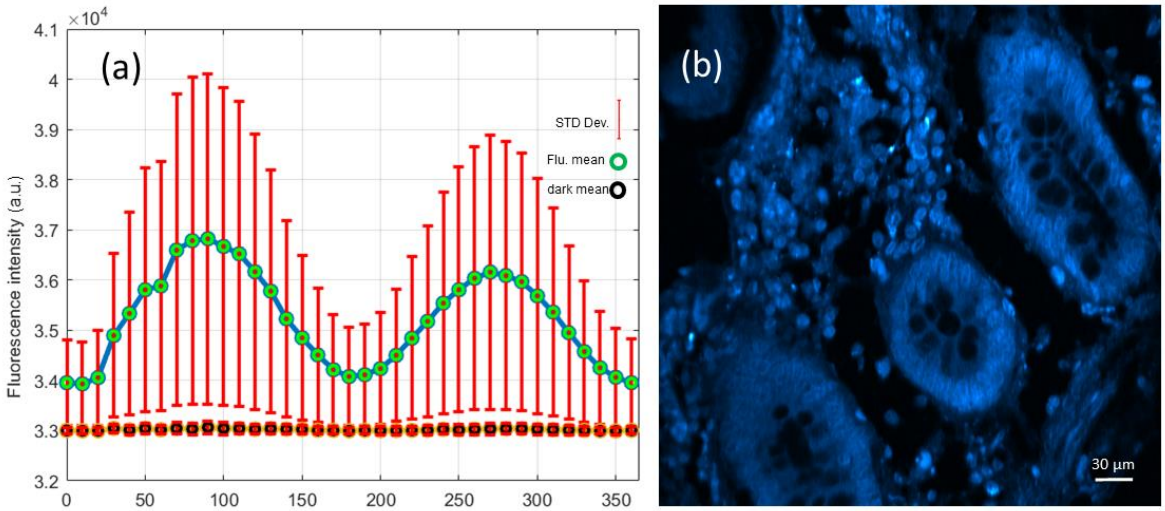

Figure 3.13. (a) Mean fluorescence intensity and standard deviation (STD) from (b) polarization-resolved 2PEF microscopy 512 × 512 images of healthy colon tissue in terms of angles from 0° up to 360° with step size of 10 degrees of rotational LP in detection compared to background.

3.3.3.4 SNR improvement by image averaging

A fundamental challenge with using fluorescence microscopy is the presence of noise. A possible source of noise is particularly relevant to the variation of the photon counts due to the stochastic nature of light emission/detection and fluorescence background, impurities or scattered light. The noise variations exists primarily due to the Poisson statistics of the incoming photons onto the detector with additional influence from sources like the detector itself, the optical setup, and the experimental parameters [57]. Shot noise as a main contribution in noise, describes the fluctuations of the number of photons counted due to their occurrence independent of each other. Averaging fluorescence images addresses the issue of eliminating shot noise, as described in equation (3.2).

$$avg = \sum_{n=1}^{N} \frac{I_n}{N} \tag{3.2}$$

Here avg is the average flurescence image, N is the number of averaging and I_n is the intensity of certain pixel in the image n. By employing this approach, the signal-to-noise ratio (SNR) associated with image quality increases proportionally to the square root of the number of averaged images, denoted as $\sqrt{N}$. Therefore, we conducted measurements to assess the background noise level induced by ambient incoming photons, as well as the averaging of 2PEF microscopy images of HT29 cells in 2D spheroids, as illustrated in Fig. (3.14). Averaging helps to smooth out noise artifacts present in individual images. Random noise, such as background fluorescence, impurities, or scattered light, tends to vary from image to image. Averaging effectively suppresses these random fluctuations, resulting in a smoother and more uniform image. Moreover, the image averaging can help minimize imaging artifacts that may be introduced by factors like detector noise, optical setup imperfections, or experimental parameters. By averaging multiple images, these artifacts are mitigated, leading to a more accurate representation of the fluorescence signal.

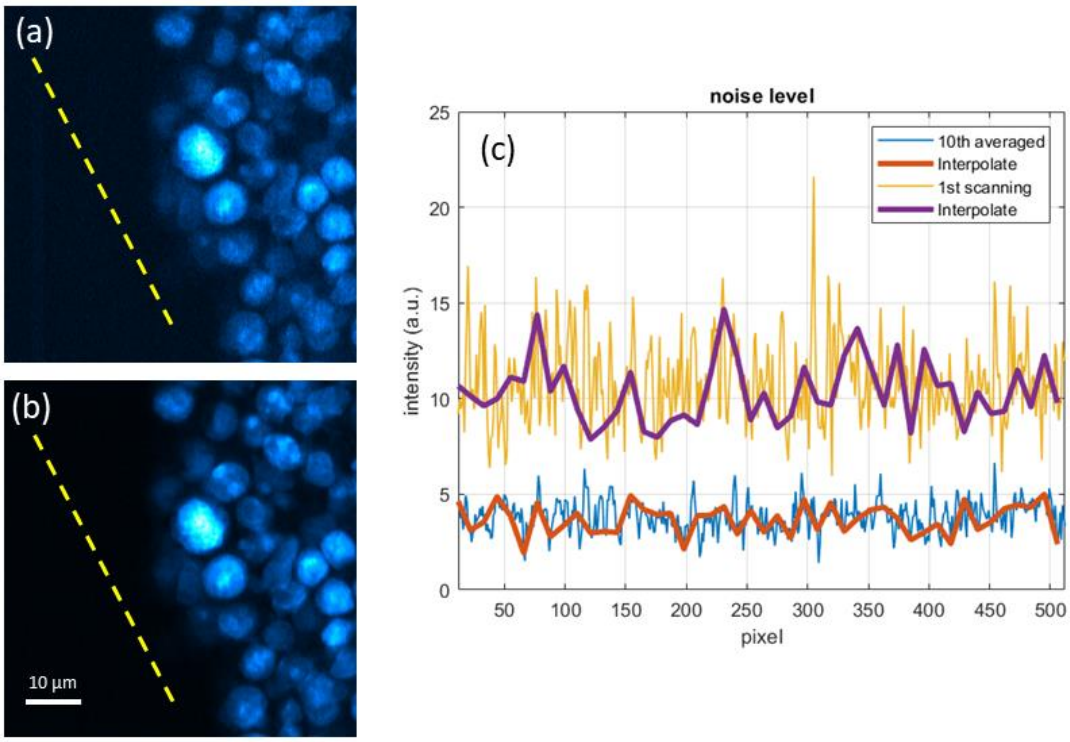

Figure 3.14. Image quality improvement by averaging. (a) 1st time scanned 2PEF image of HT29 cells in spheroid; (b) The same but averaged 2PEF image of HT29 cells in spheroid after 10 times scanning; (c) Corresponding intensity profiles versus pixles along dashed yellow lines on the background of 2PEF scanned images of (a) and (b). The SNR increases proportionally to the square root of the number of averaging, indicating that as more images are averaged, the noise level decreases, resulting in a clearer and more reliable representation of the underlying fluorescence signal.

From the results, it is observed that the mean intensity of the background noise decreased. This allows for the optimization of the number of averages, considering a trade-off between the improvement in image quality and the number of scans required. Based on the analysis presented in Fig. (3.15), the noise STD is calculated for a specific region of pixels in the background, ranging from the first scan up to 10 averaged scans.

It is found that the noise level exhibits an exponential decay with an increasing number of averages, resulting in an enhancement of the SNR. It is demonstrated that after 3 averages, the image quality improves by approximately twofold, and after 10 averages, the improvement is approximately threefold. Consequently, the optimal number of averages is proposed to be N = 3 to 4, striking a balance between image SNR improvement and a higher number of scans.

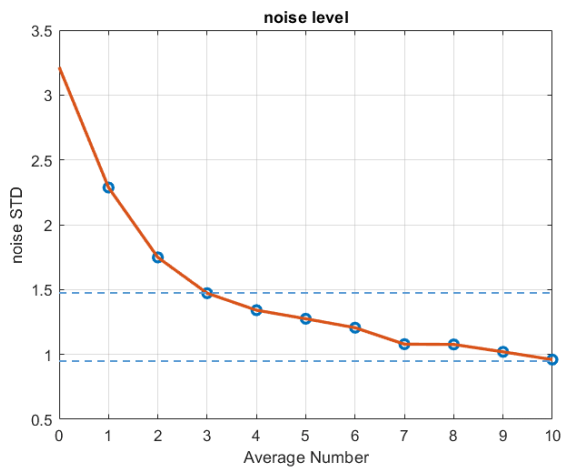

Figure 3.15. Shows the evaluation of signal-to-noise ratio (SNR) and noise sensitivity. The noise standard deviation (STD) is measured as a function of the average number, optimized through 3 times averaging. The red curve represents an exponential approximation, connecting the data points. The two blue dashed lines indicate the decrement in noise from 3 times averaging up to 10 times. The noise level is calculated by determining the STD of the background pixels in the dark region.

3.4 Polarization-resolved 2PEF microscopy imaging of cancerous colon cells compared to healthy cells

In order to take advantage of various image enhancement schemes, a versatile approach is to utilize the optical scanning microscope. This technique involves scanning a diffraction-limited spot of light relative to the specimen in a raster pattern, enabling the construction of the image point by point. Fig. (3.16) showcases the multimodal imaging of human colorectal healthy tissue (N489-2) using 2PEF integrated with white light microscopy imaging.

Crypts in colon tissue microscopy imaging exhibit characteristics of tubular structures that extend into the underlying mucosa. They appear as elongated and finger-like projections, displaying a distinctive glandular pattern. These crypts are lined with epithelial cells and surrounded by connective tissue. The visualization of crypts plays a vital role in the analysis and diagnosis of various colon-related diseases, particularly colorectal cancer.

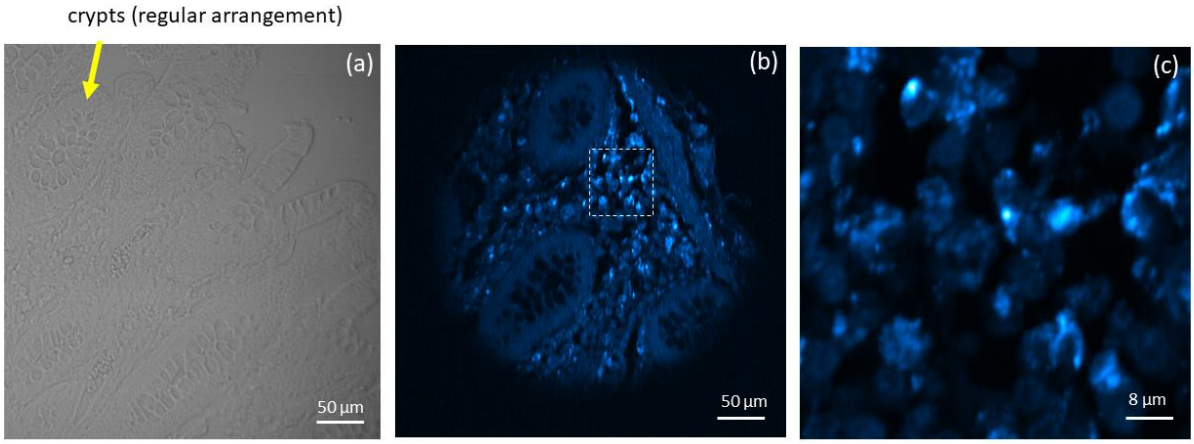

Figure 3.16. Showcases multimodal microscopy imaging of human colorectal healthy tissue. (a) White light microscopy utilizing a CCD camera; (b) Full field-of-view 512 × 512 image of 2PEF microscopy; (c) 6x Zoom in view of the 2PEF image in (b), revealing the presence of epithelial cells that line the crypts.

Colorectal cancer (CRC) originates from epithelial cells located in the colon, where the mucosa layer harbors a high concentration of these cells. Fig. (3.17) showcases multimodal microscopy images capturing the epithelial tumor cells (HT-29) within a 2D spheroid. This spheroid is a multicellular structure formed by aggregating homotypic dissociated cells. The architecture of the spheroid reveals distinct cellular layers with varying characteristics. The outer layer consists of actively proliferating cells, contributing to the overall growth of the tumor. Moving inward, we encounter an intermediate layer comprising quiescent cells that exhibit reduced proliferation and

metabolic activity compared to the outer layer. At the core of the spheroid, a necrotic region becomes evident, characterized by the presence of dark cells. The formation of these distinct layers can be attributed to the limited diffusion of oxygen and nutrients, coupled with the accumulation of waste products and carbon dioxide in the central region of the structure. These layers within the 2D spheroid reflect the environmental conditions encountered by the tumor cells, impacting their behavior and response. Understanding the dynamics and organization of epithelial tumor cells within this model is vital for comprehending the mechanisms underlying colorectal cancer progression. Valuable insights can be gained by studying cell proliferation, interactions, and the influence of therapeutic interventions, which in turn contribute to the development of improved diagnostic and treatment strategies for individuals affected by colorectal cancer [58].

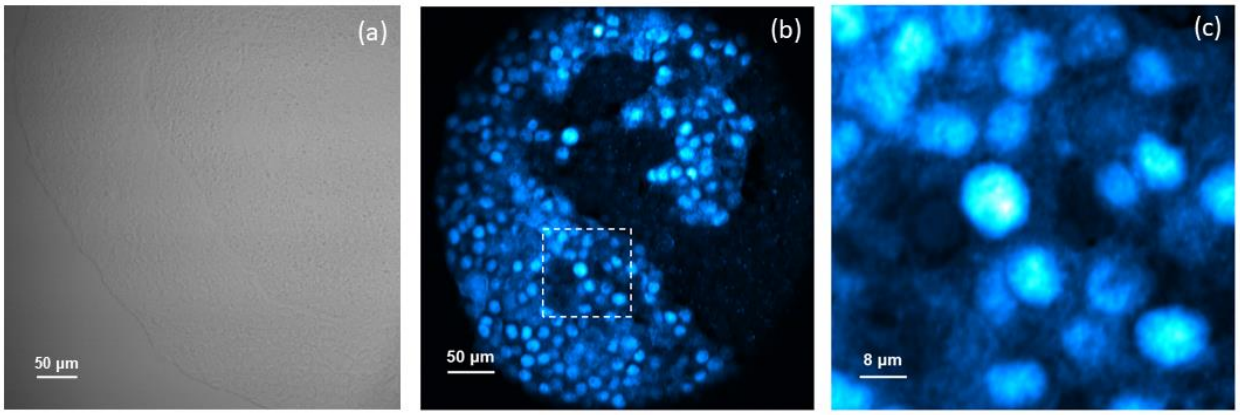

Figure 3.17. Showcases multimodal microscopy imaging of human cancerous colorectal cells in a 2D spheroid: (a) White light microscopy utilizing a CCD camera; (b) 2PEF microscopy displaying a 512 × 512 image in full field of view; (c) 6x zoom in from the 2PEF image in (b).

3.4.1 Phasor map analysis of polarization-resolved 2PEF images

The aim is to perceive the optical properties of the fluorescently excited sample at different polarization angles, enabling the observation of molecular structure and orientation through the fluorescence anisotropy effect. To achieve this, the sample is excited with polarized light, and the fluorescence signal is detected after passing through a rotating LP spanning from 0° to 180° degrees. This process generates a stack of polarimetric images from the 2PEF microscopy, representing various angles, as depicted in Fig. (3.18).

In Chapter 2 (section 2.5.1.2), a phasor analysis based on a time-varying polarimetric signal sequence was introduced. In this section, a different post-treatment protocol is applied to the entire raw image dataset to convert the angularly varying signal, which consists of a stack of images on a pixel-by-pixel basis. Analyzing the polarization-resolved signal provides information about the

molecular orientation through the nonlinear fluorescence anisotropy. As a result, the intensity of each stack of pixels in the image is dependent on the angle.

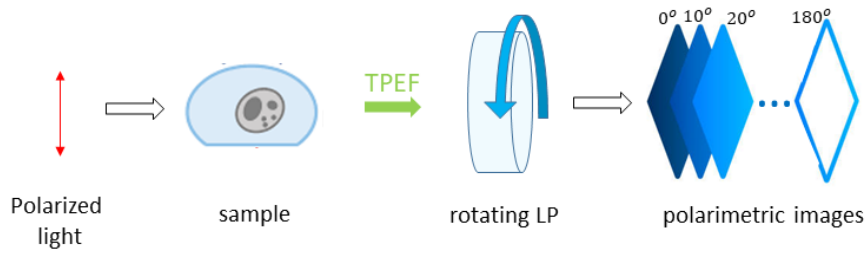

Figure 3.18. The operational scheme of the polarization-resolved fluorescence laser scanning microscope. The anisotropic emission is captured by scanning the image angle-by-angle, resulting in a stack of polarimetric images. TPEF: Two-photon excitation fluorescence; LP: Linear polarizer.

Again referring back to section (2.5.1.2), phasor map can be applied to any intensity-varying data such as fluorescence through the utilization of a Fourier transform. The angular dependent fluorescence signal sequence is subjected to Fourier transformation, resulting in a complex number that is depicted on the phasor associated with the polarization-resolved image. In this representation, the real component is represented by the s axis, while the imaginary component is indicated by the g axis on the phasor map, as demonstrated in Fig. (3.19). In the context of polarimetric fluorescence intensity extraction using our configuration, it is observed, as explained in Chapter 2, that the demodulated signal with higher harmonics exhibits a significantly weaker SNR compared to the noise level. Consequently, only the modulation amplitude and corresponding phase of the first harmonic have been considered. Similar to equations (2.24) and (2.25) in Chapter 2, the new image phasor map with coordinates $g(\Theta)$ and $s(\Theta)$, are given by equations (3.3) and (3.4).

$$g(\Theta) = \frac{\sum I(\theta)\cos(2\pi\theta.\Theta)}{\sum I(\theta)} \tag{3.3}$$

$$s(\Theta) = \frac{\sum I(\theta)\sin(2\pi\theta.\Theta)}{\sum I(\theta)} \tag{3.4}$$

where θ is the rotating angle of the LP and Θ =1/180 is the frequency used for the Fourier transform. On this basis, every single pixel can be identified as a vector in phasor space with the coordinates (x, y) mapped to (g, s). Based on the calculations in Chapter 2, the modulation m and phase φ are given by $|m| = \sqrt{s^2 + g^2}$ and $\varphi = \arctan(\frac{s}{g})$. Therefore, a stack of images of the modulated signal is constructed pixel-by-pixel for a given polarization state, which can be visualized in phasor space.

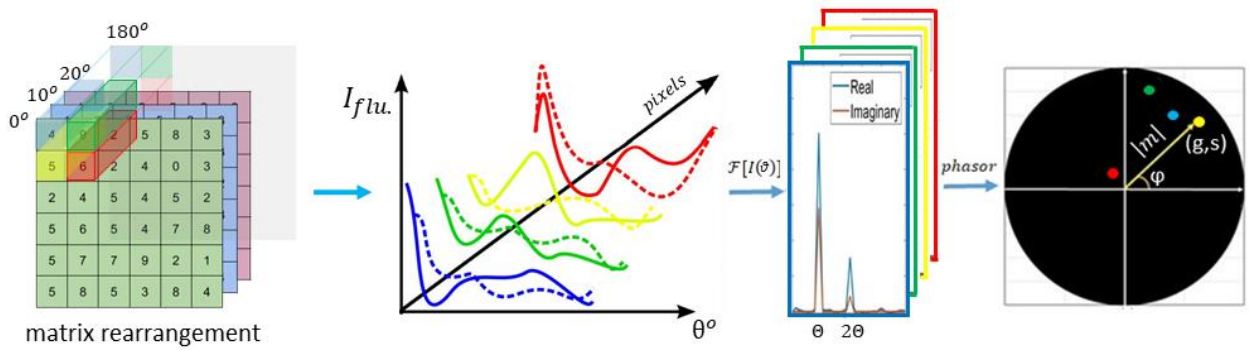

Figure 3.19. Schematic diagram of the protocol to convert the signal $I_{flu.}$ = I(θ) collected into a phasor space at the coordinates (g, s). The solid and dashed curves correspond to normal and abnormal cells, respectively. After recording each signal in different pixels for one period, they are Fourier transformed into a stack of harmonics. The first harmonic is represented here as the phasor position. The phasor of each pixel is located at a distance of $|m|$ from the center of the black circle of samples.

In Fig. (3.19), the signal sequences are assigned different colors corresponding to the pixel locations. The concept behind this assignment is that any changes in the signal will lead to noticeable movement of the phasor map on a pixel-by-pixel basis. This approach facilitates analysis as each intensity pixel $I_i(\theta)$ is uniquely mapped to a position on the image phasor plot based on its polarimetric characteristics. The key advantage of this analysis is its ability to provide localized structural information, allowing for a straightforward interpretation of polarimetric effects through a graphical representation. Ultimately, the image phasor technique offers potential applications in the diagnosis of pathologies and disorders.

3.4.2 Cross-correlation of signal sequences in different pixels

The mutual cross-correlations linked to molecular structure similarities are evaluated in order to study the similarities in pattern of signal sequences in different pixels with respect to a certain pixel in a 2PEF polarimetry image of colorectal cells, with emphasis on a pixel in the background dark side. In signal processing, cross-correlation is a measure of the similarity between two series of signals as their relative displacement changes. Consequently, a positive correlation quantifies the similarities between the two signal sequences, whereas a correlation value of zero indicates the absence of any shared similarities. To compute the cross-correlation of two discrete sequences, it evaluates the similarity between a discrete signal and delayed (lagged) copies of the other signal, considering the lag as a variable. The cross-correlation R_{xy} of two signals x[n] and y[n] at lag k can be defined by equation (3.5).

$$R_{xy}[k] = \sum_{n=-\infty}^{+\infty} x[n]\, y[n-k] \tag{3.5}$$

In this way, y[n] is delayed by lag k, and then the two signals are multiplied and added up. Cross-correlation can be employed to determine the spatial localization of fluorescence signals within cellular structures by comparing the fluorescence signal at different spatial positions within the image on a pixel-by-pixel basis. By examining the cross-correlation values at various lag positions, it becomes possible to identify regions with high or low fluorescence intensity, which can indicate variations in chromatin density. These insights contribute to a deeper comprehension of spatial organization and orientation.

In Fig. (3.20), an example of cross-correlation calculated for signal sequences of two pixels inside a cell nuclei compared to a pixel inside the adjacent cell nuclei in a 2D spheroid with respect to the background is represented. The results reveal similar patterns in the signal sequences associated with the pixels inside the cell nuclei depicted in Figs. (3.20 a) and (3.20 d), while the background remains relatively constant in comparison to any of them, as shown in Fig. (3.20 g). The significant intensity jump observed at the end of the signal (at 180°) indicates a complete period required for the signal intensity to return to 0°.

In this example, the cross-correlation between the two selected pixels inside the cell nuclei is higher than that of the two adjacent cell nuclei. Referring back to the concept of fluorescence anisotropy introduced in Chapter 1, the signal sequences within the cell nuclei signify the effect of the transition dipole moment of the localized molecules, which is detected through the rotation of the LP. Conversely, the consistent intensity level of the background indicates the independence of background intensity from angular rotations.

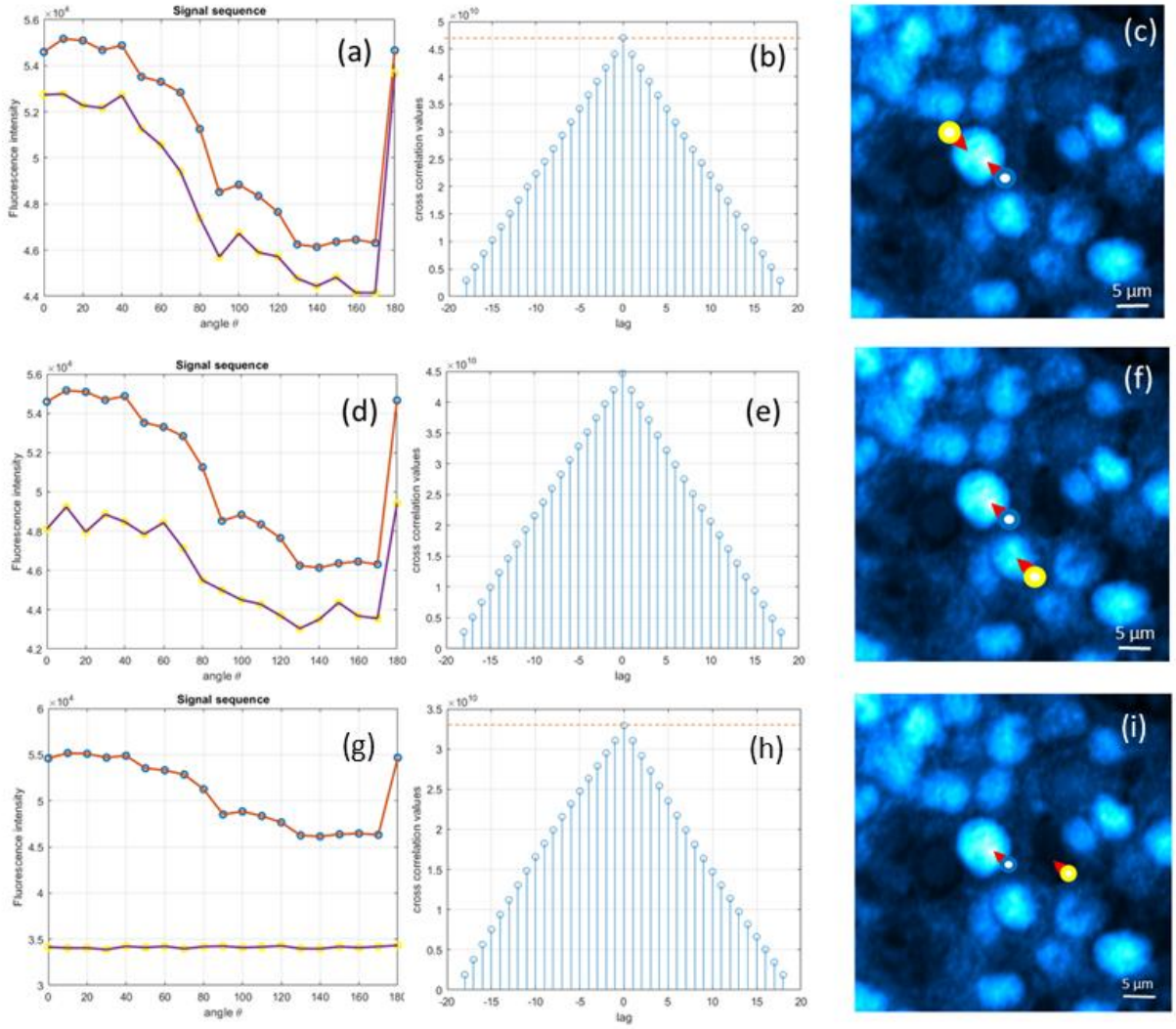

Figure 3.20. (a) Signal sequences of two pixels inside a cell nuclei that is shown in (c); (b) Cross-correlation of the signals in the same nuclei; (d) Signal sequences of two pixels from adjacent cell nuclei that is shown in (f); (e) Cross-correlation of the signals in adjacent cells nuclei. (g) Signal sequences of the pixel inside the cell nuclei compared to the pixel in background that is shown in (i); (h) Cross-correlation of the signals in the cell nuclei and background dark region.

3.4.3 polarized-resolved 2PEF phasor analysis of cancerous vs normal colon cells

By employing polarization-resolved fluorescence microscopy, it becomes possible to detect and analyze the anisotropic effects exhibited by molecules in cancerous cells compared to healthy ones. This technique allows for the examination of the polarization state and intensity of the emitted fluorescence at different excitation polarization configurations. These measurements can provide information about the molecular organization, orientation, and structural changes associated with cancerous cells [59].

The objective is to directly observe the discrimination of healthy colon cells from cancerous images pixel-by-pixel using the image phasor approach. To investigate the molecular deconstructions of cells in the presence of pathology, polarization add-ins are integrated into the 2PEF microscopy setup. Circular and linear polarized light configurations of excitation modules are employed to study colorectal cancer cells in a 2D spheroid. The polarization-resolved 2PEF microscopy images of colon healthy cells in tissue and cancerous cells in 2D spheroid using circularly and linearly polarized light are shown in Figs. (3.21 a) and (3.21 b) respectively. For data analysis, the fluorescence polarimetric images are taken from 0° up to 180° to identify the corresponding image phasor. The observed differences between cancerous and healthy cells can be attributed to various factors, including changes in chromatin structure, alterations in protein organization, and modifications in the cellular microenvironment.

The imaging and the related phasor map are repeated for three different 2PEF images in each polarization configuration to study the two normal and cancerous cases.

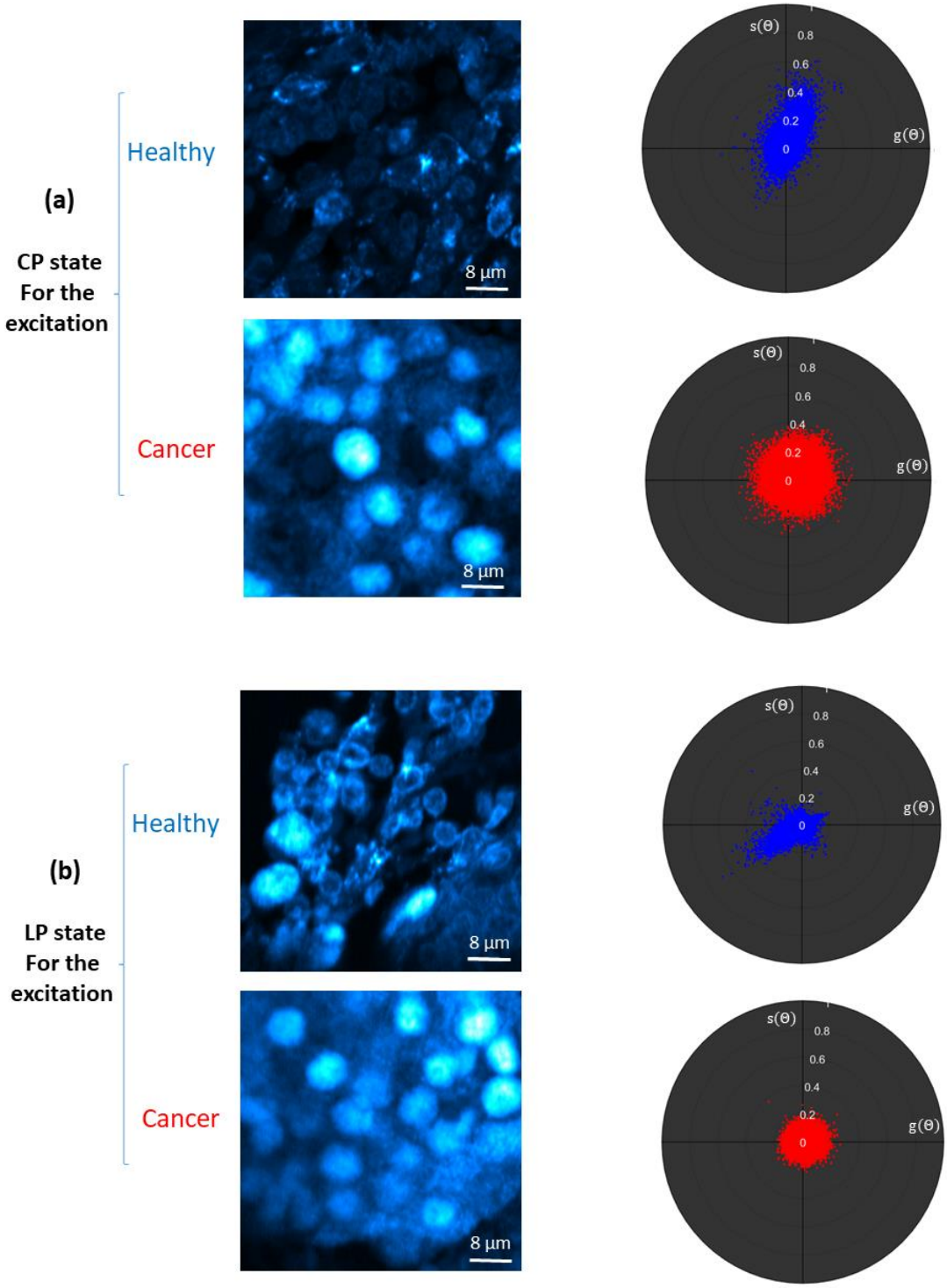

Figure 3.21. Polarization-resolved two-photon excitation fluorescence (2PEF) microscopy captured 512 × 512 images of healthy colon cells and cancerous cells. (a) Circular polarization (CP) is utilized for the excitation, accompanied by the corresponding phasor map. (b) Linear polarization (LP) is employed for the excitation, along with its corresponding phasor map.

According to the results, subtracting the fluorescence images from the background does not alter the corresponding phasor map, indicating the robustness of the phasor approach to background noise levels. Furthermore, in both polarization configurations, the image phasor map effectively distinguishes colon cancer cells from healthy cells based on the anisotropy effect. This effect is likely attributed to the depolarization caused by molecular structural and orientational changes in the cancerous cells, as depicted by the red color in the phasor map. The corresponding phasor map reveals a circular shape, indicating random molecular orientation and disruption in cancerous cells, while a more elongated shape is observed in healthy control cells. The disparity in phasor maps between the two polarization configurations is that the phasor map derived from linearly polarized light excitation appears more condensed and yields results that are seemingly more precise compared to the other configuration.

To further investigate, the SNR of the twelve fluorescence images is assessed. These images consisted of three different fluorescence images each obtained from circular and linear polarized excitation modules for both healthy and cancerous colon cells. The SNR is calculated by dividing the mean intensity by the STD of the background-subtracted fluorescence images. After subtracting the mean intensity in the dark image from the 2PEF images, the SNR is calculated as the ratio of the mean intensity divided by the STD for all pixels in the background-subtracted fluorescence images shown in Fig. (3.22).

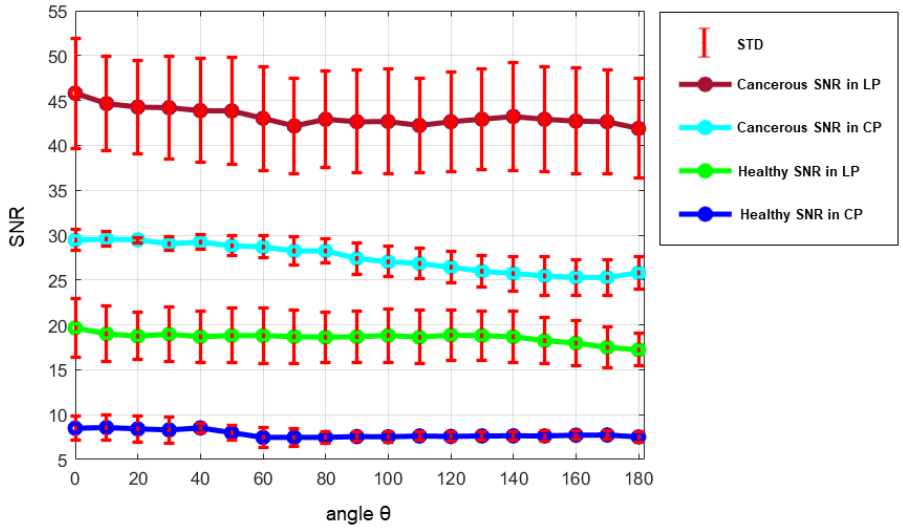

Figure 3.22. Shows the investigation of the signal-to-noise ratio (SNR) in fluorescence images of healthy colon tissue compared to colon cancer in a spheroid. The analysis is performed using both circular polarization (CP) and linear polarization (LP) in the excitation process, with three different images acquired for each polarization configuration. The standard deviation (STD) is calculated as part of the SNR evaluation.

The results demonstrate that using LP for excitation yields a higher SNR compared to CP. This indicates a trade-off in achieving a higher SNR through spatially non-homogeneous fluorophore excitation, as the excitation probability is heavily influenced by the relative orientation between fluorophores and beam polarization. When examining the SNR in the context of CP for excitation, it is observed that the error bars of healthy colon cells decrease, while those of cancerous cells increase. Conversely, when LP is employed for excitation, the error bars remain relatively stable. This observation emphasizes the importance of establishing a minimum SNR threshold to ensure reliable phasor results, which may vary depending on the specific characteristics of the sample and the attached fluorophores (e.g., in tissue or spheroid settings).

3.5 Conclusion

In this chapter, the polarization-resolved 2PEF imaging of colorectal cancer cells is studied using a phasor map data analysis. The importance of early cancer diagnosis is elucidated, highlighting the detection of changes in morphology and metabolism at the cellular/subcellular level. Additionally, the significance of current non-invasive screening techniques as an essential component of disease prevention in modern healthcare is emphasized. Specifically, a cancerous human colorectal adenocarcinoma cell line within a tumor spheroid is examined, exhibiting epithelial morphology reminiscent of colonic primary tumors. A comparison is made between these cancerous cells and normal human colonic epithelial cells in tissue.

Typically, one or multiple imaging modalities are applied, taking into consideration the trade-off between imaging resolution and penetration depth, especially in cases of positive screening results, symptoms, or risk factors. Specifically, in fluorescence microscopy, the quantification of a two-photon image is primarily focused on characterizing the two-photon fluorescence intensity and its correlation with the underlying morphology and sub-cellular structures. However, an important aspect that remains concealed is the molecular orientation that defines the complex architectures within the sample. When excited by polarized light, fluorescent samples exhibit polarized emission. This polarization arises from the selective excitation of fluorophores based on their orientation relative to the direction of the polarized excitation. Consequently, polarization-resolved 2PEF imaging overcomes the limitations of fluorescence anisotropy imaging by providing valuable information about molecular order without making any assumptions about the average orientation of the molecules.

A homemade 2PEF imaging setup is built and developed, integrating the polarization technique with linear and circularly polarized light in the excitation module. The objective is to establish an analogy between the outcomes of the two configurations, characterize the modality, and optimize the quality of fluorescence images. The data analysis involves the introduction and combination of a phasor map approach with polarization-resolved 2PEF microscopy imaging. The newly introduced phasor approach is applied to perform a graphical analysis of the extracted fluorescence signal's anisotropy on a pixel-by-pixel basis. In both polarization configurations, the image phasor map demonstrates the capability to distinguish between colon cancer and healthy cells based on the observed depolarization effect caused by molecular destruction and varying orientations in the cancerous case. It is observed that a higher SNR is achieved when using LP for the excitation, as compared to CP. This trade-off in SNR arises from the spatially non-homogeneous excitation of fluorophores, where the probability of excitation is strongly influenced by the relative orientation between the fluorophores and the polarization of the beam. It is further recognized that establishing a minimum SNR threshold is necessary to ensure reliable phasor results, considering the specific characteristics of the fluorescent sample.

In this preliminary work, repeated imaging and analysis of the related phasor maps are conducted for three different 2PEF images in each polarization configuration to study both normal and cancerous cases, resulting in confirmed feasibility of the phasor approach. However, to better validate the phasor approach, it is suggested that a higher number of samplings and validations be performed through numerical simulations, incorporating data clustering and classification approaches.

Several suggestions can be considered. Firstly, the phasor analysis can be repeated over a co-cultured sample that includes both healthy and pathological cells within the same FOV. This allows for a comprehensive evaluation of the phasor behavior in complex cellular environments. Additionally, the scattering effect at different depths of scattering within cellular layers should be determined to enhance the interpretation of phasor measurements. Calibration of the phasor map using simple optical elements, such as liquid crystals, can further improve the accuracy and precision of the phasor analysis. These steps will enable the development and validation of the phasor approach on various disorders and pathological samples, incorporating a refined analysis of the phasor sensitivity to fluorescence anisotropy while considering sample parameters such as depth position and FOV dimensions.

General conclusion

In the scope of this thesis, the focus was on both polarization-resolved label-free and fluorescence laser scanning microscopy imaging, utilizing light-matter interaction to study cellular structures and macromolecular organizations such as chromatin in order to discriminate anomalies from healthy cells. Label-free microscopy, specifically polarization-based MM microscopy, describes the linear relationship between the polarization states of the incident light beam and the resulting light after passing through a sample. This technique provides valuable information on optical activity and full polarimetric characteristics. One important component of the MM is CD, which assesses the differential absorption of left- and right-handed circularly polarized light, making it sensitive to chiral and super-helical macromolecules such as chromatin, which are densely packed inside cell nuclei. Outside the absorption band, a weak scattered light known as the CIDS signal is present.

In the first part of this work, homemade single-point spectroscopy and laser scanning microscopy imaging setups were employed. To generate circular left and right polarization states at a frequency of 50 kHz, a PEM was utilized. The reference frequency of the PEM was synchronized to a lock-in amplifier to extract the CIDS signal. The existing setup was upgraded to an open configuration to enhance performance in polarization-resolved laser scanning microscopy and confocal fluorescence microscopy. This upgrade was aimed at facilitating integration with other microscopy modalities. Furthermore, image processing programs were developed along with procedures to enable automated measurements and analysis. CIDS was validated as a tool to monitor modifications in chromatin and membrane morphology. CIDS microscopy imaging offers a simple and non-invasive technique to identify cell types, such as murine cells, which exhibit different CD influences. Statistical methods were applied to analyze data from multiple samples to validate the conclusions. The bimodal imaging method was employed on human and mouse cells, with analysis conducted through segmentation of optically active regions based on the threshold of normalized intensity images. This approach facilitated the comparison of fluorescent images with relative CIDS images, verifying the identification of mouse cells through sectioning. The CIDS images provided comprehensive information primarily about the cell membrane morphology of intact cells. Consequently, the combination of both modalities yielded complementary cellular-level information. It was demonstrated that rodent cells could be easily distinguished based on their membrane morphology, without the need for labeling or post-cellular treatments.

A framework of analytical methods, known as the phasor approach, was introduced to analyze the averaged localized polarimetric contrast and determine the mixture of structures within the illumination volume. The phasor map approach is offered as a simple and intuitive graphical representation for interpreting the polarimetric properties of a sample in microscopy modalities. When microscopic polarimetry is combined with the phasor approach, the results can be interpreted without requiring prior knowledge of complex formalism or advanced post-processing skills. In this regard, the modulated single-point CIDS spectroscopy signal was simulated from reference optically active materials, graphically analyzed with the phasor map, and compared with experimental data for the first time to our knowledge. It was demonstrated that the participation of different MM optical activities at a single point on samples can be understood using a phasor map, with the overall phasor map representing the result of these elements. The application of the phasor approach to bio-samples such as isolated nuclei indicated its sensitivity in discriminating between linear birefringence and circular dichroism, enabling direct interpretation of this analysis method. Additionally, the minimum reliable SNR of a modulated signal was estimated to be transformed and represented graphically on the phasor map.

The single-point CIDS spectroscopy was extended into CIDS laser scanning image microscopy. A lock-in detection was automated for the direct acquisition of phasor data, and new types of samples, such as progeria cells, were proposed for the analysis of chromatin. The image phasor map approach was demonstrated to provide an easy, robust, and intuitive graphical analysis for discriminating different regimes of highly compacted bio-macromolecules using polarization-resolved optical scanning microscopy. In line with this, the polarization-resolved imaging modality was integrated into a confocal fluorescence optical microscopy, and data were analyzed using statistical methods in multiple trials. The interpretation and graphical representation of the data were performed using the image phasor map.

The polarimetric imaging method was initially applied to complex crystal structures such as starch granules. These structures were analyzed by segmenting various optical active regions and graphically represented using the corresponding image phasor map, which served as a baseline for general imaging interpretation. The introduced phasor approach was then employed on chiral bio-samples, enabling the discrimination of normal HEK cells from those affected by progeria syndrome based on chromatin compaction level and nuclei morphology deformations. This discrimination was achieved using the bimodal optical laser scanning microscopy.

The application of nonlinear optical contrasts in imaging has greatly benefited from significant advancements in polarization control. As these processes involve high-order matter-field interactions, the ability to tune polarization states offers crucial insights into the structural behavior of molecular organizations. Fluorescence polarization microscopy techniques hold the potential to detect molecular structures by analyzing changes in the polarization properties of light during its interaction with molecules. This underscores the importance of polarization control in enabling new avenues for studying and characterizing complex molecular systems through nonlinear fluorescence imaging techniques. Moreover, this approach enables the improvement of imaging

quality in tissue with less being hindered by the presence of multiple scattered photons originating from deep layers.

To enhance the capabilities of 2PEF laser scanning microscopy with polarization contrast, a new homemade 2PEF microscope adapted for colon cancer diagnosis was built and developed. The proposed modality involves polarization-resolved microscopy imaging and incorporates two configurations of polarization add-ins at the excitation and detection sides. In the first configuration, CP is utilized to illuminate the sample at a non-preferential angle, while fluorescence detection is achieved by rotating a linear polarizer in the detection module. In the second configuration, rotating LP is employed to illuminate the sample, with the fluorescence signal detected at a fixed angle of another linear polarizer on the detection side.

Distinct features, such as a necrotic core and a proliferating periphery, are observed in the 2PEF microscopy images of the cancerous cells within the spheroids. The fluorescence anisotropy was measured using the configuration with rotating LP during the excitation, revealing sinusoidal behavior. Moreover, image analysis facilitated a clear differentiation between normal and cancerous 2D spheroid models. By capturing a stack of modulated signal images pixel-by-pixel, a phasor map was constructed. This new phasor map aimed to differentiate multicellular spheroids of cancerous colon cells (HT29) from noncancerous human epithelial cells (HCoEpiC) in tissue biopsies, leveraging the anisotropic effect as a structural biomarker at the molecular level. The phasor map of healthy colon cells exhibits an elongated cluster of points in specific directions, whereas the phasor map of cancerous cells shows a round shape. This round shape can be attributed to the random depolarization of light caused by molecular deformations. The findings also revealed a higher SNR in fluorescence when the excitation beam was linearly polarized compared to circular polarization. However, this higher SNR comes with a trade-off, as non-homogeneous illumination can impact the study of cells and organelles, depending on the specific applications.

Based on this preliminary work, the imaging and phasor map analysis were repeated for three different 2PEF images in each polarization configuration, yielding consistent results for both normal and cancerous cases. However, further validation of the phasor approach is necessary, which can be achieved through additional experimental measurements, numerical simulations, and the utilization of data clustering methods. To enhance validation, it is recommended that the phasor analysis be conducted on a co-cultured sample that includes both healthy and pathological cells within the same FOV. This approach will allow for the assessment of scattering effects at different depths of cellular layers and the calibration of the phasor map using simple optical elements such as liquid crystals.

Outlook

The CIDS method, along with its simple calculations, paves the way for visualizing the polarimetric contrasts of a localized region *in-situ*, enabling a better understanding of isolated cell nuclei at the nanoscale. This contributes to the development of an easy diagnostic technique for the identification of cell pathologies in *in-vivo* microscopy.

We believe that studying and integrating a clustering approach should be the immediate focus of this work. The framework of analytical approaches, such as the phasor map, can be further developed to create highly sensitive and user-friendly mechanisms for tracking of microscopic objects, including different microscopic species and phenotypes of specific viruses in the future.

Biomarkers, like molecular structures, can be individually optimized for specific applications, leading to increased diagnostic accuracy. When combined with phasor map data analysis, they provide a means to benchmark multimodal diagnostic tools. We suggest the development and validation of our phasor approach on various disorders and pathological samples through refined analysis of the phasor sensitivity to fluorescence anisotropy, while considering sample parameters such as depth position and FOV dimensions.

It is important to note that, as a future perspective for this research, the structural information of nanoscale organizations can be analyzed using various machine learning and non-parametric classification approaches in addition to phasor map data analysis. With larger fields of view being imaged and training data being automatically generated for the presented measurements. Furthermore, the adaptation of phasor map, machine learning, and clustering tools based on image analysis can be extended to 3D images.

References

[1] E. J. Kuipers, et al., "*Colorectal cancer screening - optimizing current strategies and new directions*," Nat. Rev. Clin. Oncol. , vol. 10, no. 3, p. 130–142, 2013.

[2] H. Zeng, et al., "*Optical spectroscopy and imaging for early lung cancer detection: a review*," Photodiagnosis and photodynamic therapy, vol. 1, no. 2, pp. 111-122, 2004.

[3] V. V. Tuchin, et al., Multimodal Optical Diagnostics of Cancer, 1st ed., Springer International Publishing , 2020.

[4] S. Coda, et al., "*Biophotonic endoscopy: a review of clinical research techniques for optical imaging and sensing of early gastrointestinal cancer*," Endosc. Int. Open, vol. 03, no. 05, p. E380–E392, 2015.

[5] I. Georgakoudi and K. P. Quinn, "*Optical Imaging Using Endogenous Contrast to Assess Metabolic State*," Annu. Rev. Biomed. Eng., vol. 14, no. 1, p. 351–367, 2012.

[6] P. So, et al., "*Two-photon deep tissue ex vivo imaging of mouse dermal and subcutaneous structures*," Opt. Express, vol. 3, p. 339–350, 1998.

[7] D. Kobat, et al., "*In vivo two-photon microscopy to 1.6-mm depth in mouse cortex*," J. Biomed. Opt, vol. 16, no. 106014, 2011.

[8] V. Ntziachristos, "*Going deeper than microscopy: the optical imaging frontier in biology*," Nat. Methods, vol. 7, p. 603–614, 2010.

[9] K. D. Bonin, et al., "*Two-photon electric-dipole selection rules*," J. Opt. Soc. Am., no. B1, pp. 52-55, 1984.

[10] N. Ghosh, et al., "*Mueller matrix decomposition for polarized light assessment of biological tissues*," J. Biophoton, vol. 2, no. 145, 2009.

[11] D. Axelrod, "*Carbocyanine dye orientation in red cell membrane studied by microscopic fluorescence polarization*," Biophys. J., vol. 26, pp. 557-573, 1979.

[12] P. Ferrand, et al., "*Ultimate Use of Two-Photon Fluorescence Microscopy to Map Orientational Behavior of Fluorophores*," Biophys. J., vol. 106, no. 11, pp. 2330-2339, 2014.

[13] J. Lazar, et al., "*Two-photon polarization microscopy reveals protein structure and function*," Nat. Methods, vol. 8, pp. 684-690, 2011.

[14] J. A. Dix and A. S. Verkman, "*Mapping of fluorescence anisotropy in living cells by ratio imaging. Application to cytoplasmic viscosity*," Biophys. J., vol. 57, pp. 231-240, 1990.

[15] M. Adler and T. R. Tritton, "*Fluorescence depolarization measurements on oriented membranes*," Biophys. J., vol. 53, pp. 989-1005, 1988.

[16] A. Pierangelo, et al., "*Polarimetric imaging of uterine cervix: a case study*," Opt. Express, vol. 21, pp. 14120-14130, 2013.

[17] J. Lad, et al., "*Polarimetric biomarkers of peri-tumoral stroma can correlate with 5-year survival in patients with left-sided colorectal cancer*," Sci Rep 12, vol. 12, no. 12652, 2022.

[18] B. O. Meyer, "*Multimodal Biophotonics Imaging of Cancer Biomarkers*," PhD Thesis, 2020.

[19] W. B. Coleman, "*Neoplasia, Molecular Pathology*," Elsevier, p. 71–97, 2018.

[20] P. Rawla, et al., "*Epidemiology of colorectal cancer: Incidence, mortality, survival, and risk factors*," Przeglad Gastroenterologiczny , vol. 14, no. 2, 2019.

[21] F. Bray, et al., "*Global cancer statistics 2018: GLOBOCAN estimates of incidence and mortality worldwide for 36 cancers in 185 countries*," CA Cancer J. Clin., vol. 68, no. 6, p. 394–424, 2018.

[22] S. Siri, et al., "*The Macro- and Micro-Mechanics of the Colon and Rectum I: Experimental Evidence*," MDPI-Bioengineering, vol. 7, no. 130, 2020.

[23] P. Holzer, et al., "*Surveillance of the gastrointestinal mucosa by sensory neurons*," J Physiol Pharmacol., vol. 52, no. 4 Pt 1, pp. 505-21, 2001.

[24] F. Maier, et al., "*The heterogeneous morphology of networked collagen in distal colon and rectum of mice quantified via nonlinear microscopy*," Journal of the mechanical behavior of biomedical materials, vol. 113, no. 104116, 2021.

[25] F. Varnat, et al., "*Human colon cancer epithelial cells harbour active HEDGEHOG-GLI signalling that is essential for tumour growth, recurrence, metastasis and stem cell survival and expansion*," EMBO Mol Med. , vol. 1, no. 6-7, pp. 338-351, 2009.

[26] M. A. Keum, et al., "*Clinicopathologic factors affecting recurrence after curative surgery for stage I colorectal cancer*," J. Korean Soc. Coloproctol., vol. 28, no. 1, p. 49–55 , 2012.

[27] S. L. Stewart, et al., "*A population-based study of colorectal cancer histology in the United States 1998–2001*," Cancer, vol. 107, no. S5, p. 1128–1141, 2006.

[28] R. J. Davies, et al., "*Colorectal cancer screening: Prospects for molecular stool analysis*," Nat. Rev. Cancer, vol. 5, no. 3, p. 199–209, 2005.

[29] M. S. Cappell, "*The pathophysiology, clinical presentation, and diagnosis of colon cancer and adenomatous polyps*," Med. Clin. North Am., vol. 89, no. 1, pp. 1-42, 2005.

[30] M. I. Koukourakis, et al., "*Comparison of metabolic pathways between cancer cells and stromal cells in colorectal carcinomas: a metabolic survival role for tumor associated stroma*," CANCER Res., vol. 66, no. 2, p. 632–637, 2006.

[31] M. J. Pollheimer, et al., "*Tumor necrosis is a new promising prognostic factor in colorectal cancer*," Hum. Pathol. , vol. 41, no. 12, p. 1749–1757, 2010.

[32] C. J. Gulledge and M. W. Dewhirst, Tumor oxygenation: A matter of supply and demand, Anticancer Res., 1996.

[33] E. J. Kuipers, et al., "*Colorectal cancer screening - optimizing current strategies and new directions*," Nat. Rev. Clin. Oncol. , vol. 10, no. 3, p. 130–142, 2013.

[34] Y. Hoshi and Y. Yamada, "*Overview of diffuse optical tomography and its clinical applications*," J. Biomed. Opt., vol. 21, no. 9, 2016.

[35] L. V. Wang, Multiscale photoacoustic microscopy and computed tomography, Nat. Photonics, 2009.

[36] G. Thomas, et al., "*Advances and challenges in label-free nonlinear optical imaging using two-photon excitation fluorescence and second harmonic generation for cancer research*," J. Photochem. Photobiol. B Biol., no. 141, p. 128–138, 2014.

[37] E. Lin and A. Alessio, "*What are the basic concepts of temporal, contrast, and spatial resolution in cardiac CT*," J. Cardiovasc. Comput. Tomogr. , vol. 3, no. 6, p. 403–408, 2009.

[38] D. J. Evers, et al., "*Optical spectroscopy: current advances and future applications in cancer diagnostics and therapy*," Future Oncology, vol. 8, no. 3, 2012.

[39] A. Mayer, et al., "*Two-photon laser scanning fluorescence microscopy*," Science, vol. 248, p. 73-76, 1990.

[40] F. Helmchen and W. Denk, "*Deep tissue two-photon microscopy*," Nat. Methods, vol. 2, p. 932-940, 2005.

[41] W. R. Zipfel, R. M. Williams, "*Nonlinear magic: Multiphoton microscopy in the biosciences*," Nat. Biotechnol., vol. 21, no. 11, p. 1369–1377, 2003.

[42] J. Puneet, et al., "*Fluorescence Anisotropy as a Temperature-Sensing Molecular Probe Using Fluorescein*," Micromachines , vol. 12, no. 9, p. 1109, 2021.

[43] L. Chen, et al., "*Advances of super-resolution fluorescence polarization microscopy and its applications in life sciences*," Elsevier-Computational and Structural Biotechnology Journal, vol. 18, p. 2209–2216, 2020.

[44] S. Brasselet, "*Fluorescence polarization modulation super-resolution imaging provides refined dynamics orientation processes in biological samples*," Light Sci Appl., vol. 11, no. 322, p. 11, 322 , 2022.

[45] S. Brasselet, "*Polarization-resolved nonlinear microscopy: application to structural molecular and biological imaging*," Adv. Opt. Photon. 3, 205- (2011), vol. 3, no. 3, p. 205-271, 2011.

[46] A. N. Yaroslavsky, et al., "*Fluorescence Polarization of Methylene Blue as a Quantitative Marker of Breast Cancer at the Cellular Level*," Sci. Rep., vol. 9, no. 940, 2019.

[47] H. Kamin, et al., "*Quantification of collagen networks in mammary tumors using TPEF and laser-based tomography*," Proceeding SPIE, vol. 11966, 2022.

[48] J. F. Adur, et al., "*Quantitative changes in human epithelial cancers and osteogenesis imperfecta disease detected using nonlinear multicontrast microscopy*," J. Bio. Opt., vol. 17, no. 8, 2012.

[49] A. Gasecka, et al., "*Quantitative Imaging of Molecular Order in Lipid Membranes Using Two-Photon Fluorescence Polarimetry*," Biophy. J., vol. 97, no. 10, pp. 2854-2862, 2009.

[50] A Nag and D Goswami, "*Polarization induced control of single and two-photon fluorescence*," J. Chem. Phys. , vol. 132, no. 15, 2010.

[51] S. C. J. Meskers, Circular Polarization of Luminescence as a Tool To Study Molecular Dynamical Processes, vol. 6, John Wiley & Sons, Ltd, 2022.

[52] M. Kapałczyńska, et al., "*2D and 3D cell cultures – a comparison of different types of cancer cell cultures*," Arch. Med. Sci., vol. 14, no. 4, p. 910–919, 2018.

[53] C. G Hubert, et al., "*A Three-Dimensional Organoid Culture System Derived from Human Glioblastomas Recapitulates the Hypoxic Gradients and Cancer Stem Cell Heterogeneity of Tumors Found in Vivo*," Cancer Res. , vol. 76, no. 8, p. 2465–2477 , 2016.

[54] I. Van Zundert, et al., "*From 2D to 3D Cancer Cell Models—The Enigmas of Drug Delivery Research*," Nanomaterials, vol. 10, no. 11, p. 2236, 2020.

[55] G. Thomas, et al., "*Estimating the risk of squamous cell cancer induction in skin following nonlinear optical imaging*," J. Biophotonics , vol. 7, no. 7, p. 492–505 , 2014.

[56] H. Oehring, et al., "Ultrastructure and reproduction behaviour of single CHO-K1 cells exposed to near infrared femtosecond laser pulses," Scanning, vol. 22, no. 4, p. 263–270, 2000.

[57] S. A. Haider, et al., "*Fluorescence microscopy image noise reduction using a stochastically-connected random field model*," Sci Rep., vol. 6, no. 20640, 2016.

[58] M. Acland, et al., "*Mass Spectrometry Analyses of Multicellular Tumor Spheroids*," Proteomics clinical appl., vol. 12, no. 3, 2018.

[59] W. A. Lea and A. Simeonov, "*Fluorescence polarization assays in small molecule screening*," Expert Opinion on Drug Discovery, vol. 6, no. 1, pp. 17-32, 2011.

Acknowledgements

First and foremost, I would like to express my deep gratitude to the nanoscopy group of Prof. Alberto Diaspro at the Italian Institute of Technology (IIT) and the department of Physics at the University of Genoa (UNIGE). I am incredibly thankful for the opportunity to work on this project, to contribute, and to learn in the Nikon lab, surrounded by inspiring individuals.

I would also like to extend my sincere appreciation to my supervisor, Dr. Aymeric Le Gratiet, for his unwavering trust, support, and invaluable advice that kept me motivated throughout all the challenges.

Furthermore, I am grateful to Prof. Peter E. Andersen for providing me with the opportunity to work at the Technical University of Denmark (DTU) and embark on a remarkable project to develop a homemade microscope alongside an exceptional group of individuals in the Biophotonics group. I would like to express my thanks to Prof. Lars René Lindvold for his inspiring discussions and generous assistance in sample transportation.

I am privileged to have begun my Ph.D. journey with Fabio Callegari, and it was an absolute pleasure to share both the joys and the difficulties with him. To Newsha, Milad, Atena, Barbod, Farbod, Reza in Italy, and Hossein in Iran, I extend my deepest gratitude for being the best friends and incredible sources of support.

Lastly, I would like to express my heartfelt thanks to my parents and family for their unwavering presence and support throughout this journey. I am truly grateful for the indescribable support you have provided me with.

Communications and Publications

1. Communications

1. OSA Biophotonics Congress: Biomedical Optics, 20-23 April 2020; **online**

The Biomedical Optics Congress focused on technological solutions to medical challenges and medical applications. It covered diverse, cutting-edge research and innovative new tools and techniques.

2. CLEO 2020 Conference on Lasers and Electro–Optics, 11-15 May 2020; **online**

Several talks on innovative advances, research and new technologies on all the aspects of electro-optic technologies, having applications in a number of fields, from biophotonics to advanced manufacturing, telecommunications, and autonomous vehicles industry.

3. SIF Congress, Congresso della Società Italiana di Fisica, 14-18 September 2020; **online**

Oral presentation: "Resolution improvement in circular intensity differential scattering scanning microscopy integrated with two photon fluorescence microscopy using a phasor plot approach"

4. Summer School 2020 on Computational Photonics held by Karlsruhe Institute of Technology (KIT) in Karlsruhe, Germany, 20-26 September 2020; **on-site**

5. BPS 2021, 65th Biophysical Society Annual Meeting, 22-26 February 2021; **online**

Oral presentation: "Resolution improvement in CIDS super-resolution microscopy using a phasor plot approach"

6. ECBO 2021, European Conferences on Biomedical Optics (ECBO), 20 - 24 June 2021; **online**

Oral presentation: “Multimodal polarization-resolved/fluorescence optical scanning microscopy for chromatin organization imaging”

7. EBSA 2021, 13th European Biophysics Conference in Vienna, Austria, 24-28 July 2021; **on-site**

Poster presentation: “Phasor analysis in circular polarization-resolved optical scanning microscopy for biological organization imaging”

8. SIF 107 Congress, Congresso della Società Italiana di Fisica, 13-17 September 2021; **online**

Oral presentation: “Phasor analysis in polarization-resolved optical scanning microscopy for progeria organization imaging”

9. BPS 2022, 66th Biophysical Society Annual Meeting, 22-26 February 2022; **online**

Oral presentation: “Image phasor analysis in polarization-resolved optical scanning microscopy of neuroblastoma cells”

10. Focus On Microscopy (FOM 2022), Image Analysis, 10 - 13 April 2022; **online**

Oral presentation: “Phasor map analysis in polarization-resolved optical scanning microscopy of Hutchinson-Gilford progeria cell”

11. The 10th International Graduate summer school Biophotonics '22 in Ven Iland, Sweden, 11-18 Jun 2022; **on-site**

Poster presentation: “Phasor analysis in polarization-resolved optical scanning microscopy for biological organization imaging”

2. Publications

1. "Phasor map analysis to investigate Hutchinson-Gilford progeria cell under polarization-resolved optical scanning microscopy", **A. Mohebi**, A. Le Gratiet, A. Trianni, F. Callegari, P. Bianchini, A. Diaspro; *Scientific Reports*, Vol. 12(1679), DOI: 10.1038/s41598-022-05755-1, (2022)

2. "Image phasor analysis in polarization-resolved optical scanning microscopy of neuroblastoma cells", **A. Mohebi**, A. Le Gratiet, F. Callegari, P. Bianchini, A. Diaspro; *Biophysical Journal*, Vol. 121 (3), 279a, DOI: 10.1016/j.bpj.2021.11.1356, (2022)

3. "Combined approach using circular intensity differential scattering microscopy under phasor map data analysis", **A. Mohebi**, A. Le Gratiet, R. Marongiu, F. Callegari, P. Bianchini, A. Diaspro; *Applied Optics*, Vol. 60 (6), 1558-1565, DOI: 10.1364/AO.417677, (2021)

4. "Multimodal polarization-resolved/fluorescence optical scanning microscopy for chromatin organization imaging", **A. Mohebi**, Aymeric Le Gratiet, Fabio Callegari, Paolo Bianchini and Alberto Diaspro; *Proc. (ECBO) OSA-SPIE*, Vol. 11922, Advances in Microscopic Imaging III; 119220V, DOI: 10.1117/12.2615731, (2021)

5. "Review on complete Mueller matrix optical scanning microscopy imaging", A. Le Gratiet, **A. Mohebi**, F. Callegari, P. Bianchini, A. Diaspro; *Applied Sciences* Vol. 11 (4), 1632, DOI: 10.3390/app11041632, (2021)

6. "Polarization label-free microscopy imaging of biological samples by exploiting the Zeeman Laser emission", F. Callegari, A. Le Gratiet, A. Zunino, **A. Mohebi**, P. Bianchini, A. Diaspro; *Frontiers in Physics*, Vol. 9, 758880, DOI: 10.3389/fphy.2021.758880, (2021)

7. "Multispectral Stokes/Mueller Detection Module for Multiphoton/Fluorescence Confocal Scanning Imaging Microscopy", A. Le Gratiet, R. Marongiu, M.W.W. Ashraf, **A. Mohebi**, F. Callegari, P. Bianchini, A. Diaspro; *Biophysical Journal*, Vol. 120 (3), 355a, (2021)

8. "Cellular identification between different cell types using Circular Intensity Differential Scattering Microscopy Imaging", **A. Mohebi**, A. Le Gratiet, M. Oneto, F. Callegari, P. Bianchini, A. Diaspro;
under review.